



Versuchsanstalt für Wasserbau
Hydrologie und Glaziologie
der Eidgenössischen
Technischen Hochschule Zürich

Mitteilungen

222

**Numerical Simulation of
Embankment Breaching Due to Overtopping**

Christian Volz

Zürich, 2013

Herausgeber: Prof. Dr. Robert Boes

Zitiervorschlag für VAW-Mitteilungen:

Volz, C. (2013).

Numerical Simulation of Embankment Breaching Due to Overtopping.

Mitteilungen 222, Versuchsanstalt für Wasserbau, Hydrologie und Glaziologie (VAW),
R. M. Boes, Hrsg., ETH Zürich.

Im Eigenverlag der
Versuchsanstalt für Wasserbau,
Hydrologie und Glaziologie
ETH Zürich
CH-8093 Zürich

Tel.: +41 - 44 - 632 4091
Fax: +41 - 44 - 632 1192
e-mail: info@vaw.baug.ethz.ch

Zürich, 2013

ISSN 0374-0056

Digital Object Identifier (DOI): [10.3929/ethz-a-009967594](https://doi.org/10.3929/ethz-a-009967594)

Preface

Due to the large impact of dam break flows on infrastructure and society, this research topic has been receiving scientific attention for many years. Despite this fact, there are still a number of aspects to be improved in mathematical models of dam breaching. The main objective of this research project was therefore to develop a 2D physically-based numerical model for the simulation of non-cohesive embankment breaching due to overtopping. This required capturing the relevant processes such as sediment erosion, transport and deposition by surface flow, gravitationally-induced side wall failure of the breach channel, and the interaction of the former with subsurface flow at least in a simplified manner. In contrast to parameter models, which use severe simplifications to the governing equations and are solved without spatial discretization of the site into computational cells, physically-based models solve the full flow equations, apply a more physically-based erosion modelling, and discretize the site geometry using computational meshes.

To reach this goal, Dr. Volz first analyzed the relevant embankment failure modes due to overtopping (progressive vs. head-cut erosion) as well as the main physical processes involved and their mutual interactions. In a multi-physical approach, the relevant processes are typically accounted for in specific sub-models, which are then coupled to render the aggregate numerical model. It should be pointed out here that the general working environment is the VAW natural hazard simulation software package *BASEMENT* with its 2D modules for both hydrodynamics and sediment transport.

Dr. Volz specified the needs for each sub-model and carefully tested the capabilities of existing numerical tools, from which he deduced the changes and extensions to be made. While most breach models make use of structured meshes with regular cells, Dr. Volz chose to use unstructured meshes, requiring a new spatial discretization approach on

the one hand, and a dual-mesh approach to compute the hydrodynamics and sediment transport on different meshes on the other. Unstructured meshes allow for discretization of even complex topographies and embankment geometries, the latter typically forming during dam breaching. Moreover, while most previous investigations neglect the subsurface flow through the embankment, Dr. Volz developed a 3D sub-model accounting for the effect of seepage flow both on the side wall failure and on the sediment transport along the embankment surface, respectively. Regarding the breach channel geometry, the often used approach of geometrical failure modelling based on critical failure angles was improved and extended to unstructured meshes. Also, effects of apparent cohesion were incorporated. Finally, fractional sediment transport with a distinction between bed-load and suspended-load was considered to expand the application range.

I wish to express my gratitude to the Competence Center Environment and Sustainability of the ETH Domain (CCES), who financially supported Dr. Volz' research. The co-reviews of Prof. Dr. P. Rutschmann, Technical University of Munich, and of Dr. R. Föh, VAW, are gratefully acknowledged.

Zurich, January 2014

Prof. Dr. Robert M. Boes

Acknowledgments

At first, I want to thank Dr. R. Fäh for supervising my PhD-thesis and always having time and helpful hints, and Prof. R.M. Boes for the great opportunity and support for this thesis at VAW. Furthermore, I thank my colleagues at the VAW for numerous discussions and their efforts and the knowledge dedicated to the software *BASEMENT*. I also thank Dr. R. Worni from the University of Bern for fruitful co-operations and exchange of ideas.

I am grateful to the Competence Center Environment and Sustainability of the ETH Domain (CCES) for funding this research as well as to Prof. P. Burlando for the organization of the APUNCH project and to Prof. S. Springmann and Dr. F. Morales at IGT for various discussions related to embankment breaches. I thank Prof. P. Rutschmann of TU München for the efforts related to the co-examination and Prof. W.H. Hager for suggestions and improvements regarding publications. Furthermore, I thank Dr. M. Eckert at DMT in Essen and Prof. R. Hinkelmann of TU Berlin.

During the last years, I have received support and motivation from my family and friends. Special thanks go to S. König and last but not least I want to thank all contributors to free and open source software projects and the numerous maintainers of hiking paths in the Swiss Alps for their great work.

Zurich, January 2013

Christian Volz

Contents

Preface	i
Acknowledgements	iii
Contents	v
Kurzfassung	1
Abstract	3
1 Overview	5
1.1 Introduction	5
1.2 Problem description and application range	11
1.3 State-of-the-art	17
1.4 Goals and document structure	24
2 Modelling of Overtopping Flow	27
2.1 Introduction	27
2.2 Governing equations - Shallow-Water equations	29
2.3 Empirical closures and source terms	35
2.4 Numerical modelling - Godunov approach	38
2.5 Validation for dam breaks on fixed bed	41
2.6 Summary	45
3 Modelling of Surface Erosion	47
3.1 Introduction	47
3.2 Governing equations for sediment transport	49

3.3	Empirical relations for sediment transport	56
3.4	Numerical modelling	68
3.5	Validation of bed-load transport modelling	75
3.6	Summary	79
4	Modelling of Sub-Surface Flow	81
4.1	Introduction	81
4.2	Governing equation - Richards equation	85
4.3	Empirical constitutive models	87
4.4	Numerical modelling - Lattice-Boltzmann method	90
4.5	Validation of sub-surface flow modelling	99
4.6	Summary	106
5	Modelling of Side Wall Failures	109
5.1	Overview over physical processes	109
5.2	Modelling of mass failures and movements	114
5.3	Summary	125
6	Model Coupling	127
6.1	Introduction	127
6.2	Coupling of surface flow and embankment erosion	129
6.3	Coupling with sub-surface flow	130
6.4	Time synchronization	136
6.5	Summary	138
7	Applications	139
7.1	Introduction	139
7.2	Laboratory plane dyke breach	140
7.3	Laboratory spatial dyke breach	147
7.4	Field-scale dam breach	157

7.5	Natural moraine embankment breach	166
7.6	Summary	173
8	Summary and Outlook	177
8.1	Summary	177
8.2	Outlook	180
	Appendices & Notation	182
	List of Tables	204
	List of Figures	205
	Bibliography	208

Kurzfassung

Die Überströmung und das resultierende Versagen von erodierbaren Dämmen, wie Flussdeiche, Talsperren oder natürliche Dämme, kann zu katastrophalen Ereignissen mit hohem Schadenspotenzial führen. Numerische Simulationen solcher Ereignisse sind nötig um das Prozessverständnis zu erweitern und Vorhersagen zu verbessern. Das Ziel der Arbeit ist die Entwicklung eines multi-physikalischen Ansatzes für die Simulation des strömungsinduzierten Versagens erodierbarer Dämme, bestehend aus überwiegend nicht-kohäsivem Material.

Ein numerisches Modell wurde entwickelt, um die entscheidenden physikalischen Prozesse abzubilden. Dazu gehören die Überströmung des Dammes, die dadurch induzierte Oberflächenerosion, die Sickerströmung durch den Dammkörper und das gravitationsinduzierte Versagen der steilen Seitenwände des Erosionskanals. Diese Prozesse beeinflussen sich gegenseitig auf vielfältige Weise, was im Modell zumindest vereinfacht abgebildet wird. Beispielsweise induziert die Oberflächenerosion das Versagen der Seitenwände des Erosionskanals, die Überströmung führt zur Infiltration in den Dammkörper und die scheinbare Kohäsion des Dammmaterials beeinflusst sowohl die Oberflächenerosion als auch die Stabilität steiler Seitenwände. Im Modell werden die Module gekoppelt ausgeführt, um die gegenseitigen Wechselwirkungen abzubilden. Randbedingungen müssen dynamisch gesetzt werden und Anpassungen der Berechnungsgitter sind nötig.

Die Überströmung des Dammes wird mit den 2D Flachwassergleichungen abgebildet und mithilfe einer Finite-Volumen Methode numerisch gelöst. Für die Modellierung der Oberflächenerosion werden Gleichungen für die Massenerhaltung und für den Transport des Sediments formuliert und mit einer Finite-Volumen Methode gelöst. Zusätzlich wird das Versagen der Seitenwände des Erosionskanals mit einem vereinfachten geometrischen Modell abgebildet. Für die räumliche

Diskretisierung im numerischen Modell werden unstrukturierte Gitter verwendet, wobei eine massenerhaltende "dual-mesh" Diskretisierung für den Sedimenttransport entwickelt wurde. Die Verwendung unstrukturierter Gitter ermöglicht die Anwendung auf Szenarien mit komplexer und unregelmässiger Geometrie.

Desweiteren wurde ein Sickerströmungsmodell entwickelt, welches die 3D Richards-Gleichung basierend auf der Lattice-Boltzmann Methode löst. Das Modell verwendet hierfür ein strukturiertes 3D Gitter zur Abbildung der Strömung im Dammkörper und wird mit den anderen Prozessen gekoppelt ausgeführt. Die resultierenden Porenwasserdrücke im Dammkörper werden verwendet um die Auswirkungen der scheinbaren Kohäsion abzuschätzen.

Das gekoppelte Modell wurde schliesslich auf Laborversuche eines ebenen und eines räumlichen Deichbruchs angewandt. Um die Anwendbarkeit des Modells auf gross-skalige Szenarien zu testen, wurden zusätzlich ein kontrollierter Dammbbruchversuch sowie das Versagen eines natürlichen Moränendamms qualitativ untersucht. Die Ergebnisse der kalibrierten Modelle bestätigen die grundlegenden Modellannahmen und demonstrieren die Anwendbarkeit des numerischen Modells auf realistische und grossräumige Szenarien mit komplexer Geometrie.

Alle numerischen Ansätze und Verfahren wurden in die an der VAW entwickelten Software *BASEMENT* integriert. Dadurch sollen die Vorteile und Möglichkeiten die eine praxistaugliche Software bietet ausgenutzt werden und der Wissenstransfer gefördert werden.

Abstract

The overtopping and subsequent failure of earth embankments including dykes, reservoir dams, tailing dams or natural embankments is a major engineering concern causing hazardous events of large destructive potential. Improvements of numerical simulations of such breach events are important for the understanding of the involved processes and to improve the model predictions. The purpose of this work is the development of a multi-physical simulation approach for non-cohesive earth embankment failures due to overtopping and progressive erosion which is applicable to practical engineering scenarios.

A numerical model is developed considering multiple relevant physical processes, as the overtopping flow, the embankment surface erosion, the sub-surface flow through the embankment and side wall failures at the deepening breach channel. These processes have mutual interactions which shall be considered. For example, the surface erosion triggers the side wall failures, the overtopping flow leads to infiltrations into the embankment and the apparent cohesion of the material influences the surface erosion and the side wall stabilities. Coupling algorithms are implemented to consider these mutual interactions and to obtain a combined modelling approach. Boundary conditions must be set dynamically and mesh adaptations are required during breaching.

The overtopping flow is simulated with the 2D Shallow-Water equations using an explicit Finite-Volume method combined with a Godunov-type approach. To simulate the embankment surface erosion, empirical transport formulas and advection-diffusion equations are applied for bed- and suspended-load transport in combination with 2D sediment mass continuity equations using a Finite-Volume method. Additionally, the lateral breach widening, caused by gravitationally-induced side wall failures, is modelled with a geometrical approach which is enhanced to consider effects of apparent cohesion. For spatial discretization, an ac-

curate novel dual-mesh approach with separate, unstructured meshes for mass conserving hydrodynamic and sediment transport computations is developed. The use of unstructured meshes hereby allows for applications to project sites with complex geometries and topographies.

Furthermore, a sub-surface flow model solving the 3D Richards equation is developed based on the Lattice-Boltzmann method. It applies a structured 3D mesh to simulate the water infiltration and the variably-saturated flow in the embankment and provides the input data needed to assess effects of apparent cohesion.

The combined model is applied to two recent laboratory studies concerning plane and spatial dyke breaches. These enable detailed comparisons between the measured and simulated breach formations, which are needed to confirm the basic model assumptions. To test the model on field-scale scenarios, a controlled dam breach and a failure of a naturally formed moraine embankment are additionally investigated. The results demonstrate the model applicability to realistic scenarios of large extents and complex geometries.

The developed numerical approaches are integrated into the software *BASEMENT*, thereby exploiting advantages and features of a mature software framework and promoting the transfer of knowledge to engineering practice.

1

Overview

1.1 Introduction

1.1.1 Relevance of embankment breaches

In situations where reservoir or stream water levels exceed an earth embankment crest, water overtops the embankment and forms an initial breach channel. The breach channel progressively enlarges with time, leading to a further increase in the overtopping flow. These self-enhancing processes rapidly widen the breach channel and eventually may lead to a complete failure of the structure. This progressive erosion of earth embankments is a major engineering concern and can cause hazardous flood events with large destructive powers regarding human life and properties. In order to prevent or mitigate such events, to create hazard maps and evaluate evacuation measures, there is need to investigate the involved processes with numerical methods. In Switzerland, for example, the hazard map assessment for emergency and evacuation planning of large dams is the third pillar of dam safety philosophy (StAV, "Stauanlagenverordnung") and therefore carries large practical significance.

Due to the growth in population and infrastructure, the destructive potential of river dyke or dam breaches and related flood events is steadily increasing. Furthermore, flood events caused by heavy rain or storm events have increased in intensity and frequency during the past decades. Such catastrophic events have to be supposed to happen more often in the future due to the climate changes and human influences, as stated e.g. by the Fourth Intergovernmental Panel on Climate Change

Assessment - IPCC (2007). The combination of increased destructive potential and more frequent occurrences thereby emphasizes the need for improved numerical assessment tools.

Beside the threat of extreme precipitation and storm events, the occurrence of landslides or avalanches into reservoirs or dammed lakes can generate impulse waves acting as triggering mechanism for embankment failures. Such events may lead to an embankment overtopping and initiate embankment failures due to progressive erosion. Likewise, landslides can form temporal natural embankments which block stream courses and impound temporal lakes. The retreat of glaciers in mountainous regions can also lead to the formation of temporal glacial lakes, which are impounded by the remaining glacial moraines. Such natural embankments then may drain suddenly in case of full or partial failure and generate hazardous flood and debris flows with fatal consequences (Clague and Evans (2000)). These events are expected to be even more affected by the climate change as outlined by Stoffel and Huggel (2012) with focus on alpine regions.

Furthermore, an increasing number of dams will be needed in the next decades to satisfy the raising electricity demands in combination with the increasing importance of sustainable energy sources like water power. This is especially true with regard to pump-storage hydroelectricity which is needed for load balancing and to ensure supply of peak electricity demands.

In addition to the construction of new embankments, the maintenance and enhancement of existing embankments is also an important engineering task which is expected to gain more significance in the near future due to the above mentioned reasons and may profit from improved numerical modelling tools. Man-induced causes such as sabotage and terrorist attacks are also gaining attention as possible source of sudden or progressive embankment failures (Nistor and Rennie (2005)).

1.1.2 Numerical simulations of embankment breaches

In engineering practice often the assumption of instantaneous embankment failures is made. This assumption eases the numerical treatment since only the flood wave propagation has to be considered. Much research was dedicated to this flood wave propagation, and stable and accurate numerical shock-capturing techniques were developed in the last decades for this type of problems (Zoppou and Roberts (2003)). These instantaneous failures are labelled dam 'break' events in this work and are distinguished from gradual embankment failures which are denoted as 'breach' events.

The assumption of instantaneous dam breaks is often too conservative for gradual embankment failures in practice and leads to unrealistic overestimations of the peak breach discharges. Further, relevant information like the duration from breach initiation until the formation of peak discharge, which is an important parameter regarding evacuation measures and warning systems, require considerations of the gradual breach progress. In addition, investigations whether the overtopping flow is able to initiate the breach, and whether the breaching will lead to a complete failure or eventually will come to an end, need to consider the gradual breaching.

Despite the significance of numerical investigations, simulations of gradual breaches and the involved erosion processes gained attention only recently. This is mainly attributed to the interdisciplinary aspects of the task, comprising hydraulics, soil mechanics and sediment transport, the complexity of the involved processes and the limited understanding of the process interactions. Several different fields of expertise are involved in breach formation and need to be considered in a combined multi-physical approach for reliable breach modelling.

This work aims at simulating the relevant processes and wants to provide a multi-physical numerical tool for embankment breach simulations. It shall contribute to gain further knowledge about the involved processes and allow for applications to embankment breach scenarios of practical relevance.

1.1.3 Examples of earth embankment breaches

Erodible earth embankments can be found in many different locations, with different shapes and for different purposes around the world. In the following list, they are categorized in four major groups which differ in purpose, configuration and their hazardous potentials in case of breaching. Figure 1.1 depicts examples for corresponding historical breach events. Despite the differences in dimensions, material and inner structures of these embankment types, they often show common failure mechanisms.

River or coastal dykes. These dyke structures are typically of small or medium size, up to several meters in height. Standard dyke structures often consist of sediment material found in the vicinity. Although dykes may be constructed with inner cores, filter zones and surface protections, they are often rather simple homogeneous structures and as such are a focus of this work. River dykes usually are situated along a water course and are overtopped laterally, whereas coastal dykes are typically overtopped in frontal direction and additionally have to withstand significant wave impacts and periodic wave overtopping. Overtopping of river or coastal dykes during flood events is a major engineering problem and can cause wide-ranging flooding and inundation of areas situated next to the dykes. Figure 1.1 (a) depicts the flooding of the Rhine valley upstream of Lake Constance due to a dyke breach during the flood event of 1927 (IRR (1992)).

Reservoir dams. These embankment structures are often of medium or large size and are typically constructed with multiple inner zones and having inner cores. Erodible reservoir dams are subject to similar failure mechanisms due to overtopping as dykes, although the geotechnical failure processes can become more complex and difficult to assess. According to the statistics of the International Commission on Large Dams (ICOLD) about 80 % of the large dams are constructed as earth or rockfill dam structures having overtopping as a major cause for failure (Niemayer (2007)). The release of large

water amounts during a dam breach event may lead to subsequent dam or dyke failures along the downstream river reach.

Examples of recent and documented dam breaches are the Tous dam breach which took place in 1982 in Spain (Alcrudo and Mulet (2007)) or the Teton dam breach of 1976 in Idaho, USA, as illustrated in Figure 1.1 (b). Overtopping can also happen during the construction of the embankment, as it took place at the Oro dam in Brazil in 1958 causing several hundreds of victims (Broich (1997)).

Tailings dams. Tailings dams are special cases of reservoir dams and are usually build for temporary use only and, thus, are often simpler structures. They are typically constructed for the storage of waste waters for mining or industrial purposes and can impose large threats on people and environment in case of breaching due to the toxicity contained in the waste waters.

A famous example is the tailings dam failure at the Los Frailes lead-zinc mine at Aznalcóllar in Spain, illustrated in Figure 1.1 (c), which released 4-5 million m³ of toxic liquid jeopardizing a downstream national parc (Achterberg *et al.* (1999) or Aguilar *et al.* (2000)). An overview over major tailings dam failures in Europe is given by Rico *et al.* (2007), thereby identifying overtopping as a significant failure mechanism among others.

Natural embankments. Beside artificial man-made embankment structures, another important category concerns natural embankments. These can be formed as natural terminal moraines by glaciers or by landslides or avalanches which are temporally blocking river courses. Natural embankments often consist of alluvial material with wide-ranging grain compositions and may be of complex geometry and large extents. These embankments are often homogeneous, without inner zonal structures or surface protections, and therefore are less cumbersome regarding the complexity of the involved geotechnical aspects. They are therefore also a focus of the present work. Natural embankments usually exist only temporarily

for time periods of hours up to years until a sudden or prolonged breach event occurs (Schuster and Costa (1986)).

A catastrophic historical disaster resulted from a rock landslide embankment on a tributary of the Ticino river in southern Switzerland in 1513. It resulted in the flooding of the city of Biasca and drowned hundreds of people (Evans *et al.* (2011)). A more recent example is the glacial lake outburst flood of the Ventisquero Negro glacial lake in Argentina in 2009, which was investigated by Worni *et al.* (2012) and is illustrated in Figure 1.1 (d). Comprehensive overviews over past events are given in Clague and Evans (2000) or Evans *et al.* (2011).



(a) Alpenrhein, Switzerland (1929)
(Int. Rheinregulierung (1992))



(b) Teton Dam, USA (1976)
(U.S. Bureau of Reclamation)



(c) Aznalcóllar tail. dam, Spain (1998)
(Aguilar *et al.* (2000))



(d) Ventisquero Negro, Argentina (2009)
(Worni *et al.* (2012))

Figure 1.1: *Historical breach events of earth embankments.*

1.2 Problem description and application range

1.2.1 Embankment failure types

This work focuses on erodible earth embankment structures. Other dam types, like arch dams or gravity concrete dams, have different failure mechanics without breach development and may lead to rather instantaneous failures (Singh (1996)). Earth embankments can fail partially or fully due to several different causes. Overall, the major failure types are identified as:

- Failure due to overtopping,
- Internal erosion ('piping'),
- Structural failure due to slope instabilities or foundation failures, and
- Dynamic loads due to earthquakes.

According to Singh (1996), Foster *et al.* (1998) or Wahl (1998), failure due to overtopping is the most common failure type of earth embankments. This statement holds true for dams as well as for dykes and thereby highlights the importance of this failure type. Frequencies of these failure types are illustrated in Figure 1.2 separately for river dykes and reservoir dams according to the data of Foster *et al.* (1998).

These failure types are not mutual exclusive and multiple types may occur during a single breach event. Therefore it is often difficult to classify historical events according to these categories. For example, internal erosion of a flow channel through the embankment ('piping') or a settling over time can trigger the formation of an initial breach which is subsequently overtopped. Such a failure sequence happened at the Teton dam which failed due to overtopping that probably had been initialized by foregoing piping erosion and a collapse of the piping channel. Consequently,

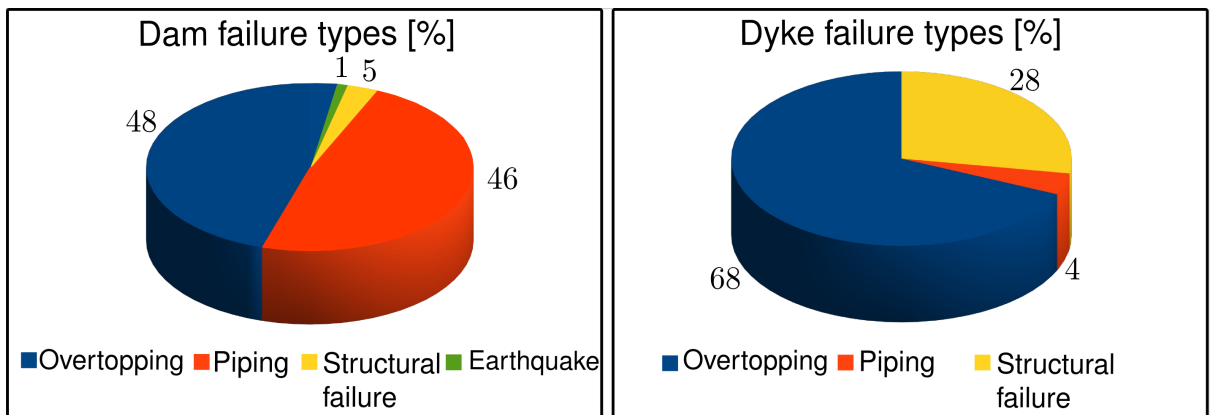


Figure 1.2: Most common failure mechanisms for erodible dams (left) and dykes (right) (modified after Foster *et al.* (1998) and Landestalsperrenverwaltung-Sachsen (2005))

different breach types may be investigated with tools suitable for embankment overtopping by assuming an appropriate initial breach of adequate size. This initiation of overtopping can happen due to numerous different mechanisms. Amongst others, these can be extreme storm events, impulse waves, piping erosion, settling, earthquakes or wave induced erosion. These aspects emphasize the importance of improved assessment tools for gradual embankment breaches due to overtopping.

1.2.2 Embankment failure modes due to overtopping

In general, the failure of erodible embankments due to overtopping can be further classified into different failure modes. The occurrence of these failure modes thereby depends mainly on the material composition and the inner structure of the embankment.

Laboratory and field investigations indicate that non-cohesive and homogeneous embankments often show a gradual and progressive breach advance which therefore is denoted here as 'progressive erosion'. The downstream embankment face thereby flattens progressively and is often said to rotate around a pivot-point near the downstream toe (Pickert *et al.* (2004)). The left part of Figure 1.3 sketches principal aspects of the breach development in case of progressive erosion.

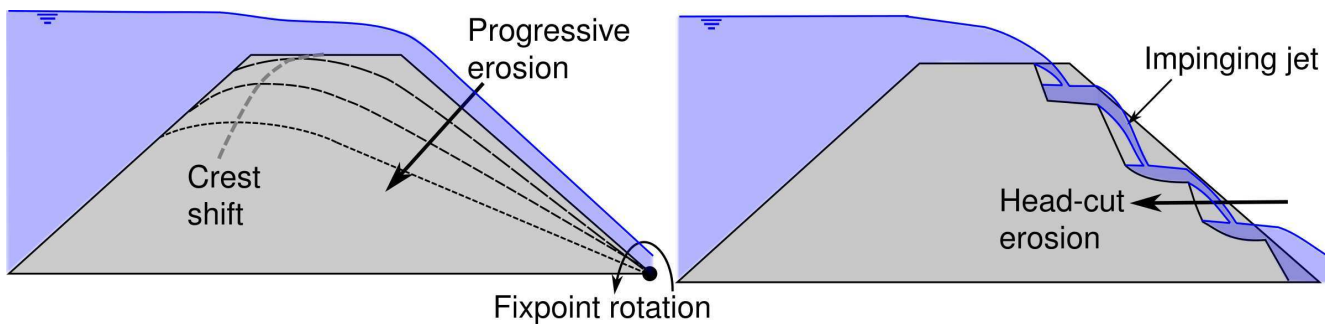


Figure 1.3: Sketch of progressive erosion of non-cohesive embankment (left) and head-cut erosion of cohesive embankment (right). Arrows indicate the travelling of the erosion front.

In contrast, embankments consisting of cohesive material typically show a different failure mode. The failure occurs more discontinuously and the downstream embankment erodes in vertical steps due to the impinging forces of the formed waterfalls. The erosion front hereby travels from the downstream embankment toe backwards to the crest. This erosion mechanism is also labelled 'head-cut erosion' in literature (Hahn *et al.* (2000)) and exhibits strong 3D flow characteristics as sketched in the right part of Figure 1.3. Due to the complex 3D nature of these flow characteristics, they are difficult to capture numerically. This failure mode is not investigated in this work. Nevertheless, it is noted that after some time, when the breach discharge increases and the erosion front reaches the embankment crest, the vertical bed steps often vanish and a continuous downstream face is formed again, allowing for a treatment as progressive breach erosion. Hence, the methods developed for progressive erosion may in principle also be extended to later breach phases of cohesive embankments. Furthermore, special approaches were presented approximating and simplifying this head-cut erosion with conventional sediment transport formulas (Wu (2007)).

For cohesive embankments, the breach progress generally depends strongly on material parameters such as the degree of soil compaction and the water content as stated e.g. by Morris *et al.* (2008). In contrast, progressive embankment breaches, involving mainly non-cohesive material, are said to be less dependent on the material properties as outlined

by Sametz (1981). Regarding embankments made of large sized material, like boulders or blocks, which are not embedded within a sand matrix, an additional failure mode is sometimes distinguished. An 'interlocking' of the blocks is observed in such cases, which is caused by mutual and stabilizing contact interactions of the blocks and can act as a surface protection for the embankment slopes (Morris *et al.* (2008)).

Figure 1.4 depicts a classification of these three failure modes depending on the grain sizes of the embankment material after Morris *et al.* (2008). The present work only deals with embankment breaches caused by progressive surface erosion. As can be seen in the Figure, the progressive erosion has to be expected to take place for a wide range of grain sizes, ranging from about medium silt up to coarse gravel.

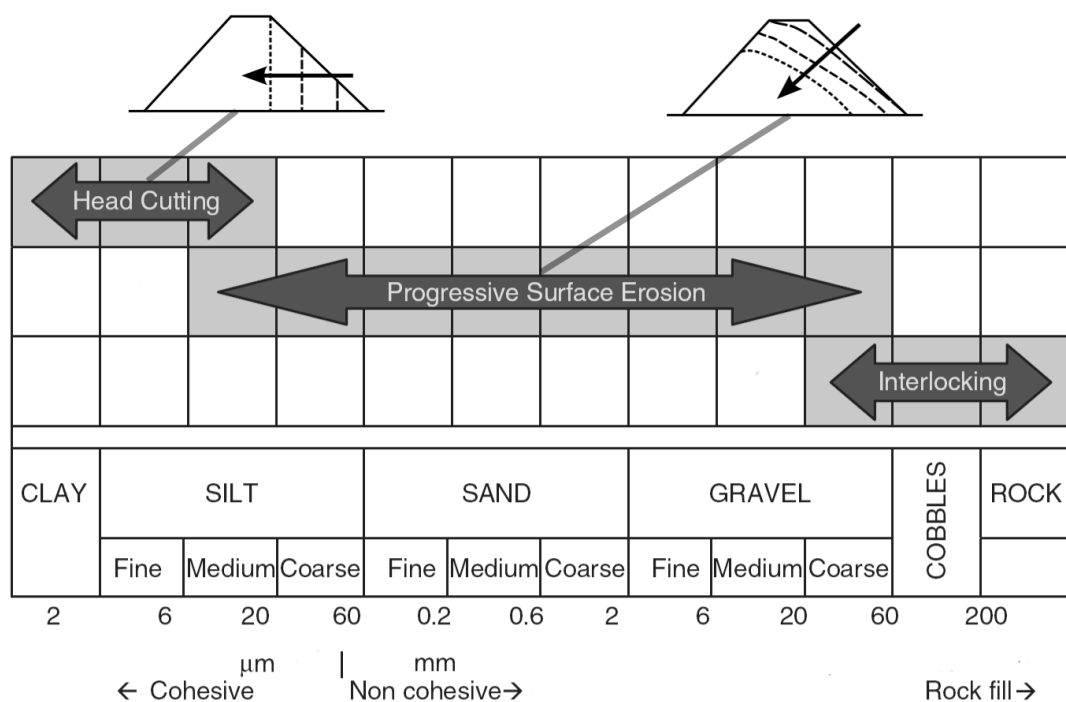


Figure 1.4: Failure modes due to overtopping classified by the grain diameters of the embankment material modified after Morris *et al.* (2008).

For heterogeneous, i.e. zoned, embankments for example with inner clay core, the failure mechanics can change drastically compared to homogeneous embankments. Clay-compacted cores can offer a large resistance to surface erosion, leading to an undercutting of the core with

subsequent bending and cantilever failure processes (Stanczak (2008), Schmocker *et al.* (2011)). Such complex geotechnical aspects need special considerations in order to be represented accurately in numerical modelling approaches and are excluded from the investigations in this work. The presented model, however, is in principle also applicable to heterogeneous composite embankments with zoned inner structures and surface protections by considering local differing grain compositions. The application range thereby comprises in particular embankments with filter zones or surface protection cover, which are not expected to substantially alter the progressive erosion mechanics.

1.2.3 Relevant processes - multi-physical approach

Numerical investigations of embankment breaches are challenging due to the multiple physical processes which are involved and interact with each other. Figure 1.5 illustrates a simplified sketch of these processes which should be addressed in numerical approaches. The most relevant processes are identified as:

1. The hydrodynamics of the overtopping flow,
2. The flow-induced erosion and sediment transport. This erosion of the embankment surface is denoted as 'surface erosion' or 'vertical erosion',
3. The gravitationally-induced failures of the steep side walls at the breach channel. These failures are denoted here as 'lateral erosion' since they widen the breach in transversal direction to the flow. Both erosion mechanisms together (2.+3.) are addressed as 'embankment erosion' in this work, and
4. The sub-surface flow through the embankment body, influencing the particle stability due to effects of apparent cohesion¹.

¹Possible foundation problems due to uplift pressures on the embankment caused by the sub-surface flow is an important dam safety issue as well, but is not investigated within the scope of this work.

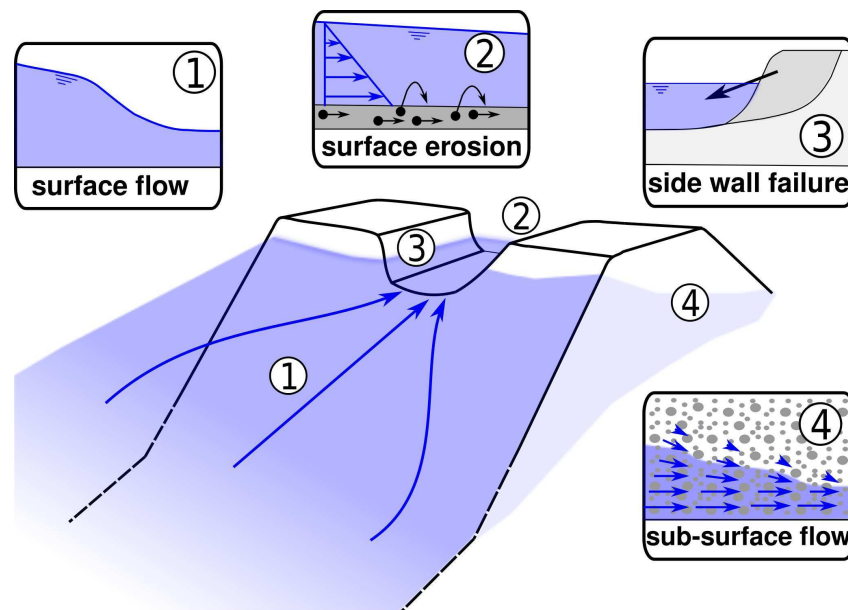


Figure 1.5: Major relevant physical processes involved in breaching.

Besides the modelling of these processes, their mutual interactions also need to be considered. The overtopping flow induces the erosion of the embankment surface, which acts as a trigger for the gravitationally-induced side wall failures. The sub-surface flow within the embankment determines the resulting pore-water pressures and water saturations, which have influences on the apparent cohesion of the embankment material and, hence, the erosion processes. It is in turn affected by the overtopping flow and corresponding water infiltrations into the embankment. And, obviously, the embankment erosion also has strong impacts on the overtopping flow.

These processes and their mutual interactions are only partially understood up to now and can be reproduced by numerical models in a limited way only. They partially differ in their dimensions, time-scales and process continuity, complicating the numerical treatment. Further research in experiments and numerical modelling is needed to improve the understanding of these processes and their interactions (Morris *et al.* (2008)). Due the involved complexities, this work aims to provide a simplified multi-physical modelling approach with sub-models for each of these processes. Coupling algorithms and techniques thereby have to be developed to combine these processes to an integrated modelling approach.

1.3 State-of-the-art

1.3.1 Classification of modelling approaches

Many numerical modelling approaches were developed for progressive embankment breaches and can be categorized by their spatial dimensions and degree of simplifications. They are often distinguished in 'parameter models' and 'physically-based models'² as illustrated in Figure 1.6.

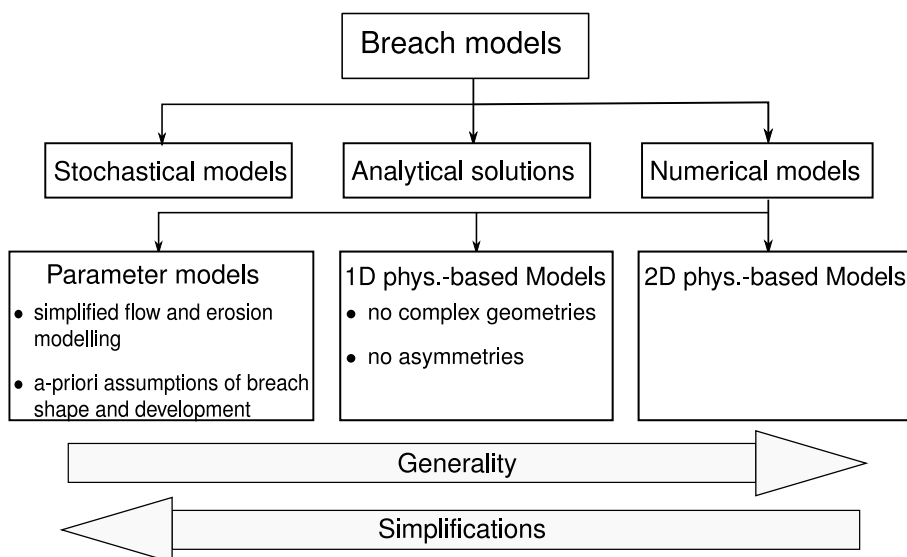


Figure 1.6: *Classification of breach models according to their generality and adopted simplifications.*

Parameter models usually apply simplifications to the governing equations and are solved without spatial discretizations of the project site into computational cells. These models often integrate uncertainties of different processes into a single integral parameter with limited physical meaning. An overview is given in Singh (1996), whereas popular and widely used models are for example the BREACH model (Fread (1985)) or the Breach Erosion of Earthfill Dams (BEED) model (Singh *et al.* (1988)).

²Note that these terms are sometimes used with different meanings in literature. For example, Wahl (1998) uses the term physically-based models for numerical approaches which are categorized as parameter models here.

Physically-based models, in contrast, solve the full flow equations, apply a more physically-based erosion modelling and discretize the site geometry using computational meshes. These physically-based models are more generally applicable and can be further divided into 1D and 2D approaches, whereas the dimensions relate to the governing equations for hydrodynamic and sediment transport modelling.

Beside numerical approaches, a variety of analytical solutions and stochastic relationships have been derived for assessments of breach outflow hydrographs. However, analytical models require large simplifications and are hardly applicable to scenarios of practical relevance. In stochastic models, correlations are determined between the unknown variables, as e.g. the peak discharge, and typical embankment characteristics, as its width, length or storage volume. These models rely on a profound empirical data base which is usually difficult to obtain. Furthermore, it is often not feasible to transfer relations from one project site to another what limits their practical use.

In the following sections, a brief introduction into the modelling approaches is given and a literature review of physically-based 1D and 2D models is presented. A comprehensive review of existing modelling approaches was also recently published by the ASCE/EWRI-Task-Committee (2011).

An interesting alternative for practical applications is the combination of different breach model types. Such a combination of an easy-to-use parameter model with a 2D physically-based model was investigated for example by Vonwiller *et al.* (2011). The basic idea was to combine the advantages of the parameter model after Macchione (2008) with the physically-based 2D model developed in this work. It could be shown that the parameter model can be calibrated based upon multiple runs of the physically-based model with varied parameter sets, in a way that it shows similar results within the investigated parameter range. Such a calibrated parameter model then is able to capture effects of local site geometries to some extent and could serve as an easy-to-use warning tool or as a fast breach module within a real-time Decision Support System (DSS).

1.3.2 Physically-based models

Physically-based models discretize the computational domain with a large number of cells on which the governing equations are solved. Such models are challenging with respect to the modelling of the multiple physical processes and are demanding regarding the model robustness and the computational expense. Tables 1.1 and 1.2 provide an overview over physically-based 1D and 2D models with their main features and characteristics as presented in literature.

Using 1D models it could be demonstrated that robust and shock-capturing numerical schemes in combination with empirical sediment transport formulas can reproduce the surface erosion successfully. Such 1D models allow for insights in the validity of several model assumptions. They are especially promising regarding evaluations of improvements of distinct model features and therefore often focus on a special aspect for which they present a novel treatment. However, the assumption of 1D flow characteristics is not appropriate for practical use and they suffer in principle from their lacking ability to consider the lateral breach widening due to side wall failures.

Two-dimensional models solve the 2D Shallow-Water equations (SWE) for the simulation of the overtopping flow and apply 2D sediment continuity equations in combination with transport formulas. The computational domain is discretized with a 2D surface mesh on which the governing equations are numerically solved. This model type requires more efforts for the mesh generation and the model set-up and leads to comparably large computational expense. In contrast to 1D models, however, they are applicable to realistic scenarios with complex site geometries and flow patterns.

These 1D and 2D physically-based breach models can be categorized in many respects regarding the representation of the physical processes and the applied numerical techniques. For example, nearly all models make use of structured meshes, with the exceptions of the recent models of Cao *et al.* (2011) and Sabbagh-Yazdi and Jamshidi (2012). This is a limiting constraint for practical applications. Flexible and adaptable un-

Table 1.1: Comparison of different physically-based 1D models (FD = Finite-Differences, FV = Finite-Volumes, Zonal = composite embankments).

1D models							
Researcher	Year	Type	Bed-load	Susp.-load	Slope failure	See-page	Zonal
Tings. & Chin.	2001	FD	X	-	meth. of slices	-	-
Leopardi <i>et al.</i>	2002	?	X	-	-	-	-
Wu & Wang	2008	FV	-	X	-	-	-
Stanczak	2008	?	X	-	-	simplified	X
Pontillo <i>et al.</i>	2010	FV	X	-	-	-	-

structured meshes often are advantageous and can be seen as state-of-the-art regarding flood modelling and natural hazard simulations involving irregular geometries.

Some of the first breach models applied Finite-Difference (FD) methods for the simulation of the overtopping flow (Broich (1997) or Tingsanchali and Chinnarasri (2001)). The simulation of the overtopping flow involves changes in the flow regime regarding sub- and supercritical flow conditions and, hence, is numerically challenging. Recent models instead often apply Finite-Volume (FV) methods in combination with shock-capturing Godunov schemes (Godunov (1959)). These models proved to be robust and accurate for these flow conditions and prevent the occurrence of instabilities. Furthermore, the FV method allows for strict mass continuity in the simulations. With the exception of the model of Balmforth *et al.* (2008), all listed breach models of the last decade make use of the FV method in combination with a Godunov-type approach, what makes it a state-of-the-art technique.

Simulations of breach events require the modelling of surface erosion of the embankment material. The breach models hereby differ in the type of erosion mechanisms which are considered. Several models only consider bed-load transport, as e.g. the models of Tingsanchali and Chinnarasri (2001), Leopardi *et al.* (2002), Pontillo *et al.* (2010), Broich (1997) or Wang and Bowles (2006). Al-

Table 1.2: Comparison of different physically-based 2D models (FD = Finite-Differences, FV = Finite-Volumes, Zonal = composite embankments).

2D models								
Researcher	Year	Type	Bed-load	Susp.-load	Slope failure	See-page	Zonal	Mesh type
Broich	1997	FD	X	-	diffusion	-	-	struct.
Paquier	2002	?	-	X	-	-	-	struct.
Wang & Bow.	2006	FV	X	-	meth. of slices	-	-	struct.
Faeh	2007	FV	X	X	failure angles	-	X	struct.
Balmforth <i>et al.</i>	2008	FD	X	X	-	-	-	struct.
Cao <i>et al.</i>	2011	FV	-	X	failure angles	-	-	unstruct.
Wu <i>et al.</i>	2012	FV	-	X	failure angles	-	-	struct.
Sabb. & Jam.	2012	FV	-	X	meth. of slices	-	X	unstruct.

though the bed-load transport formulas were not derived for embankment breach conditions, promising results were obtained. In contrast, some modellers developed or adopted special erosion modelling approaches which shall be better suited for embankment breach conditions as Leopardi *et al.* (2002) and Pontillo *et al.* (2010).

Other researchers, however, identified suspended-load transport as crucial transport mechanism during the strong overtopping flow, especially regarding fine-grained embankment material. Therefore they focused on suspended-load transport and implemented corresponding advection-diffusion equations describing the movement of the sediment particles in suspended-phase (Paquier (2002), Wu and Wang (2008), Cao *et al.* (2011)³ or Sabbagh-Yazdi and Jamshidi (2012)). However, these models do not explicitly consider the bed-load transport, what makes their applicability questionable, especially if coarse-grained embankment material is present.

A more comprehensive treatment is the consideration of both transport mechanisms, bed- and suspended-load transport, simultaneously. Only few breach models, however, implemented both mechanisms in

³They used bed-load transport formulas to determine suspended sediment concentrations which were used in advection-diffusion equations.

combination as Faeh (2007) and Balmforth *et al.* (2008). Larger programming and computational efforts are required and additional problems arise regarding the portioning of material between bed- and suspended-load.

The interconnection of hydrodynamics and sediment transport can be considered to different degrees in the models. It is often distinguished between uncoupled and coupled models, whereas the latter consider interactions of bed-level changes with the overtopping flow more tightly. Models using an uncoupled approach were presented e.g. by Broich (1997), Wang and Bowles (2006), Faeh (2007) or Balmforth *et al.* (2008)⁴. In contrast, the recent models of Wu and Wang (2008), Cao *et al.* (2011) or Sabbagh-Yazdi and Jamshidi (2012) applied a fully-coupled modelling. The necessity and the advantages and disadvantages of coupled approaches for gradual breach modelling hereby are still seen as a matter of debate and require additional investigations.

Another important erosion mechanism for embankment breaches are the side wall failures during the later breach stages. These processes are generally difficult to model accurately, and therefore it has to be relied on simplifying assumptions. One-dimensional models usually ignore the side wall failures, which occur mainly transversal to the flow direction. A simple diffusion-based approach leading to a smooth flattening of the breach side walls was applied by Broich (1997) in his 2D model. A commonly used and simple approach for the approximation of the slope failure is the geometrical modelling based on critical failure angles. Cao *et al.* (2011) applied a single critical failure angle, whereas Faeh (2007) and Wu *et al.* (2012) distinguished between failure angles above and below the water surface. Another type of slope failure modelling was performed in 1D by Tingsanchali and Chinnarasri (2001) using the 2D method of slices (see also chapter 5.2.1) along the flow direction. Furthermore, Sabbagh-Yazdi and Jamshidi (2012) used the 2D method of slices along the breach channel side walls and Wang and Bowles (2006) coupled their 2D model with a 3D method of slices.

⁴It is noted that some publications concerning breach models did not explicitly mention whether a coupled approach was applied or not.

Furthermore, it is known that the water saturations and pore-water pressure distributions, resulting from water infiltration and sub-surface flow within the embankment, determine apparent cohesion effects which influence the embankment erosion. Nevertheless, nearly all breach models neglected the sub-surface flow in the embankment and apparent cohesion effects in the past. Only Stanczak (2008) reported a simplified modelling approach for infiltration processes of wave induced embankment overtopping.

Numerical breach models were often not or hardly validated, since measurements are difficult and only few data are available regarding these hazard events. The models are often at best compared with estimated integral outflow hydrographs reconstructed from downstream observations. Faeh (2007) validated his model against outflow hydrographs at dyke breaches, Balmforth *et al.* (2008) validated against wave induced erosion volumes measured in the laboratory and Cao *et al.* (2011) compared with laboratory measurements of outflow hydrographs. More detailed and meaningful comparisons and validations against the temporal progress of the breach formation were successfully made in 1D by Wu and Wang (2008) and Pontillo *et al.* (2010). In 2D, Wang and Bowles (2006) compared at least the final simulated breach cross section width with the measured geometry and Wu *et al.* (2012) and Sabbagh-Yazdi and Jamshidi (2012) compared the longitudinal breach advance. However, no detailed comparisons with the 3D spatial breach development were presented up to now.

Conclusively it can be stated that applications of 2D physically-based models led to promising results and have the potential to provide reliable modelling tools for embankment breaches. Nevertheless, the models still have severe limitations and neglect essential parts of the relevant processes and their interactions. There is need for further model improvements and investigations regarding the validity of the applied simplifications. The goals and model improvements pursued in this work are briefly summarized in the next section.

1.4 Goals and document structure

The main goal of this work is the development of a 2D physically-based model for non-cohesive embankment breach modelling. The identified relevant processes shall be captured hereby at least in a simplified way. The model shall provide a unified modelling approach, including the embankment breaching and the subsequent flood wave propagation and sediment movements in the affected downstream areas.

Major goals and aspects addressed in this work are summarized as follows:

- Most breach models make use of structured meshes with regular cells. The use of unstructured meshes is numerically more challenging but allows for flexible mesh adaptations and local mesh refinements. These are crucial aspects for practical engineering purposes, in particular with regard to natural embankments with complex geometries. In this work, unstructured meshes are applied, whereas a discretization approach is developed for accurate terrain representations and strict mass continuity (chapters 2 and 3),
- Previous investigations neglected the sub-surface flow through the embankment body, which affects the side wall failures and the surface erosion. This is seen as a limiting constraint and was identified as deficiency or open task in previous investigations, as e.g. in Tingsanchali and Chinnarasri (2001), Faeh (2007) or Al-Riffai and Nistor (2010). A 3D sub-surface model therefore is developed (chapter 4) and coupled with the other processes (chapter 6),
- The geotechnical modelling of gravitationally-induced side wall failures is generally difficult, but is known to be of major importance. The often used approach of geometrical failure modelling, based on critical failure angles, needs further investigations and improvements. Herein, it is extended to unstructured meshes, and effects of apparent cohesion are incorporated (chapter 5),

- Limited validations were made for numerical breach models in the past. Many models were successfully tested only on integral parameters, like the breach outflow hydrograph. However, no detailed comparisons of the 3D breach formation were made. Such comparisons are possible due to recent laboratory studies and are presented in chapter 7 together with field-scale applications to natural hazard events of practical relevance,
- Embankment erosion modelling was limited to homogeneous embankments and a single mean grain diameter in most previous models. As a consequence, these models have difficulties in coping with wide-ranging grain compositions and cannot consider heterogeneous embankments or surface protections. Fractional sediment transport should be considered in combination with bed- and suspended-load transport to enlarge the application range (chapter 3), and
- The presented models in literature are often academic tools hardly suited for practical applications. To improve this situation, the developed algorithms and methods are integrated into the natural hazard simulation software *BASEMENT* (Faeh *et al.* (2012)). Integrating the developed algorithms and approaches into a mature and productive modelling software offers several advantages concerning practicability and future model extensions.

2

Modelling of Overtopping Flow

2.1 Introduction

The overtopping flow over embankments is in general three dimensional and usually highly turbulent with large Reynolds numbers and considerable water-sediment interactions. The numerical simulation of such flow conditions using the 3D Reynolds-averaged Navier-Stokes equations (RANS) is complex and time consuming and has large demands regarding the spatial and temporal model resolutions and corresponding boundary and initial conditions. Therefore, and with regard to practical engineering purposes, several simplifications usually have to be adopted.

The overtopping of non-cohesive embankments leads to a gradual progressive breach process. The streamlines are hereby mainly parallel to the embankment surface. The water depths h are typically small and shallow in relation to the wave lengths L of the flow ($L/h > 20$). Following these assumptions, it is justified to neglect the vertical velocity component and to assume a hydrostatic pressure distribution over the depth. The RANS equations then can be vertically integrated and the unknown pressure variable eliminated. This leads to the formulation of the 2D Shallow-Water Equations (SWE) which are commonly applied for the modelling of embankment breaches and flood wave propagations and are accepted as appropriate mathematical model for the study of dam break waves as summarized by Toro (2001). A comprehensive derivation from the RANS equations by depth-integration is presented for example in Faeh *et al.* (2012).

At embankment breach events, it must be dealt with rapidly accelerating flows. Figure 2.1 schematically sketches the geometries and typi-

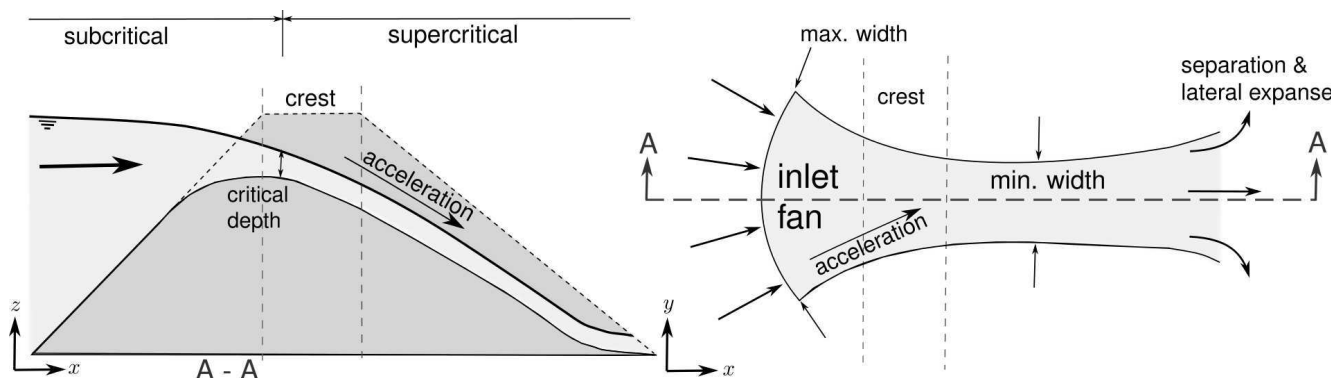


Figure 2.1: *Left: cross-sectional view through breach channel with transition from sub- to super-critical flow conditions. Right: top-view of curved breach channel with converging inlet fan and expansion zone.*

cal flow conditions encountered at gradual embankment breaches. The flow accelerates along the downstream embankment slope and usually changes from sub- to supercritical flow conditions around the embankment crest. Furthermore, the converging shape of the breach channel ('inlet fan') leads to an acceleration and concentration of the flow in direction of the narrowing breach channel. Leaving the breach channel, the streamlines diverge, the flow velocity slows down and the flow overtops the side walls and expands laterally (Chanson (2004a)). Downstream of the embankment, a hydraulic jump may develop with associated strong energy dissipation and complex flow patterns.

In order to obtain robust and stable hydrodynamic simulations of these flow conditions, special shock-capturing schemes have to be applied and were developed in the past. In addition, regarding embankment breaches, large sediment masses are moved and steep slopes and rapid changes in the topography can emerge and influence the flow patterns. Therefore, and because of the mostly irregular terrain topography, one has to cope with flow over strongly uneven bed surfaces raising the need for accurate terrain representations in the numerical model.

At first, the governing equations and empirical closures are presented and underlying assumptions and simplifications are briefly discussed in sections 2.2 and 2.3. An overview over the numerical solution techniques

tom shear stresses, whereas $\tau_{xx}, \tau_{xy}, \tau_{yx}, \tau_{yy}$ denote the depth-averaged turbulent shear stresses. Using these notations, the continuity and x -, y -momentum equations of the SWE can be written as

$$\frac{\partial h}{\partial t} + \frac{\partial(uh)}{\partial x} + \frac{\partial(vh)}{\partial y} = 0, \quad (2.1)$$

$$\frac{\partial u}{\partial t} + u \frac{\partial u}{\partial x} + v \frac{\partial u}{\partial y} + g \frac{\partial h}{\partial x} = -g \frac{\partial z_B}{\partial x} - \frac{1}{\rho h} \left[\tau_{Bx} - \frac{\partial(h\tau_{xx})}{\partial x} - \frac{\partial(h\tau_{xy})}{\partial y} \right], \quad (2.2)$$

$$\frac{\partial v}{\partial t} + u \frac{\partial v}{\partial x} + v \frac{\partial v}{\partial y} + g \frac{\partial h}{\partial y} = -g \frac{\partial z_B}{\partial y} - \frac{1}{\rho h} \left[\tau_{By} - \frac{\partial(h\tau_{yx})}{\partial x} - \frac{\partial(h\tau_{yy})}{\partial y} \right]. \quad (2.3)$$

The momentum dispersion terms, which describe the effect of the non-uniformity of the velocity distribution over depth (Malcherek (2009)), are hereby neglected. Introducing the friction slope S_f and the bed slope S_B the SWE can be re-formulated in conservative form as it is applied herein. The conservative form is favourable regarding the treatment of shock-waves and abrupt changes in the flow variables. With the conserved variables \mathbf{U} , the flux vectors \mathbf{F} , \mathbf{G} and the source term vector \mathbf{S} the equations can be written as

$$\mathbf{U}_t + \mathbf{F}(\mathbf{U})_x + \mathbf{G}(\mathbf{U})_y - \mathbf{S} = 0 \quad (2.4)$$

with

$$\mathbf{U} = \begin{pmatrix} h \\ uh \\ vh \end{pmatrix}, \mathbf{F} = \begin{pmatrix} uh \\ u^2h + \frac{1}{2}gh^2 - \nu_t h \frac{\partial u}{\partial x} \\ uvh - \nu_t h \frac{\partial u}{\partial y} \end{pmatrix},$$

$$\mathbf{G} = \begin{pmatrix} vh \\ uvh - \nu_t h \frac{\partial v}{\partial x} \\ v^2h + \frac{1}{2}gh^2 - \nu_t h \frac{\partial v}{\partial y} \end{pmatrix}, \mathbf{S} = \begin{pmatrix} 0 \\ gh(S_{fx} - S_{Bx}) \\ gh(S_{fy} - S_{By}) \end{pmatrix}. \quad (2.5)$$

The subscripts t, x, y hereby denote partial derivatives with respect to time and spatial directions.

In this formulation it is made use of Boussinesq's eddy viscosity concept with the turbulent eddy viscosity ν_t . To solve the equations for the conserved variables \mathbf{U} , additional empirical relations are needed to close the equations. Closures are needed for the source terms and the turbulent shear stresses and are presented in section 2.3. The applied numerical approaches used to determine the flux vectors \mathbf{F} , \mathbf{G} and to update the conserved variables \mathbf{U} are described in section 2.4.3.

2.2.1 Discussion of simplifying assumptions

The application of the SWE comprises multiple simplifying assumptions:

- Neglect of vertical accelerations,
- Hydrostatic pressure distribution,
- Mild channel slopes,
- No significant interactions of sediment transport with the flow, and
- Friction laws formulated for 1D normal flow are applicable to unsteady 2D flow simulations.

These assumptions are generally questionable with regard to applications to embankment breaches. The validity and several aspects of these assumptions therefore are briefly discussed in the following sections with special regard to the conditions present at embankment breaches and wave propagations in steep mountainous terrains.

Vertical accelerations & hydrostatic pressures

In situations of an instantaneous dam break at a non-erodible flat plane, where the dam is suddenly removed, vertical accelerations take place especially at the front of the developing wave in downward direction. Such vertical accelerations occur especially at the first moments of the dam break wave formation after dam removal. The deviations resulting from

the use of depth-averaged models, which neglect these vertical accelerations, were examined in numerical studies in the past. Basco (1989) and Mohapatra *et al.* (1999) came to the same conclusion that these deviations are small and negligible for engineering applications.

However, regarding overtopping flow over embankments with steep slopes, rapid vertical flow acceleration occurs in downstream direction with associated curved water surface profiles. This can at least locally invalidate the assumption of a hydrostatic pressure distribution over depth. In principle, the SWE can be extended for such conditions by adding additional terms considering the effects of non-hydrostatic pressure distributions. The resulting Boussinesq equations include third-order terms whose numerical solution demands for corresponding third-order accurate numerical solution schemes (Abbott (1979)). Another method to incorporate effects of non-hydrostatic pressure distributions using extended 2D SWE, resolving the vertical direction with additional variables and equations, was presented recently by Krüger and Rutschmann (2006), based on similar extensions to the 1D SWE of Steffler and Jin (1993) and Khan and Steffler (1996). Using a SUPG (Sreamline Upwind Petrov Galerkin) Finite-Element model, they showed that modelling of shock-waves at super-critical flow conditions could be improved by taking into account vertical profiles of pressure and velocity distributions. The use of such higher-order solution schemes, the use of additional equations or the application of the full RANS equations is, however, numerically challenging and requires large computational efforts, especially regarding unstructured meshes, and is therefore of questionable benefit for breach modelling.

An alternative, simplifying approach to approximate the vertical acceleration and the resulting non-hydrostatic pressure distribution was recently presented by Denlinger and Iverson (2004) and Denlinger and O'Connell (2008). They estimate the vertical velocity distribution $w(z)$ based on the water surface curvature in relation to the bed-slope of the uneven terrain. Using this estimate for $w(z)$, a depth-averaged vertical acceleration w can be determined.

Then, based upon this vertical acceleration, the gravitational acceler-

ation g is modified as g^* to account for the non-hydrostatic effects and is inserted into the momentum equations without the need for additional modifications. The correction term is derived from the kinematic boundary conditions and reads

$$g^* = g + \frac{\partial w}{\partial t} + u \frac{\partial w}{\partial x} + v \frac{\partial w}{\partial y}. \quad (2.6)$$

This modified gravitational acceleration is a simple way to approximately account for non-hydrostatic effects with comparably low additional computational demands, using the standard solution schemes. Denlinger showed that the method produces improved results on a steep chute when compared to experimental results, although the effects were rather small. This method was also investigated and tested in the scope of this work. However, the modifications of the gravitational acceleration led to oscillations and no significant improvements in the flow variables could be observed in the tests. Further investigations are necessary to check the applicability of the method to unstructured meshes and to determine the cause for the numerical instabilities. Therefore the method was not adopted in this work and the effects of non-hydrostatic pressure distributions are neglected here as in previous breach models.

Steep embankment slopes

The derivation of the SWE bases on the assumption of mild slopes. The conditions $\cos \delta \approx 1.0$ and $\sin \delta \approx 0.0$ are assumed to be satisfied, where δ is the inclination of the bed surface. This assumption leads to deviations from the real solution in case of inclined slopes at steep embankments, even if the vertical pressure distribution is assumed hydrostatic.

Formulating the SWE for inclined slopes using local coordinate systems can improve the situation. Such approaches were presented for example by Gray *et al.* (1999) or recently by Sabbagh-Yazdi *et al.* (2007), who investigated steep chute flows with regular geometries. Assuming an inclined slope in x -direction, the flow variables are transformed for the

inclined coordinate-system (*) and inserted into equation 2.4 as

$$x^* = \frac{x}{\cos \delta}, z^* = \frac{z}{\cos \delta}, u^* = \frac{u}{\cos \delta}, h^* = h \cos \delta. \quad (2.7)$$

Following this approach, a vertical velocity component can be derived from the solution as $w = u \sin \delta$. Sabbagh-Yazdi *et al.* (2007) noted that the standard solution schemes for the SWE equations can be applied to the modified equations. However, the standard solution schemes, like the often applied Riemann solvers, do not account for the inclined slope and the vertical velocity component and therefore differ conceptually from such an approach.

Broich (1997) instead argued that the presence of steep slopes at embankment breaches leads to average errors significantly smaller than 10%, under consideration of the rapid flattening of the slopes over time. Following this statement, the effect of the steep slopes is neglected in this work.

Effects of water-sediment interactions

Another limitation of the presented formulation of the SWE is the assumption of clear water flow. The term clear water indicates that the effects of bed- and suspended-load transport on the fluid density and flow behaviour are neglected.

In scenarios where this assumption may be jeopardized, e.g. in presence of fine material leading to hyper-concentrated flows, a variable fluid density and additional terms must be added to the equations to account for the resulting effects. For example, the generalized SWE presented by Wu (2007) comprise an additional term for the consideration of the volume occupied by the transported sediment masses in the continuity equation and additional momentum losses due to water-sediment interactions based on a varying fluid density. A more explicit modelling of the water-sediment interactions can be achieved by using numerical approaches which consider additional momentum equations for the sediment-phase and estimate the momentum exchange with the water-

phase (see section 3.2.1).

In case of non-cohesive embankments which are mainly made of rather coarse-grained material, like sand or gravel, these effects are assumed to be of minor importance. This aspect is briefly discussed in section 3.2.1 dealing with the modelling of surface erosion.

Nevertheless, these effects become more influential in case of applications to strong overtopping flow and fine-grained material with significant suspended-load transport. Future investigations and quantifications would be beneficial to be able to assess the impacts and application range of the made assumption for practical applications.

2.3 Empirical closures and source terms

2.3.1 Friction source term

The friction slope S_f in the source term vector is determined using the quadratic resistance law. The components in x - and y -directions are determined as

$$S_{fx} = \frac{u\sqrt{u^2 + v^2}}{gc_f^2 h}, S_{fy} = \frac{v\sqrt{u^2 + v^2}}{gc_f^2 h}. \quad (2.8)$$

The dimensionless friction coefficient c_f in the equation can be evaluated using different friction laws. The Strickler friction coefficient k_{str} is used in this work and it is determined as follows, whereas the hydraulic radius is approximated by the water depth h^2

$$c_f = k_{str} \frac{h^{1/6}}{\sqrt{g}}. \quad (2.9)$$

²Using h as an approximation of the hydraulic radius is commonly done in 2D models, since the cells have no information about the geometry of the cross-section or the width of the flow channel.

In the presence of tiny water depths, for example at the dry-wet interfaces, the determination of the friction slope can lead to divisions by very small values. To circumvent numerical instabilities, the term is treated in a semi-implicit manner as outlined in Faeh *et al.* (2012).

2.3.2 Bed slope source term and C(onservation)-property

The numerical treatment of the bed slope term S_B on the unstructured cells is formulated based on the method presented by Komaei (2004). Using the Finite-Volume (FV) method the bed slope term is integrated over the cell area as

$$\iint_A \mathbf{S}_B dA = \iint_A \begin{pmatrix} 0 \\ ghS_{Bx} \\ ghS_{By} \end{pmatrix} dA = gV_w \begin{pmatrix} 0 \\ -\frac{\partial z_B(x,y)}{\partial x} \\ -\frac{\partial z_B(x,y)}{\partial y} \end{pmatrix}. \quad (2.10)$$

To evaluate this term, the cell water volume V_w and the cell slopes $\partial z_B/\partial x, \partial z_B/\partial y$ are required for each cell. The corresponding computations for triangular cells are outlined in Faeh *et al.* (2012) and involve basic geometrical considerations. Quadrilateral cells are treated in the same manner by dividing them into triangles³ and applying the same methods on each triangle separately. The approach results in a well-balanced scheme regarding the flux gradients and the bed source term as proven by Komaei (2004). The Conservation (C)-property is thereby fulfilled (Bermudez *et al.* (1998)), i.e. when simulating a reservoir with still water above an uneven bed the occurrence of non-physical fluxes is prevented.

³The quadrilateral cell is divided up into four triangles. These triangles are obtained by connecting the cell vertices with the cell midpoint. The bed-level of the midpoint is determined by inverse-distance weighted interpolation from the bed-levels at the vertices.

2.3.3 Turbulence modelling

Modelling of the SWE can be distinguished by the degree of turbulence modelling which is applied. For many practical problems in river engineering the effects of turbulence are not explicitly modelled but incorporated in the bed friction term. The simplest way to explicitly account for flow turbulence is the use of algebraic turbulence models based on Boussinesq's eddy viscosity concept. The turbulent shear stresses are then calculated as

$$\tau_{xx} = 2\rho\nu_t \frac{\partial u}{\partial x}, \tau_{yy} = 2\rho\nu_t \frac{\partial v}{\partial y}, \tau_{xy} = \rho\nu_t \left(\frac{\partial u}{\partial y} + \frac{\partial v}{\partial x} \right), \tau_{yx} = \rho\nu_t \left(\frac{\partial u}{\partial x} + \frac{\partial v}{\partial y} \right). \quad (2.11)$$

These turbulent shear stresses are added as source terms to the equations following the method of Mohammadian and Roux (2006). A main task hereby is the evaluation of the velocity gradients in x - and y -directions for the unstructured cells and is outlined in Faeh *et al.* (2012). The turbulent eddy viscosity ν_t is derived dynamically as

$$\nu_t = \frac{1}{6} \kappa u^* h \quad (2.12)$$

with the von Kármán constant $\kappa = 0.4$ and the shear velocity u^* (Malcherek (2009)).

Preliminary numerical investigations in this work indicated that turbulence modelling based on the Boussinesq's eddy viscosity concept had no significant effects on the breach simulations and therefore is not further discussed. In contrast to local flow around fixed obstacles with strong flow separations, the embankment erosion rather forms a stream-lined channel minimizing flow separations as outlined by Chanson (2004a). Furthermore, the use of a first-order accurate numerical scheme in combination with unstructured meshes in this work adds artificial diffusivity to the solution, which may compensate for diffusivity introduced by the flow turbulence. Out of these reasons, and because considerable additional computational efforts would arise, the neglect of explicit turbulence modelling seems justified for embankment breach applications.

2.4 Numerical modelling - Godunov approach

2.4.1 Spatial discretization

The spatial discretization of the computational domain in discrete cells and vertices⁴ is an essential aspect of the numerical modelling. Unstructured meshes consist of irregular distributed vertices which are connected to obtain triangular or quadrilateral cells on which the governing equations are solved. The use of unstructured meshes thereby offers various advantages compared to structured meshes. They allow for a flexible adaptation of the cell edges to irregular geometries at the project site, which is of major importance for practical applications. In addition, they allow for local mesh refinements in areas of special interest and the use of large cell sizes in outer regions. This results in a reduction of the total number of cells in the mesh and consequently can lead to more efficient simulations. As a drawback, the internal storage and the solution algorithms are more complex and computationally more costly.

In the last years, several 2D models with Godunov-type approaches were presented using unstructured meshes, like e.g. Valiani *et al.* (2002), Yoon and Kang (2004) or Begnudelli and Sanders (2006).

Generally, one can distinguish between two different discretization approaches for the FV method:

Cell-Centered = the unknown flow variables are defined at the center of the cells. The control volumes for flux integration equal the cell shapes, or

Cell-Vertex = the unknown flow variables are defined at the mesh vertices. The control volumes for flux integration are constructed around each vertex.

For the hydrodynamic computations, a cell-centered spatial discretization is applied, as illustrated in Figure 2.3. The conserved variables, h ,

⁴The terms 'vertex' and 'node' are used interchangeable in this work for discrete points (x,y,z) in the mesh defining the cell shapes.

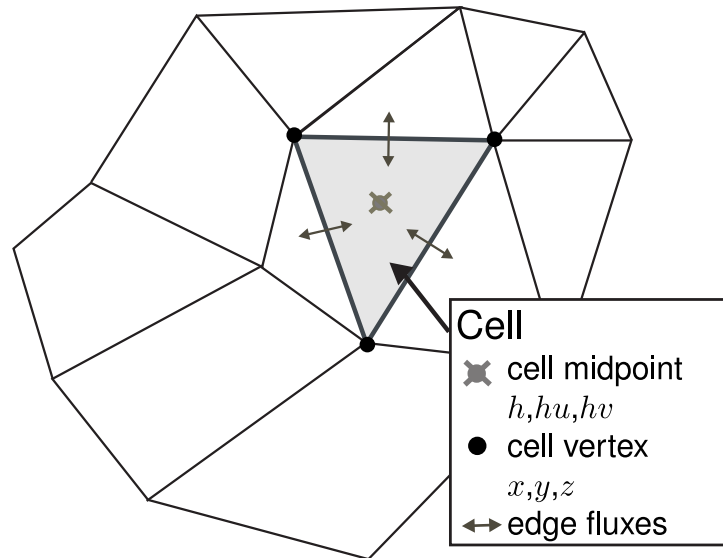


Figure 2.3: Cell-centered discretization for hydrodynamic modelling with linear varying bed-levels over the cell.

u_h and v_h , are hereby defined at the cell-centers and assumed constant over each cell.

Cell-centered schemes can further be distinguished in the way the terrain is represented. The bed-levels z_B of the topography can either be set constant over the cell or can be defined at the vertices. The latter approach allows for a linear variation of the bed-level within each cell. Differing from schemes with constant bed-levels, this approach is second-order accurate regarding the representation of the terrain. This discretization scheme is adopted herein and generally offers a good relation between accuracy and performance as stated by Begnudelli *et al.* (2008)). Similar, Schubert *et al.* (2008) mentioned that it can lead to second-order convergence rates for uneven terrains where the mesh representation limits accuracy, even if the flux computation is only first-order accurate. Such an accurate terrain representation is seen advantageous especially with regard to embankment breaches and mountainous regions, where complex terrains with abrupt changes in bed-levels and slopes are encountered.

2.4.2 Time integration and CFL -criterion

The model applies an explicit Euler time integration of first order accuracy. In explicit schemes, the time step size is constrained by numerical stability conditions. The Courant-Friedrichs-Lewy (CFL)-criterion (Courant *et al.* (1928)) is applied on an edge basis to guarantee appropriate time step sizes Δt during the simulation. It can be written with $l =$ edge length, $|u| = \sqrt{u^2 + v^2}$ and $c = \sqrt{gh}$ as characteristic wave speed as

$$CFL = \frac{|u| + c}{l/\Delta t} \leq 1.0. \quad (2.13)$$

Such explicit time integrations are often preferred to implicit ones in shock-capturing schemes (Zoppou and Roberts (2003)). For non-linear governing equations, implicit schemes result in non-linear equation systems which either require iterative solutions or linearisation. Whereas iterative solutions can be computationally costly, linearisation of the equations can lead to deterioration in stability and accuracy especially for strongly unsteady flows like wave propagations. Implicit schemes with large time step sizes may also lead to problems regarding the moving boundaries at the interface of wet and dry cells as mentioned by Beffa (1994).

In addition, the combined execution of multiple sub-models, which is a main aspect of this breach modelling approach, is expected to be more robust and more tightly coupled if explicit schemes are used with corresponding small time step sizes.

2.4.3 Flux calculations and solution update

The FV method is used in combination with a standard Godunov-type approach for the solution of the governing equations 2.4. Following this method, the governing equations are integrated over the cell areas and the edge fluxes are determined using Riemann-solvers. The solution procedure is presented in Appendix A.

2.5 Validation for dam breaks on fixed bed

As a consequence of disastrous dam break events in the past, instantaneous dam breaks over fixed bed were studied extensively (Chanson (2004b)). A number of analytical solutions were derived which can be used to validate numerical codes. Such analytical solutions were chosen here and compared with the numerical results obtained by quasi-1D models in a rectangular channel with a high mesh resolution. Additionally, the historical dam break event of the Malpasset dam in France was investigated. These tests shall validate the hydrodynamic modelling and demonstrate its robustness and applicability to transitional flow conditions and flood wave propagations.

2.5.1 Quasi-1D dam break flows

Dam break on dry terrain

The simplest dam break case is an instantaneous dam break over a flat and dry terrain without friction losses. The problem was solved analytically already in the 19th century by Ritter (1892). Ritter's work was initiated and motivated by the catastrophic failure of the South Fork dam in the USA, which was one of the major dam break events at this time (Chanson (2004b)).

Initially, a constant water depth of h_0 was set at the upstream part of the model reach and dry conditions were set at the downstream part. At time $t = 0.0$ s, the dam was suddenly removed and a dam break wave emerged. In the left part of Figure 2.4 the dimensionless analytical and numerical solutions are compared. The resulting simulated depth is illustrated at $t = 30.0$ s and compares excellent with the analytical solution. The solution consists of a parabolic water profile, with the wave front travelling downstream with a speed of $2\sqrt{gh_0}$, and a rarefaction wave travelling upstream with a speed of $\sqrt{gh_0}$.

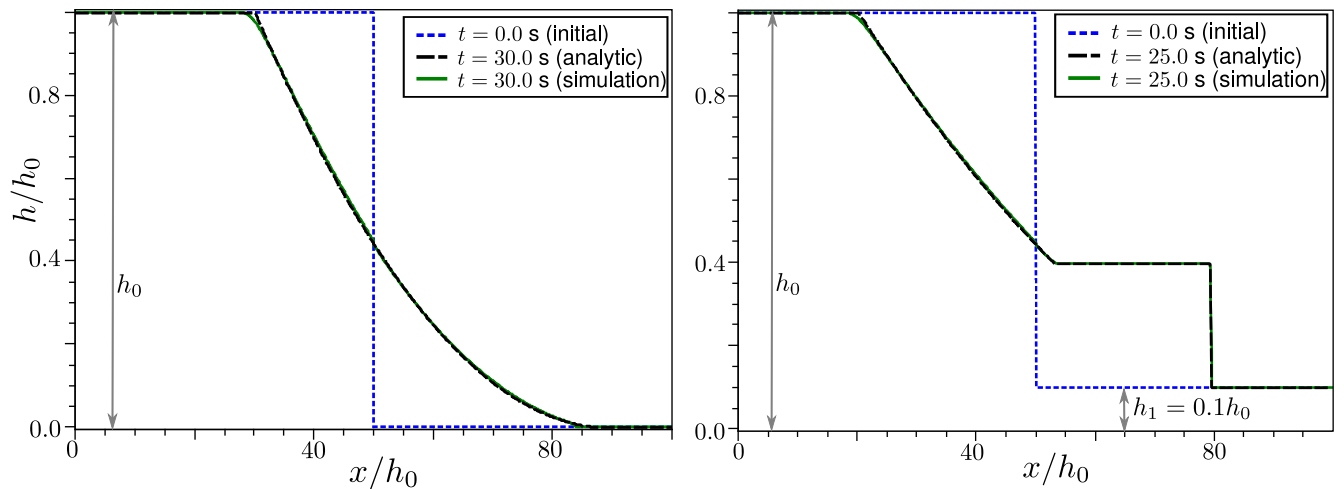


Figure 2.4: Comparison between analytical (dashed) and numerical (solid) solutions. Left: sudden dam break on dry terrain at $t = 30.0$ s. Right: sudden dam break on wet terrain at $t = 25.0$ s.

Dam break on wet terrain

The evolution of a dam break wave over a wet and frictionless flat terrain was analytically solved by Stoker (1957) and is presented in a simple form in Chanson (2004a). It differs thereby substantially from the dry bed solution. At the upstream part of the model reach an initially constant water depth of h_0 was set, and in the downstream part a water depth of $h_1 = 0.1h_0$. In this scenario a shock wave is formed and propagates in downstream direction. Behind the shock-wave a section with constant water depth develops and a rarefaction wave of parabolic shape emerges in upstream direction. In the right part of Figure 2.4 the dimensionless numerical and analytical solutions of the water depths are illustrated at $t = 25.0$ s. The downward travelling shock wave thereby is captured well.

Dam break on sloped terrain

Dressler (1958) presented an approximate analytical solution for non-linear waves evoked by dam breaks in a sloping channel without consideration of friction losses. A steep channel configuration with a slope of 1v:1h was examined. A constant water-level $\zeta = h_0$ was set in the upstream domain, whereas the downstream part was set to dry conditions.

The numerical results again compare well with the analytical solutions and are presented for different times in dimensionless form in Figure 2.5⁵.

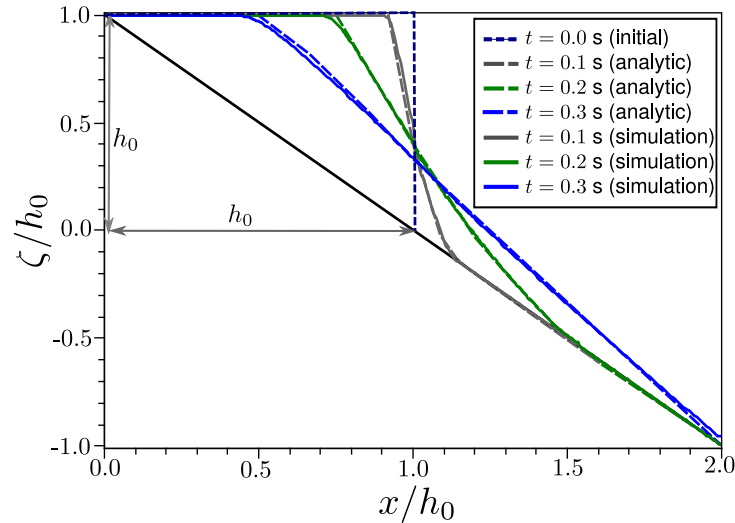


Figure 2.5: Sudden dam break on sloped terrain - comparison between approximated analytic (dashed) and numerical (solid) results for $t = 0.1$ s, 0.2 s, 0.3 s.

2.5.2 Malpasset dam break

The Malpasset dam was a concrete arch dam located in a narrow gorge of the Reyran river valley in France. The dam failed suddenly in 1959 possibly due to uplift pressures at the foundations (Londe (1987)). It received lots of attention in literature and was used for the validation of various numerical codes because of its unique data availability concerning the spatial and temporal development of the flood wave. The water-levels could be partially reconstructed based on the successive destructions of transformer stations by the flood wave. The data was used to validate the numerical approach on an unstructured mesh built of $\sim 22,000$ cells representing the strongly irregular topography. A uniform friction value of $k_{str} = 30 \text{ m}^{1/3}/\text{s}$ was set over the whole domain and a fixed, non-erodible

⁵It is noted that Dressler's analytical solution solves the SWE in a similar formulation as the numerical model. As a consequence, it is subject to the same limitations concerning the assumption of mild slopes. The obtained agreement therefore must not be interpreted as validation for 'real' dam break flows on steep slopes.

bed was assumed. A constant water-level of 100 m was set in the reservoir. The downstream river valley was assumed to be initially dry.

In Figure 2.6, a snapshot of the downstream propagating flood wave is illustrated and comparisons are shown between the maximum measured and simulated water-levels at different locations P_i along the left and right sides of the river valley (see Valiani *et al.* (2002) for details). A further opportunity for model comparison is provided by the results of other numerical models in literature. For this purpose the results of two other numerical models with higher-order schemes are additionally compared (Valiani *et al.* (2002) and Yoon and Kang (2004)).

Regarding the uncertainties in the measured data, the simulation results are in satisfying accordance with the field data. The propagation of the flood wave can be basically reproduced and the model is stable and deals with dry-wet interfaces successfully. The comparisons with both other numerical models also reveal only minor differences, although these models apply higher-order schemes. This observation strengthens the importance of accurate terrain representations for scenarios with strongly irregular topography.

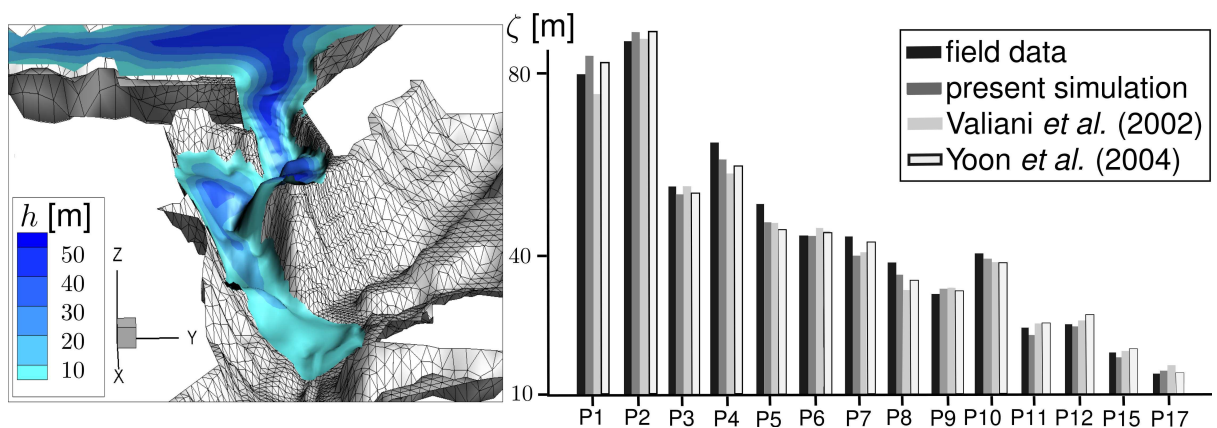


Figure 2.6: Left: snapshot of flood wave propagation at $t = 100$ s. Right: comparison of maximum water-levels with measured field data and other numerical models at various locations.

2.6 Summary

The Shallow-Water equations are used for the simulation of embankment overtopping and the subsequent downstream wave propagation. The assumptions of shallow water flow and hydrostatic pressure distributions are often said to be applicable to progressive breaches of non-cohesive embankments, where the streamlines are mostly parallel to the bed surface. However, they may be violated especially in case of steep embankment slopes. Furthermore, strong water and sediment interactions may influence the flow properties, especially in presence of fine-grained material. Model improvements regarding these aspects are currently discussed in literature and have the potential to enhance the hydrodynamic modelling, but are not applied herein.

An important aspect for practical scenarios is the use of flexible, unstructured meshes consisting of triangular and quadrilateral cells. Unstructured meshes can be adapted to local site geometries and allow for local mesh refinements. For these reasons an unstructured mesh with a cell-centered spatial discretization is applied. The bed-levels hereby are defined at the cell vertices, allowing for a second-order accurate terrain representation which is seen advantageous for embankment breaches and mountainous regions.

The model implements a first-order accurate shock-capturing Godunov-type approach in combination with an exact Riemann solver. As a consequence, it successfully handles transitional and super-critical flow conditions which must be expected during overtopping. An explicit solution technique is applied for the modelling of the overtopping flow. The numerical scheme further satisfies the Conservation-property and applies an accurate treatment for dry-wet interfaces. Future enhancement regarding the implementation of higher-order schemes are possible but increase the computational expense.

To test and validate the modelling approach, several test cases were investigated regarding sudden dam breaks and wave propagations over non-erodible, fixed beds. First, the model was compared with analyti-

cal solutions of 1D dam break waves over dry, wet and sloped terrains. Finally, the historical Malpasset dam break event was simulated and compared to field measurements and results of other numerical simulations. Overall, the model results compare well against the analytical, measured and numerical solutions. The wave propagation and flow patterns can be reproduced in an efficient and robust way, suitable for embankment breach simulations on complex terrains.

3

Modelling of Surface Erosion

3.1 Introduction

During embankment overtopping, bottom shear stresses are exerted upon the embankment material which mobilize the particles and transport them with the flow in downstream direction. Depending upon the strength of the water flow and the particle mobility, sediment transport processes are often divided into three main categories as shown in Figure 3.1:

- Bed-load transport,
- Suspended-load transport, and
- Wash-load.

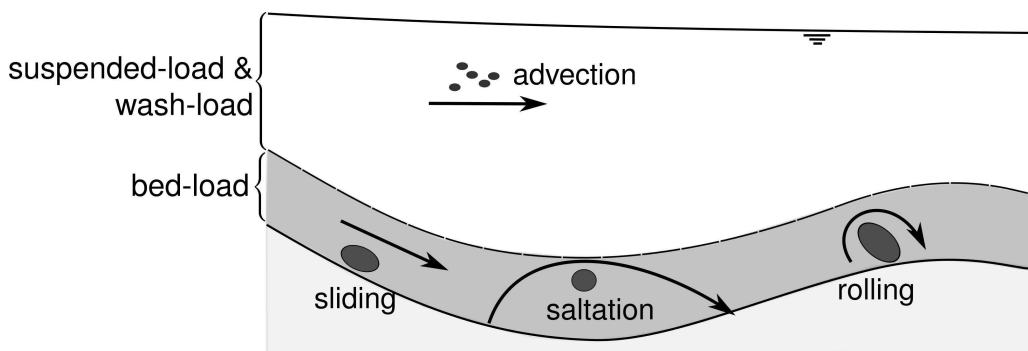


Figure 3.1: *Transport modes of bed- and suspended-load.*

Coarse-grained material, like gravel, is supposed to be transported mainly as bed-load during overtopping of embankments. The mobilized particles at the embankment surface slide, saltate and roll in direction of the flow and come to rest in downstream areas. Differing from this

situation, in case of strong overtopping flow and fine-grained material, like fine sand or silt, the suspended-load transport becomes increasingly important. The small particles are lifted up by the acting forces, stay in suspension due to the flow turbidities and are advected over larger distances until they settle again. Wash-load thereby can be seen as special case of suspended-load with particular fine particles and is not discussed here separately.

In general, a physically accurate modelling of sediment transport processes is extremely complex and a fundamental research topic. The sediment transport is strongly dependent on 3D turbulent, coherent flow structures as well as highly unsteady, turbulent bursts and it depends on the dynamical forces acting on individual particles and their mutual interactions (Gyr and Hoyer (2006)). Numerical approaches resolving the spatial and temporal scales of the turbulent eddies, and approaches taking into account the individual particle movements and interactions, are out of the scope of this work. These would also require extensive computational powers, making them unsuitable for practical embankment breach applications.

The classical approaches for sediment transport, in contrast, rely on empirically derived transport formulas estimating the transport rates in dependence of integral flow and material properties. Many empirical formulas for bed- and suspended-load transport were derived which determine the transport or entrainment rates as function of the bottom shear stress τ_B exerted upon the material. Due to the empirical nature of these formulas, calibration is usually needed to account for local site conditions.

Despite the underlying limitations and simplifications, several numerical models based on empirical transport formulas were applied successfully to embankment breaches in the past. Here, the breach modelling makes use of such empirical formulas in combination with an Exner-equation based approach, including fractional transport and sorting processes for multiple grain classes. The applied methods principally base on the approach presented by Faeh (2007) for 2D bed- and suspended-load transport on a structured mesh. A main effort of this work hereby is the adaptation to unstructured meshes, which are seen as vital and

crucial requirement for many practical applications¹.

In section 3.2 the governing equations are presented and underlying assumptions are discussed. The empirical approaches for sediment transport are presented in section 3.3. In section 3.4 the focus is laid on the spatial discretization, and the numerical approaches are briefly presented. Finally, two reference tests are used to validate the modelling in section 3.5 and a summary is given in section 3.6.

3.2 Governing equations for sediment transport

3.2.1 Discussion of simplifying assumptions

The modelling approach applied in this work relies on several main assumptions:

- Momentum exchange between the sediment- and water-phases can be neglected,
- Equilibrium transport occurs,
- The material porosity is constant over time, and
- Empirical 1D relations derived for the estimation of transport rates are also applicable to 2D modelling and conditions present at embankment breaching.

The validity of the first three assumptions are briefly discussed in the following sections with regard to embankment breaches and possible future enhancements are mentioned. The assumptions underlying the empirical closures for sediment transport are discussed separately in section 3.3.2.

¹The development and implementation of the suspended-load transport modelling were made in the scope of other activities and were not part of this work.

Momentum exchange between sediment- and water-phases

A main assumption adopted for the modelling approach is that momentum exchanges between the sediment- and water-phases can be neglected. Therefore no additional momentum equation is formulated for the sediment-phase. Only mass conservation principles are applied to the sediment-phase, leading to the formulation of sediment continuity equations. This assumption is plausible as long as temporal variations of the bed-levels z_B are small in comparison to temporal variations of the water depths h . This condition can be expressed as

$$\frac{\partial z_B}{\partial t} \ll \frac{\partial h}{\partial t}. \quad (3.1)$$

Although the transport rates during embankment breaches can be large, this assumption is often said to be justified especially if explicit solution schemes are applied. Using explicit schemes, the time step sizes are limited to small values due to stability constraints (*CFL*-criterion) and the accumulated bed-level changes during each time step are typically very small. Hence, the assumption of different scales of changes in bed-levels and flow variables is usually valid for explicit schemes as stated e.g. by Saiedi (1997) or Savary (2007). These different scales were also confirmed by the comparison of uncoupled and semi-coupled simulations made in section 6.2 of this work. This assumption is also strengthened by the study of Balmforth *et al.* (2008), who investigated effects resulting from adding additional terms for momentum exchange and reported insignificant influences in their breach simulations. Furthermore, a comparative study of different models for dam break flows over mobile bed of Soares-Frazao *et al.* (2012) came to the conclusion that a key problem of transport modelling lies in the uncertainties in the empirical closures rather than the governing equations.

Nevertheless, this assumption may be a limiting constraint for some scenarios, in particular in presence of fine material and corresponding large suspended-load transport. To overcome this limitation, some improved modelling approaches were developed in the last years, but are not applied in this work for the reasons given below.

So called 'two-layer approaches' were introduced by Capart (2000) for sudden dam break flows on mobile beds. A bottom layer is used to simulate bed-load transport and another layer is applied for the water flow and suspended-load transport. Hereby, continuity and momentum equations are solved separately for each phase and additional terms are added to account for the inter-facial momentum exchange between the layers. This 1D approach was recently further developed by considering different velocities in the layers (Capart and Young (2002)) or varying sediment concentrations over the depth (Spinewine (2005)). Amoudry and Liu (2009) proposed a 2D model which explicitly simulates continuity and momentum equations for the sediment- and the water-phases, taking into account the inter-facial momentum transfer. These approaches raise several difficulties, however, like the modelling of the momentum transfer and the specification of adequate boundary and initial conditions for the sediment-phase. Furthermore, they lead to increased computational costs and are complex to implement. Out of these reasons, the practical applicability of such approaches is questionable up to now. Beside these two-layer approaches, alternative and simpler approaches were presented approximating the momentum exchange with additional terms in the momentum equations of the water-phase only (section 2.2.1).

Non-equilibrium transport

The commonly applied empirical sediment transport formulas were derived for equilibrium conditions. In presence of unsteady and accelerated flows, however, adaptation lengths and times are needed for the equilibrium transport to be established. The effects of non-equilibrium transport are sometimes considered by formulating an additional equation which sets the spatial changes in the local transport rates proportional to a difference between the actual transport rate and the equilibrium transport capacity (Bell (1989) or Bell and Sutherland (1989)). This can be interpreted as a simple relaxation of the actual transport rate towards the equilibrium transport capacity. The relaxation factors are the temporal and spatial adaptation lengths, which need to be estimated and are, for

example, sometimes set to average saltation step lengths of the particles. The formulation after Wu (2004) can be written in one dimension with q_{B*} = actual transport rate, q_B = equilibrium transport capacity and L_s = spatial adaptation length as

$$\frac{\partial z_B}{\partial t} + \frac{\partial q_{B*}}{\partial x} = \frac{1}{L_s}(q_{B*} - q_B). \quad (3.2)$$

Similar non-equilibrium equations were formulated for 2D modelling and the suspended-load transport. The implementation of such approaches necessitates an implicit solution procedure and therefore cannot be easily implemented in the current explicit model. Therefore the non-equilibrium effects are neglected in this work.

Possible alternatives for explicit models are recent approaches which apply stochastic bed-load transport modelling and are capable to incorporate non-equilibrium effects to some extent as presented e.g. by Kuai and Tsai (2009).

These non-equilibrium effects are of special importance in local areas where strong spatial gradients of the transport rate occur, e.g. at the transition from non-erodible to mobile beds or the scour at bridge piers. In scenarios of gradual embankment breaches these effects are supposed to be less significant, because the transport rates increase gradually during the overtopping and the flow is gradually accelerated along the downstream slope. Neglecting the non-equilibrium effects thereby may impact mainly the erosion around the embankment crest.

The significance of these non-equilibrium effects also depends on the relation of the cell sizes Δx to the adaptation length. At field-scale scenarios with large cell sizes these non-equilibrium effects are less significant, whereas at laboratory-scale their influence is much more pronounced. This is seen problematic in particular with regard to the suspended-load transport. Hereby the assumption is made of an equilibrium concentration profile over the water depth, which is supposed to need much longer distances to develop than the equilibrium conditions for the bed-load transport.

Sediment porosity

The material compaction during embankment construction often reduces the material porosity p . This is especially true in case of cohesive material and in case of wide-ranging grain mixtures, where small particles fit into the pores between the larger ones. This aspect is problematic regarding the modelling of erosion and subsequent deposition of the material. The porosity of the original, compacted material may change significantly after its erosion, transport and subsequent deposition. This effect, and the influence of grain sorting on the porosity, are currently not accounted for in the model and would require treating the porosity as locally and temporarily varying variable.

3.2.2 Governing equations for sediment transport

By applying mass conservation principles to the sediment-phase one can derive the global sediment mass continuity equation (Malcherek (2009)). It is often labelled the Exner-equation, named in honour of the Austrian sedimentologist Felix M. Exner (Cunge *et al.* (1980)). The Exner-equation is solved in order to determine the updated bed-levels z_B . The total sediment balance over all grain classes n_g and sediment layers over the depth leads to following formulation as

$$(1 - p) \frac{\partial z_B}{\partial t} + \sum_{g=1}^{n_g} \left(\frac{\partial q_{Bg,x}}{\partial x} + \frac{\partial q_{Bg,y}}{\partial y} \right) = \sum_{g=1}^{n_g} (s_{lg} - s_g), \quad (3.3)$$

where p = sediment porosity, n_g = number of grain classes and $q_{Bg,x}$, $q_{Bg,y}$ = components of bed-load fluxes of grain g in x - and y -directions. The source terms s_{lg} and s_g are described below.

Beside the total sediment balance, additional continuity equations are formulated separately for each grain class g in case of fractional sediment transport. These equations are labelled 'sorting equations' here. The change of volume occupied by a grain class g is balanced over the volume

$V_{bal,g} = V_{cv,g} + V_{sub,g}$. Hereby, $V_{cv,g}$ is the bed-load control volume in which bed-load transport takes place² and $V_{sub,g}$ is the volume of the first underlying sediment layer. A definition sketch is illustrated in Figure 3.2 introducing these parameters. The variable z_B describes the surface bed-level, z_F the bottom of the bed-load control volume and z_{sub} the bottom level of the underlying sediment layer.

The grain compositions β_g of the bed-load control volume hereby are of interest and can change depending on the net sediment in- or outflow and the source terms.

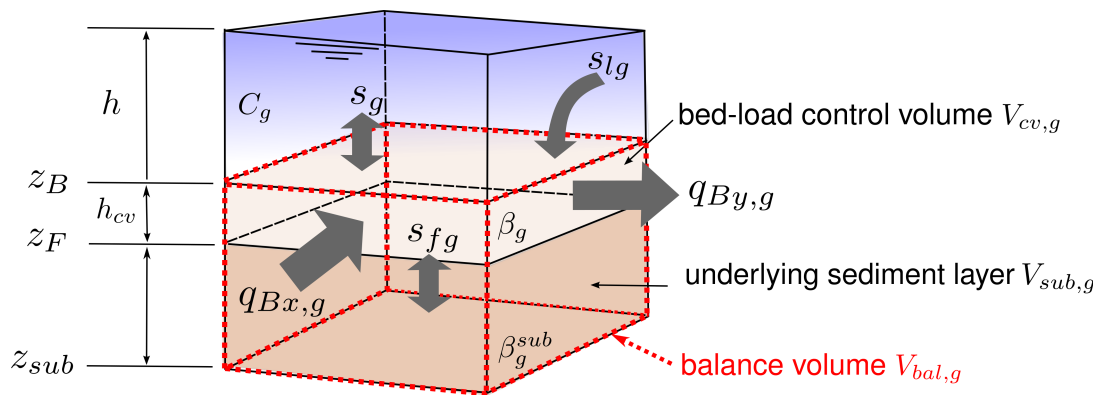


Figure 3.2: Definition sketch of balance volume $V_{bal,g}$ (dashed) with fluxes and source terms used to derive the bed material sorting equations.

Three different source terms are distinguished:

- External sediment source s_{lg} to add or remove sediment from the cell. It is defined positive if sediment enters the bed-load control volume,
- Exchange between bed- and suspended-load described with source term s_g by balancing deposition and entrainment rates. The source term is defined positive if sediment leaves the bed-load control volume by entrainment, and
- Source term s_{fg} describes the virtual exchange of material between the bed-load control volume and the underlying sediment layer with

²In literature the notations 'mixing layer' or 'active layer' are also often used for the bed-load control volume.

grain composition $\beta_{sub,g}$. This term is defined positive if sediment enters the bed-load control volume³.

The resulting 2D sorting equations are formulated for each grain class separately as

$$\frac{\partial V_{bal,g}}{\partial t} = (1-p) \left[\underbrace{\frac{\partial(\beta_g(z_B - z_F))}{\partial t}}_{\text{vol. change in control volume}} + \underbrace{\frac{\partial(\beta_{sub,g}(z_F - z_{sub}))}{\partial t}}_{\text{vol. change in sub-layer} = -s_{fg}^4} \right] = -\frac{\partial q_{Bg,x}}{\partial x} - \frac{\partial q_{Bg,y}}{\partial y} - s_g + s_{lg}.$$

Re-arranging these terms and introducing the source term s_{fg} and the bed-load control volume thickness $h_{cv} = z_B - z_F$ leads to following formulation which is applied in this work. The n_g sorting equations are solved to determine the grain compositions β_g as

$$(1-p) \frac{\beta_g h_{cv}}{\partial t} + \frac{\partial q_{Bg,x}}{\partial x} + \frac{\partial q_{Bg,y}}{\partial y} = s_{lg} + s_{fg} - s_g \quad g = 1 \dots n_g. \quad (3.4)$$

The suspended-load transport is determined by solving n_g advection-diffusion equations, which describe the advective and diffusive movement of the suspended particles in the water-phase. The depth-averaged grain concentrations C_g hereby are the primary variables which need to be determined. The 2D advection-diffusion equations can be written as (Chanson (2004b))

$$\frac{\partial}{\partial t} (C_g h) + \frac{\partial}{\partial x} \left(C_g h u - h \Gamma \frac{\partial C_g}{\partial x} \right) + \frac{\partial}{\partial y} \left(C_g h v - h \Gamma \frac{\partial C_g}{\partial y} \right) = s_g, \quad g = 1 \dots n_g \quad (3.5)$$

³This is a special kind of source term, because it does not change the overall grain volume within the balance volume $V_{bal,g}$ and is not related with a physical movement of particles.

⁴This formulation is valid for bed erosion only, where material of $\beta_{sub,g}$ leaves the underlying layer. In case of deposition, $\beta_{sub,g}$ must be replaced by β_g entering the layer.

where Γ is the turbulent diffusivity which is set equal to the turbulent eddy viscosity as $\Gamma = \nu_t = \kappa/6.0hu_*$. As mentioned above, the source term s_g describes the exchange between bed- and suspended-load and couples these advection-diffusion equations with the sediment continuity equations.

The equations 3.3, 3.4 and 3.5 form a system of $(2n_g + 1)$ equations for the solution of the $(2n_g + 1)$ primary variables, namely z_B , β_g and C_g . The bed-load fluxes q_B , the source terms and the thickness of the bed-load control volume h_{cv} are secondary variables, which need additional empirical closures to be specified.

3.3 Empirical relations for sediment transport

3.3.1 Critical shear stress for inception of transport

The critical shear stress $\tau_{g,crit}$ for incipient motion of grain size d_g is an important threshold for sediment transport modelling. It describes the stability of particles within the grain matrix and influences the rate of bed- or suspended-load transport during embankment overtopping. This parameter is applied in the model in dimensionless formulation as Shields-parameter $\Theta_{g,crit}$ with the specific density $s = \rho_s/\rho$ as the ratio of sediment and fluid density as

$$\Theta_{g,crit} = \frac{\tau_{g,crit}}{\rho(s-1)gd_g}. \quad (3.6)$$

The Shields-parameter is determined in the model using the empirical Shields-diagram (Shields (1936)) applied in a parametrized form (Faeh *et al.* (2012)). The Shields-diagram is subject to similar assumptions as are made for the derivations of the empirical transport formulas, like e.g. moderate bed slopes. These are, however, often invalid for embankment breach conditions. The values of the Shields-diagram are therefore modified to better account for the special conditions present at embankment breaches using the relations outlined below.

Correction for steep local slope

To consider the influence of steep slopes, multiple corrections were proposed in the past. These account for the gravity influence by modifying the critical shear stress of incipient motion $\tau_{g,crit}$. These modifications result in increased transport rates at the downstream embankment face and reduced ones at the upstream face.

Correction factors $k_{\delta_1}, k_{\delta_2}$ accounting for local slopes in flow direction and in transverse direction were proposed by van Rijn (1989) and are applied in this work as

$$\tau_{g,crit'} = \tau_{g,crit} k_{\delta_1} k_{\delta_2}, \quad (3.7)$$

with

$$k_{\delta_1} = \frac{\sin(\gamma_{rep} + \delta_1)}{\sin \gamma_{rep}},$$

$$k_{\delta_2} = \cos \delta_2 \sqrt{1 - \frac{\tan^2 \delta_2}{\tan^2 \gamma_{rep}}}, \quad (3.8)$$

whereas $\tau_{g,crit'}$ denotes the modified critical shear stress, γ_{rep} is the angle of repose and δ_1 and δ_2 represent the slope angles in flow direction and in its transverse direction⁵.

In this formulation it is assumed that the slope becomes unstable at γ_{rep} and therefore $\tau_{g,crit'}$ reduces to zero at this slope angle. This original approach was modified here to consider stabilizing effects of the slope due to apparent cohesion by replacing γ_{rep} with the slope failure angle γ_{dry} . This angle incorporates stabilizing effects of apparent cohesion and enables the possibility for steeper slopes to develop and is a function of the water saturation and pore-water pressure as presented in section 5.2.2.

In situations with steep slopes where $\tau_{g,crit'}$ vanishes, the correction can lead to divisions by zero for some transport formulas, as e.g. the

⁵The slope angles are formed with the horizontal line and are defined negative in case of a downward slope and positive in case of an upward slope.

formula after Wu (2004), having the parameter in the denominator. Wu (2004) therefore introduced an alternative correction which modifies the bottom shear stress τ_B instead of $\tau_{g,crit}$, thereby preventing divisions by zero.

It is also noted that according to Chen *et al.* (2010) both kind of approaches have the problem that they do not exactly represent the balance of forces on arbitrary sloped terrains in a physically correct way. Out of this reason, they proposed an alternative approach which modifies both the bottom shear stress and the critical shear stress simultaneously. However, due to its increased complexity and larger computational efforts, it is not adopted herein and left for future investigations.

Correction for apparent cohesion

As outlined in chapter 5, the pore-water pressure p_w and water saturation θ influence the shear strength of the embankment material due to apparent cohesion. Apparent cohesion increases the particle stability, analogous to the cohesion of cohesive soils, thereby increasing the critical shear stress for incipient motion and reducing the surface erosion. This stabilizing impact can be expressed with an additional shear strength τ_{coh} due to apparent cohesion using equation 5.3 as

$$\tau_{coh} = (p_a - p_w)\theta \tan \gamma_{rep}. \quad (3.9)$$

For the computation of τ_{coh} , the pore-air p_a and pore-water p_w pressures and the water saturation θ are needed, which are provided by the sub-surface flow modelling (see chapter 4).

This additional shear strength is not included in the Shields-diagram. Therefore it shall be incorporated into the Shields-parameter to consider its effect on the surface erosion. For this task it has to be related to the integral flow properties. A virtual scenario is considered assuming that apparent cohesion is the only resistant force of a particle to the flow. Then, a force balance can be written for the particle at critical condition of incipient motion, whereas the hydrodynamic force is in equilibrium with

the stabilizing force due to apparent cohesion as

$$C_D \frac{1}{2} \rho u_{crit}^2 A_{||} = \tau_{coh} A_{||}, \quad (3.10)$$

where u_{crit} is the critical near-bed velocity, C_D a drag coefficient (assumed to 1.0) and $A_{||}$ the exposed area to the flow. The near-bed velocity u_{crit} can be expressed in terms of the shear-stress velocity u_* using Nikuradse's velocity law for wall-bounded turbulent flows at rough conditions. It reads

$$u(z) = \frac{u_*}{\kappa} \ln\left(\frac{z}{k_s}\right) + 8.5. \quad (3.11)$$

The height z above the embankment for the near-bed velocity is set to the roughness height k_s . Introducing the constant B_1 one obtains

$$u_{crit} = u_* \underbrace{\frac{1}{\kappa} \ln(1) + 8.5}_{B_1} = u_* B_1. \quad (3.12)$$

Using the definition of the Shields-parameter in equation 3.6 and the relation 3.10, the additional component due to apparent cohesion $\Theta_{g,coh}$ is derived as

$$\Theta_{g,coh} = \frac{u_*^2}{(s-1)gd_g} = \frac{2\tau_{coh}}{B_1^2 \rho (s-1)gd_g}. \quad (3.13)$$

Inserting τ_{coh} and introducing the constant B_2 leads to the following formula applied in this work

$$\Theta_{g,coh} = \frac{2}{\underbrace{C_D B_1^2}_{B_2}} \frac{(p_a - p_w)\theta \tan \gamma_{rep}}{\rho (s-1)gd_g}. \quad (3.14)$$

The parameter $\Theta_{g,coh}$ hereby describes the additional grain stability due to apparent cohesion and is added to the value from the Shields-diagram. For partially-saturated conditions, the stability is increased and, hence, the surface erosion is reduced. For fully-saturated or dry conditions, the stability is reduced to the original value from the Shields-diagram. In general, this modification is less significant for large grain sizes d_g , where the gravitational forces are dominant compared to the apparent cohesion.

The above derivation assumes idealized conditions which differ from the real situation. Modifications of this theoretical value therefore are needed and adopted, as follows:

- The grains subject to surface erosion are lying on the embankment surface. They are not embedded in a grain matrix in all directions. This situation reduces the apparent cohesion compared to the theoretical value and is considered with a reduction of the constant B_2 by a factor of 2.0.
- During overtopping, water infiltrates into a thin near-surface layer at the embankment. This process leads to the formation of higher saturations within the near-surface layer reducing the apparent cohesion. The sub-surface flow model, however, cannot resolve this process adequately with its spatial discretization due to the small layer height and because infiltration and erosion take place simultaneously. To consider this aspect, the constant B_2 must be further reduced and is a calibration factor here. Based on the model tests in chapter 7, this effect was estimated as a further reduction of B_2 by a factor of 5.0. Future studies should be made to improve this estimation or to derive enhanced numerical treatments of this effect.

Since infiltration and surface erosion usually both increase with the water depth h , it is assumed that the same constant B_2 can be used for conditions of small depths at breach initiation as well as for large depths at later breach phases.

- Another aspect concerns the treatment of the collapsed and deposited masses. It is assumed here that the deposited material is fully-saturated, due to the strong interactions with the overtopping flow. Hence, $\Theta_{g,coh}$ vanishes for the deposited material, which therefore will be often eroded more rapidly than the underlying material in its original state. This special treatment is applied if the deposition height exceeds the mean diameter d_m of the grain composition.

Correction for ex- and infiltration

In addition to the above mentioned aspects, $\tau_{g,crit}$ is also influenced by water ex- and infiltration processes. Upward seepage ('ex-filtration') occurs when the pore-water pressure in the soil material exceeds the water pressure in the overtopping flow. Then additional lift-forces may act on the bed particles and increase their mobility and even cause soil liquefaction in extreme situations (Ali *et al.* (2003)). This effect was investigated by Cheng and Chiew (1999) who derived a formula to quantify the reduction of $\tau_{g,crit}$ as

$$\tau_{g,crit'} = \tau_{g,crit} \left(1 - \frac{v_{up}}{v_{up,crit}^k} \right), \quad (3.15)$$

with v_{up} = upward directed seepage velocity, $v_{up,crit}$ = critical seepage velocity and k = dimensionless empirical parameter. Applying this formula requires the determination of the empirical parameters k and $v_{up,crit}$. Further, it was noted that $\tau_{g,crit'}$ additionally depends on the angle of the upward seepage direction and the grain sizes.

Differing from this situation, downward directed seepage ('infiltration') is sometimes said to reduce the bottom shear stress and consequently the surface erosion. An empirical relation for the reduced bottom shear stress $\tau_{B'}$ due to infiltration was derived by O'Donnel (2000) as

$$\tau_{B'} = \tau_B \left(1 - 13.89 \frac{v_{down}}{u_*} \right), \quad (3.16)$$

with v_{down} = infiltration seepage velocity.

These empirical approaches are, however, of limited use for the breach model and are not considered here. They were derived for idealized conditions and additional laboratory studies are required to derive the empirical parameters. Furthermore, the issue whether infiltration or ex-filtration increases or reduces the particle mobility is still a matter of debate in literature. Contradicting results were pointed out by Lu *et al.* (2008) and additional research was suggested.

Correction for hiding and exposure effects

During fractional transport in presence of wide-ranging grain compositions, the inception of particle motion is altered due to hiding of fine grains behind larger grains and the exposure of large grains to the flow. A hiding and exposure function ψ_g is introduced to consider these effects, which is multiplied with the Shields-parameter $\Theta_{g,crit}$. It is applied in the formulation proposed by Ashida and Michiue (1971) and is computed as function of the grain diameter d_g and the mean grain diameter d_m as

$$\psi_g = \begin{cases} \left(\frac{\log 19}{\log(19d_g/d_m)} \right)^2 & \frac{d_g}{d_m} \geq 0.4 \\ 0.85 \frac{d_m}{d_g} & \frac{d_g}{d_m} < 0.4. \end{cases} \quad (3.17)$$

3.3.2 Empirical closures for bed-load transport

Meyer-Peter & Müller formula (MPM)

The bed-load flux q_{Bg} is needed for the solution of the governing equations and is determined with empirical transport formulas. The formula of Meyer-Peter and Müller (1948) determines the bed-load transport capacity for grain class g . It is applied separately for each grain class as

$$q_{Bg} = 8.0 \sqrt{(s-1)g} \left(\Theta_g - \Theta_{g,crit} \frac{k_{str}}{k'_{str}} \right)^{3/2} d_g^{3/2}, \quad (3.18)$$

where k_{str} = calibrated friction coefficient and k'_{str} = grain size friction coefficient.

A modified version of this MPM formula was presented by Wong and Parker (2006) and is labelled from here on 'modified-MPM' formula. The main differences in their derivation, including the original data sets of Meyer-Peter and Müller (1948), are the removal of the bed form roughness term and a corresponding reduction of the pre-factor. These modifications seem adequate for embankment breaches, since no forma-

tion of regular bed-forms is expected. It is applied in this work as

$$q_{B,g} = 4.0\sqrt{(s-1)g}(\Theta_g - \Theta_{g,crit})^{3/2}d_g^{3/2}. \quad (3.19)$$

This bed-load formula is used for the embankment breach applications in chapter 7, whereas the pre-factor was varied for the different scenarios in between 4.0-6.0.

Discussion and limitations

Most empirical transport formulas were derived by studies of sediment movements in laboratory flumes under idealized conditions. The underlying assumptions are often invalid at conditions during embankment breaching and are briefly discussed hereafter.

Unsteady flow conditions: During embankment breach events the flow is accelerated, and changes from sub- to super-critical flow conditions are to be expected, especially regarding the first breach stage with steep slopes. Most transport formulas were derived for sub-critical and normal flow conditions, however. Their suitability for embankment breach events therefore is generally questionable. At later breach stages, which are important for the formation of the peak discharge, the underlying assumptions are more appropriate since the embankment slopes are flattened rapidly and the flow often approaches quasi-steady flow conditions.

Compacted material: Embankment structures often consist of compacted material, which is placed in layers during construction and is densified to decrease seepage rates and increase the erosion resistance. The effects of soil compaction are thereby of major importance for cohesive material and are generally less significant for non-cohesive material.

Nevertheless, according to laboratory investigations of Gauche *et al.* (2010), compaction also alters the erosion characteristic of non-cohesive material. They observed that compaction usually decreases the transport rate, although in some cases with

strong bottom shear stresses an increase was observed. They did not provide practical recommendations but highlighted the need for further research and the derivation of specially suited transport formulas for compacted material at embankment breaches.

Steep slope: Especially during the first stages of embankment overtopping, one has to deal with flow over steep embankment slopes. This is problematic since most empirical transport formulas were derived for mild slopes in river streams. The MPM and the modified-MPM formula were derived based on experimental data concerning moderate slopes up to about 2%. The influence of steep local slopes is incorporated to some degree in the model, however, by modifying the critical shear stress of incipient motion as outlined above in section 3.3.1.

Influence of lateral slope: In addition to the sediment transport in stream-wise direction, a transversal component of the transport rate is considered using the empirical approach after Ikeda (1982) as applied in Faeh (2007) for 2D simulations. This lateral transport component $q_{Bg,lat}$ accounts for situations with a bed slope transversal to the flow direction, as e.g. along the breach side walls, leading to a gravitationally-induced drift in the direction of particle motion. It is determined as function of the stream-wise bed-load flux q_{Bg} as

$$q_{Bg,lat} = 1.5 \sqrt{\frac{\tau_{crit,g}}{\tau_B}} q_{Bg}. \quad (3.20)$$

3.3.3 Empirical closures for suspended-load transport

Determination of entrainment and deposition rates

The source term s_g addresses the exchange of suspended material with the bed-load control volume. Its computation is tied to the idea of estimating the net exchange as difference between the entrainment rate E_g and the deposition rate D_g as

$$s_g = E_g - D_g. \quad (3.21)$$

The deposition rate D_g of suspended material is evaluated as the product of the near-bed concentration $C_{nb,g}$ of a grain class g multiplied with its settling velocity w_{Sg} as

$$D_g = \beta_g C_{nb,g} w_{Sg}. \quad (3.22)$$

A variety of different semi-empirical approaches were presented in literature to estimate the settling velocities w_{Sg} of particles. A comprehensive overview was presented in Fentie *et al.* (2004). Here, the settling velocities are determined after van Rijn (1984). The other semi-empirical parameter, the near bed concentration $C_{nb,g}$, is more difficult to determine. It has to be estimated using simplifying assumptions, since the depth-averaged model contains no information about the vertical concentration profile but only provides a depth-averaged concentration C_g . The near-bed concentration is related to C_g using the formula of Lin (1984), which assumes equilibrium conditions, as

$$C_{nb,g} = C_g \left(3.25 + 0.55 \ln \left(\frac{w_{Sg}}{\kappa u_*} \right) \right). \quad (3.23)$$

The entrainment rate E_g of particles into suspended state in the water column is estimated in a similar way. It is assumed hereby that an equilibrium is formed between entrainment and settlement of particles at the reference height z_R . The entrainment rate is then computed as a product of a reference concentration C_{Rg} and the settling velocity w_{Sg} of the grain class g as

$$E_g = \beta_g C_{Rg} w_{Sg}. \quad (3.24)$$

Several empirical formulas were proposed to determine the reference concentration based on integral flow properties for depth-integrated models and an overview is given in Camenen and Larson (2008). In this work the formula after van Rijn (1984) is applied with the dimensionless grain diameter $D_g^* = ((s - 1)g/\nu^2)^{1/3} d_g$ as

$$C_{Rg} = 0.015 \frac{d_g}{z_R} \frac{((\tau_B - \tau_{crit,g})/\tau_{crit,g})^{3/2}}{D_g^{*0.3}}. \quad (3.25)$$

The reference height is determined as function of the grain composition and the water depth as applied in the work of Faeh (2007) as $z_R = \max(3d_{90}, 0.1h)$.

These empirical parameters were used in the presented form and were not adjusted or calibrated in the model applications.

Discussion and limitations

In general, the empirical formulas used for the estimation of entrainment and deposition rates suffer from similar uncertainties and problems as mentioned for the bed-load transport. The aspects listed above in section 3.3.2 therefore also apply to the suspended-load transport.

3.3.4 Portioning between bed- and suspended-load

In this modelling approach bed- and suspended-load can be applied in combination. Therefore it has to be determined whether a particle is transported as bed- or suspended-load in the model. This decision is often made depending on the bottom shear stress and the particle settling velocity. Liu (1957) introduced the dimensionless Movability Number Mn as indicator, which relates the shear stress velocity u_* to the settling velocity w_{Sg} as

$$Mn = \frac{u_*}{w_{Sg}}. \quad (3.26)$$

Many theoretical and empirical investigations were made regarding the relation of Mn and the motion of particles as suspended-load. Table 3.1 presents an overview of different published data on the inception of suspended-load transport in terms of Mn , based on a summary of Chanson (2004b). Regarding these data, Mn ranges in between values of ~ 0.2 - 2.0 . Here, the criterion suggested by van Rijn (1984) is adopted for the inception of suspended-load transport.

Table 3.1: Comparison of different Movability numbers Mn for inception of suspended-load transport based on Chanson (2004b).

Bagnold (1966)	$Mn > 1.0$	Inception of suspended load transport
van Rijn (1984)	$Mn > 4/D_g^*$ $Mn > 0.4$	In case of $1 < D_g^* \leq 10$ In case of $D_g^* > 10$
van Rijn (1984)	$Mn > 10.0$	Dominant suspended load transport
Julien (1995)	$Mn > 0.2$ $Mn > 2.5$	Inception of suspension under turbulent conditions Dominant suspended load
Raudkivi (1989)	$Mn > 1.7$	Suspended load transport

The portioning between bed- and suspended-load transport is eventually determined in dependence of Mn introducing the transport allocation factor Π , which represents the suspended-load portion of the total transport. It is determined as

$$\Pi = \begin{cases} 0.0 & Mn < 0.4 & \text{(only bed-load)} \\ 0.25 + 0.325 \log(Mn) & 0.4 \leq Mn \leq 10.0 & \text{(bed- and suspended-load)} \\ 1.0 & Mn > 10.0 & \text{(only suspended-load)} \end{cases} \quad (3.27)$$

In case of fractional transport, the settling velocity w_{Sg} is determined for each grain class separately. As a consequence, different values for Mn_g and Π_g are obtained and applied to each grain class separately allowing for a flexible portioning of bed- and suspended-load transport. For example, if the embankment material consists of a wide-ranging grain distribution, the fine-grained material may be transported dominantly as suspended-load and the coarse-grained material as bed-load.

3.4 Numerical modelling

3.4.1 Dual-mesh approach

As described in section 2.4.1, a cell-centered discretization scheme is used for the hydrodynamic modelling. The flow variables are defined at the cell centers and the bed-levels z_B at the cell vertices. This discretization allows for linear variations of the bed-level within each cell enabling a second-order accurate terrain representation. It would be generally desirable to use this discretization scheme for the sediment transport modelling, too, in particular for scenarios with complex terrains like embankment breaches. However, current sediment transport models are based either on structured meshes or use a cell-vertex discretization with constant bed-levels over the cells.

If the spatial discretization of the hydrodynamics is also applied for the sediment transport modelling, one is confronted with multiple problems which are illustrated in Figure 3.3 and summarized as follows:

- Changes in the sediment volume of a cell by in- or outflowing sediment fluxes must be distributed to the vertices of this cell. However, this distribution is not unique and it is not clear by which criterion this should be done (Figure 3.3 (a)),
- Changes in bed elevation z_B of a vertex do not only affect the sediment volume of this cell, but the sediment volumes of all adjacent cells too. This is problematic especially regarding the sediment mass continuity (Figure 3.3 (b)), and
- These mutual influences between adjacent cells correspond to diffusive fluxes between the cells. In case of fractional transport with multiple grain classes, these may even lead to an undesired mixing of the grain compositions.

Herein a solution strategy for these problems is proposed which maintains the second-order accurate terrain representation for the hydrody-

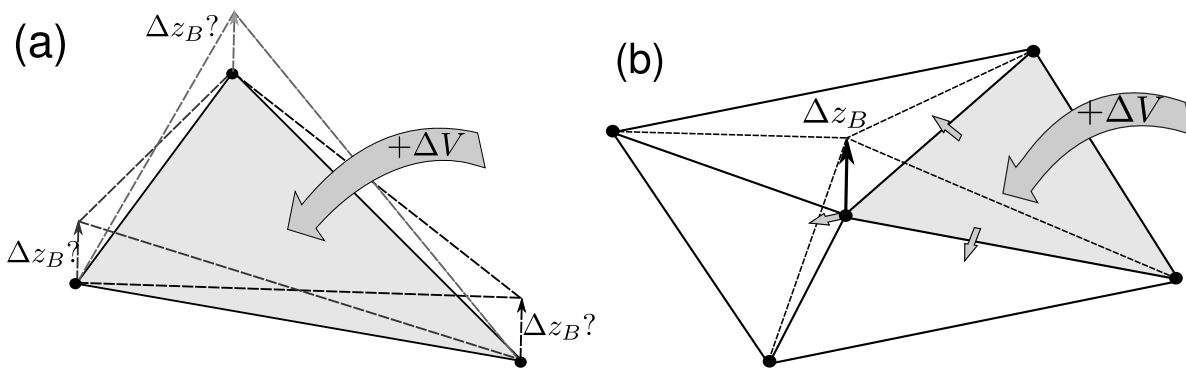


Figure 3.3: (a) Non-unique distribution of incoming sediment volume to the cell vertices. (b) Change of vertex elevation influences the sediment volumes of adjacent cells.

namics. The basic idea is to apply an additional mesh for the sediment transport. Since hydrodynamics and sediment transport are then computed on separate meshes, this spatial discretization is labelled 'dual-mesh' approach here.

The cells for the sediment transport are set around the vertices of the original mesh as Median Dual cells. These are formed by connecting all edge midpoints and cell midpoints around a vertex as it is illustrated in the left part of Figure 3.4. Both types of meshes hereby make use of the same mesh vertices where the bed-levels are defined. From here onward, cells and edges of the additional mesh are referred to as 'sediment cells' and 'sediment edges', whereas those of the original mesh are labelled 'hydraulic cells' and 'hydraulic edges'. Analogous, the different meshes are labelled 'sediment mesh' and 'hydraulic mesh'.

The bed-levels z_B and the grain fractions β_g are defined at these sediment cells and set constant over each cell. One obtains a standard cell-vertex FV method for the sediment transport on the additional mesh. In contrast, the hydrodynamic computations still use a cell-centered approach and profit from the accurate representation of the topography. The previously mentioned problems are thereby avoided. Changes of a sediment cell volume do not influence adjacent sediment cells and sediment mass continuity is guaranteed. These properties are illustrated in the right part of Figure 3.4, which shows a cross-sectional view

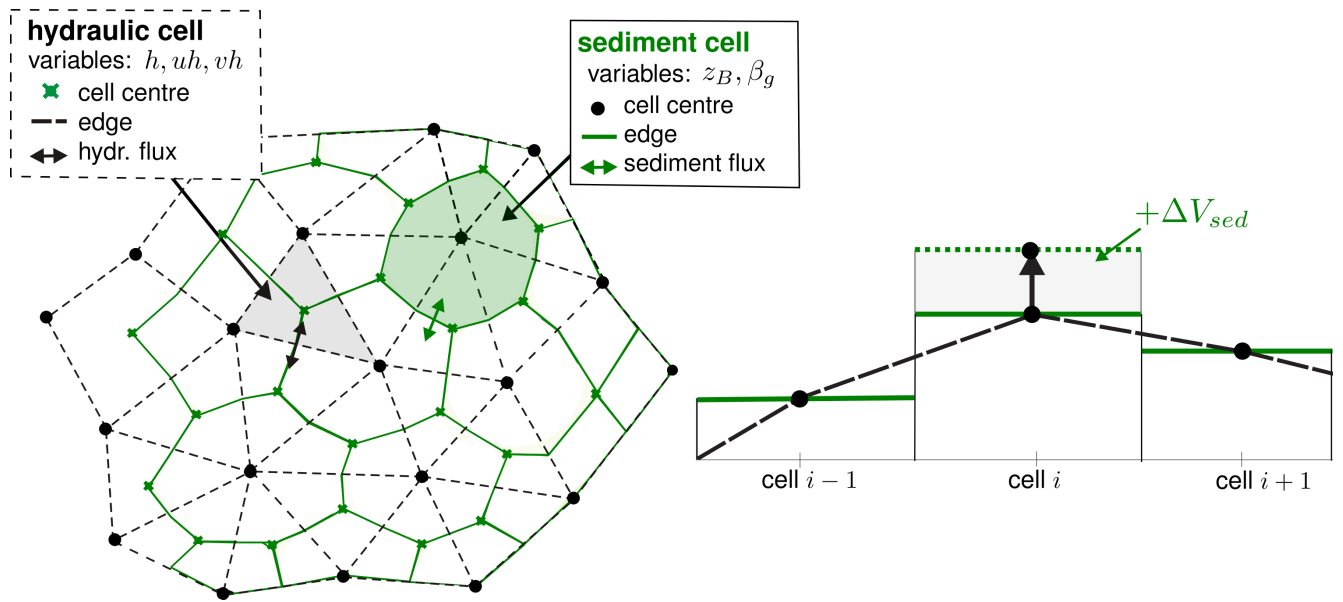


Figure 3.4: *Dual-mesh approach - cell-centered discretization for hydrodynamic computations (dashed), cell-vertex discretization for sediment computations (solid). Left: top-view on mesh. Right: idealized cross-sectional view with local sediment input ΔV_{sed} .*

through the sediment mesh. It illustrates that a volume change in a sediment cell of ΔV_{sed} does neither affect the sediment volumes of the adjacent sediment cells nor creates artificial fluxes.

Furthermore, one can prove that the sediment volume ΔV_{sed} , which is added by raising a vertex elevation, is equal in size for both meshes. As a consequence, it is guaranteed that the overall volumes embraced by the meshes will not diverge over time. Figure 3.5 illustrates the added volumes in both meshes. In its left part, the additional volume ΔV_{hyd} is shown which results for a triangular cell in the hydraulic mesh. The right part of the Figure shows the additional volume ΔV_{sed*} which results for the corresponding part of the sediment cell⁶.

This volume identity can be proven with basic geometrical considerations for triangles, whereas A_{hyd} and A_{sed*} are the base areas of the

⁶The volume ΔV_{sed*} is only a portion of the total volume ΔV_{sed} added to the sediment cell by raising its vertex elevation. It is only that portion associated with a specific hydraulic cell.

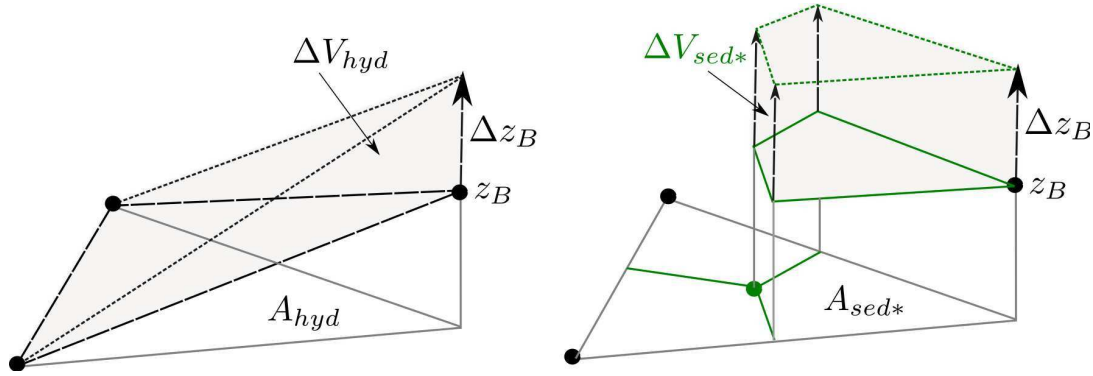


Figure 3.5: Raising the vertex elevation modifies embraced volumes of both meshes. Left: additional volume ΔV_{hyd} for hydraulic cell. Right: additional volume ΔV_{sed*} for sediment cell.

hydraulic cell and the associated part of the sediment cell:

$$\begin{aligned} \Delta V_{hyd} &= \frac{1}{3} A_{hyd} (z_B + \Delta z_B) - \frac{1}{3} A_{hyd} z_B = \frac{1}{3} A_{hyd} \Delta z_B \\ \Delta V_{sed*} &= \underbrace{A_{sed*}}_{\frac{1}{3} A_{hyd}^7} \Delta z_B = \frac{1}{3} A_{hyd} \Delta z_B = \Delta V_{hyd}. \end{aligned} \quad (3.28)$$

This identity of $\Delta V_{hyd} = \Delta V_{sed*}$ holds true for all hydraulic cells surrounding the sediment cell. Therefore the raise of a vertex elevation is guaranteed to add equal volumes to both meshes. For quadrilateral cells this identity is difficult to prove exactly, due to the lack of a clearly defined cell slope. If all vertices lie on a plane, however, the above considerations are trivially extended to quadrilateral cells by dividing them into triangles.

To assess the mass conserving property of the dual-mesh approach in the various model tests, two parameters are introduced:

- The total mass error E_{tot} [m^3] of the sediment material. It is determined by balancing all in- and outflowing boundary sediment fluxes $Q_{B,in}(t)$, $Q_{B,out}(t)$ and the change of total sediment volume

⁷It is made use of the mathematical theorem stating that the area of a triangle is divided into three equally sized areas by its median lines.

$V_{sed,total}(t)$ within the entire computational domain over time as

$$E_{tot} = \left| \sum_t Q_{B,in} \Delta t - \sum_t Q_{B,out} \Delta t + V_{sed,total}(t) - V_{sed,total}(t=0) \right|, \quad (3.29)$$

and

- The area specific mass error E_{spec} [m]. It avoids the dependence on the size of the computational domain by dividing the total mass error E_{tot} [m³] through the area A_{tot} [m²] of the computational domain as

$$E_{spec} = \frac{E_{tot}}{A_{tot}}. \quad (3.30)$$

These mass errors are expected to be in the range of numerical round-off errors, since the dual-mesh approach is strictly mass conserving.

3.4.2 Vertical discretization & surface protection

The computational mesh represents a spatial discretization of the terrain surface. To be able to distinguish between different material compositions β_g over the depth, an additional vertical discretization with multiple sediment layers is applied as sketched schematically in Figure 3.6. This vertical discretization can be used to represent various embankment features as

- Surface protection layer of the embankment slopes, consisting of gravel or boulders protecting the underlying finer material from erosion,
- Fine-grained inner core with low hydraulic permeability, and
- Coarse-grained filter zones at the embankment bottom and downstream toe to lower the seepage line.

To consider the sediment layers in the modelling approach, a 1-layer concept is adopted as introduced by Hirano (1971), where the sediment transport and the exchange with the underlying material takes place

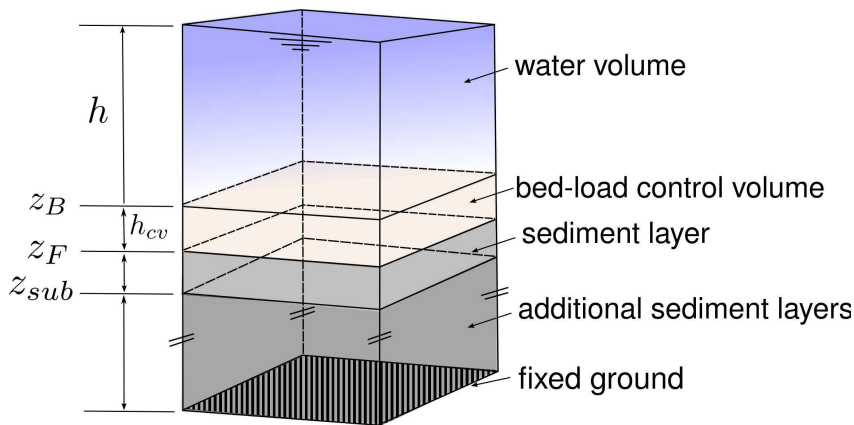


Figure 3.6: Vertical discretization with bed-load control volume and underlying sediment layers of different grain compositions.

within a single uppermost layer, the bed-load control volume. If the bed-level z_B changes over time, a vertical sediment flux arises between the bed-load control volume and the underlying layer. All other sediment layers underneath the first remain unchanged until their overlying layers are completely eroded.

Thickness of bed-load control volume

The sorting of sediment material takes place in the bed-load control volume. Therefore its thickness $h_{cv} = z_B - z_F$ is an important simulation parameter for fractional transport. It influences how fast the material can adapt to the present flow conditions and how fast changes in the soil composition propagate downstream. If h_{cv} is chosen small, this adaptation occurs fast and the fine grains are removed rapidly, coarsening the grain composition and slowing down the erosion process (Kroekenstoel and van Velzen (2010)). If h_{cv} is chosen large, the soil composition needs more time to adapt to the flow conditions.

One can distinguish between approaches which determine the thickness h_{cv} depending on the flow conditions (e.g. Borah *et al.* (1982)), as a function of the present grain mixture or using a constant value. Contradicting recommendations are found in literature regarding the use of these different approaches. If no bed forms evolve, a relation of

the thickness to the grain composition may be adequate as stated by Kroekenstoel and van Velzen (2010). Such an approach is applied here, due to its simplicity and because no formation of bed forms is expected during breaching.

A variety of different estimations for h_{cv} were proposed in the past. Here, the thickness is determined as a function of the d_{90} diameter of the grain mixture after a modified approach of Malcherek (2009) as $h_{cv} = 5d_{90}$. This approach is used because it leads to rather large values compared to other estimations, what is seen appropriate regarding the large erosion rates during embankment breaches. This thickness is computed separately for each sediment cell and, hence, can vary over space and time.

Modelling of embankment surface protection

Two different conceptual approaches can be used in the model for the representation of surface protection layers of the embankment slope.

One concept is the use of coarse-grained material in the upper sediment layer, consisting of erosion-resistant material. The corresponding critical shear stresses of incipient motion have to be overcome by the overtopping flow before breach initiation starts.

A different concept is needed for the representation of surface protections based on vegetation covers, geo-textile liners or similar erosion-resistant material, which cannot be modelled adequately with empirical transport formulas. An overview over different approaches was presented by Samani and Kouwen (2002). Among others, it is distinguished between approaches based on maximum flow velocities, maximum bottom shear stresses or equivalent grain diameters with corresponding stability characteristics. Here, the stability of the surface protection bases on the definition of a maximum bottom shear stress $\tau_{crit,init}$. The surface is treated as non-erodible until the bottom shear stress exceeds this initial threshold $\tau_B > \tau_{crit,init}$ at least once. Then, the surface protection is removed from the cell and the bed-level is no longer treated as fixed. Val-

ues for maximum shear stresses of vegetation covers range widely from a few N/m^2 up to hundreds N/m^2 for root-permeated soils as mentioned by Quan and Oumeraci (1989). The Bundesamt für Wasserwirtschaft (1982) estimates values in between 30-50 N/m^2 for grass covers.

It is emphasized, however, that this approach simplifies the real situation for vegetation covers. In reality the resistant shear stresses vary over the soil depth due to root density variations. Furthermore, the vegetation also influences the near-bed flow conditions and may reduce the bottom shear stress exerted by the overtopping flow.

In principal, both conceptual approaches could be combined together, e.g. in cases of surface protections consisting of boulders which cannot move freely but are interconnected with each other and require an initial triggering mechanism to be firstly mobilized. However, the adequateness of these concepts to represent embankment surface protections in a realistic way is not investigated within the scope of this work and remains an open task.

3.4.3 Solution of governing equations

The FV method in combination with an explicit Euler time integration is applied for the solution of sediment continuity equations and the advection-diffusion equations. The continuity equations are integrated over the sediment cell areas, whereas the advection-diffusion equations are integrated over the hydraulic cell areas. The applied solution schemes are presented in Appendix B.

3.5 Validation of bed-load transport modelling

Validation of sediment transport modelling is generally a difficult task due to the complex processes and mathematical descriptions involved. Two often used reference tests regarding bed erosion and aggradation are

presented hereafter⁸. These tests have no direct link to embankment breaches, but shall validate the correct implementations and functioning of the numerical algorithms and the dual-mesh approach. Model applications to embankment breach scenarios are presented in chapter 7.

3.5.1 Formation and propagation of a sediment front

This test deals with bed aggradation due to sediment overloading. The sediment input at the upper channel end was chosen considerably larger than the transport capacity of the flow, leading to the formation of an aggradation front which travelled downstream. The test is used to investigate whether the model can reproduce this sediment front formation and its propagation. The experiments were conducted in a laboratory flume and are described in Saiedi (1981a) and Saiedi (1981b).

Sediment with a uniform grain size distribution of $d = 2$ mm was used with a porosity of $p = 0.37$. The channel was 18 m long and 0.6 m wide with a slope of 0.1%. It was discretized in the model using an unstructured grid consisting of ~ 1000 triangular cells and its bottom was treated as non-erodible. The friction coefficient was set to $k_{str} = 60$ m^{1/3}/s, following the recommendation of the experimenter. First, a uniform flow with constant inflow of $Q_{in} = 0.098$ m³/s and a water depth of $h = 0.22$ m was established. Then, the inflow was fed with a sediment supply of 3.81 kg/min, exceeding the transport capacity.

The formation and propagation of the sediment front were captured well in the simulation, and the experimental results were basically reproduced as illustrated in Figure 3.7. The total sediment mass error was determined to $E_{tot} < 10^{-10}$ m³ and the area specific mass error to $E_{spec} < 10^{-12}$ m. The sediment mass continuity therefore is strictly satisfied using the dual-mesh approach, despite the occurrence of large and rapid bed-level changes.

⁸No tests are presented for suspended-load transport, but can be found in Faeh *et al.* (2012).

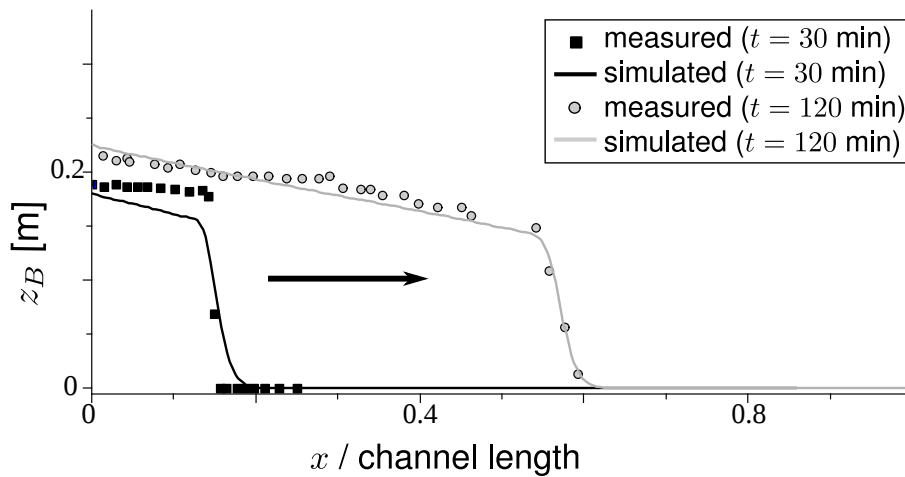


Figure 3.7: Comparison of measured and simulated bed-levels of the aggradation front at two times $t = 30 \text{ min}$, 120 min .

3.5.2 Grain sorting - formation of armouring layer

A test series was performed by Günter (1971) dealing with bed erosion in a laboratory flume. He was interested in the sorting of different sized grain classes and in the formation of a bed armouring layer over time. The experiments were conducted using a series of different runs, whereas here the experiment 'No. 3' was selected. The material was represented with six grain classes as presented in Table 3.2 and a porosity of $p = 0.37$. The straight and rectangular experimental flume was 40 m long and 1 m wide.

Table 3.2: Initial grain composition of the mobile bed represented with six grain classes.

Grain 1	Grain 2	Grain 3	Grain 4	Grain 5	Grain 6
0.51 mm	1.52 mm	2.55 mm	3.60 mm	4.65 mm	5.60 mm
35.9 %	20.8 %	11.9 %	17.5 %	6.7 %	7.2 %

As initial state, a mobile bed with a slope of 0.25 % was set and discretized with ~ 2000 cells. A constant friction coefficient of $k_{str} = 52 \text{ m}^{1/3}/\text{s}$ was used for the whole domain. The inflow discharge was set to $Q_{in} = 56 \text{ l/s}$ at the upper channel end. No sediment entered the channel, which led to bed erosion. The bed finally approached a quasi-equilibrium

state with an armouring layer protecting it from further erosion.

In general, it can be stated that the simulation of an armouring layer formation is numerically very challenging. The test is, however, known to perform well with the transport formula after Hunziker and Jaeggi (2002), whose derivation included the test data. This formula is therefore used for this test case and allows for the validation of the correct implementation of the grain sorting processes.

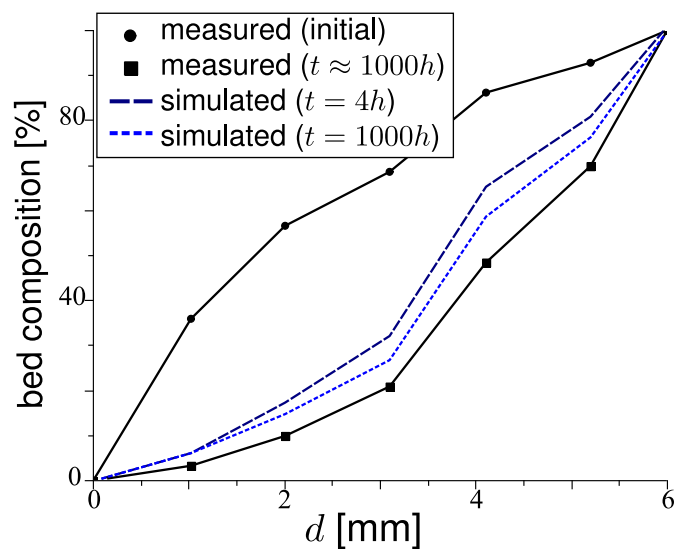


Figure 3.8: Final grain compositions of bed armouring layer in experiment and simulation.

The simulated grain compositions of the armouring layer are compared with the measured values in Figure 3.8 and show good accordance. The sediment mass errors were determined to $E_{tot} < 10^{-12} \text{ m}^3$ and $E_{spec} < 10^{-13} \text{ m}$, lying within the range of round-off errors. These results demonstrate the correct implementation of fractional transport modelling and the sediment mass conserving property of the dual-mesh approach.

3.6 Summary

The applied governing equations for sediment mass continuity and advection-diffusion transport were presented and their numerical solutions based on explicit FV methods were introduced leading to first-order accurate schemes. Furthermore, the adopted simplifications were discussed with special regard to embankment breaches. As future model enhancement, especially taking into account non-equilibrium transport seems promising. The consideration of a varying material porosity may also improve the modelling in cases of compacted embankment material.

Empirical closures for the bed- and suspended-load transport were outlined and their underlying assumptions and limitations regarding their application to non-cohesive embankment breaches were discussed. Furthermore, modifications of the Shields-parameter for the inception of particle motion were presented to include effects of steep slopes and apparent cohesion for embankment erosion. Further investigations of the complex effects of apparent cohesion and their interaction with the embankment erosion are recommended.

A novel dual-mesh approach with separate meshes for hydrodynamic and sediment transport modelling was developed and implemented. A cell-vertex discretization is applied for the sediment transport, whereas a cell-centered discretization with varying bed-level over the cell is used for the hydrodynamic modelling. The dual-mesh approach is thereby strictly mass conserving and it preserves the second-order accurate terrain representation of the hydrodynamic modelling.

In addition, the vertical discretization with multiple sediment layers was presented. The model allows for different soil compositions to be specified over the depth, enabling in principle the representation of heterogeneous embankments. It is also possible to consider embankment surface protections by either adopting a coarse-grained surface layer or specifying a critical initial shear stress which must be overcome. These aspects are, however, not focused here and additional investigations are necessary to evaluate their suitability for breach modelling.

The bed-load transport modelling and the dual-mesh discretization were tested on two reference laboratory studies of a sediment front propagation and an armouring layer formation. The model successfully reproduced both tests involving single grain and fractional transport. The obtained results demonstrate the correct model implementations and the mass conserving property of the dual-mesh approach.

4

Modelling of Sub-Surface Flow

4.1 Introduction

It is well known that the soil shear strength and slope stabilities of earth embankments depend on the internal water saturations and pore-water pressures. Analysis of sub-surface flow and water infiltration into embankments therefore is an important aspect for stability evaluations and should be considered in breach models.

Earth embankments consist of particles of different sizes and shapes which are connected to the surrounding particles at contact points. The pore space in between the particles is filled with air or water forming a two- or three-phase system. Since the exact positions and shapes of the particles and pores are usually unknown, these small-scale properties are averaged over a Representative Elementary Volume (REV) to obtain macroscopic properties for practical use (Bear and Cheng (2010)). An important parameter to characterize the degree of water within the pores of the REV is the dimensionless water content, which is defined as

$$\theta_w = \frac{\text{water volume within REV volume}}{\text{bulk REV volume}}. \quad (4.1)$$

If the pores are completely filled with water, the soil is said to be saturated and the saturated water content θ_S equals the material porosity. The residual water content θ_R characterizes the immobile part of the pore-water which remains after water drainage and adheres to the particles. Using these parameters, the dimensionless effective water saturation θ is

introduced as primary variable for sub-surface flow modelling as

$$\theta = \frac{\theta_w - \theta_R}{\theta_S - \theta_R}. \quad (4.2)$$

The parameter θ varies in between 0.0 for (residual) dry conditions and 1.0 for saturated conditions. Other major parameters for sub-surface flow are the pore-water pressure p_w and the pore-air pressure p_a within the granular pores. The pore-water pressure is also used in a pressure-head formulation as $h_w = p_w/(\rho g)$.

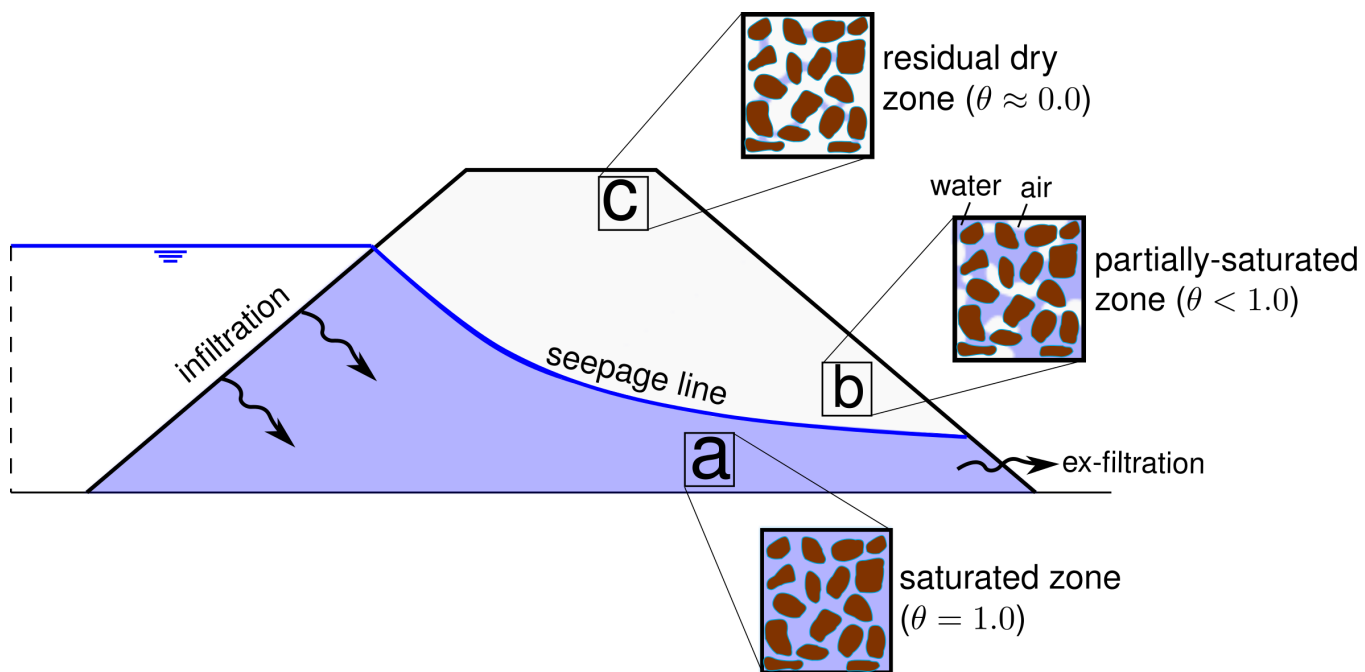


Figure 4.1: Cross-sectional view of embankment with zones of different water saturations.

One has usually to deal with zones of different water saturations within the embankment structure. These zones show different characteristics regarding the soil shear strength and the water movement. These characteristics and underlying physical processes are briefly summarized below.

Saturated zone. In the saturated zone the granular pores are completely filled with water ($\theta = 1.0$). It is situated below the seepage line¹ in the embankment as sketched in Figure 4.1 (a). The water-phase within this zone is continuous allowing for the transmission of the water pressure and leading to a positive and increasing pore-water pressure over the depth.

The conductivity of the water flow in this zone is described with the hydraulic conductivity k_f . It is a material property and is generally small for fine-grained material, as silt or fine sand, due to its small pores and tortuous flow paths. In contrast, it is larger in coarse-grained material, as sand or gravel, due to the larger pore-volumes.

Partially-saturated zone. This zone is situated above the seepage line as illustrated in Figure 4.1 (b). The granular pores are partially filled with water and air forming a three phase system with the soil material. Between the particles, contractile skins or membranes of water develop. Due to surface tension effects at these curved membranes, matric suction arises which connects the particles with each other as a stabilizing force. For a single curved membrane with the radii r_1 and r_2 the matric suction is theoretically determined with the water surface tension σ_w as (Bear and Cheng (2010))

$$p_a - p_w = \sigma_w \left(\frac{1}{r_1} + \frac{1}{r_2} \right). \quad (4.3)$$

These stabilizing contractile skins increase the soil shear-strength. This effect is often labelled 'apparent cohesion' since it acts similar as the cohesion in cohesive soils². The empirical 'water retention curve' is often used to characterise the matric suction of a soil at different water saturations by specifying a relation $p_a - p_w = f(\theta)$ or $h_w = f(\theta)$. It can be experimentally derived by determining how

¹Instead of 'seepage line', the exchangeable terms 'phreatic surface', 'saturation line' or 'saturation front' are often used in literature. It characterizes the transition from saturated to partially-saturated conditions.

²Details regarding the soil shear-strength and its physical description are outlined in chapter 5.1.2 dealing with slope stabilities.

much water is retained in the soil by the matric suction, if a negative pressure is applied to drain it. During drainage, at first the larger pores are drained where smaller matric suction occurs. Thereafter, the smaller pores are drained where larger matric suction occurs.

In the partially-saturated zone, the passage of water is hindered by the air-phase present in the pores. The flow paths become longer and more tortuous, leading to a reduction of the hydraulic conductivity. This reduction is expressed with the dimensionless relative conductivity k_r , which reduces from 1.0 in the saturated zone to smaller values at lower saturations and approaches its minimum at the residual water content. This effect is important for the flow in the partially-saturated zone, as e.g. during water infiltration into the embankment. The empirical relation describing k_r as a function of the water saturation, $k_r = f(\theta)$, is labelled the 'relative hydraulic conductivity curve' here.

Residual zone. In the residual zone, the air-phase occupies large parts of the pores as shown in Figure 4.1 (c). Although the matric suction may further increase with lowering saturation, the soil shear strength typically is reduced since only few contractile skins can develop between the particles. As a consequence, the stabilizing effect of apparent cohesion vanishes at dry conditions.

Furthermore, as outlined above, the relative hydraulic conductivity k_r approaches its minimum value in the residual zone.

Due to these different characteristics of the mentioned zones, a variably-saturated flow modelling needs to be considered in the breach model.

In section 4.2, the physical and mathematical descriptions of sub-surface flow are briefly presented and the empirical relations are given in section 4.3. Then, the numerical modelling approach and its application to variably-saturated flow is outlined in section 4.4. In section 4.5 the implemented method is tested and validated and section 4.6 summarizes the contents and findings of this chapter.

4.2 Governing equation - Richards equation

In general, distinction is made between pore-scale and macroscopic descriptions of the water flow. Pore-scale models explicitly represent the granular pores and the tortuous flow paths and are therefore limited to small laboratory scales and are mainly used to derive soil parameters. Macroscopic models, in contrast, operate with REV-averaged variables without knowledge of the detailed pore-distributions, allowing for model extents ranging from metres up to kilometres.

A further model distinction can be drawn by the degree to which the air-phase is considered in the mathematical framework. Three main approaches are often distinguished:

- Flow analysis in embankments is often performed solving the 'groundwater flow equation' for sub-surface flow with a free surface. A common formulation is

$$S_0 \frac{\partial h_w}{\partial t} = \nabla(K(h_w)\nabla h_w), \quad (4.4)$$

with S_0 as the specific yield and the soil conductivity K . The free surface introduces non-linearities, which are typically weak and are either treated with iterations or are linearised. Many numerical models were presented solving this equation in an efficient and robust way. The flow in the partially-saturated zone is hereby neglected and only the water-phase is considered.

- The 'Richards equation' accounts for variably-saturated flow. Constitutive models consisting of a water retention curve and a relative hydraulic conductivity curve allow for an approximation of the multi-phase flow with a single partial differential equation. It bases on the assumption that the air-phase is always continuous and in contact with the atmosphere and therefore at atmospheric pressure ($p_a = 0$). Multiple formulations of the Richards equation in terms of different primary variables were derived.

- A more general approach is the derivation of separate differential equations for the air- and water-phases. These coupled equations describe the fluid flow of each phase separately considering their mutual influences (Bear and Cheng (2010)). The numerical solution of the coupled equations, however, is challenging, computationally expensive and sometimes prone to numerical instabilities (Pham-Van *et al.* (2011)).

The groundwater equation is regarded as inappropriate for the breach model, since the flow in the partially-saturated zone and water infiltrations cannot be addressed. A full two-phase flow modelling, in contrast, seems necessary only if the assumptions made for the Richards equation are no longer appropriate. During embankment overtopping, for example, situations can arise where air is trapped and compressed in regions surrounded by water. Then the assumption of atmospheric air pressure is violated (D'Eliso *et al.* (2006)). Nevertheless, the assumption is usually said to be accurate enough for almost all practical applications (Lam *et al.* (1987)). Solving the Richards equation therefore is seen as a good compromise between overall accuracy and practicability and is adopted herein.

The Richards equation was derived by Lorenzo A. Richards (1931) based on the assumption that Darcy's law for saturated flow can be extended to the unsaturated zone using a hydraulic conductivity which is a function of the saturation. It is a non-linear partial differential equation of parabolic type, which can be formulated in form of an advection-diffusion equation (ADE). The Richards equation is applied in an effective saturation formulation for θ as primary variable as

$$\frac{\partial \theta}{\partial t} - \nabla (K \nabla z) - \nabla (D \nabla \theta) = 0, \quad (4.5)$$

with $D = K \frac{\partial h_w}{\partial \theta}$,

and it is used in a mixed saturation and pressure head formulation for θ

and h_w as

$$\frac{\partial \theta}{\partial t} - \nabla (K \nabla z) - \nabla (D \nabla h_w) = 0, \quad (4.6)$$

with $D = K$,

where D is the diffusivity and K is the soil conductivity. The latter is determined as the product of the dimensionless relative conductivity k_r and the saturated hydraulic soil conductivity k_f as $K = k_r(\theta)k_f$.

In contrast to the θ formulation, the mixed θ - h_w formulation correctly reproduces the continuous transition of the pressure at the interface of soils with different material properties. Hence, the mixed θ - h_w formulation should be applied in cases of heterogeneous embankments with core or filter zones. Applying the θ formulation may result in incorrect pressure discontinuities at the material interfaces. The θ formulation, instead, has advantageous stability conditions for infiltration into dry soils, since the diffusion variable equals the conserved quantity (Ginzburg (2006)) and therefore is recommended for homogeneous embankments.

These formulations of the Richards equation are made dimensionless for the computation using the cell size Δx as length scale and the time step size Δt as the temporal scale.

4.3 Empirical constitutive models

Empirical closures for the water retention curve $h_w = f(\theta)$ and the relative hydraulic conductivity curve $k_r = f(\theta)$ are required to solve the Richards equation. As mentioned above in section 4.1, the water retention curve $h_w = f(\theta)$ describes how much water is retained in the soil by matric suction during water drainage. The relative hydraulic conductivity curve $k_r = f(\theta)$ describes the water mobility depending on the water saturations.

Two different constitutive models are often employed to describe these relationships and are implemented in this work. These constitutive models thereby rely upon empirical soil parameters.

One approach is the model after Brooks and Corey (1964) and Mualem (1976) (BCM). The following relations are used for the BCM model with the empirical soil parameter λ as

$$\begin{aligned} h_w(\theta) &= h_s \theta^{-1/\lambda}, \\ k_r(\theta) &= (h_w/h_s)^{-(4\lambda+2)}, \\ \frac{\partial h_w}{\partial \theta} &= -\frac{h_s}{\lambda} \theta^{-\frac{1}{\lambda}-1}. \end{aligned} \quad (4.7)$$

The derivative of the pore-water pressure head with respect to the water saturation $\partial h_w/\partial \theta$ is additionally given, because it is needed in the numerical approach as described below.

Another approach is the model after van Genuchten (1980) and Mualem (1976) (VGM). It is used here in a modified version after Vogel *et al.* (2001). For this VGM model the relations and derivative are

$$\begin{aligned} h_w(\theta) &= \frac{-1}{\alpha} \left[-\varkappa\left(\frac{\beta}{\theta}\right) \right]^{1/n}, \\ k_r(\theta) &= \sqrt{\theta} \left(\frac{1 - \varkappa^m(\theta/\beta)}{1 - \varkappa^m(1/\beta)} \right)^2, \\ \frac{\partial h_w}{\partial \theta} &= \frac{1 - m}{\beta m \alpha} \frac{\theta^{-1/m-1}}{\beta} - \varkappa\left(\frac{\beta}{\theta}\right)^{-m}, \end{aligned} \quad (4.8)$$

with $m = 1 - 1/n_V$, $\varkappa(x) = 1 - x^{1/m}$ and $\beta = (1 + (-\alpha h_s)^{n_V})^m$. The soil characteristics are described by the empirical soil parameters α and n_V .

The soil parameters for these relationships are usually derived either by in-situ or laboratory measurements. Alternatively, tabulated values are given in literature for different soil compositions as for example in Vogel *et al.* (2001).

Another required soil parameter is the air-entry pressure head h_s . It specifies the matric suction at which air begins to enter the largest granular pores during soil drainage and, hence, characterizes the transition from the saturated to the partially-saturated zone.

Following Ginzburg *et al.* (2004), the primary variable θ can be used for the partially-saturated zone as well as for the saturated zone. Therefore the water retention curve $h_w = f(\theta)$, which is defined for the partially-saturated zone only, has to be extrapolated linearly into the saturated zone. This can be written as

$$h_w(\theta) = (\theta - 1) \underbrace{\frac{\partial h_w}{\partial \theta} \Big|_{\theta=0}}_P + h_s, \quad \theta \geq 1.0 \quad (4.9)$$

with P as the gradient of the water retention curve at the transition to the saturated zone ($\theta = 1.0$)³. This extrapolation has the advantage that no special treatment and no change in the variables must be considered regarding the transition from partially-saturated to saturated zones or vice versa. It leads to an artificial compressibility error in unsteady simulations, however. This error is neglected in this work for simplicity, but in principle can be reduced by implementing sub-iterations as outlined by Ginzburg *et al.* (2004).

³The *modified* Version of the VGM model is used instead of the original VGM model in order to prevent an infinite gradient P at the transition between the partially-saturated and saturated zone. In case of $h_s = 0.0$, the modified version reduces to the original VGM model.

4.4 Numerical modelling - Lattice-Boltzmann method

4.4.1 Introduction

The numerical solution of the Richards equation is challenging due to strong non-linearities introduced by the constitutive models. Furthermore, at the interfaces between different soils in heterogeneous embankments, steep jumps and abrupt changes in the variables may occur. Despite these difficulties, models were presented in the past solving the Richards equation based on Finite-Difference (FD) or Finite-Element (FE) methods with success. Commercial programs and free source codes for the 3D Richards equation are available using FE and FD methods (Voss and Provost (2010) or Niswonger *et al.* (2006)). However, such codes are limited flexible regarding the coupling with surface flow models and the adaptation to time dependent changes in the mesh geometry and boundary conditions during embankment breaching. Therefore it was decided to implement a new sub-surface model and integrate it into the breach model to obtain full flexibility.

A novel application of the Lattice-Boltzmann method (LBM) to the Richards equation was recently presented by Ginzburg *et al.* (2004) and Ginzburg (2006)⁴. Ginzburg adapted solution strategies for anisotropic advection-dispersion problems to different formulations of the Richards equation, including the θ and mixed $\theta-h_w$ formulations.

The application of the LBM has some favourable characteristics making it an alternative choice compared to classical continuum approaches. The method is simple to implement in 3D and allows for the modelling of complex geometries using bounce-back boundaries. In addition, the method is local and therefore suited well for parallel execution. The LBM

⁴Many Lattice-Boltzmann models were developed and applied for two-phase sub-surface flow at pore-scale in the past. The numerical method is suited well for this task, due to its simple treatment of the complex granular matrix with bounce-back conditions. These approaches differ from the presented macroscopic approach, however.

and its computational framework generally can be applied for the solution of various types of macroscopic governing equations. Important application fields are e.g. the solution of the Navier-Stokes or Shallow-Water equations. Several approaches solving the ADE were also proposed in the past (Flekkoy (1993), van der Sman and Ernst (1999) or Ginzburg (2005)). The choice of the LBM therefore also reflects the opportunity to possibly extend the method in future to other processes, like the 3D overtopping flow or the movement of the collapsed masses after side wall failures, using an unified modelling framework on a common mesh.

Out of these reasons, this recently presented LBM approach was chosen and implemented for the breach model. Furthermore, as a side-effect, it is noted that to the author's knowledge there are no published applications of this method, beside the idealized validation tests of Ginzburg and simple 1D tests of Liu (2012). Hence, there is need to further investigate this novel approach with regard to scenarios of practical relevance. Its applicability to variably-saturated flow is investigated in this work with a focus on flow through earth embankments.

4.4.2 Boltzmann equation and BGK approach

The underlying theory of the LBM bases on the Boltzmann equation from kinetic theory which was derived by the Austrian physicist and philosopher Ludwig E. Boltzmann. The Boltzmann equation is a mesoscopic governing equation which is positioned in between microscopic particle-based dynamics and macroscopic continuum approaches, as they are used for the classical computational fluid dynamics, as shown in Figure 4.2.

The Boltzmann equation is formulated for a particle distribution function $f(\vec{r}, t)$ of particles in the 6D phase-space as indicated in Figure 4.3. This phase-space is formed by the three spatial coordinates and the three velocity components $\vec{r}(\vec{x}, \vec{v})$. The distribution function can be seen as a representation of particles at time t with locations and velocities in between \vec{r} and $\vec{r} + \Delta\vec{r}$. The integration of the distribution function f over the

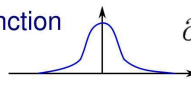
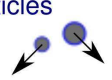
Level of description	Conceptual approach	Governing equations
macroscopic	continuum fields 	Navier-Stokes eq. $\partial_t u + (u \cdot \nabla)u = -\frac{1}{\rho} \nabla P + \nu \Delta u$
mesoscopic	particle distr. function 	Boltzmann eq. (BGK) $\partial_t f + (v \cdot \nabla)f = -\frac{1}{\tau}(f - f^{eq})$
microscopic	particles 	Particle mechanics $\frac{d^2 r_i}{dt^2} = -\sum_{j>i} \nabla V_{ij}$

Figure 4.2: Comparison of different levels of description and conceptual approaches applied to determine fluid motion.

phase-space hereby results in the macroscopic fluid density ρ . Since the LBM is used in this work to solve the macroscopic Richards equation, the function f may be interpreted as a directional saturation density, whereas the integration of f over the phase-space results in the macroscopic water saturation θ .

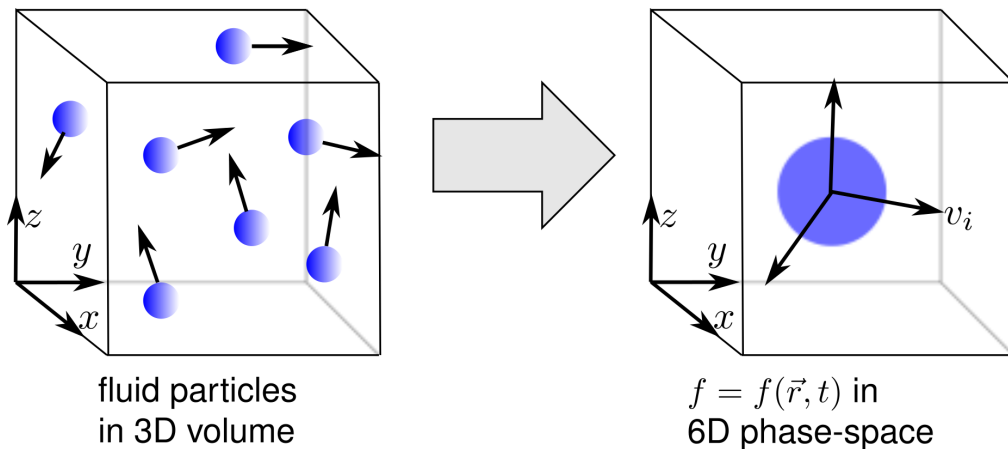


Figure 4.3: Definition sketch of the distribution function f of the Boltzmann equation.

The Boltzmann equation for the scalar distribution function f can be written in 1D as (Mohamad (2011))

$$\frac{\partial f(\vec{r}, t)}{\partial t} + v \frac{\partial f(\vec{r}, t)}{\partial x} = \Omega, \quad (4.10)$$

with Ω as the collision operator, which describes the mutual influences of distribution functions f on each other.

This partial-differential equation has the simple form of a single linear transport equation, even in higher dimensions. The main problem for solving the Boltzmann equation, however, is the treatment of its complex collision operator Ω . Simplifying approaches are needed and were introduced for its approximation. The single relaxation time BGK (Bhatnagar-Gross-Krook, 1954)-approach thereby is often applied and can be seen as a pre-requisite for the success of LBM models in the past. Using the BGK approach, the collision is considered as a simple relaxation of the distribution function f towards its equilibrium state, characterized by the local equilibrium distribution function f^{eq} . The collision operator then results to $\Omega = \omega(f - f^{eq})$ with the collision frequency ω .

In addition, more complex approximations of the collision operator were presented and a comprehensive overview over different methods and their derivations is given in Succi (2001).

4.4.3 Numerical solution approach - Lattice Boltzmann Method

The Boltzmann equation 4.10 is solved in a discrete formulation along discrete directions on a regular mesh, the 'lattice'. The resulting numerical approach is therefore called the Lattice-Boltzmann Method. It was historically derived from the particle-based Lattice-Gas Cellular-Automata (LGCA) as outlined in Succi (2001). The basic modification thereby is the replacement of the discrete particles in the LGCA with the distribution function f .

The uniform computational lattice is constructed with quadratic cells in 2D or cubic cells in 3D using a set of n_q discrete linkages \vec{c}_q , which connect the grid cells with each other. A necessary pre-requisite of the LBM is to provide sufficient symmetry of these linkages in the lattice (Succi (2001)). The applied computational cells with their linkages are depicted in Figure 4.4 for two and three dimensions. In 2D simulations, a mesh with

$n_q = 9$ different linkages is used (D2Q9) and in 3D simulations $n_q = 15$ different linkages are applied (D3Q15⁵).

The directions of the n_q discrete linkages are set in 2D as

$$\vec{c}_q = c_m \left\{ (0, 0), (1, 0), (0, 1), (-1, 0), (0, -1), (1, 1), (-1, 1), (-1, -1), (1, -1) \quad q = 0..8 \right.$$

and in 3D as

$$\vec{c}_q = c_m \begin{cases} (0, 0, 0), (1, 0, 0), (0, 1, 0), (-1, 0, 0), (0, -1, 0), (0, 0, 1), (0, 0, -1), & q = 0..6 \\ (1, 1, 1), (-1, 1, 1), (-1, -1, 1), (1, -1, 1), & q = 7..10 \\ (1, 1, -1), (-1, 1, -1), (-1, -1, -1), (1, -1, -1). & q = 11..14 \end{cases}$$

Since the Richards equation is used in dimensionless formulation here, the 'mesh speed' results to $c_m = 1$ in the numerical method.

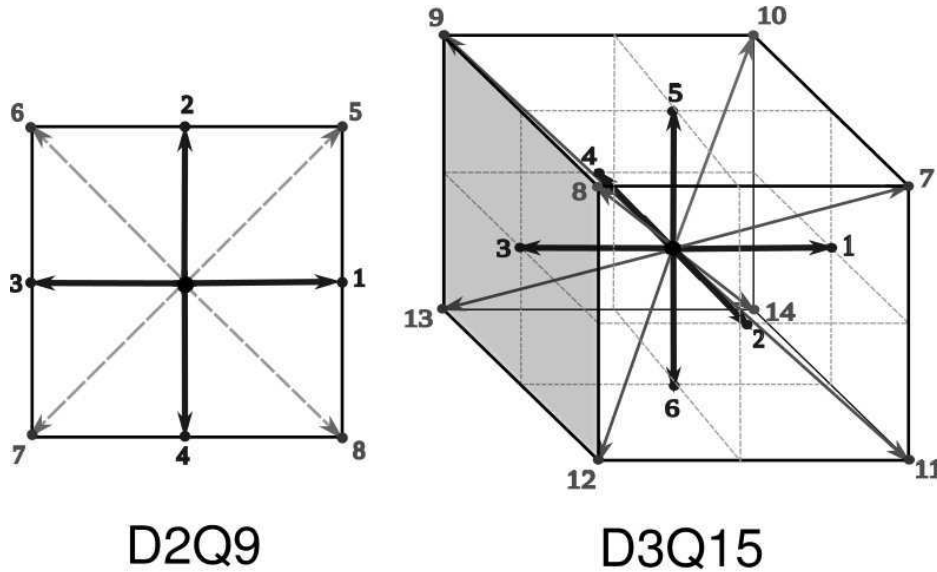


Figure 4.4: Left: 2D lattice cell with $n_q = 9$ linkages (D2Q9). Right: 3D lattice cell with $n_q = 15$ linkages (D3Q15).

The discrete form of the Boltzmann equation in combination with the

⁵It is common terminology to refer with Dn_D ($n_D = 1, 2, 3$) to the dimension of the problem and with Qn_q to the number n_q of linkages.

BGK approach for the collision operator is written for the n_q directions as

$$\underbrace{f_q(\vec{r} + \Delta t \vec{c}_q, t + \Delta t)}_{\text{advection}} = \underbrace{f_q(\vec{r}, t) + \omega [f_q(\vec{r}, t) - f_q^{eq}(\vec{r}, t)]}_{\text{collision}} + q_{q,inf}/c_m. \quad q = 1..n_q \quad (4.11)$$

The parameter ω is determined as a function of the macroscopic diffusivity D as (Mohamad (2011))

$$\omega = \frac{-1.0}{D/c_s^2 + 0.5}. \quad (4.12)$$

As a consequence, a large diffusivity leads to prolonged times until the equilibrium state is approached, whereas for a small diffusivity the equilibrium is approached more rapidly. The macroscopic diffusivity D is determined as a function of the soil conductivity and differs for the θ and the θ - h_w formulation as

$$D = \begin{cases} K(\theta)P(\theta) & \theta \text{ formulation} \\ K(\theta) & \theta\text{-}h_w \text{ formulation.} \end{cases}$$

The parameter c_s^2 is determined as c_m/ϑ with the free adjustable constant ϑ . The term $q_{q,inf}$ on the right hand side of equation 4.11 represents an external source for modelling water infiltration into the embankment, e.g. due to rainfall.

Mainly three explicit computational steps are applied to solve equation 4.11, whereas the first two steps are analogous to particle-based approaches:

1. Propagation of the distribution functions f_q from cell to cell along the lattice linkages \vec{c}_q . This propagation step is also often called 'advection' or 'streaming' step,
2. Collision operator for f_q within the cells, and
3. Update of the macroscopic variables θ and h_w from the computed values f_q at the new time level.

Propagation step

At the propagation step, the distribution functions f_q are just moved along the discrete lattice linkages \vec{c}_q from each cell to its adjacent cells. At the lattice boundaries special treatments are required which are described below.

Collision step

Using the BGK approach, the collision operator reduces to a relaxation towards the local equilibrium distribution. The equilibrium distribution function f^{eq} hereby is the key element of the collision step where the main physics of the problem is included. As indicated above, the solution strategy in the LBM stays largely the same even for different physical problems, like e.g. fluid motion governed by the Navier-Stokes equation, Shallow-Water equations or ADE. The model framework can be adapted to different physical problems mainly by replacing f^{eq} .

For simulations of the Navier-Stokes equations with the LBM, the equilibrium distribution function bases on the famous Maxwell-Boltzmann distribution from statistical mechanics. For an advection-diffusion type problem, which is considered here, the equilibrium distribution can be derived from the Boltzmann equation using a Chapman-Enskog expansion and applying conservation principles. For details about the mathematical derivation see for example Mohamad (2011). In this work, only the first order accuracy of the equilibrium function is taken into account, adapted to the Richards equation, which was provided in a general formulation by Ginzburg *et al.* (2004).

The equilibrium distribution function f_q^{eq} is determined in dependence of the macroscopic variables as $f_q^{eq} = f(\theta, h_w)$. The determination of f_q^{eq} is outlined in 2D and 3D in Appendix C for the θ and θ - h_w formulations.

The numerical method is local because the equilibrium function needs no information from adjacent cells. This is an advantageous property especially regarding the parallelization of the code and increases its parallel

efficiency⁶.

Update of macroscopic values

The macroscopic variables of interest, θ , h_w and the Darcy velocity \vec{v}_f , can eventually be derived from the computed distribution functions f_q at the new time level.

The saturation θ is simply obtained by summing up the distribution functions of all directions n_q of a cell. Afterwards, the pore-water pressure head h_w can be derived using the water retention curve. According to Ginzburg *et al.* (2004) one obtains

$$\theta = \sum_{q=0}^{n_q} f_q \quad , \quad h_w = f(\theta)$$

$$\vec{v}_f = (\theta_s - \theta_r) \cdot \left[\sum_{q=0}^{n_q} \vec{c}_q f_q^{eq} + \begin{pmatrix} c_{x0} & \cdots & c_{xn} \\ c_{y0} & \cdots & c_{yn} \end{pmatrix} \cdot \begin{pmatrix} f_0^{eq} - f_0 \\ \vdots \\ f_n^{eq} - f_n \end{pmatrix} \right] \quad (4.13)$$

The derived macroscopic variables then are used for the computation of the updated equilibrium distribution functions $f_q^{eq} = f(\theta, p_w)$ at the new time level. With these values at hand, in combination with the boundary conditions, the next time iteration step can be started.

Treatment of boundary and initial conditions

At the lattice boundaries the values of the distribution function f_q in the incoming directions at the new time level are unknown and must be supplied. The following three types of boundary conditions were implemented for embankment breach scenarios:

- Standard bounce-back boundaries are used for solid walls, as e.g. at the fixed ground. The unknown, incoming distribution functions f_q

⁶In this work an OpenMP parallelization was implemented for shared-memory architectures demonstrating an excellent speed-up.

are set equal to the outgoing, anti-symmetric values \overline{f}_q to simulate wall reflection as

$$f_q(\vec{r}) = \overline{f}_q(\vec{r}). \quad (4.14)$$

This type of boundary condition allows for even complex boundaries to be easily implemented,

- Water infiltration caused by a water depth h above the soil is modelled using a Dirichlet pressure boundary. A hydrostatic pressure distribution and equilibrium conditions are thereby assumed at the boundary. The corresponding equilibrium distribution functions f_q^{eq} for the incoming directions are then evaluated as (see also Appendix C)

$$f_q(\vec{r}) = \begin{cases} -\overline{f}_q(\vec{r}) + 2.0t_q c_s^2 \theta & \theta \text{ formulation} \\ -\overline{f}_q(\vec{r}) + 2.0t_q c_s^2 h_w & \theta-h_w \text{ formulation.} \end{cases} \quad (4.15)$$

For the mixed $\theta-h_w$ formulation, the water depth can be directly used as pore-water pressure head. For the θ formulation the water saturation θ is needed instead. It can be derived from the water depth by applying the inverse water retention curve $\theta = f(h_w)$, and

- The seepage flow out of the embankment is modelled with a combined approach. In the saturated zone ($\theta \geq 1.0$) a Dirichlet boundary with constant saturation of 1.0 is set at the boundary cells, leading to an outflow. In the partially-saturated zone ($\theta < 1.0$) a bounce-back boundary is set.

The exact treatment of sloped or curved boundaries can become difficult, especially in three dimensions. Here, for simplicity, the sloped embankment faces are approximated using a series of steps with reflection angles of 0° , 45° or 90° . These simplifications may reduce the numerical accuracy in the vicinity of the embankment faces. More accurate boundary treatment schemes could be implemented alternatively if higher accuracies are needed (Ginzburg and d'Humières (1996),

Mei *et al.* (1999)).

As initial conditions, either the initial pore-water pressures or saturations in the embankment have to be specified. The initial distribution functions then are evaluated based on these macroscopic values assuming equilibrium conditions as

$$f_q = f_q^{eq}(h_w, \theta). \quad (4.16)$$

A more accurate representation of the initial conditions can be achieved by additionally considering the first order Chapman-Enskog expansion of the distributions function (Ginzburg *et al.* (2004)), but is not considered here.

4.5 Validation of sub-surface flow modelling

The model was first tested and validated against idealized test cases. In addition, it was applied to laboratory- and field-scale embankments as well as homogeneous and heterogeneous embankments as described in the following sections.

4.5.1 Saturated flow in confined domain

Homogeneous domain

As a first test, the steady-state sub-surface flow in a 3D cubic lattice of 1x1x1 m was chosen with a cell size of $\Delta x = 0.01$ m. The hydraulic conductivity of the soil was set to $k_f = 0.001$ m/s. At the west boundary a hydrostatic pressure head of $h_w = 5$ m was placed and at the east boundary $h_w = 2$ m. The other boundary cells of the computational domain were treated as bounce-back boundaries. This idealized test configuration results in a confined, saturated sub-surface flow with the analytical solutions for the pressure gradient and the Darcy velocity as

$$i = \partial h_w / \partial x = -3, \quad v_f = 0.002 \text{ m/s}. \quad (4.17)$$

The obtained model results are illustrated in the left part of Figure 4.5 and are the same for the θ and the mixed θ - h_w formulation. The simulated pressure gradient and the velocity field are constant and equal to the analytical solutions.

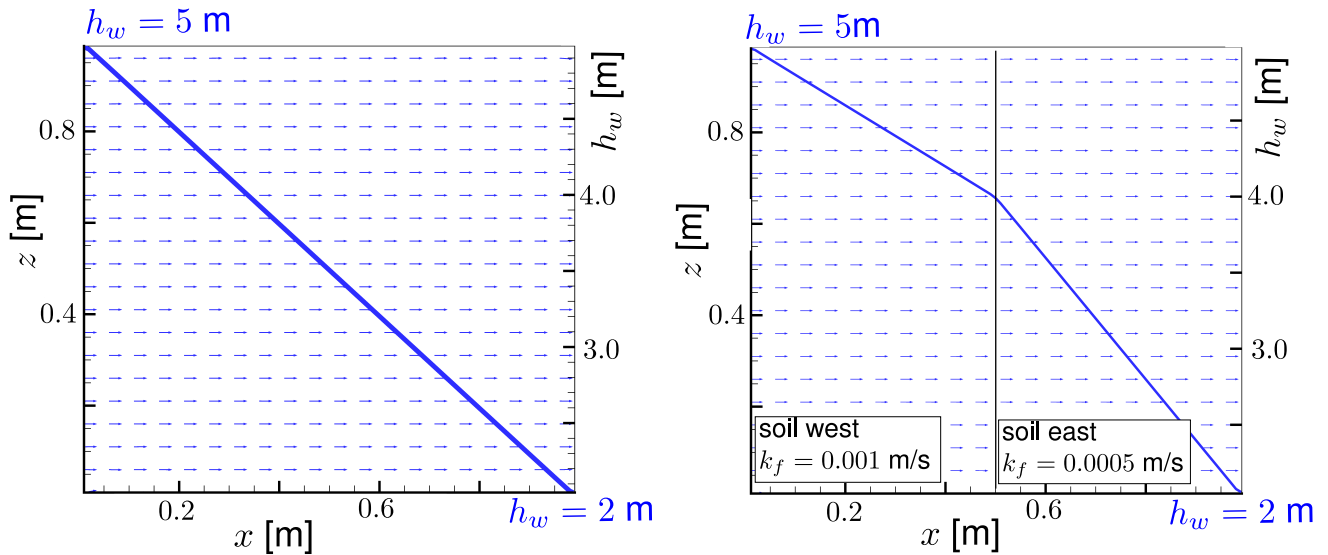


Figure 4.5: Cross-sectional view of pressure-head and velocity field of flow within confined domain. Left: homogeneous soil. Right: heterogeneous soil.

Heterogeneous domain

The right part of Figure 4.5 presents a modified scenario with two different soils within the computational domain. In the west part of the domain a hydraulic conductivity of $k_f = 0.001$ m/s was set, whereas in the east part $k_f = 0.0005$ m/s was applied. The analytical solutions for this test configuration are obtained as

$$i_{west} = \partial h_w / \partial x = -2, \quad i_{east} = \partial h_w / \partial x = -4, \quad v_f = 0.002 \text{ m/s.} \quad (4.18)$$

The obtained numerical results are shown in the right part of Figure 4.5 and are in agreement with the analytical solutions.

4.5.2 Water infiltration into partially-saturated soil

A second test was made to investigate unsteady flow within the partially-saturated zone. In this example the downward propagation of an infiltration front into a clay soil was considered. A 3D lattice was applied with 1x1x1 m extension. The cell and time step sizes were set to $\Delta x = 0.01$ m and $\Delta t = 1.0$ s. The same scenario was also investigated with the FE-model HYDRUS in the work of Vogel *et al.* (2001) and successfully used by Ginzburg *et al.* (2004) as validation test.

The VGM model was applied for the description of the clay soil properties. The soil parameters $\alpha = 0.8$ 1/m and $n_V = 1.09$ were taken from Vogel *et al.* (2001) as well as the hydraulic conductivity of $k_f = 5.55E - 7$ m/s. As initial condition, a negative hydrostatic pore-water pressure distribution (= suction) with a total head of $h_w + z = -10$ m was set. At the top of the domain a constant infiltration source was placed with $q_{inf} = 2.78E - 7$ m/s.

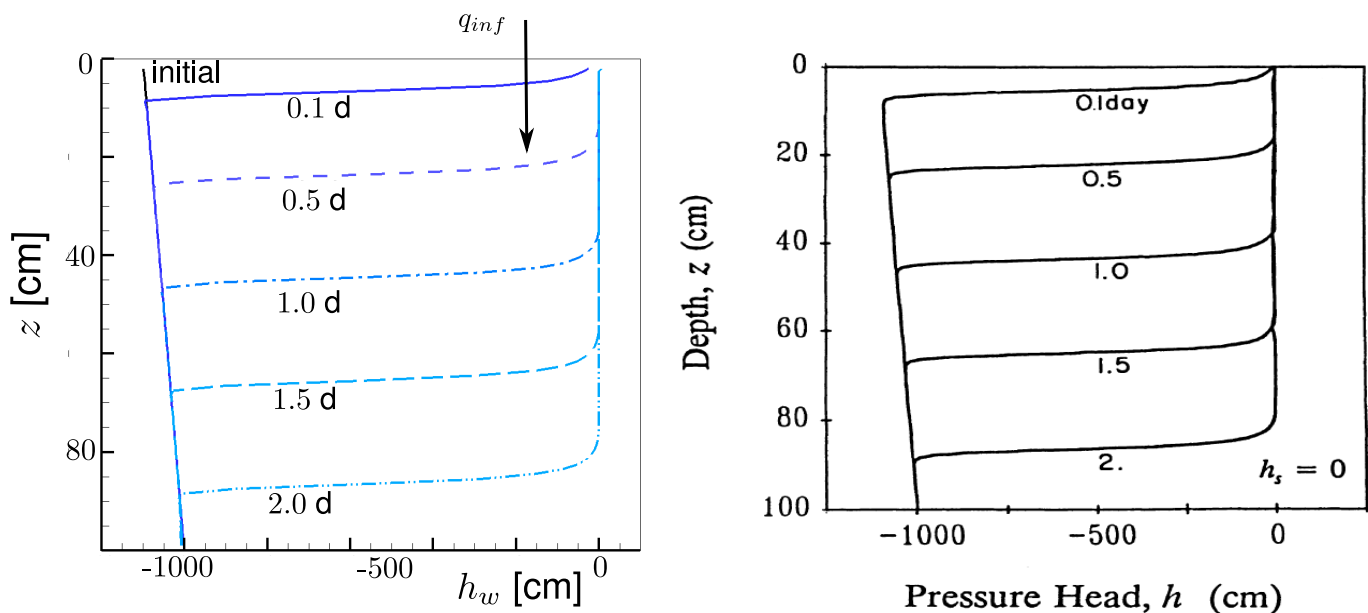


Figure 4.6: Vertical infiltration front propagation into a partially-saturated soil. Results of the LBM-model (left) and a FE-model (right, after Vogel *et al.* (2001)).

The temporal evolution of the infiltration front was simulated with the air-entry pressure head $h_s = -1E - 7$ m. The propagation of the infiltra-

tion front is depicted in Figure 4.6. It is compared with the results obtained with the FE-model by Vogel *et al.* (2001) indicating only negligible deviations. The test validates the model implementation for unsteady flow in the partially-saturated zone and also confirms the results previously obtained by Ginzburg *et al.* (2004).

4.5.3 Flow through laboratory-scale dyke

This test concerns 3D unsteady sub-surface flow through a laboratory dyke. A dyke was investigated of 0.6 m height, 4.0 m length, 0.4 m width and a hydraulic conductivity of $k_f = 9.5E - 4$ m/s⁷ (Pham-Van (2009) and Pham-Van *et al.* (2011)). The selected cell and time step sizes were $\Delta x = 0.01$ m and $\Delta t = 0.5$ s. At the upstream dyke slope a time-dependent pressure boundary was placed according to the raising water-level in the experiment. At the downstream dyke slope a seepage outflow boundary was set.

Table 4.1: *Water contents and soil parameters for sub-surface flow modelling.*

θ_R [-]	θ_S [-]	k_f [m/s]	n_V [-]	α [1/m]	h_s [m]
0.01	0.49	$9.5E - 4$	2.68	14.5	-0.035

The VGM model was applied, whereas the soil parameters and the saturations are listed in Table 4.1 and were selected for sand material as tabulated in Vogel *et al.* (2001). The measured propagation of the seepage front and the simulated saturation distributions are depicted in Figure 4.7 and are in accordance with each other. The VGM model hereby showed a more robust behaviour than the BCM model for parameter variations.

⁷The value given in the reference of $k_f = 0.95E - 4$ m/s is supposed to be a typo and is not plausible regarding the measurements.

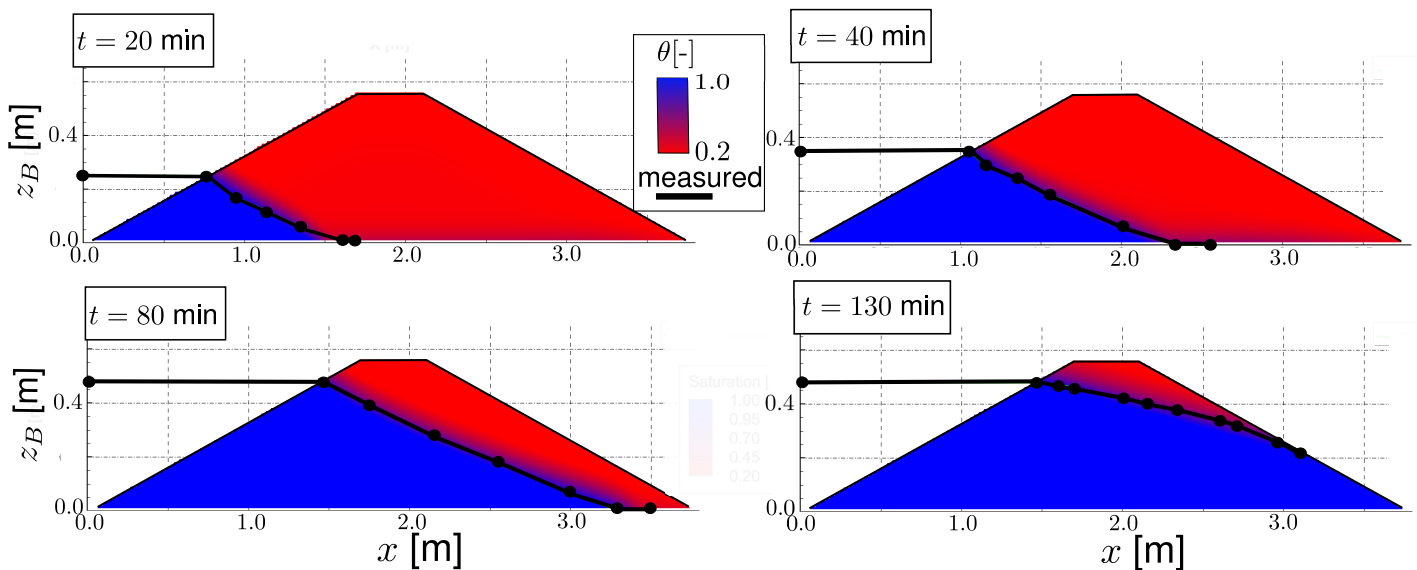


Figure 4.7: Comparison of simulated and measured propagation of seepage front in laboratory dyke at times $t = 20$ min, 40 min, 80 min, 130 min.

4.5.4 Flow through field-scale dam

To test the model on field-scale scenarios, two model configurations were selected from Bowles (1984). These scenarios concern steady-state conditions in homogeneous and heterogeneous dams and were recommended as tests for variably-saturated seepage modelling in the work of Chapuis *et al.* (2001).

Homogeneous dam

The first test (9-5a in Bowles) regards a homogeneous dam with the geometry and hydraulic conductivity given in Table 4.2. The cell and time step sizes were set to $\Delta x = 0.5$ m and $\Delta t = 5$ s. A constant pressure head was set at the upstream dam slope of $h_w = 18.5$ m and a seepage boundary condition was used to model the outflow at the toe of the downstream dam slope. The other boundary cells were modelled with bounce-back boundaries. The VGM model was applied ($\alpha = 5.14$ 1/m and $n_V = 1.69$), which showed again a more stable behaviour than the BCM model. An air-entry value of $h_s = -0.05$ m was used.

The resulting seepage line and velocity distribution within the dam

Table 4.2: Geometry and hydraulic conductivity of homogeneous field-scale dam.

length [m]	width [m]	height [m]	crest [m]	k_f [m/s]
100	40	20	$x = 50-60$	$6.67E - 6$

body are illustrated in Figure 4.8 and are in qualitative agreement with the results presented in Bowles (1984).

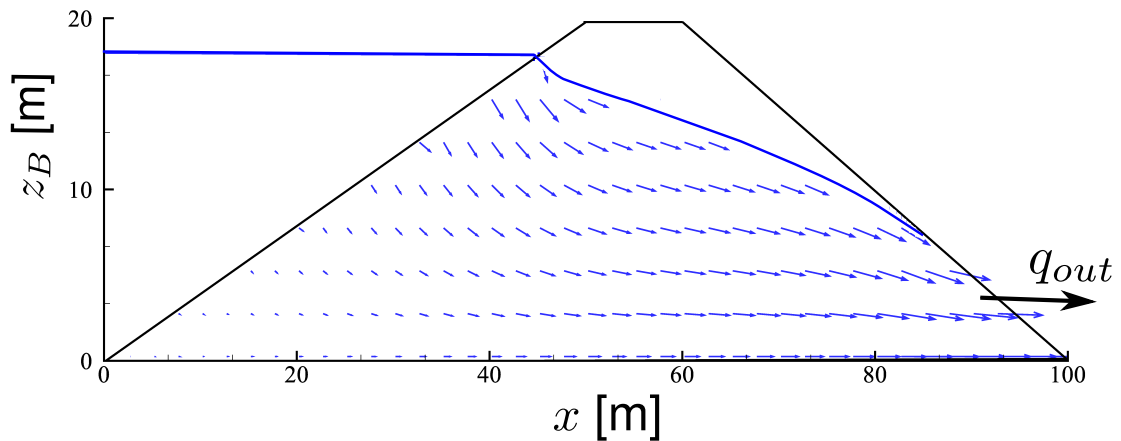


Figure 4.8: Steady state sub-surface flow through homogeneous, field-scale dam (9-5a in Bowles).

The total specific outflow rate per unit width at the downstream dam slope was estimated by Bowles (1984) to $q_{out} = 2.13E - 5$ m²/s, neglecting flow in the partially-saturated zone. Numerical simulations with FE-models led to values of $q_{out} = 2.35E - 5$ m²/s (Crespo (1993)) and $q_{out} = 2.28E - 5$ m²/s (Chapuis and Aubertin (2001)). Using the LBM, a specific discharge of $q_{out} = 2.34E - 5$ m²/s was obtained which compares well to the previous investigations. The water table reached the downstream dam slope at an elevation of about 7.5 m which lies in between the 6.5 m of Bowles (1984) and the 9.0 m of Chapuis and Aubertin (2001).

Heterogeneous dam

The second test (9-5b in Bowles) concerns a heterogeneous dam with the geometry given in Table 4.3. A highly permeable filter zone is installed at the downstream toe, which shall lower the seepage line and thus stabilize the dam slope.

Table 4.3: *Dam geometry of heterogeneous field-scale dam.*

length [m]	width [m]	height [m]	crest [m]
190	40	45	$x = 90-100$

The cell and time step sizes and the air-entry pressure head were set as before. Pressure boundaries representing a constant water level of $h_w = 40$ m were placed at the upstream dam slope. At the downstream slope seepage boundaries were applied to simulate water outflow, whereas all other boundary cells were treated as bounce-back boundaries. The VGM model was used again with the soil parameters given in Table 4.4.

Table 4.4: *Soil properties applied for the dam material and the filter zone.*

material	α [1/m]	n_V [-]	k_f [m/s]
dam material	2.0	1.41	$2E - 7$
filter material	14.5	2.68	$1E - 4$

The simulated seepage line was lowered towards the filter zone as illustrated in Figure 4.9 and qualitatively fits the result obtained by Bowles (1984). The pressure continuity at the interface between the different soil materials was also reproduced with the mixed $\theta-h_w$ formulation. The modelled specific outflow rate per unit width was $q_{out} = 3.4E - 6$ m²/s, which is in a reasonable range compared to the flow rates of $q_{out} = 3.8E - 6$ m²/s determined by Bowles (1984) as well as $q_{out} = 5.1E - 6$ m²/s

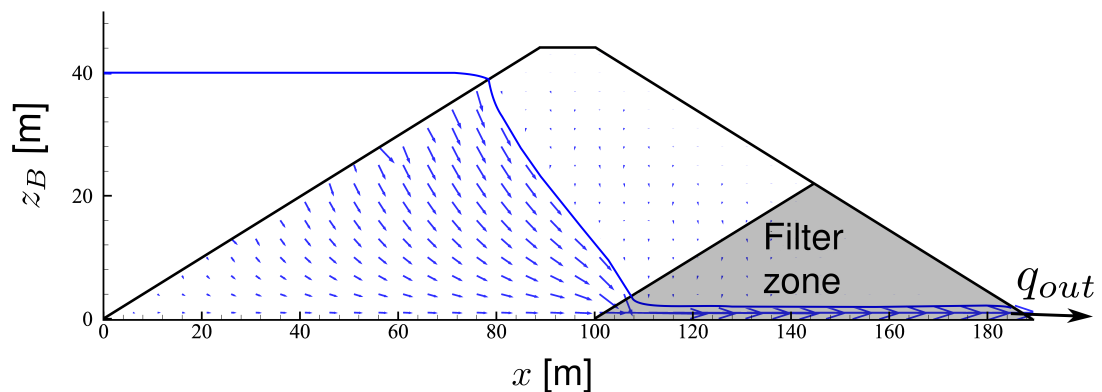


Figure 4.9: *Steady state sub-surface flow through heterogeneous, field-scale dam with permeable toe filter zone (9-5b in Bowles).*

(Crespo (1993)) and $q_{out} = 4.23E - 6$ m²/s (Chapuis *et al.* (2001)⁸) computed with FE-models.

4.6 Summary

In this chapter a numerical solution approach for the 2D and 3D Richards equation was presented and validated. The Richards equation is seen as good compromise between accuracy and efficiency regarding the variably-saturated flow modelling within earth embankments. The underlying assumption of a continuous air-phase at atmospheric pressure is valid in most cases.

The numerical approach bases on a recent adaptation of the Lattice-Boltzmann method to the Richards equation. Ginzburg's derivations and approaches using the θ and mixed $\theta-h_w$ formulations were hereby applied in combination with two constitutive models of VGM and BCM type. The Lattice-Boltzmann method has advantageous properties especially regarding its simplicity, the flexible bounce-back boundaries and its parallel efficiency. However, it relies on structured meshes which are less flexible regarding adaptations to local geometries and complicate the model coupling with the 2D unstructured surface mesh.

⁸The unit given in the reference of m²/min should read m²/s.

The model was successfully validated against multiple test cases confirming the approach and the made assumptions. Beside idealized tests for steady and unsteady flow involving simple geometries, model applications to practically relevant scenarios of laboratory- and field-scale embankments led to satisfying results and were stable over a wide parameter range. These successful applications indicate the suitability of the method for realistic engineering scenarios. Future work and additional tests should be made, however, to further investigate possible strengths and limitations of this method. The θ formulation has better stability properties and should be used for homogeneous embankments. The pressure continuity between different soils, in contrast, can only be correctly reproduced with the mixed $\theta-h_w$ formulation, which therefore should be used for heterogeneous embankments. In addition, the VGM model showed a more stable behaviour than the BCM model and is recommended.

Enhancements of the model could comprise a consideration of higher order accuracies for the equilibrium distributions, sub-iterations to reduce the compressibility error, anisotropic flow conditions and more accurate representations of sloped or curved boundaries. To further improve the stability for heterogeneous embankments, the development of a variable switching procedure could be an option, whereas the mixed $\theta-h_w$ formulation is applied only in areas with changing soil properties and the θ formulation otherwise.

5

Modelling of Side Wall Failures

5.1 Overview over physical processes

5.1.1 Introduction

Surface erosion induced by the overtopping flow leads to the formation of a breach channel, which deepens with time and steepens the breach side walls. These side walls eventually collapse into the breach channel due to the destabilizing forces and widen the breach channel in lateral direction transverse to the flow. These gravitationally-induced failures take place discontinuously from time to time when the breach side walls get too steep or the infiltrating water lowers the soil shear strength and increases the water load. The collapsed masses thereby constitute an essential portion of the total moved masses, especially during the later breach stages as noted by Franca and Almeida (2002) and Pickert *et al.* (2011). Franca and Almeida (2002) even mention a ratio of 80 % for the moved masses from lateral erosion to those from surface erosion for rock-fill dams. Consequently, the lateral erosion is of major importance for the breach advance and must be taken into account.

A large variety of different side wall failure types were reported in literature. Their occurrence depends upon the embankment geometry and the material properties. For homogeneous and non-cohesive embankments, the most common failure types are of planar, wedge and rotational type as stated by Kliche (1999) and illustrated in Figure 5.1. At planar or wedge failures, the masses move out and slide down along a planar or gently undulating surface. In addition, in presence of cohesive materials, toppling failures due to undercutting are reported. The flow erosion

hereby removes the underlying supporting material below the breach side wall, leading to a toppling of the overlying material into the breach channel. This work focuses on the lateral erosion due to planar or wedge shaped failures.

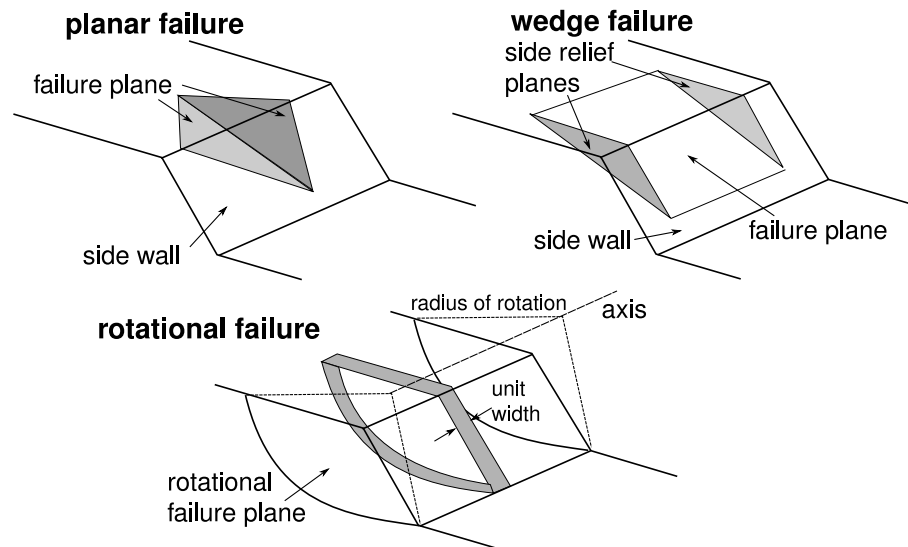


Figure 5.1: *Common failure types at non-cohesive homogeneous embankment side walls: planar, wedge and rotational failures (modified after Kliche (1999)).*

In addition to the lateral breach widening, the upstream or downstream embankment faces may also collapse during the breach event. Such failures are often singular events which can lead to instantaneous mass displacements of much larger extends compared to the local and frequent side wall failures at the breach channel. In this work, as in most other breach models, such embankment slope failures are not specially treated, although they can have crucial impacts if they occur.

In the following sections, first a brief introduction is given into geotechnical aspects of side wall failures and mass movements. Afterwards, an overview of modelling techniques is presented and the applied numerical modelling is outlined and validated using idealized test cases in section 5.2. A summary is given in section 5.3.

5.1.2 Soil shear strength and slope stability

Side wall failures have to be expected if the resistant shear forces are smaller than the acting shear forces along the failure plane. Stability analysis therefore involves the determination of the soil shear strength τ_s along the failure plane. This shear strength depends on the material weight and additional loads above the failure plane which are represented by the total stress σ_n . Furthermore, pore-water pressures and saturations affect the shear strength and should be addressed (Evans *et al.* (2011)). Beside these factors, other influences may play an important role, like the particle cohesion and soil weathering. Inner erosion due to piping and living organisms can also impact slope stability (Pickert *et al.* (2004)) but is neglected here for simplification.

The concept of 'effective stresses' was introduced by Terzaghi (1936) and forms the base for the study of saturated soil mechanics. The conceptual model behind the effective stress is the distinction between the acting total stress σ_n and the pore-water pressure p_w between the particles surrounded by water. Subtracting the pore-water pressure from the total stress leads to a useful measure of the contact forces between the particles (Verruijt (2006)). This excess value of $\sigma_n - p_w$, the effective stress, is the main parameter for saturated soil mechanics and a measurement of the soil shear resistance. The slope will collapse along a failure plane when the acting shear stress exceeds the resistant shear strength τ_s given by

$$\tau_s = c_{coh} + (\sigma_n - p_w) \tan \gamma_{rep}. \quad (5.1)$$

The cohesion c_{coh} describes cohesive effects between the particles and is dropped from here on, since only non-cohesive materials are focused. This relationship implies that an increase in pore-water pressure leads to a reduction of the effective stress and can reduce the slope stability.

This often used concept is valid for saturated soils only and cannot be applied to the partially-saturated zone. For such purposes, the concept of effective stress was extended to partially-saturated conditions. A con-

stitutive relationship was presented by Fredlund *et al.* (1978) introducing two different friction angles. The additional internal friction angle γ^b is related to the matric suction $p_a - p_w$. The shear strength τ_s then is formulated as

$$\tau_s = (\sigma_n - p_a) \tan \gamma_{rep} + \underbrace{(p_a - p_w) \tan \gamma^b}_{\text{apparent cohesion}}. \quad (5.2)$$

The outermost right-hand term considers the stabilizing influence of apparent cohesion in partially-saturated soils. According to Fredlund *et al.* (1978), this stabilizing effect is described by the angle γ^b . It is often said to be smaller or equal to the angle of repose (Fredlund and Rahardjo (1993)) and has to be determined in laboratory studies. It is not constant, however, and reduces to smaller values for increasing matric suction and therefore was criticized for its interpretation as friction angle by Oberg and Salfors (1997) or Lu (2008).

To remove the dependence on γ^b , Vanapalli *et al.* (1996) and Oberg and Salfors (1997) proposed similar modifications. They argued that the extent to which the matric suction contributes to the shear strength is related to the water saturation. If the water saturation and the associated contractile skins between the particles increase, then the matric suction is more effective in tying particles to each other. Their approach can be interpreted as an approximation of $\tan \gamma^b \approx \theta \tan \gamma_{rep}$, thereby assuming proportionality to the water saturation. Although measurements rather indicate a non-linear relationship, this approximation is said to be adequate with an error of less than 20% for most soils (Oberg and Salfors (1997)). It leads to the shear strength

$$\tau_s = (\sigma_n - p_a) \tan \gamma_{rep} + \underbrace{(p_a - p_w) \theta \tan \gamma_{rep}}_{\text{apparent cohesion, } \tau_{coh}}. \quad (5.3)$$

This relationship offers the possibility to evaluate the soil shear strength and the apparent cohesion τ_{coh} without further need for laboratory studies, if the water saturation, the water retention curve and the angle of repose are known.

Using this equation, the soil shear strength shows a smooth transition

to equation 5.1 at saturated conditions ($\theta = 1.0$, $p_a = p_w$), where the apparent cohesion τ_{coh} vanishes. Similar, τ_{coh} also vanishes at residual dry conditions ($\theta = 0.0$). In between, at partially-saturated conditions, a maximum value of the soil shear strength occurs enabling steep breach side walls.

5.1.3 Movement of collapsed masses

The consideration in the previous section analyses under which conditions a side wall failure has to be expected. It does not investigate the subsequent movement of the collapsed masses, however. If the soil shear strength is exceeded, then the masses start to slide, flow or roll along the failure plane and come to rest again in the shallow regions of the breach channel or are partially washed away by the stream flow. This movement of the collapsed masses determines the redistribution of the material after failure and, hence, influences the breach formation.

The actual physical processes of the mass movements are highly complex. The occurring flow characteristics vary from slow laminar to rapid turbulent flows, and from mud- or debris-flows to particle avalanches, demonstrating the complexity of the involved processes (Evans *et al.* (2011)). In case of mud- or debris-flows, solid particles can collide, rotate and vibrate during their movements thereby dissipating energy and influencing the fluid viscosity and the flow rheology. These processes are further complicated by the interactions with the strong overtopping flow. Regarding these difficulties, severe simplifications are necessary to be able to account for the mass movements in the breach model.

5.2 Modelling of mass failures and movements

5.2.1 Overview over modelling techniques

Modelling of side wall failures

In general, the numerical modelling of 3D slope failures is a challenging task and fundamental research topic. Multiple modelling approaches were developed in the past with different degrees of simplifications, accuracy and computational expense as briefly summarized below.

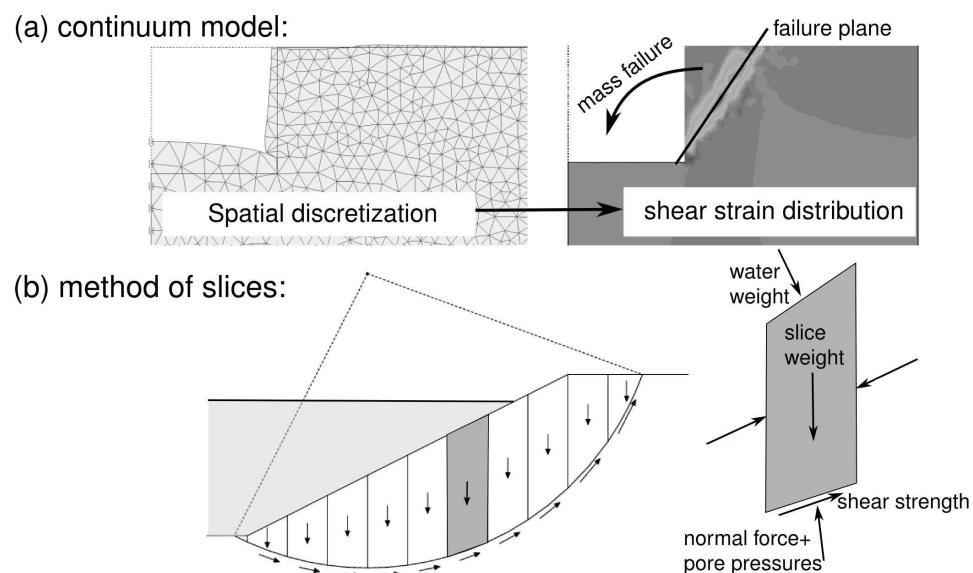


Figure 5.2: (a) 2D Continuum modelling of side wall failure in breach channel (modified after Morales (2010)). (b) 2D Limit-equilibrium method ('method of slices') for a rotational failure.

'Continuum models' are comprehensive analysis tools for slope failures, which are broadly applicable to composite embankment structures and to situations where a non-linear stress-strain behaviour must be considered (Evans *et al.* (2011)). These models are capable of incorporating influences of water saturations and are not limited to special failure types. Differential equilibrium stress-strain relations are formulated and solved numerically on 3D meshes representing the embankment body.

Finite-Element or Finite-Difference methods are usually applied for the solution of the resulting system of equations. A 2D model applied to a side wall failure in a breach channel is sketched in Figure 5.2 (a) after Morales (2010). Such continuum modelling is usually applied to earth embankments. In case of mostly zoned embankments consisting of large cobbles or boulders, in contrast, dis-continuum approaches or combined approaches may be more appropriate.

Continuum modelling in 3D typically requires large computational powers and leads to time step sizes which are significantly smaller than those of the overtopping and surface erosion modelling. Coupling breach models with such continuum models therefore may significantly slow down the combined simulation.

'Limit-equilibrium methods' investigate the equilibrium conditions of the soil material which is supposed to fail. The embankment is hereby divided into 2D slices or 3D columns. Then, the acting and resisting shear stresses and moments are balanced along a chosen failure plane as sketched in Figure 5.2 (b). Due to the soil discretization into vertical slices or columns, such approaches are often labelled as 'method of slices' in literature. A factor of safety is evaluated along the failure plane which is defined as the ratio of actual shear resistance to the required equilibrium value. If the factor of safety is smaller than one, the slope is considered as unstable and a failure has to be expected. These methods rely on a-priori estimations of failure planes along which the failure takes place. Iterative search algorithms are required to locate the failure plane with the smallest factor of safety.

These search algorithms lead to large computational costs in three dimensions and differ conceptually from the continuum approaches applied for the water flow and surface erosion modelling. Further difficulties for breach modelling are that most limit-equilibrium methods are limited to 2D analyses of vertical cross sections and cannot be easily adapted to unstructured meshes, raising the need for the development of special numerical techniques.

The term 'kinematic approaches' is used here to denote preliminary assessments of the slope stability relying upon basic geotechnical considerations. These are heuristic approaches based on strongly simplifying assumptions without detailed evaluations of stresses or momentum balances. Therefore these methods are only limited applicable, mainly to surface-near failures of small extends, and can hardly account for complex failure patterns. A variant is the 'geometrical approach', which bases upon the idea that a slope failure takes place if the slope becomes steeper than a critical failure angle. Using such an approach, one is limited to local mass failures for small regions as defined by the computational cell sizes. On the other side, such a geometrical approach is simple and necessitates no complex search algorithms for failure planes and therefore requires significantly less computational costs than limit-equilibrium or continuum modelling approaches.

In this work, a geometrical approach was chosen for side wall failure modelling. Experimental observations, like for example Pickert *et al.* (2011) or Spinewine (2005), indicate that the lateral breach widening is mainly due to surface-near and planar or wedge-shaped failures with regard to non-cohesive earth embankments. Therefore a geometrical approach based on critical failure angles may capture the main aspects of the breach widening at least approximately and thereby profit from its simplicity and the small computational expense. Such approaches were already applied in previous embankment breach models on structured meshes, like e.g. Faeh (2007) or Wu *et al.* (2012). The adaptation to unstructured meshes is not straightforward, however. Furthermore, the effects of apparent cohesion were neglected in previous approaches and shall be incorporated here to enhance the failure modelling.

Modelling of mass movements

An accurate physically-based modelling of the dynamical mass movements after slope failures is an open research task (e.g. Cundall (2001)) and is poorly understood up-to-now (Evans *et al.* (2011)). In the past decades, various approaches were presented for the modelling of the

mass movements resulting from slope failures or landslides. Continuum models were applied to simulate debris- or mud-flows with appropriate rheological flow models in Eulerian formulation (Takahashi (1981), Iverson (1997)) or in Lagrangian formulation (Chen and Lee (2004)). As alternative modelling concept, distinct-element methods were applied to the simulation of mass movements as interactions of solid particles. A brief overview is given in Cundall (2001). In addition, D'Ambrosio *et al.* (2003) proposed a model for mass movements based on the numerical method of Cellular-Automata.

Such approaches have in common that they are numerically challenging, computationally costly in three dimensions and require large amounts of input data often not available. As mentioned above, the situation is further complicated by the strong interactions of the moving masses with the overtopping flow through the breach channel.

Due to these complexities, several breach models in the past did not account for this mass movement at all. Instead, they simply removed the collapsed masses from the simulation as Tingsanchali and Chinnarasri (2001) or Wang and Bowles (2006). This mass removal bases on the assumption that these masses are totally washed away immediately by the overtopping flow. This assumption, however, is doubtful and contradicts experimental observations, especially regarding mass failures of larger extent and coarse-grained material.

Other modellers made the simplifying assumption of a continuous and smooth failure process with small and frequent mass displacements using simple geometrical considerations. This treatment as continuous process is advantageous regarding the numerical treatment and stability aspects as stated by Broich (1997). It may be adequate for residual dry or saturated conditions without apparent cohesion, sometimes encountered in laboratory studies or dams made of gravel or cobbles, where the side walls immediately adapt to the angle of repose with small and frequent mass movements. However, laboratory and field-scale investigations rather indicate the occurrence of steep side walls with more discontinuous mass collapses of larger extents and mass movements over larger distances into the breach channel (Pickert *et al.* (2011) or Lövoll

(2004)).

An advantageous property of the geometrical approach is seen in the possibility to capture the mass movement in a simplified manner by assuming a special deposition angle for these collapsed masses after failure. This deposition angle is chosen significantly smaller than the side wall angle. Then, after failure, mass movements take place in direction of the cell gradients from one cell to another, leading to a sliding of the collapsed masses into the shallow regions of the breach channel where they come to rest. Obstacles in the sliding path are hereby accounted for and the extent of the mass sliding can be controlled by adjusting the deposition angle.

As a consequence, the geometrical approach is used in this work for both tasks: the indication of the occurrence of side wall failures as well as for the estimation of the dynamical sliding and redistribution of the collapsed masses after failure.

5.2.2 Critical failure angles

Review of failure angles at embankment breaches

The geometrical approach essentially relies on reasonable assumptions about the forming side wall angles. The literature review on observed side wall angles in breach channels reveals partially contradicting statements. Niemayer (2007) summarized that data analysis of previous investigations lead to the conclusion that angles of $\sim 45^\circ$ are most frequently observed. In contrast, the breach channels during breach formation at non-cohesive embankments are described in other investigations as having very steep or nearly vertical side walls in the upper part (Coleman *et al.* (2002), Morris *et al.* (2008)). For cohesive material the study of Sametz (1981) mentions nearly vertical side walls and field-scale investigations of Morris *et al.* (2008) reported even overhanging side walls. These steep angles are possible due to the stabilizing effects of cohesion and apparent cohesion and may vary temporarily depending on the water saturations in the material (Pickert *et al.* (2004)).

These contradicting observations can be brought together as stated by Morris *et al.* (2008). The small side wall angles may form some time after breaching, when the material dries out and finally slides into the formed breach channel. These smaller angles therefore should not be mistaken as an adequate approximation of the actual failure angles during the breach event. Setting the critical failure angle to such small values in the range of the angle of repose, as it was done in many breach models before, therefore must be questioned regarding earth embankment breaches (Morris *et al.* (2008)).

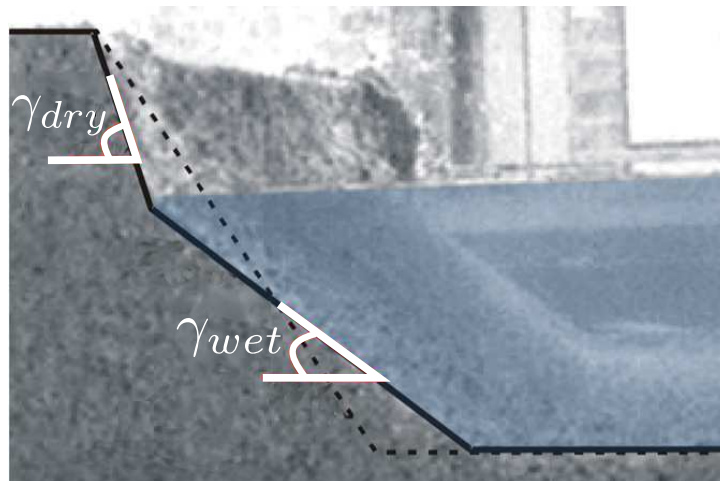


Figure 5.3: Critical failure angles above and below the water surface in an experimental flume (modified after Spinewine *et al.* (2007)).

Laboratory- and field-scale investigations also indicate that the assumption of a single failure angle within the breach channel is inadequate (e.g. Spinewine *et al.* (2007), Soares-Frazaio *et al.* (2007), Worni *et al.* (2012)). These observations show the formation of different failure angles in the lower and upper parts of the breach channel as illustrated in Figure 5.3. These breach geometries with steep slopes at the upper parts of the breach channel and shallow slopes in the lower parts are sometimes described as having trapezoidal or parabolic shape (Morris *et al.* (2008)). Furthermore, as mentioned above, the failure angles are no pure material property and are not constant over time, but are a function of the varying pore-water pressures and water saturations, respectively.

Determination of critical failure angles

Out of the before-mentioned reasons, three different critical failure angles are distinguished in the numerical approach.

1. The **dry failure angle** γ_{dry} for partially-saturated material at the breach side walls above the water surface. This angle can exceed γ_{rep} due to the stabilizing effect of apparent cohesion as a function of the saturations and pore-water pressures.

Based on the geotechnical considerations presented above, the angle is assumed here to be directly correlated with the soil shear strength. It is determined in a heuristic manner in dependence of τ_{coh} as given in equation 5.3. The function $\tau_{coh} = f(\theta, p_w)$ is hereby normalized by dividing it by its maximum value $\tau_{coh,max}$, leading to values in between 0.0-1.0. It is then multiplied with an angle γ_{coh} which describes the maximum additional steepness of the side walls due to apparent cohesion. The side wall angle γ_{dry} is eventually determined as

$$\gamma_{dry}(\theta, p_w) = \gamma_{rep} + \frac{\tau_{coh}(\theta, p_w)}{\tau_{coh,max}} \gamma_{coh} \quad (5.4)$$

The shape of the function of γ_{dry} depends on τ_{coh} which again is a function of the water retention curve and the saturations. Three characteristic curves of γ_{dry} are qualitatively sketched in Figure 5.4 (a) for three typical soil materials.

For fully-saturated conditions ($\theta = 1.0$) and residual dry conditions ($\theta = 0.0$) the failure angle reduces to the angle of repose. In between, at partially-saturated conditions, it increases up to the maximum value of $\gamma_{rep} + \gamma_{coh}$. The angle γ_{coh} must be supplied by the modeller and may be derived from laboratory or field observations of breach side wall geometries.

2. The **wetted failure angle** γ_{wet} for material below the water surface, which is assumed to be fully-saturated. It can be supposed to be in

the range of the angle of repose

$$\gamma_{wet} \approx \gamma_{rep}. \quad (5.5)$$

In general, one could question the need for this failure angle, since it is included as special case in γ_{dry} . Nevertheless it is introduced here, since the surface-near water infiltration into the breach side walls is difficult to be resolved and captured adequately by the sub-surface model. This is especially true at breach initiation under small water depths.

3. The **deposition failure angle** γ_{dep} for material resulting from mass failures. It approximates the complex movement of the collapsed masses into the breach channel after failure¹. Setting γ_{dep} to values significantly smaller than γ_{rep} allows for a more realistic modelling of the discontinuous mass sliding into the breach channel over larger distances. The angle is determined as a function of the water saturation as

$$\gamma_{dep}(\theta) = \gamma_{dep} - \theta\gamma_{dep}'. \quad (5.6)$$

The material is hereby assumed to develop more momentum for the mass sliding proportional to its water saturation. This leads to a reduced angle γ_{dep} for larger saturations as sketched in Figure 5.4 (b)². A-priori estimations of this failure angle are difficult, however, since accurate measurements of the mass sliding are usually not available.

These distinct failure angles allow for the representation of complex breach shapes and discontinuous mass failures and mass redistributions over larger distances. The approach therefore seems capable to represent the basic characteristics of observed side wall failures, if appropriate failure angles are supplied.

¹It is noted that γ_{dep} also has an additional stabilizing and smoothing effect in the transport modelling, helping to prevent occurrences of non-physical artefacts, like e.g. steep peaks of deposited material at the dry-wet interfaces.

²To reduce calibration efforts, the parameter γ_{dep}' is not varied in the simulations and assumed to have a value of 2° .

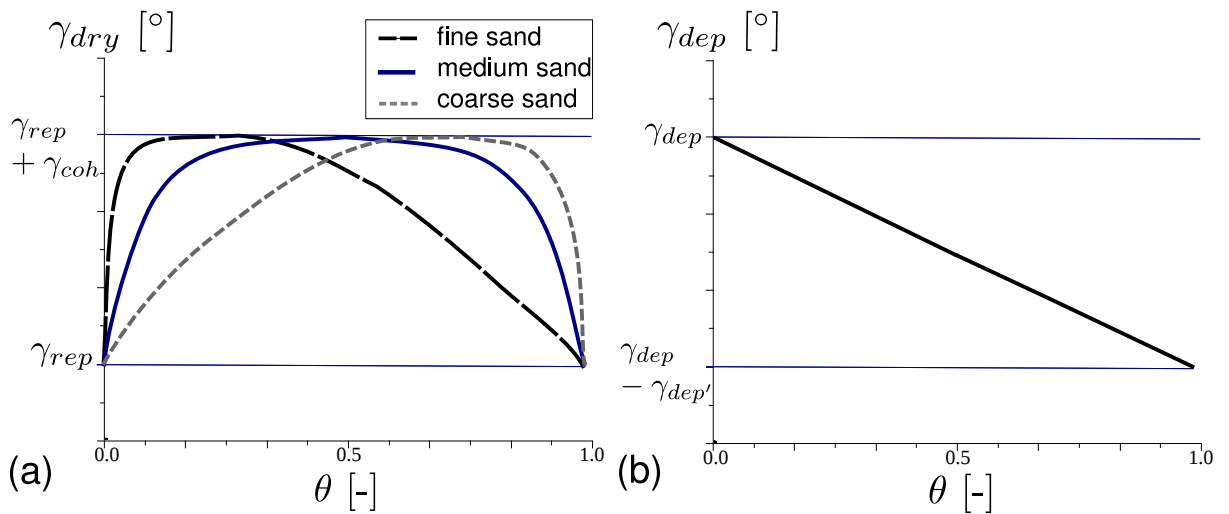


Figure 5.4: Critical failure angles (a) γ_{dry} and (b) γ_{dep} as functions of the water saturation θ .

5.2.3 Failure algorithm for unstructured meshes

The geometrical approach bases on the assumption that slope failures take place if the cell slope becomes steeper than a critical value. If the critical value is exceeded, then sediment masses slide from the upper part of the side wall in downward direction and finally deposit in the lower part until the critical angle has formed.

The approach is applied to the cells of the hydraulic mesh. This is advantageous because these have well-defined slopes determined by their vertex elevations³. Figure 5.5 sketches the rotation of the cell which is subject to the failure, and defines the main geometrical parameters of the algorithm.

A similar approach of a bank-failure operator applied to 2D unstructured meshes was recently presented by Swartenbroekx *et al.* (2010). However, due to the use of the dual-mesh approach, the computational algorithm differs significantly from their method and is therefore outlined in detail in Appendix D. The main computational steps of the algorithm

³A problem for quadrilateral cells is the ambiguous cell slope if the vertices do not lie on a plane. In such cases, the slope is determined by dividing the cell into four triangular cells by connecting the vertices with the cell midpoint and arithmetic averaging of the cell slopes of the obtained triangles.

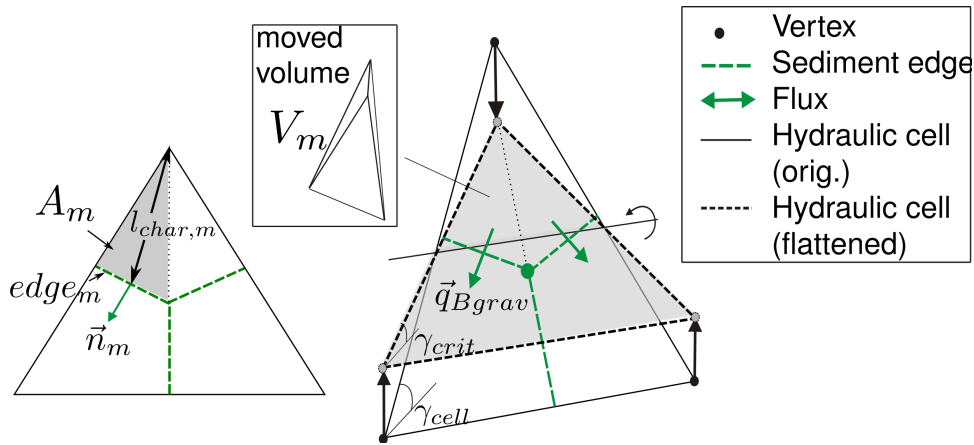


Figure 5.5: Configuration sketch and definition of parameters. Left: top view on hydraulic cell (solid) and parts of sediment cells (dashed). Right: Moved volume and cell rotation.

and modifications for fractional transport are presented. The algorithm is generally sensitive to the mesh resolution which is also briefly discussed in Appendix D.

5.2.4 Validation tests

Vertical bed step

The first test considers a nearly vertical bed step as initial configuration, representing a steep breach channel side wall. In the lower part of the bed step, a pool of standing water was placed to check the correct assignment of the critical failure angles above and below the water surface. The critical angles were set to $\gamma_{dry} = 40^\circ$ and $\gamma_{wet} = \gamma_{dep} = 15^\circ$, whereas γ_{dry} was assumed constant for simplification.

Figure 5.6 depicts the initial and the resulting final configurations. The latter indicates the flattening of the vertical bed step and the correct formation of the two different failure angles above and below the water level after the slope failure. The same configuration was obtained for single and multiple grain soil compositions. The total and specific mass errors, defined in equations 3.29 and 3.30, were determined as $E_{tot} < 10^{-10} \text{ m}^3$ and as $E_{spec} < 10^{-13} \text{ m}$, confirming the mass continuity of the dual-mesh

approach.

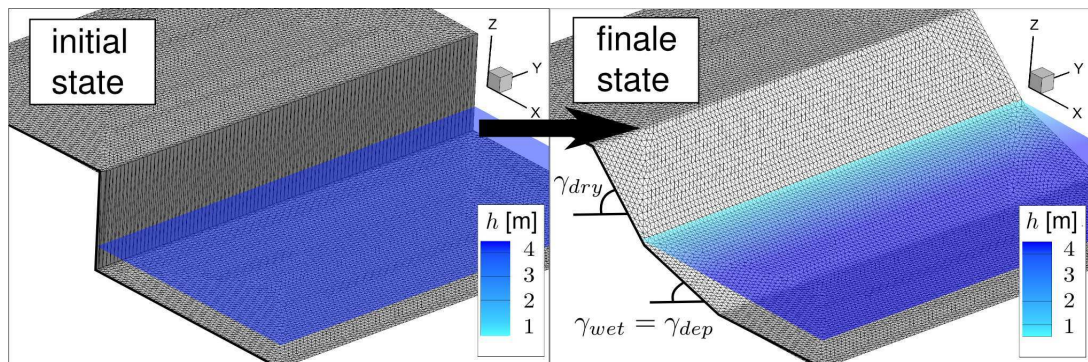


Figure 5.6: Failure of vertical bed step with standing water pool. Left: initial configuration with bed step. Right: final configuration after failure.

Complex terrain - sediment peak

An additional configuration was simulated to examine the spatial behaviour of the algorithm. A nearly vertical peak with quadratic base area was placed in the middle of a completely dry terrain as indicated in Figure 5.7. The failure angles were set to constant values of $\gamma_{dry} = \gamma_{dep} = 15^\circ$ over the entire computational domain. During the simulation the peak side walls were flattened and a symmetrical cone-shaped final configuration formed around the original peak center. The final slopes formed an angle of 15° as expected and identical results were obtained for simulations with single and multiple grain classes. Furthermore, the sediment mass continuity was again maintained with mass errors of $E_{tot} < 10^{-10} \text{ m}^3$ and $E_{spec} < 10^{-13} \text{ m}$.

Inclined bed step with apparent cohesion

This test case deals with the variable critical failure angle γ_{dry} within partially-saturated soils, which is a function of the water saturation and pore-water pressure. An inclined bed step was set as initial configuration with a constant slope of 32 %. The failure angles were chosen as $\gamma_{rep} = \gamma_{dep} = 10^\circ$ and the apparent cohesion was considered with

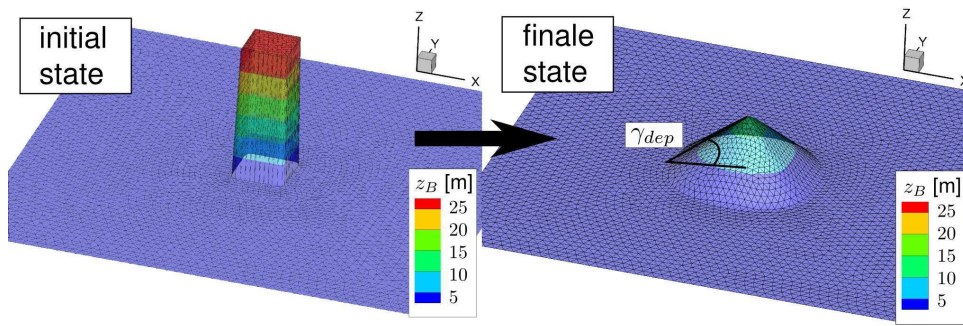


Figure 5.7: Failure of a vertical peak with quadratic base area in a dry terrain. Left: initial configuration with peak. Right: final configuration after failure.

$\gamma_{coh} = 40^\circ$. A linearly decreasing saturation θ was set from the bottom to the top. Further, τ_{coh} was assumed to increase linearly with decreasing θ for simplification. Figure 5.8 depicts the initial configuration and the resulting final configuration after the simulation. At the upper region, the model set-up led to a parabolic shape of the slope as expected, which is formed by the successively increasing failure angle γ_{dry} with increasing height due to apparent cohesion.

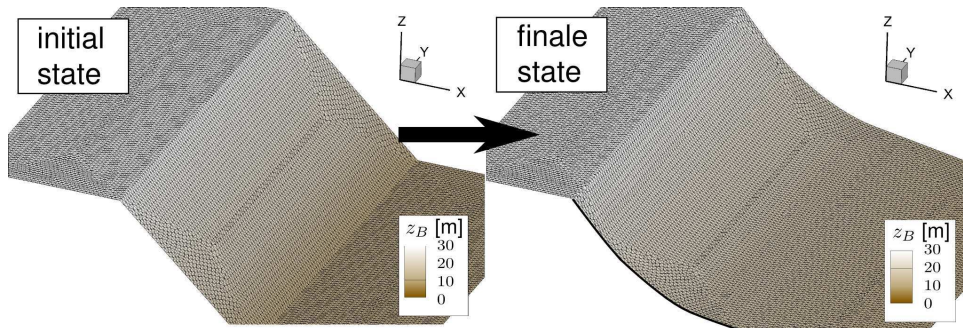


Figure 5.8: Failure of inclined bed step in a domain with linearly decreasing θ from bottom to top. Left: initial configuration with inclined bed step. Right: final configuration after failure.

5.3 Summary

A geometrical approach is applied for the modelling of side wall failures during the breach event. It bases on the simplifying assumption that slope failures occur if the breach side walls exceed a critical failure angle. The

approach is applicable to surface-near failures of planar or wedge shape, which are of major importance for the lateral breach widening. Spatially extended failures of embankment slopes and complex conditions in heterogeneous embankments, however, are difficult to address adequately using this approach. Additional influences on the slope stabilities, like the water load or soil weathering, are neglected.

Three different failure angles are distinguished for material above and below the water surface and for the collapsed material resulting from the side wall failure. These angles allow for modelling of complex breach shapes and they approximate the discontinuous mass sliding after failure. Basic geotechnical considerations are made to incorporate effects of apparent cohesion. The theoretical soil shear strength is hereby correlated with the critical failure angle in a heuristic manner.

A novel failure algorithm was developed which is applicable to unstructured meshes. It is specially adapted to the dual-mesh approach presented in chapter 3 and subsequently guarantees strict sediment mass continuity. The algorithm was successfully validated against idealized test configurations, investigating the correct assignment of the critical failure angles and its suitability for complex spatial terrains. Furthermore, it was successfully applied to scenarios of single and multiple grain classes and the mass continuity was confirmed. The algorithm is mesh-dependent and a fine mesh resolution is recommended especially in those regions where small water depths occur. The use of unstructured meshes with the possibility of local mesh refinements is favourable in this regard.

As future enhancement, the replacement of the geometrical approach for the indication of side wall failures with a limit-equilibrium method or a continuum modelling approach could essentially improve the model.

6

Model Coupling

6.1 Introduction

Sub-models are used to simulate the different breach processes and need to be executed in a combined way regarding the mutual interactions between each other. The sub-models must exchange their computed set of variables and they have to set their boundary conditions dynamically as function of these variables. A simplified sketch of the mutual dependencies and data exchanges is illustrated in Figure 6.1.

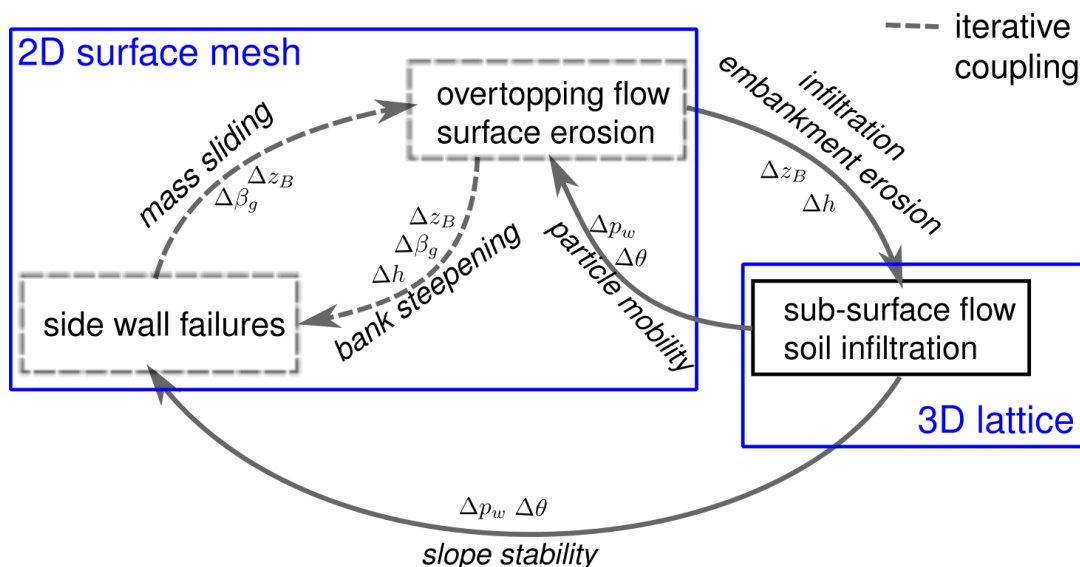


Figure 6.1: Model coupling and data exchange for combined modelling of breach processes. These processes are modelled on different computational meshes.

The sub-surface flow influences the side wall stability and the surface erosion due to apparent cohesion effects. The water saturations θ and pore-water pressures p_w hereby serve as input parameters and have to be provided. The sub-surface flow is influenced itself by the embank-

ment erosion and the overtopping flow which leads to infiltrations into the embankment body. The overtopping flow induces the erosion of the embankment surface and triggers the side wall failures. This embankment erosion Δz_B in turn influences the water depths and flow characteristics. From the model perspective, there is need to control these interconnections and the mutual data exchange.

The embankment erosion necessitates permanent adaptations of the mesh geometry and model boundaries. A major difficulty hereby is the coupling of these processes with the sub-surface flow, because they operate on different mesh types, the unstructured 2D surface mesh and the structured 3D lattice, respectively. The terms 'surface mesh' and 'lattice' are used from here on to denote these meshes. Mesh adaptations become necessary for the combined model execution and are presented in section 6.3.

Differing from this situation, the overtopping flow and the embankment erosion operate on the same 2D surface mesh, what eases their combined execution. These processes strongly interact with each other, however, and a tightly coupled modelling may be needed as investigated in section 6.2.

Further important coupling aspects are the time synchronization of the sub-models and the overall performance of the combined model. Different types of time synchronization were applied and are discussed in section 6.4. To be practically applicable and efficient, the performance of the sub-models should not differ substantially from each other. At first glance, this aspect seems problematic for the sub-surface flow modelling, which is three dimensional with a large number of cells and corresponding large computational expense per time step. The sub-surface flow operates on larger time-scales, however, and allows for larger time step sizes than the other sub-models. It thus requires a smaller number of total computational steps. Therefore the overall computational costs, relative to the simulation time, do not differ crucially between the sub-models.

Various programming techniques can be used to transfer data between the numerical sub-models. Data can be exchanged between dif-

ferent programs via external files, memory blocks or network data packages. It can also be exchanged between sub-models within a single program using internal data structures. Here, the sub-models were integrated into the framework of the natural hazard simulation software *BASEMENT*. This integrated modelling allows for a simple and efficient data exchange and synchronization using internal data structures and simplifies the model handling.

6.2 Coupling of surface flow and embankment erosion

Regarding the interconnection of the hydrodynamics of the overtopping flow and the embankment erosion one can distinguish between three basic modelling techniques. These are the uncoupled, semi-coupled and fully-coupled modelling, which differ in degree and type how mutual interactions of changes in bed-levels and flow properties are taken into account during each time step. Each of these modelling approaches has different advantages and disadvantages which have been discussed controversially in literature over the last years. Overviews are given by Kassem and Chaudhry (1998) and Cao *et al.* (2002) with partially contradicting recommendations. Uncoupled and semi-coupled modelling was implemented in the model.

These aspects are discussed and the necessity for (semi) coupled modelling is investigated in Appendix E with regard to non-cohesive progressive embankment breaches.

The considerations and obtained results indicate that in case of explicit breach simulations the uncoupled modelling is often adequate. Hereby the overtopping flow is computed first for the small explicit time step size, and afterwards the embankment erosion is determined based on this computed flow field. The uncoupled modelling is therefore adopted in this work due to its flexibility and better performance with respect to practical applications. In special cases with particular fine-

grained material and strong suspended-load, however, tests are recommended to examine whether (semi) coupled modelling becomes necessary.

6.3 Coupling with sub-surface flow

6.3.1 Necessity of coupled modelling

The surface and sub-surface flow differ significantly in their flow velocities and the corresponding time-scales. Flow velocities of the surface flow are in a typical range of ~ 0.1 - 10.0 m/s, whereas those of the sub-surface flow are orders of magnitudes slower in a range of $\sim 10^{-7}$ - 10^{-3} m/s. As a consequence, Morris *et al.* (2008) stated that it is usually justified to de-couple these processes. They proposed to first calculate the sub-surface flow through the embankment and then to set these results as constant during the breach event, thereby neglecting the sub-surface flow during the event. The validity of this assumption depends on the breach duration, which can differ significantly from minutes to days for different events. It also depends on the hydraulic conductivity k_f of the embankment material. In case of coarse-grained material with large k_f values, as e.g. often adopted in laboratory experiments, the saturations may change notably during breaching, as it was observed e.g. in the study of Schmocker and Hager (2008)¹. Furthermore, it has to be expected that the infiltration into the embankment during prolonged overtopping changes the saturations at least in the surface-near regions, thereby having impacts on the apparent cohesion.

Due to these aspects, unsteady coupled simulations of surface and sub-surface flow are proposed and implemented here. Depending upon the investigated scenario, however, it may be an option to de-couple the processes.

¹It is noted that in laboratory studies with non-compacted material, preferential flow paths may form within the embankment which speed-up the advance of the saturation front.

6.3.2 Data exchange and boundary conditions

Allocation table

The data exchange between the unstructured 2D surface mesh, representing the embankment surface, and the structured 3D lattice, representing the 3D embankment body, requires the definition of an allocation table. This allocation table specifies the spatial relations between the cells of the different mesh types. It is formulated in terms of c_{2D} , denoting a cell of the surface mesh, and $c_{3D,top}$, denoting a cell in the uppermost layer of the lattice. Following this terminology a relationship in form of $c_{2D} \rightleftharpoons c_{3D,top}$ is needed for all participating cells to organize the mutual data exchange. These relations are stored in the allocation table which is created in two subsequent steps:

1. The 2D surface mesh is projected on top of the 3D lattice, and
2. The relations $c_{2D} \rightleftharpoons c_{3D,top}$ are determined by evaluating the overlapping portions of the cells. A relation is set between two cells if one lies completely within the perimeter of the other. Depending on the different cell sizes, a cell $c_{3D,top}$ may thereby relate to multiple cells c_{2D} and vice versa. In case of partially overlapping cells, the cell-midpoints are chosen as indicator for the spatial relation.

This algorithm guarantees that all cells are finally connected with one or multiple cells of the other mesh within the overlapping region².

Boundary conditions for embankment erosion

The saturations θ and pore-water pressures p_w are needed as boundary conditions for the cells c_{2D} of the 2D surface mesh. They serve as input parameters for the determination of the apparent cohesion, which affects

²The allocation table is created only once at the simulation start. No table updates are needed afterwards since the embankment erosion affects only the vertical bed-levels z_B , whereas the x - y vertex coordinates and the vertical projection remain unchanged.

the surface erosion and side wall failures. These variables are provided by the sub-surface model and handed over using the allocation table.

The sub-surface flow model hereby provides a vertical distribution of saturation and pressure values over the embankment height. From this vertical distribution, a value is interpolated at the center bed-level of cell c_{2D} and used for the set-up of the boundary conditions. If the cell c_{2D} is connected to multiple lattice cells $c_{3D,top}$, then an arithmetic averaging is additionally applied to determine mean saturation and pressure values.

Boundary conditions for sub-surface flow

The boundary conditions for the 3D lattice cells are set dynamically depending on the water depths h of the overtopping flow. The water depths are provided by the surface flow model using the allocation table. If the lattice cell $c_{3D,top}$ is connected to multiple cells c_{2D} , then a mean water depth is determined by arithmetic averaging.

This water depth is passed down the vertical layers underneath the uppermost cell $c_{3D,top}$ of the structured 3D lattice until an active cell $c_{3D,a}$ is found. Only these active lattice cells take part in the simulation. Corresponding boundary conditions are then assigned to all adjacent boundary cell-faces of this active cell. This dynamical boundary assignment is needed due to the unsteady overtopping flow and the mesh adaptations during breaching. This procedure is visualized in simplified manner in Figure 6.2 for a cross-sectional view through the embankment.

Different types of boundary conditions are applied depending on the water depth of the overtopping flow:

- If the water depth h is larger than or equal to a minimum threshold value³, then a constant pressure-boundary is assigned. The assumptions of a hydrostatic pressure distribution and of equilibrium conditions for the distribution function hereby are made as outlined in section 4.4.3, and

³The threshold value is selected as the minimum water depth h_{min} , which is also used in the surface flow model to determine if cells are treated as dry or wetted.

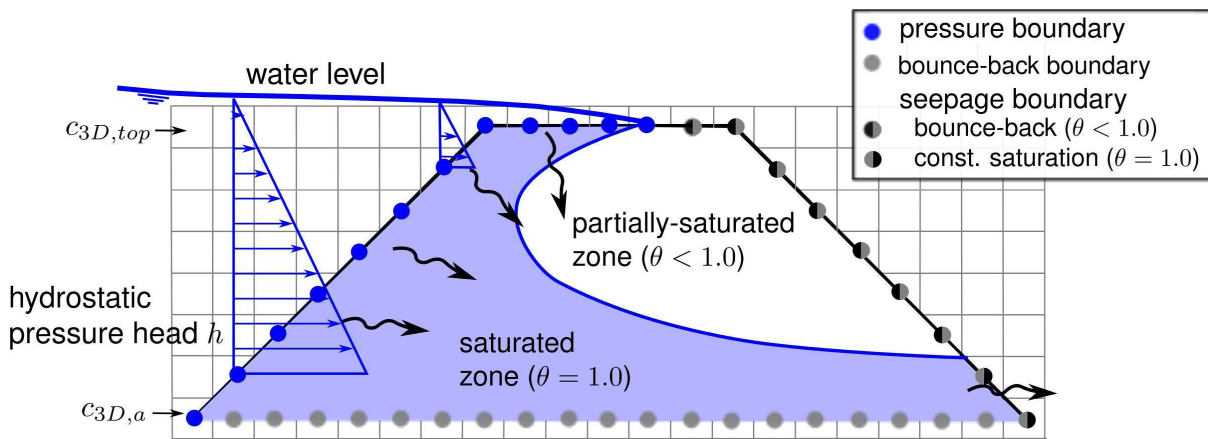


Figure 6.2: *Dynamical assignment of pressure, seepage and bounce-back boundaries for the sub-surface flow as a function of the overtopping flow depths.*

- If the water depth h is smaller than the minimum threshold value, an outflow seepage boundary is assigned. Depending on the water saturation θ at this location, this boundary acts either as bounce-back boundary ($\theta < 1.0$) or constant saturation boundary ($\theta = 1.0$) where water flows out of the embankment, as described in section 4.4.3, and
- In a final step, after the dynamical boundary assignment, bounce-back boundaries are set to the base of the embankment and to all other remaining boundary cell-faces which have no boundary conditions assigned yet.

It is noted hereby that the exchanged water masses between the sub-surface and surface flow are not considered as source term in the mass continuity equation. If water infiltrates into the embankment, then these water masses are not removed from the overtopping flow. Similar, if water flows out of the embankment, it is not added to the overtopping flow. Mass conservation of the water-phase is thus not strictly guaranteed in such cases. This simplification seems justified, since these exchanged water masses are negligible in relation to the amounts of overtopping water.

6.3.3 Lattice adaptation

Most sub-surface flow models solving the 3D Richards equation do not allow for changes in the mesh geometry during run-time. Mesh adaptations, which are necessary for the combined breach simulation, therefore are hardly possible and would invoke repeated time-consuming pre-processing steps after each data exchange. Hence, a new sub-surface model was developed and integrated into *BASEMENT*. It allows for flexible lattice adaptations during breaching and eases the required data exchange.

The basic idea of the lattice adaptation hereby is to update the 3D lattice, by de-activating or activating cells. This is done each time when parts of the embankment are eroded or material is deposited due to surface erosion or side wall failures.

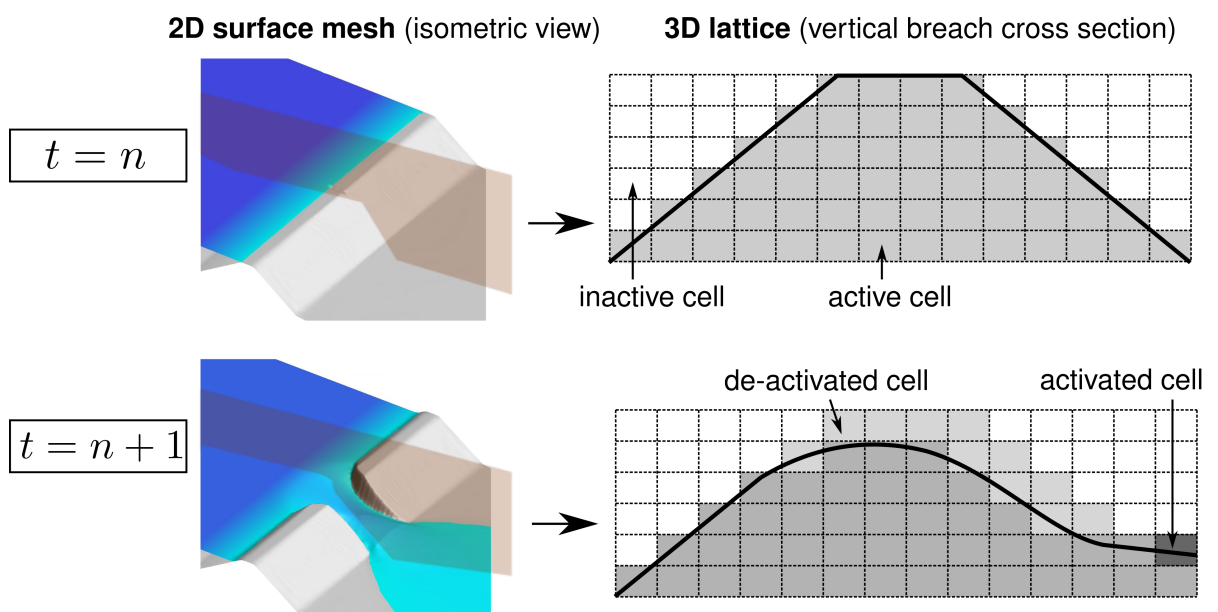


Figure 6.3: Update of 3D lattice due to breach advance in between two time levels $t = n$ and $t = n + 1$ with de-activated (light) and activated (dark) cells.

To accomplish the dynamical lattice adaptation, the 2D surface mesh is overlain over the 3D lattice. Then all 3D lattice cells situated above the surface mesh are de-activated, whereas the other lattice cells are

activated⁴. Eventually, the remaining active lattice cells represent the adapted 3D embankment body at the current breaching stage. The basic procedure is sketched in Figure 6.3 for a vertical breach cross section and can be described as follows:

- The *light* cells are de-activated at the new time level $t = n + 1$, because the corresponding parts of the embankment were eroded since the last data exchange at $t = n$. These de-activated cells are excluded from the computations and dynamical boundary conditions are set for the adjacent cell faces as outlined above, and
- The *dark* cells, in contrast, are activated for the sub-surface flow simulation, because embankment material has been deposited. Sub-surface flow now takes place within this deposited material.

The cell de-activation generally is robust and not prone to stability problems. It can, however, lead to situations with isolated cells in the mesh which have no or only few adjacent active cells. In such situations stability problems were observed which are probably due to small saturations θ in combination with the strongly non-linear water retention curves. Therefore a minimum threshold of $\theta_{min} = 0.001$ was introduced which prevented the occurrence of instabilities.

The cell activation during run-time is more problematic and requires a reasonable choice of initial conditions. Initial values hereby must be provided for the probability distribution functions f and f^{eq} in the activated cell. The selection of appropriate initial values showed influences on model stability. Simply equating these values to those of the surrounding active cells led in some cases to instabilities. Setting f and f^{eq} to the equilibrium values corresponding to the overtopping water depth $f = f^{eq}(h)$ showed a more stable behaviour and was therefore adopted. Nevertheless, if convergence problems arise due to the cell-activation

⁴To determine if the lattice cell is situated below or above the surface mesh, it is checked if its midpoint is above or below the plane which is formed by the corresponding triangular or quadrilateral element.

during run-time, it may simply be switched off in the model. This is usually acceptable since the depositions are of minor importance for the sub-surface flow and apparent cohesion⁵.

Another aspect of the flow within the deposited material is that the lattice adaptation only considers changes in the bed-levels Δz_B but not in the material compositions β_g . The latter are possible due to grain sorting effects at fractional transport simulations. These changes in principal also affect the hydraulic conductivity, the porosity and the constitutive model of the soil which are input parameters for sub-surface flow modelling. An automatic derivation of these empirical parameters would be required to consider these changes, which is out of the scope of the present work.

6.4 Time synchronization

To set the dynamical boundary conditions of the sub-models, data communication must take place after specific time intervals, what necessitates a synchronisation procedure. Two concepts for the time synchronization are hereby often used for explicit coupled modelling.

The sub-models can be executed in a 'synchronous' manner with a common time step size. To guarantee stable combined execution, the common time step size must be set to the smallest of all sub-models, which is determined by stability conditions as the *CFL*-criterion. However, in cases where the time step sizes differ considerably between the sub-models, such a restriction can lead to inefficient and inaccurate simulations. Consequently, this synchronization technique is suited well especially for sub-models operating on similar time-scales.

Another approach is to execute the models in an 'asynchronous' manner with their individual optimum time step sizes. This time synchronization does not suffer the computational inefficiency due to small time step sizes. Therefore it is advantageous regarding the coupling of sub-models

⁵Surface erosion and side wall failure modelling apply special treatments for the deposited material which are less dependant on the saturations.

with largely differing time-scales. Disadvantages are larger synchronization efforts and the need for data interpolations of the exchanged variables between the different time levels.

Synchronization of surface flow and embankment erosion

Time synchronization between the surface flow and the embankment erosion is implemented in synchronous manner. The time-scales of the processes can be in a similar range and a tight coupling is needed. Following this approach, a minimum time step size Δt_{min} is determined based on the *CFL*-criterion for the surface flow and is also applied to the other sub-models. The algorithm waits until all sub-models have completed the computation of the current time step until it proceeds with the determination of the new common time step size, resulting in a synchronous advance in time. Data exchange takes place at the end of each time step without the need for data interpolations.

Synchronization of surface and sub-surface flow

An asynchronous time synchronization was chosen for the surface and sub-surface flow modelling, due to their differing time-scales. The sub-surface flow model hereby applies its individual time step size, which is usually much larger than that of the surface flow model. During this time step size, multiple smaller time steps are computed for the surface flow. As soon as the surface flow model reaches or exceeds the time level of the sub-surface model, the data variables $(h, \Delta z_B, \theta, p_w)$ are mutually exchanged and the 3D lattice is updated. Afterwards, the new individual time step sizes are determined and the next computational step is started.

6.5 Summary

Embankment breach modelling involves different physical processes which are simulated with multiple sub-models. These need to be executed in a combined approach to consider mutual influences. All sub-models were therefore integrated into the modular software framework *BASEMENT*. The use of a single software framework offers various advantages, like simple data transfer, and eases model handling.

Uncoupled, semi-coupled and fully-coupled modelling approaches are distinguished for the interconnection between the surface flow and the embankment erosion modelling. The differences between uncoupled and coupled modelling are expected to be small for the progressive erosion of non-cohesive embankments if an explicit scheme is applied. The latter leads to small time step sizes and corresponding small bed-level changes during each computational time step. The differences were examined for plane and spatial embankment breaches and no significant deviations were observed, indicating the adequateness of uncoupled modelling for many cases. Accurate fully-coupled models were presented recently and could improve erosion modelling, but are problematic and less flexible regarding the consideration of bed-load transport and non-erodible beds.

The surface and sub-surface flow models operate on different mesh types and dimensions. The combined modelling requires an allocation table which defines the mutual relations between the cells of both meshes. It also requires adaptations of the 3D lattice for the sub-surface flow to incorporate changes in the embankment geometry during runtime. An algorithm was developed for automatic lattice adaptation, where cells are activated or de-activated depending on the breach advance, and for dynamical assignment of boundary conditions.

The sub-models are coupled using explicit time synchronizations. The coupling of surface flow and embankment erosion bases on a synchronous advance in time, i.e. all sub-models apply a common time step size. In contrast, surface and sub-surface flow models are combined using an asynchronous time synchronization with individual time step sizes.

7

Applications

7.1 Introduction

Several embankment breach studies were selected to test the breach model and to investigate the model sensitivity to parameter variations.

Laboratory-scale experimental studies with simple geometries are of limited practical relevance and can suffer problems regarding scale effects. These studies are made under controlled conditions with accurate instrumentation, however, and offer the unique possibility to validate the separate model components in detail against measurements. In the last decades, research was intensified on such experimental studies and an overview was given by the ASCE/EWRI-Task-Committee (2011). Recently, investigations with high-quality and continuous data measurement techniques were advanced. Schmocker and Hager (2009) investigated scale effects of a series of plane embankment breaches due to overtopping over the full crest width. A spatial dyke breach, starting from a pilot channel, was investigated by Pickert *et al.* (2011) including measurements of the 3D breach evolution over time. The latter two experimental studies were selected here for model tests in sections 7.2 and 7.3. In particular the detailed comparison of 3D breach shapes can give new insights into the side wall failure modelling and has not been used for model validation up to now.

Differing from this situation, comparisons with field-scale embankment breaches usually allow for qualitative comparisons only. The limited accessibility and instrumentation during hazard events hinder detailed investigations and measurements. Nevertheless, field-scale scenarios are important to test the model applicability and robustness for

practical relevant scenarios of large extents with complex geometries and boundary conditions. Only few cases are known of controlled field-scale embankment breaches which could provide an improved data base for comparison. Due to the lack of such investigations, a controlled dyke breach experiment due to overtopping of a segment of the Rhône dam at Baltschieder in the Swiss Canton of Wallis was originally intended as test case for this work and is described in Morales *et al.* (2011). However, the dyke body could withstand the overtopping flow due to the presence of large gravel and boulders in the sand matrix. The event showed mainly erosion due to piping effects and is not suited as model test for progressive breach erosion. Another controlled breach event was investigated near the Røssvassdammen dam in Norway within the scope of the IMPACT project (Morris (2004), Lövoll (2004)). Despite significant data uncertainties, this event was selected as model application and is presented in section 7.4.

Investigations and measurements of natural embankment breaches are generally even more difficult. These events are hardly predictable and the local sites are often situated in mountainous regions with rarely populated areas, which are not accessible during breaching. Hence, the main problem for simulations of such natural hazard events is the lack of available data (Cao *et al.* (2011)). Investigations are usually only possible after the event has happened, trying to reconstruct the actual failure processes. A recent field study concerning a natural moraine embankment failure in the Patagonian Andes was made by Worni *et al.* (2012) and the data was used for numerical simulations in section 7.5.

7.2 Laboratory plane dyke breach

7.2.1 Experimental set-up

Schmocker and Hager (2009) investigated the erosion of a series of homogeneous earth dykes of different dimensions due to overtopping flow at laboratory-scale. The dyke was overtopped over its full crest width,

resulting in a quasi-2D plane breach without lateral erosion due to side wall failures. This idealized set-up allows for investigations of the purely vertical erosion process. The characteristics of the dyke geometry and material are listed in Table 7.1. Figure 7.1 illustrates the experimental set-up with the flume and the dyke body.

Table 7.1: Laboratory dyke geometry and material properties.

length l_E [m]	width [m]	height h_E [m]	crest width [m]	slope [-]	porosity [-]	grain density [kg/m ³]	mean grain diameter [mm]
0.90	0.20	0.20	0.10	1v:2h	0.40	2650	2.0

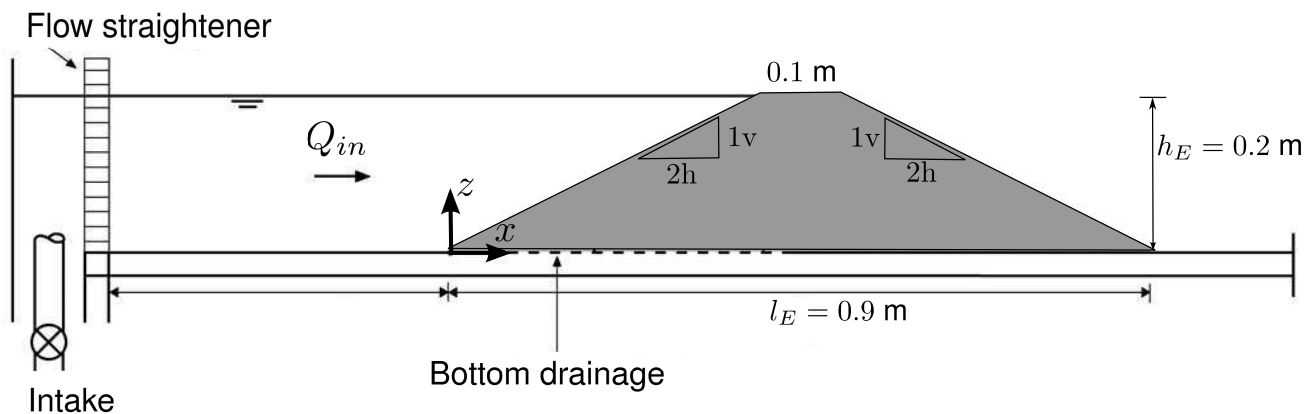


Figure 7.1: Experimental set-up of plane dyke breach with flow direction from left to right (modified after Schmocker and Hager (2009)).

The dyke was built of non-cohesive, homogeneous sand material of 2 mm grain diameter which was loosely placed without compaction. To prevent slope failures of the downstream dyke face, a bottom drainage was placed underneath the dyke which lowered the seepage line immediately to the floor. The inflow discharge was kept constant during the experiment at $Q_{in} = 13$ l/s, leading to a strong overtopping and rapid erosion of the dyke. Continuous measurements were made of the water surface ζ and the bed elevation z_B , allowing for detailed comparisons with numerical results.

7.2.2 Numerical set-up

In the numerical model the experimental flume was discretized using an unstructured grid with ~ 2700 triangles, which was locally refined at the dyke body. The dyke was represented with erodible material whereas the rest of the flume was set to non-erodible, fixed bed conditions. A constant friction coefficient was calibrated to $k_{str} = 45 \text{ m}^{1/3}/\text{s}$ and set over the entire domain. The inflow boundary was modelled using the constant inflow rate Q_{in} and as outflow boundary a weir was placed far enough downstream to prevent backwater effects. The CFL -number was set to 1.0 which led to small time step sizes in the range of $\Delta t \approx 0.001 \text{ s}$. As outlined in section 6.2, the time step sizes are sufficiently small so that uncoupled modelling is justified.

The surface erosion was modelled with the modified-MPM transport formula as presented in section 3.3.2. No suspended-load transport was observed in the experiment and therefore was neglected in the model. Furthermore, no sub-surface flow was considered, since an effective bottom drainage was installed and the saturation was guessed to $\theta = 0.5$ within the dyke, due to the lack of measurements.

7.2.3 Qualitative and quantitative results

In the simulation, the observed change in flow regime from sub-critical flow in the upper flume to super-critical flow at the downstream dyke face was captured and imposed no stability problems. The hydrodynamic and sediment transport modelling proved to be stable throughout the breach.

The dyke was eroded strongly during the first 15 s of the simulation. The flow accelerated along the downstream dyke face and was super-critical with the Froude-number $Fr > 1.0$ as shown in the right part of Figure 7.3. The maximum bottom shear stresses of $\tau_B \approx 40 \text{ N/m}^2$ occurred during the start of overtopping, when the slopes were steepest (Figure 7.3, left). Due to the surface erosion along the downstream slope, the dyke crest shifted into upstream direction and the slope was flattened rapidly. During this breach phase, a rotation of the dyke surface

around a downstream pivot point can be noted (Figure 7.2, bottom right), which is in agreement with other experimental observations as e.g. by Coleman *et al.* (2002).

After this first breach phase, the erosion rate slowed down gradually and the dyke approached a quasi-stable configuration. In Figure 7.2 the obtained numerical results of the dyke and water surface profiles are illustrated for different times and compared with the experimental measurements.

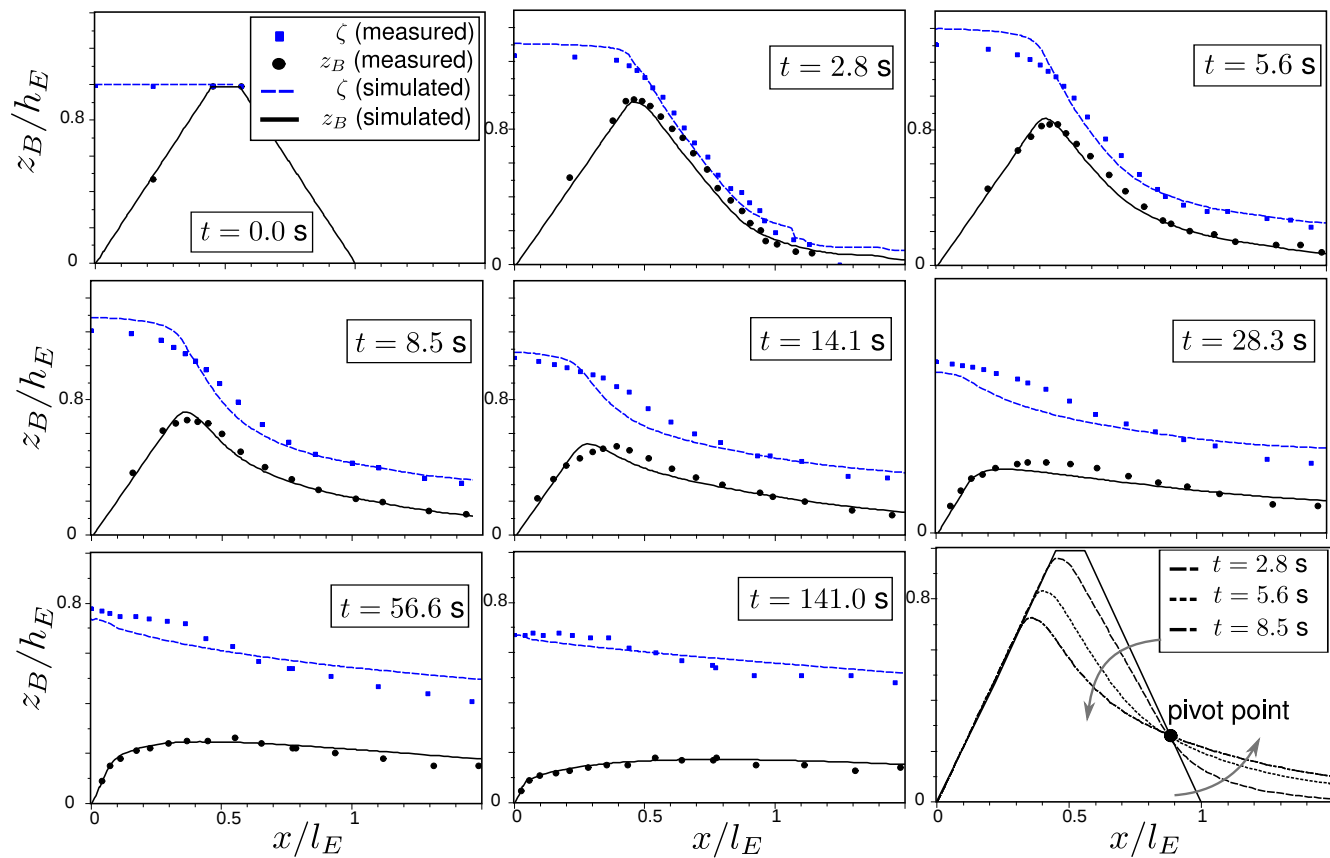


Figure 7.2: Dyke z_B and water-level ζ profiles at different times t . Bottom right: rotation of dyke profiles around a pivot point during the first breach phase.

The numerical results are in good agreement with the measured dyke profiles and water-levels throughout time. Deviations are observed in form of increased water elevations during the initial overtopping around ~ 5 s and of the water surface curvatures around the dyke crest. These may be attributed to the neglect of vertical accelerations in the SWE on the initially steep slope. Further, slight deviations of the crest shape can

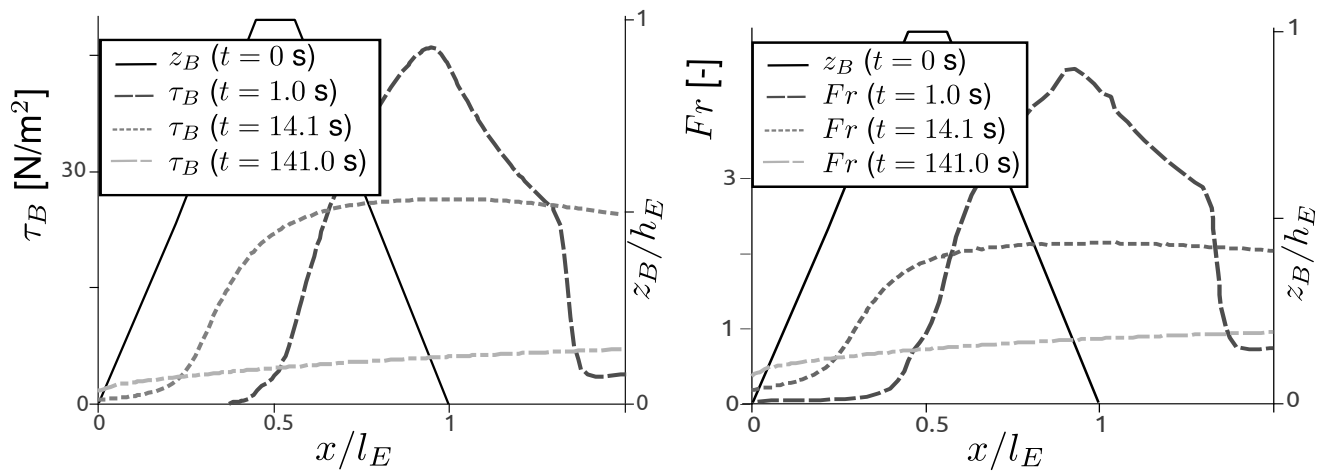


Figure 7.3: *Bottom shear stresses τ_B (left) and Froude-numbers Fr (right) for different times t .*

be noticed, which are again supposed to be due to the neglect of vertical accelerations and to non-equilibrium effects of the bed-load transport.

The overall successful modelling of the plane dyke breach indicates that the empirical transport formula is applicable to non-cohesive embankment breaches, although several assumptions of its derivation are violated. This observation agrees with results of previous investigations. The model results also prove the sediment mass continuity of the dual-mesh approach with total and area specific mass errors smaller than $\sim 10^{-10} \text{ m}^3$ and $\sim 10^{-12} \text{ m}$, respectively.

7.2.4 Sensitivity analyses

To improve the understanding of the influences of different model parameters, sensitivity analyses were made. Parameters with major effects on the embankment erosion and of special significance for model calibration are the

- Bed-load transport formula,
- Friction coefficient, and
- Sediment porosity.

Bed-load transport formula

A variety of different transport formulas were investigated for this test case. Beside the modified-MPM formula, the transport formulas of Parker (1990), Hunziker and Jaeggi (2002), Rickenmann (1991) and Wu (2004) were additionally tested as they are implemented and described in Faeh *et al.* (2012). In Figure 7.4 (a) the obtained dyke profiles are illustrated and compared at two different times.

The results reveal large differences in dyke erosion especially at the first breach phase, whereas the modified-MPM formula shows the best fit with the measurements and is therefore used from here on in this work.

Furthermore, in principal, all transport formulas led to similar shaped profiles and differed mainly in the temporal breach advance. Hence, they can be calibrated to fit the measurements by modifying their pre-factors. An exception was the formula of Rickenmann, which led to a significantly steeper slope immediately downstream of the crest compared to the other formulas. This result is surprising because the formula was derived for steep slope conditions. It is noted, however, that the combination of this formula with the local slope correction (section 3.3.1) is questionable and that the model performance depends on the special condition of strong overtopping flow for which these formulas were not originally derived. At the later breach phase, with less erosion and flattened slopes, all formulas produced similar dyke shapes.

Friction coefficient and sediment porosity

The friction coefficient was varied as $k_{str} = 40, 45, 50 \text{ m}^{1/3}/\text{s}$ to test the model sensitivity. The simulation results are depicted in Figure 7.4 (b) at two times. The model did not react very sensitively to these variations, but notable changes of the dyke profiles were observed. The variation of the friction coefficient therefore is a major calibration parameter for embankment breach simulations.

Furthermore, the porosity p of the embankment material has significant impacts on the dyke erosion. This sensitiveness is quite obvious and

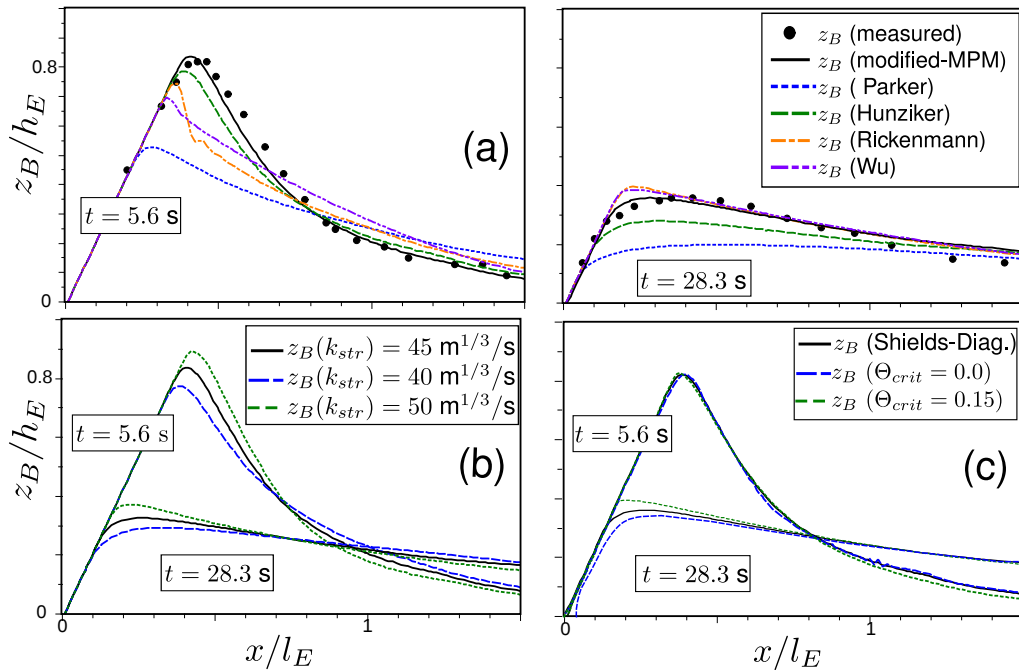


Figure 7.4: *Top (a): dyke surface profiles z_B obtained with different bed-load formulas at $t = 5.6$ s, 28.3 s. Bottom: (b) sensitiveness to variations of friction coefficient (left) and, (c) Θ_{crit} (right).*

not illustrated here, since the porosity directly determines how the transport rate translates to the erosion depths. The porosity is often known from laboratory investigations or is taken from tabulated values. Otherwise, if the embankment material was compacted or the porosity of a grain mixture is unknown, it is an important calibration factor as well.

Inception of sediment transport

Investigations were also made concerning the influence of the Shields-parameter, which determines the inception of sediment transport. Figure 7.4 (c) illustrates effects which resulted from variations of Θ_{crit} within the wide range of 0.0-0.15. It can be seen that these variations had only minor effects on the computed dyke profiles. This observation is attributed to the occurrence of large bottom-shear stresses immediately after overtopping, strongly exceeding the critical shear stresses of incipient motion.

This insensitivity to Θ_{crit} indicates that the apparent cohesion and

grain compositions of embankments may often have no crucial impacts on the formation of the peak breach discharge, because Θ_{crit} is strongly exceeded during the later breach phases. This argumentation holds true at least if the overtopping flow is strong and the water depths are large. In other situations, for example during breach initiation under small water depths, Θ_{crit} has significant influences and can even determine whether a breach event is triggered or not. Similar, after formation of flattened and moderate embankment slopes the influence of Θ_{crit} is also more pronounced again (Figure 7.4 c).

7.3 Laboratory spatial dyke breach

7.3.1 Experimental set-up

In contrast to the idealized plane dyke breach, in realistic breach scenarios the overtopping flow erodes an initial breach channel which enlarges progressively with time and forms a 3D breach shape. In laboratory experiments of Pickert *et al.* (2011), the spatial breach of a homogeneous dyke was investigated and started by overtopping a small pilot channel. Dimensions and material properties of the dyke are listed in Table 7.2 and were also used for the numerical model set-up. The pilot channel was 5 mm high and 25 mm wide and was located at a side glass wall for observation. The experimental set-up is sketched in Figure 7.5 including three observation profiles. Out of three tests with different grain sizes, that with the coarsest mean diameter $d_m = 0.64$ mm was chosen for simulation because it showed no cohesive effects. Furthermore, a bottom drainage was installed at the downstream dyke toe to lower the seepage line and to prevent it from reaching the downstream dyke face.

The reservoir level was held constant during the experiment at $\zeta = 0.3$ m by controlling the inflow discharge. Several parameters were recorded continuously, allowing for detailed comparisons:

- The flume outflow was determined with a downstream weir and was used to estimate the breach discharge,
- The sum of eroded masses was weighed continuously, and
- The 3D breach geometry was recorded along the three observation profiles at multiple times.

Table 7.2: *Laboratory dyke geometry and material properties.*

length [m]	width [m]	height [m]	crest width [m]	slope [-]	porosity [-]	grain density [kg/m^3]	mean diam. [mm]
1.9	1.0	0.3	0.1	1v:3h	0.43	2650	0.64

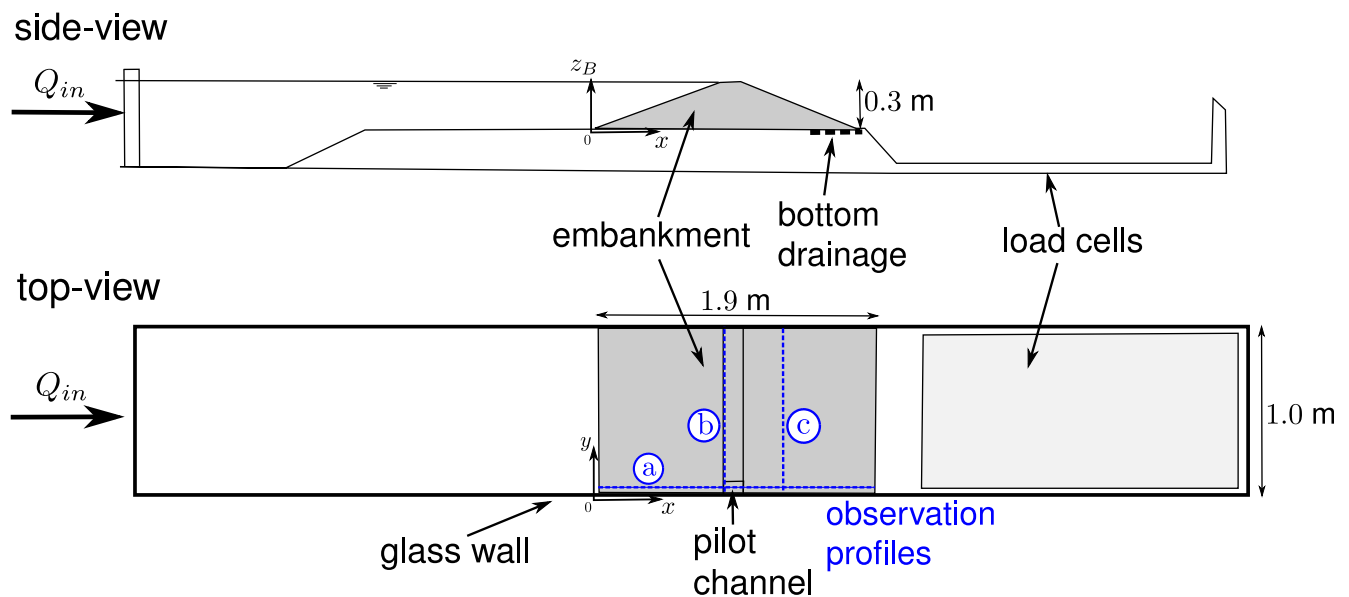


Figure 7.5: *Sketch of experimental set-up of spatial dyke breach based on Pickert et al. (2011). The breach advance was recorded along the observation profiles (a),(b),(c).*

7.3.2 Numerical set-up

The experimental flume was discretized using an unstructured grid with $\sim 17,000$ cells. The grid was locally refined at the embankment body and further refined around the pilot channel, leading to minimum cell sizes of $\Delta x \approx 0.2$ mm. The channel bottom was set as non-erodible and a single grain sediment was used to represent the dyke material. The friction coefficient was selected as $k_{str} = 47 \text{ m}^{1/3}/\text{s}$ over the entire mesh. The *CFL*-number was set to 1.0 leading to small time step sizes around $\Delta t \approx 0.002$ s.

The downstream boundary condition was modelled as an outflow weir and set far enough downstream to prevent backwater effects. A special treatment was needed to establish the constant water-level ζ in the upstream reservoir. For this purpose a Proportional-Integral-Derivative (PID) controller was applied which controlled the inflow rate as a function of the reservoir water level, $Q_{in} = f(\zeta)$, so that the water-level remained constant (see Faeh *et al.* (2012) for details on the PID-controller).

The surface erosion was again determined with the modified-MPM transport formula. As for the plane dyke breach, no significant suspended-load transport was observed by the experimenters and therefore was neglected in the simulation. The geometrical approach was used to simulate the side wall failures and requires appropriate choices of the critical failure angles. The failure angle below the water-level was set to $\gamma_{wet} = 37^\circ = \gamma_{rep}$. The angle for apparent cohesion was set to $\gamma_{coh} = 43^\circ$, what allows for maximum failure angles above the water-level of $\gamma_{dry} = 80^\circ$, lying within the range of the observed upper side wall angles. The deposition angle was set to $\gamma_{dep} = 15^\circ$.

Despite the installed bottom drainage, the water saturations may have influenced the dyke erosion at the later breach phases. The sub-surface flow was therefore considered in the simulations. A steady-state solution for a completely filled reservoir was computed and set as initial condition. The bottom drainage hereby was considered by setting $\theta = 0.0$ at the downstream toe. The VGM model was applied and the model pa-

parameters are given in Table 7.3. The obtained seepage line for steady state conditions is illustrated in Figure 7.6 and compares well with the measurement.

Table 7.3: Parameters applied for sub-surface flow modelling at laboratory spatial dyke.

θ_R [-]	θ_S [-]	k_f [m/s]	α [1/m]	n_V [-]	h_s [m]	Δx [m]	Δt [s]
0.01	0.43	$5E - 5$	12	2.3	-0.01	0.01	5.0

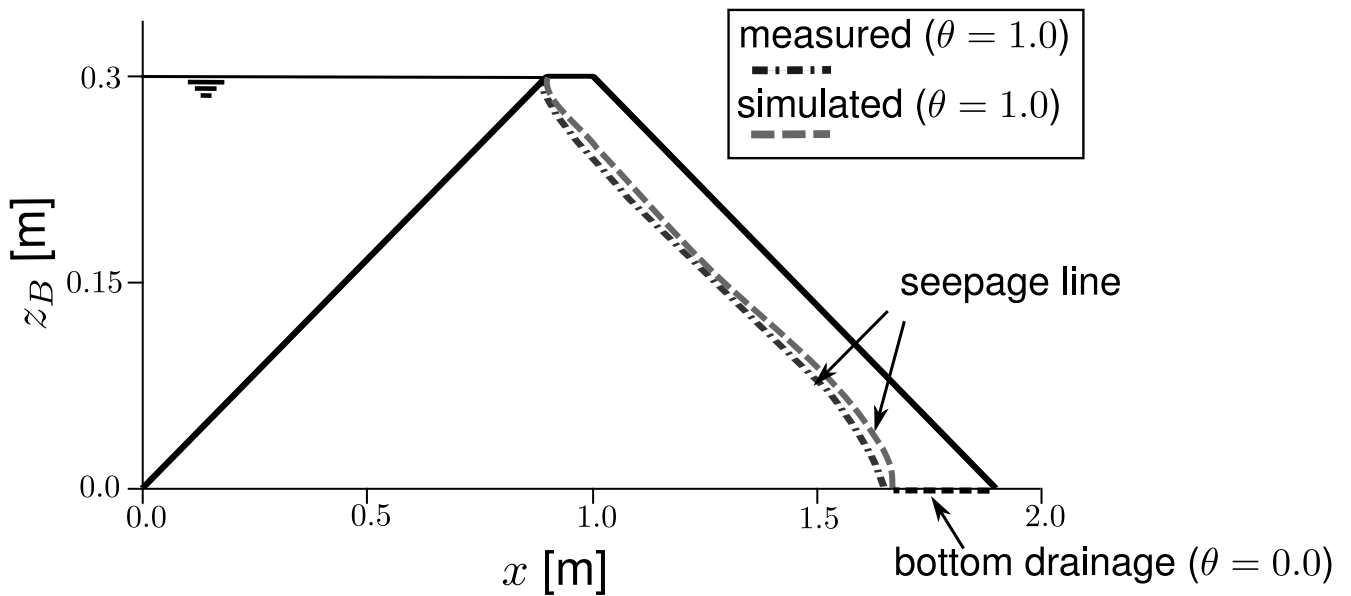


Figure 7.6: Simulated and measured seepage lines through a cross-section of the dyke body for steady-state initial conditions before overtopping.

7.3.3 Qualitative results

Figure 7.7 qualitatively illustrates the computed temporal advance of the spatial breach. Three general breach phases were observed in the simulation which were also identified in the experiments by Pickert *et al.* (2011) as

1. 'Initiation phase' with small water depths and few erosion (~ 30 s),
2. 'Breach formation' with a vertical recess due to surface erosion (~ 70 s), and
3. Final 'breach phase' with a rapid increase in the breach outflow (~ 100 s). The lateral erosion is increasingly affecting the breach formation.

Another qualitative observation is the formation of a curved, hour-glass shaped breach at the later breach phase. Due to the model set-up, only one half of this symmetric shape is formed as indicated in Figure 7.7. This characteristic breach shape was also reported in other studies as Coleman *et al.* (2002) or Rozov (2003). The overtopping flow hereby forms a streamlined inflow-fan at the embankment in a way to minimize the occurring energy losses and flow separations as outlined by Chanson (2004a).

7.3.4 Quantitative results

The integral parameters 'breach discharge' and 'sum of eroded material' are compared in the left part of Figure 7.8. The data was only recorded over ~ 120 s, because thereafter the constant reservoir water-level could no longer be established.

The breach outflow is of special relevance for practical applications and was captured well throughout time. In a similar way, the sum of the eroded masses could be reproduced in the simulation, which indicates an adequate representation of the overall breach advance.

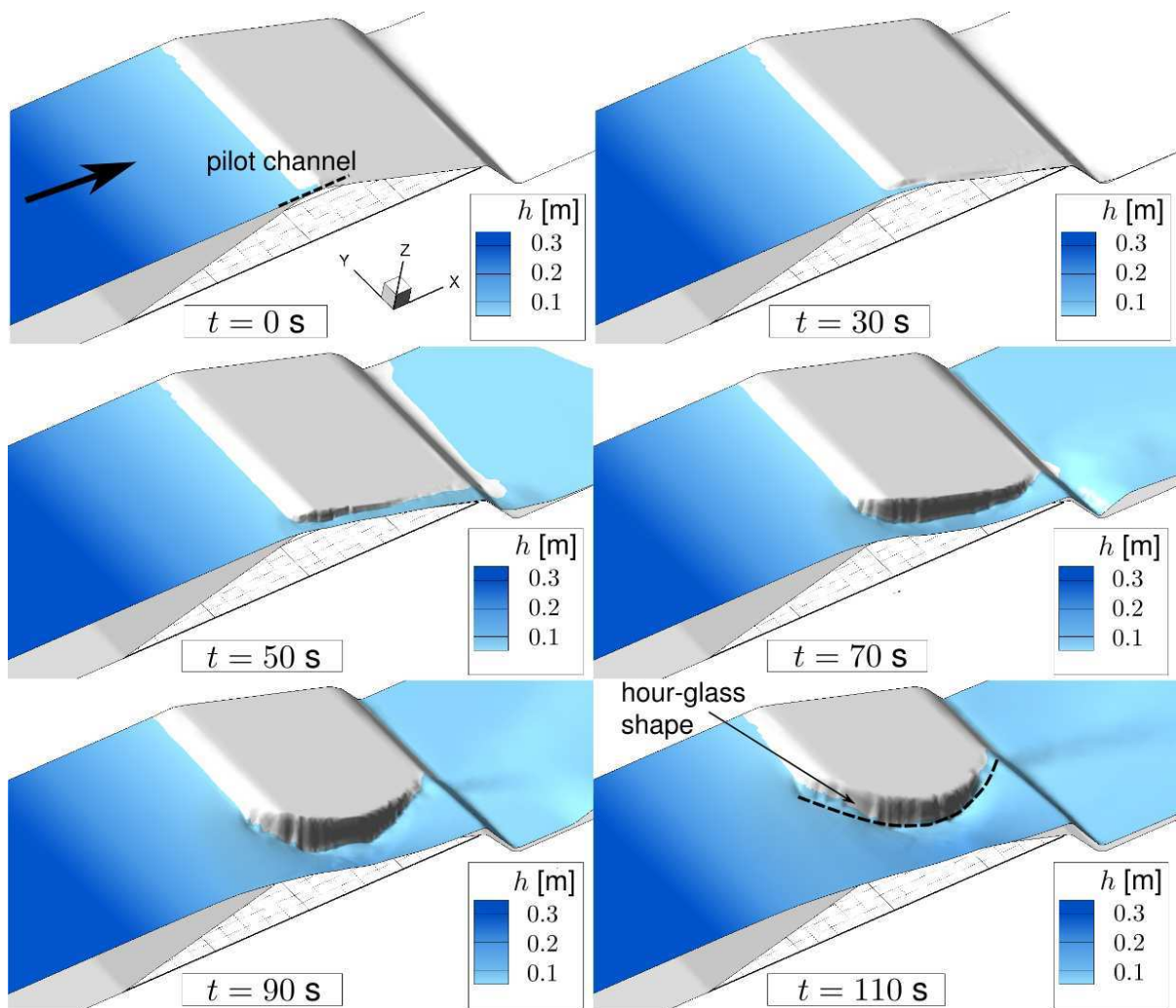


Figure 7.7: Qualitative simulated spatial dyke breach development at different times t with hour-glass shaped breach formation. The arrow indicates the flow direction.

Nevertheless, these integral parameters do not give full insight into the actual breach processes and do not provide sufficient validation of the side-wall failure modelling. Therefore the 3D breach geometries were additionally compared.

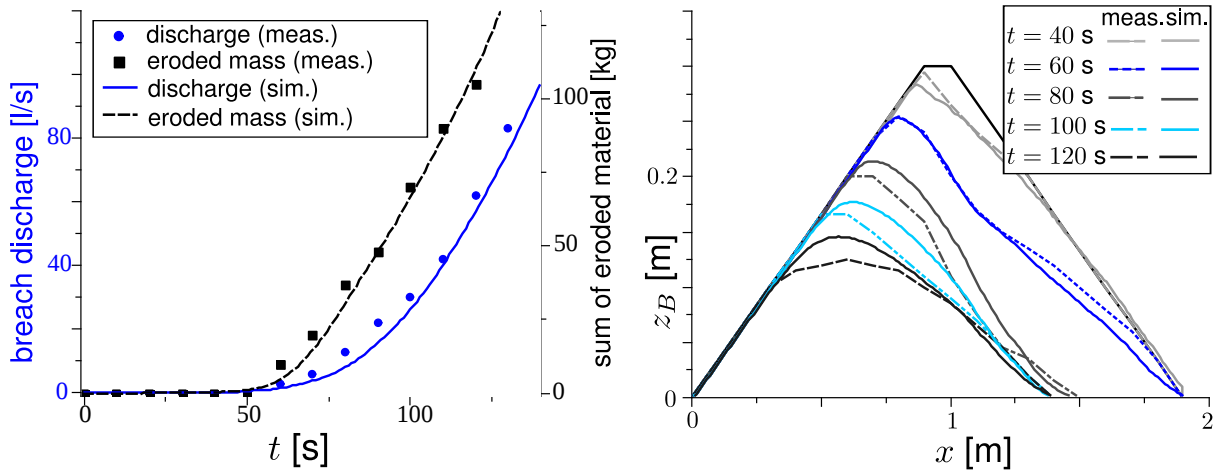


Figure 7.8: *Left: breach outflow and sum of eroded masses at spatial dyke breach. Right: development of measured (meas., dashed) and simulated (sim., solid) longitudinal breach profiles at different times at observation profile (a).*

The longitudinal dyke erosion is compared with the test data in the right part of Figure 7.8 along observation profile (a) as shown in Figure 7.5. The computed longitudinal profiles are in satisfying accordance throughout the simulation. As observed for the plane dyke breach, the deviations concern mainly the crest shape.

In addition to the longitudinal profiles, the profiles at two transversal cross-sections through the embankment were compared. One cross-section is recorded across the upper crest $x = 0.9$ m and the other at $x = 1.3$ m downstream of the crest at observation profiles (b) and (c). The lateral breach widening depends strongly on the side wall failures and therefore is a good indicator if these processes can be captured adequately with the geometrical approach.

Figure 7.9 illustrates the measured and computed transversal profiles at both cross sections. One can easily note that the measured profiles do not have simple rectangular or triangular shape as it is sometimes assumed in numerical approaches. As a consequence, multiple critical

failure angles have to be distinguished to capture their shape. Comparing the results, the model could essentially reproduce the transversal profiles at both cross sections over time with satisfying accuracy.

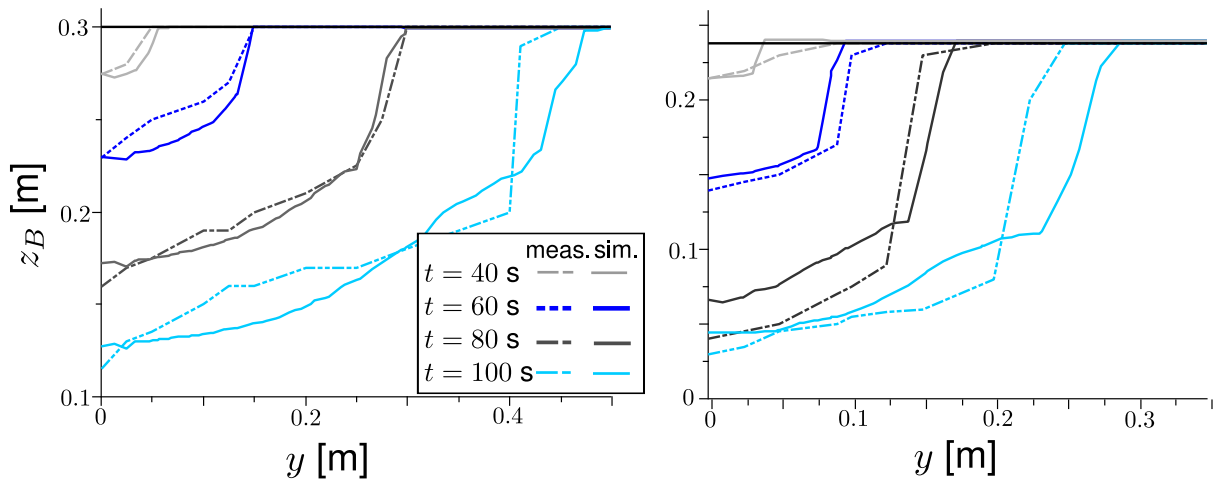


Figure 7.9: Development of measured (meas., dashed) and simulated (sim., solid) transversal breach profiles at different times. Left: observation profile (b). Right: observation profile (c).

Overall, the model reproduced the integral parameters as well as the 3D spatial breach formation. These results confirm the applicability of the geometrical side wall failure modelling despite its large simplifications. This seems true at least for non-cohesive embankments if adequate failure angles are used. Furthermore, the sediment masses were again strictly conserved using the dual-mesh approach.

The effects of apparent cohesion led to an increased dyke erosion during the later breach stages. As soon as the dyke was eroded up to the seepage line, the apparent cohesion was reduced leading to an increase in surface erosion. This aspect had the tendency to improve the results, since the surface erosion was slightly underestimated at the later breach phases otherwise.

Despite the promising model performance it is noted that Pickert *et al.* (2011) also reported effects which cannot be captured by the numerical model and demonstrate its limitations. They observed side-wall failures to happen less frequently but of larger extent. According to their statements, the side walls did not immediately adapt to the angle of repose below the

water surface, or below the seepage line, as it is assumed in the model.

7.3.5 Sensitivity analysis

Additional investigations were made regarding the sensitivity of model parameters. Thereby the focus was laid on the side wall failure angles, which could not be investigated with the plane dyke test.

Critical failure angles

The sensitivity of the breach formation to the critical failure angles was investigated by varying these parameters. The critical failure angle below the water surface γ_{wet} hereby was excluded from the analysis since it is not regarded as a calibration parameter and equals the angle of repose.

The sensitivity of the failure angle above the water surface γ_{dry} was investigated by varying γ_{coh} as 38° , 43° , 48° . The resulting deviations at observation profile (b) are illustrated in the left part of Figure 7.10. These variations did not lead to substantial differences in the breach formation and the model reacted mildly sensitive. In particular, it is noted that γ_{dry} is of minor importance for breach initiation and becomes more influential at later breach phases.

The deposition angle γ_{dep} , which determines the sediment redistribution after slope failures, was varied as 13° , 15° , 17° . The obtained results at observation profile (b) are illustrated in the right part of Figure 7.10. Compared to γ_{dry} , the variations of γ_{dep} resulted in more significant changes in the breach formation, indicating model sensitivity towards γ_{dep} . For $\gamma_{dep} = 15^\circ$, the material is redistributed widely over the breach channel and is rapidly eroded due to the strong acting bottom-shear stresses. The decrease of γ_{dep} did not lead to large effects on the breach development. The increase of γ_{dep} , however, led to material depositions closer to the side walls, thereby blocking and slowing down the breach widening and causing its underestimation.

In general, the sensitivity upon γ_{dep} is rather unsatisfactory, because

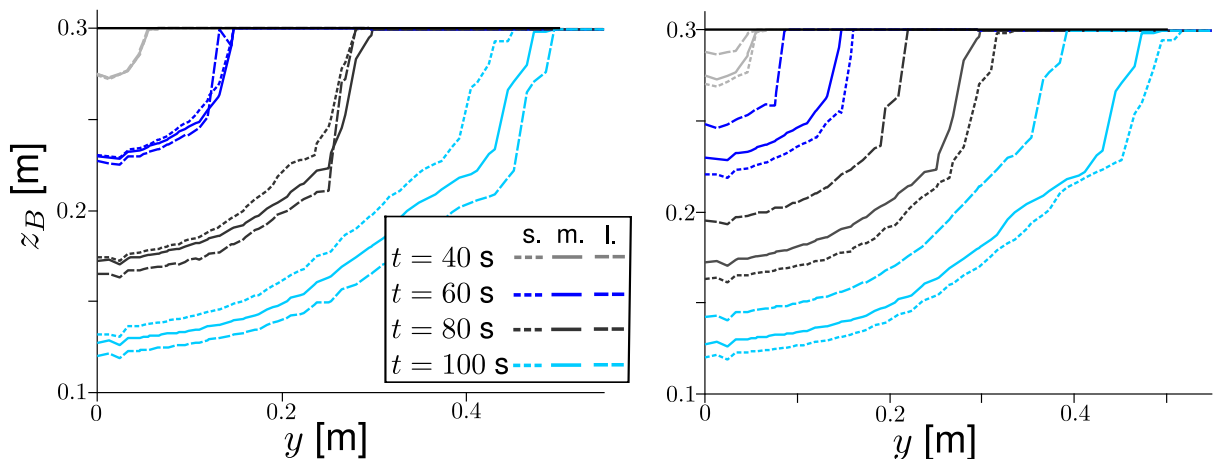


Figure 7.10: *Left: transversal breach profiles at observation profile (b) for variations of γ_{coh} . Right: transversal breach profiles for variations of γ_{dep} . (s. = small, m. = medium, l. = large).*

it is difficult to derive a-priori from field measurements or material properties. Following the made investigations, it is recommended to find values small enough to prevent the blocking of the lateral breach widening so that the model prediction is on the safe side. The chosen value of 15° for this test case may serve hereby as a guideline. The investigations also demonstrate that the additional failure angle γ_{dep} is needed for the geometrical approach. Using only two different failure angles, as it was sometimes done in the past by setting $\gamma_{dep} = \gamma_{rep}$, does not correctly reproduce the spatial breach formation with its discontinuous mass movements.

Suspended-load transport at laboratory-scale

Although no suspended-load transport was observed in the experiment, its influence on the breach formation was examined due to the small mean grain diameter $d_m < 1$ mm.

During the first two breach phases with small water depths, nearly no entrainment of particles into suspension occurred in the simulation. Therefore the results did not differ notably from simulations with solely bed-load transport as expected. In contrast, at the later breach phase the water depths increased and particles were entrained into suspension.

The resulting suspended-load transport significantly increased the dyke erosion, which proceeded much too rapidly. Variations of the Movability number Mn within a reasonable range of 0.2-2.0 were tested, modifying the portioning between bed- and suspended load (section 3.3.4), but could not prevent the particle entrainment.

As mentioned in section 3.2.1, a main reason for this unexpected simulation behaviour is supposed to be the underlying assumption of a vertical equilibrium concentration profile over the flow depth. This assumption seems problematic especially for small-scale laboratory experiments with comparably small cell-sizes and flow turbidities. Therefore the activation of suspended-load transport for such laboratory-scale experiments can lead to unrealistic overestimations of the embankment erosion. The implementation of a non-equilibrium transport model could improve this situation by considering an adaptation length and time for the development of equilibrium conditions.

7.4 Field-scale dam breach

7.4.1 Site conditions and set-up

The model was also applied to a dam breach at field-scale in Norway. The field investigations of the planned and controlled dam breach were made as part of the IMPACT-project (Lövoll (2004) and Morris (2004)). The test site is located in the middle of Norway near the town of Mo i Rana. The left part of Figure 7.11 depicts the test site with the upstream located Røssvassdammen Dam and the downstream Røssåga River. The test dam was built downstream of the Røssvassdammen Dam and is shown in the right part of the Figure. This scenario allowed to fill and control the water-level of the upstream reservoir to some extent by regulating the Røssvassdammen Dam flood gates.

Out of several scenarios investigated within the scope of the IMPACT project, the overtopping of a homogeneous gravel dam was chosen for simulation (test nr. 3 after Lövoll (2004)). The dam was several meters



Figure 7.11: *Left: site overview with Røssvassdammen Dam and test dam location. Right: initial set-up of non-cohesive gravel dam (modified after Lövoll (2004)).*

high with relatively steep slopes as given in Table 7.4. A pilot channel of 0.1 m depth and 2 m width was placed at the centre of the dam to start the progressive erosion due to overtopping. The dam material consisted of a wide-ranging grain composition of gravel embedded into a sand matrix. The representation of this grain composition and the material properties are listed in Table 7.5 as used in the model.

Table 7.4: *Geometry of the field-scale test dam.*

width [m]	length [m]	height [m]	crest width [m]	slope upstream [-]	slope downstr. [-]
20	40	5	2	1v:1.9h	1v:1.6h

The breach event was initiated by increasing the water-level in the reservoir in a step-wise manner until overtopping started and surface erosion occurred. The reservoir water-level was not hold constant during breaching, but dropped rapidly. The breach discharges were deduced from measured water-levels downstream of the dam. Contradicting descriptions of the total water volume impounded by the dam were found in the above mentioned references and the water-levels immediately upstream of the dam are not known exactly. Therefore the impounded volume was estimated in this work to $V \approx 70,000 \text{ m}^3$ in a way to be able to reproduce the measured total outflow sum. The inflow into the reser-

voir was set to $Q_{in} = 1.2 \text{ m}^3/\text{s}$ following Lövoll (2004). Furthermore, no details about the sub-surface flow and the saturations within the dam are known.

Table 7.5: Grain classes and properties of the dam material applied in the model.

grain 1	grain 2	grain 3	porosity	grain density	γ_{wet}	γ_{coh}	γ_{dep}
0.3 mm	2.4 mm	15 mm	[-]	[kg/m ³]	[°]	[°]	[°]
28.0 %	32.0 %	40.0 %	0.224	2773	42	38	15

7.4.2 Numerical set-up

The upstream reservoir, the embankment and the downstream river were discretized with an unstructured mesh consisting of $\sim 4,000$ triangles which is illustrated in Figure 7.12. The mesh was locally refined at the dam location and at the pilot channel. Three grain classes were applied to represent the grain composition of the dam material as given in Table 7.5.

The wetted failure angle γ_{wet} was set to the angle of repose $\gamma_{rep} = 42^\circ$ given in the references. The deposition angle was set to $\gamma_{dep} = 15^\circ$ as for the laboratory spatial breach. Steep side walls were reported at the end of the breach what was considered by setting $\gamma_{coh} = 38^\circ$, allowing for maximum side wall angles of 80° .

The reservoir water-level was set to the crest height of the dam and an external source was used to represent the inflow Q_{in} into the reservoir from the Røssvassdammen Dam. As outflow boundary condition a weir was placed downstream of the dam where the breach discharge was measured. The friction coefficient was determined dynamically based on the d_{90} diameter of the varying grain compositions as $k_{str} = \varphi/d_{90}^{1/6}$, whereas $\varphi = 15$ was calibrated in a way that a friction coefficient of $k_{str} \approx 25 \text{ m}^{1/3}/\text{s}$ resulted for the initial grain composition¹. The CFL -number in the simulation was set to 1.0 leading to time step sizes of $\Delta t \approx 0.02 \text{ s}$.

¹In river flows typically larger $\varphi \approx 21 - 26$ are chosen, which correspond to less friction. The larger calibrated friction losses in this work may indicate the increased friction losses due to water-sediment interactions and turbulent losses.

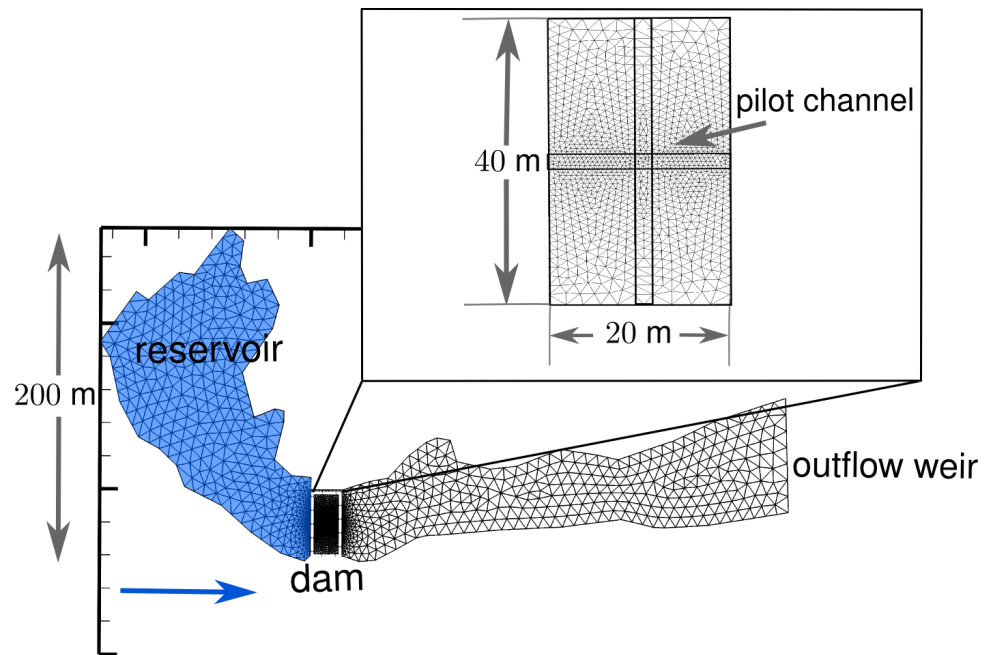


Figure 7.12: Unstructured mesh representing reservoir, dam and downstream river with close-up of the mesh refinement at the dam. The arrow indicates the flow direction.

The surface erosion was modelled with the modified-MPM formula, which was adapted to fractional transport using a hiding and exposure-function as outlined in chapter 3.3.1. In addition, suspended-load transport was activated and applied for all grain classes².

Table 7.6: Parameters applied for sub-surface flow modelling at field-scale dam.

θ_R [-]	θ_S [-]	k_f [m/s]	α [1/m]	n_V [-]	h_s [m]	q_{inf} [mm/h]	Δx [m]	Δt [s]
0.01	0.224	$1E - 5$	6	1.9	-0.01	4	0.2	5.0

The sub-surface flow was simulated under the assumption that the reservoir water-level was filled to the dam crest and the water infiltrated into the upstream slope over a time period of 8 h. The hydraulic conductivity, the water contents and the VGM soil parameters were estimated

²Differing from the above mentioned situation at laboratory-scale, the assumption of an equilibrium concentration profile over the water depth is less problematic at field-scale due to the larger cell sizes and flow turbidities.

based on the grain composition and are listed in Table 7.6. The obtained solution, which had not yet reached steady-state conditions, was then set as initial condition and is illustrated in Figure 7.13 (a) in terms of the water saturation.

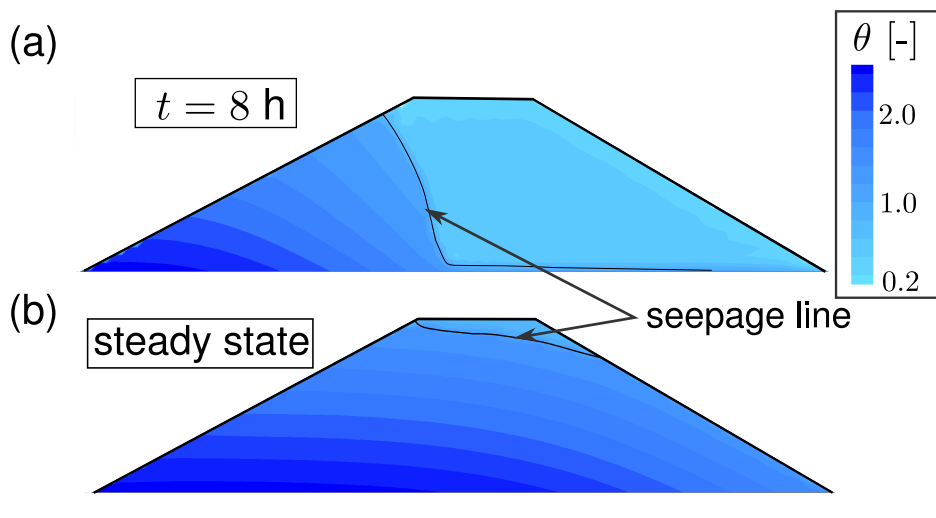


Figure 7.13: Saturation distributions within dam body with indicated seepage line (a) after 8 h and (b) at steady-state conditions.

7.4.3 Qualitative and quantitative results

An erosion channel developed at the downstream dam slope and enlarged over time.

The upstream crest was lowered causing the discharge to increase rapidly and leading to an abrupt dropping of the reservoir water-level. Analogous to the laboratory spatial breach, the distinct breach phases were observed and the hour-glass shaped inlet fan was formed. The combined model was thereby stable throughout time.

The reports of Lövoll (2004), however, also indicate the occurrence of cohesive effects which the model cannot reproduce adequately. Head-cut migration took place and undercutting was reported which formed overhanging breach side walls.

The measured breach outflow and the final breach width can be used

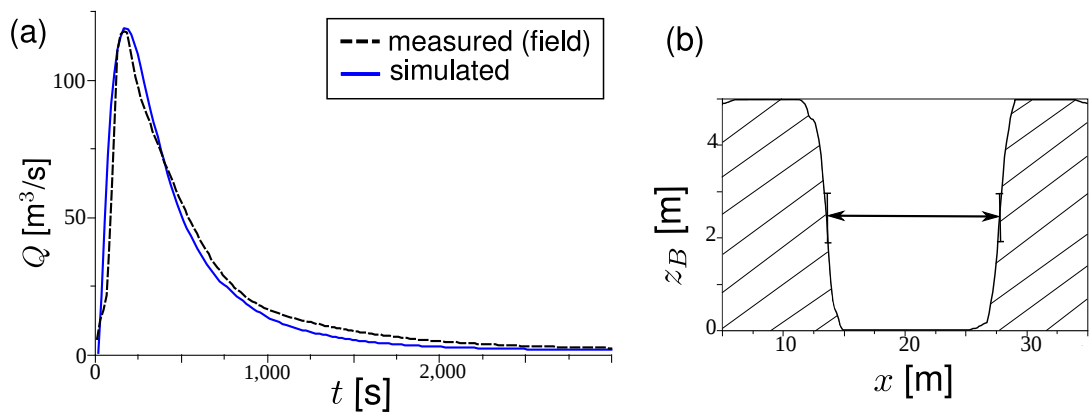


Figure 7.14: (a) Comparison of simulated (solid) and measured (dashed) breach outflow hydrographs. (b) Simulated final breach cross section.

for comparison with the numerical results as illustrated in Figure 7.14. The time needed until the breaching started is not compared here, due to the uncertainties and difficulties concerning the reservoir water-level and the cohesive effects, which strongly influence breach initiation. The final breach width of ~ 12 m in the simulation is in satisfying agreement with the reported width of ~ 10 m. Furthermore, the breach outflow hydrograph and the peak discharge are in accordance with the measured values for this model set-up and demonstrate the model applicability to field-scale scenarios. Absolute and area specific sediment mass errors again confirmed the sediment mass continuity.

7.4.4 Sensitivity analysis

Several model settings, which could not be investigated with the laboratory tests outlined above, were additionally investigated regarding their model sensitivity.

Transport mechanisms of surface erosion

Breach models often differ in the type of transport mechanism which is focused. Some models are limited solely to bed-load transport, whereas others regard suspended-load transport only. Others again, as the presented model, consider both transport mechanisms in combination.

To find out whether one of these mechanisms is dominant, the test was modelled with de-activated suspended-load as well as with de-activated bed-load transport. The obtained results are illustrated in the left part of Figure 7.15 and are compared with the result of the combined approach.

The results show distinct deviations in both model runs from the combined approach. The breach discharges and the embankment erosion are underestimated in both cases. Furthermore, the test with activated suspended-load had a much longer breach initiation phase compared to the test with activated bed-load ($\Delta t_{susp} \gg \Delta t_{bed}$). This indicates that during breach initiation under small water depths the bed-load transport is dominant and has to be considered, whereas at the later breach phases both transport mechanisms may be effective to a similar extent.

In the author's opinion, these results call into doubt especially the restriction to solely suspended-load transport for embankment breaches. This can underestimate, in particular, the embankment erosion at breach initiation and at scenarios involving wide-ranging grain compositions with coarse grains. It is therefore recommended to activate both transport mechanisms for such field-scale scenarios.

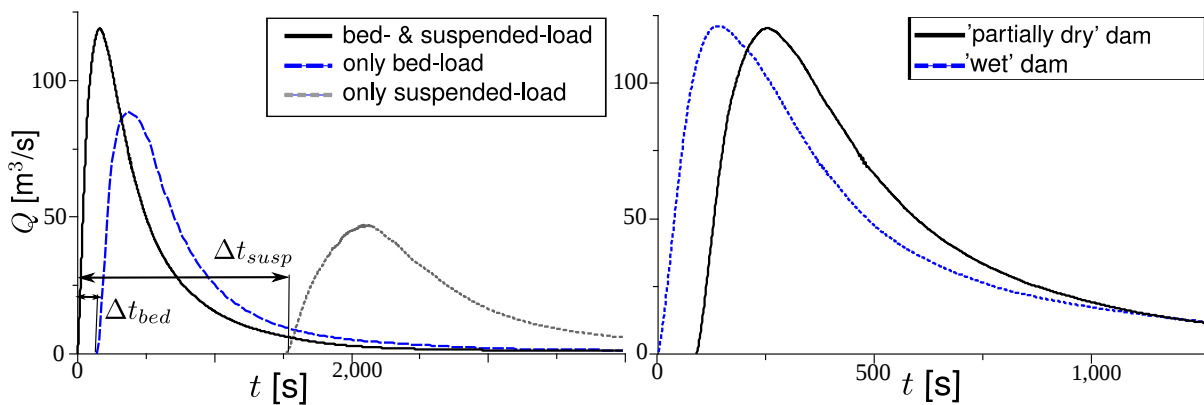


Figure 7.15: *Left: comparison of breach discharges obtained using different transport mechanisms. Right: comparison of breach discharges for different saturation conditions.*

Influence of water saturations

To qualitatively examine the influence of the water saturations and pore-water pressures on the breach formation, an additional scenario was investigated. Steady-state seepage ('wet condition') was established within the dam body where the seepage line reached the downstream dam face and large parts of the dam were fully-saturated as shown in Figure 7.13 (b).

The simulated breach hydrograph is shown in the right part of Figure 7.15 and is compared with that of the original scenario ('partially-dry condition'). It can be seen that under wet conditions the dam failed more rapidly. The high water saturations of the material reduced the apparent cohesion and subsequently increased the surface erosion, speeding-up the breach formation. Furthermore, the side wall angles are much smaller at wet conditions than at partially-dry conditions, what leads to the formation of different breach shapes.

Despite these differences, however, the resulting breach hydrographs had similar shapes and peak discharges. These observations of a more rapid breach formation in combination with similar breach hydrographs thereby qualitatively fit those of Al-Riffai and Nistor (2010) in their experimental investigations. Further investigations and quantitative comparisons should be made to clarify these aspects.

Influence of grain classes and control volume thickness

The dam material has to be represented with a discrete number of grain classes n_g in the model. The selection criteria for n_g hereby are not clearly defined and conflicts may arise between accuracy and computational expense. Hence, the model sensitivity was investigated regarding this aspect. The original set-up represents the material with three grain classes as stated above. Additional simulations were made using a single grain class with $d_m = 5$ mm and using a total of six grain classes listed in Table 7.7.

The computed breach discharges are shown in the left part of Figure 7.16. Regarding the simulations with three and six grain classes, only minor deviations occurred. This result is in agreement with the before-mentioned statement that the overtopping flow often strongly exceeds the critical shear stresses, even for the largest grain sizes. The usage of a single grain class, however, led to a more rapid breach formation here. This result is attributed to the lack of the coarse grains and the fine grains with apparent cohesion, which can slow down the breach initiation.

Table 7.7: Grain classes used for the representation of the embankment material composition.

grain 1	grain 2	grain 3	grain 4	grain 5	grain 6
0.18 mm	0.60 mm	1.80 mm	3.50 mm	10.00 mm	35.00 mm
10.0 %	10.0 %	15.0 %	20.0 %	25.0 %	20.0 %

It is thus recommended to use multiple grain classes and fractional transport for the representation of wide-ranging grain compositions. To reduce computational costs, the number of grain classes should be increased until only minor deviations occur.

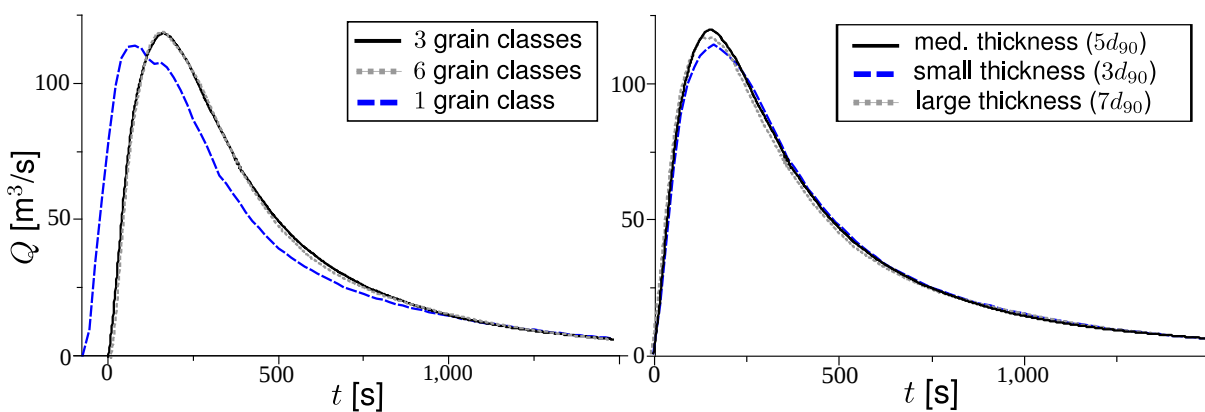


Figure 7.16: Left: comparison of breach discharges for different numbers of grain classes n_g . Right: comparison of breach discharges for different control volume thicknesses h_{cv} .

Another simulation parameter for fractional transport is the thickness of the bed-load control volume h_{cv} (see Figure 3.6). The sensitivity of this

parameter was investigated by varying it as $3d_{90}$, $5d_{90}$, $7d_{90}$. The obtained results are shown in the right part of Figure 7.16, whereas the model did not react sensitively to these variations.

7.5 Natural moraine embankment breach

7.5.1 Site conditions and field investigations

In May 2009 a naturally formed moraine embankment failed in a mountainous region in the Patagonian Andes in southern Argentina. The moraine embankment was formed by the Ventisquero Negro glacier which is situated at the Rio Manso valley. Due to continuous glacier retreat in the last decades, it continuously lost volume and size and left behind a glacial lake impounded by its moraine embankment. The embankment failed after long-during rainfall and produced a Glacial Lake Outburst Flood (GLOF) into the downstream situated areas. This GLOF was accompanied by large sediment movements and destructions of infrastructure and tourist facilities. The event took place at night in a rarely populated region and, hence, only few observations were reported.

Worni *et al.* (2012) analysed this natural hazard event and made analyses of aerial photos and field investigations of the local site conditions. In addition, simulations were made in co-operation using the breach model presented in this work. This test case essentially aims at qualitative comparisons with the field measurements and investigates the model applicability to natural hazard events. The use of unstructured meshes is advantageous for such scenarios, due to its flexible representation of the irregular geometries and the strongly varying topography. The following notes summarize the main characteristics of the breach event.

- Pictures A, B, C in Figure 7.17 illustrate the dimensions of the glacial lake and the extensions of the spatial breach after failure. A large breach channel developed at the lake outlet and enlarged progressively over time. Field investigations indicate that the nar-

rowest section of the final breach is located at its upstream end and widens in downstream direction to a width of ~ 70 m. The breach had a total length of ~ 350 m and was eroded vertically up to ~ 50 m. The lake water-level dropped about 27 m in height and the total released water volume was reconstructed to $\sim 10^7$ m³ based on the lake bathymetry.

- Further downstream the sediment-laden flow entered a wide floodplain where large amounts of the sediment masses were deposited as depicted in pictures D and E. In the upper areas larger sediment grain sizes were deposited first, whereas the finer grains deposited further downstream leading to a gradation of the grain mixtures. The investigations of the sediment depositions also indicated that hyper-concentrated flow probably took place during the breach event.
- The flood propagation led to downstream inundations, thereby destroying parts of the forests and roads as indicated in picture F. According to reports of eye-witnesses the flood event had a duration of several hours, whereas no detailed information about flood extent and discharges could be reconstructed.

Worni *et al.* (2012) deduced multiple possible failure mechanisms which may have caused the breach event. The rising lake water-level could have led to an increase of the lake outflow, triggering the embankment breach due to progressive erosion. This process could have been supported by floating ice blocks in the lake, temporarily blocking the lake outlet and leading to an initial wave formation after their sudden removal. Another scenario bases on the assumption that parts of the embankment consisted of ice blocks forming an inner ice core. The rising water-level increased the hydrostatic pressure on this ice core, which finally could have been destabilized causing an abrupt failure of parts of the moraine embankment.

Here, the assumption is made that the first scenario took place and a progressive breach formation developed. The breach was initiated in the

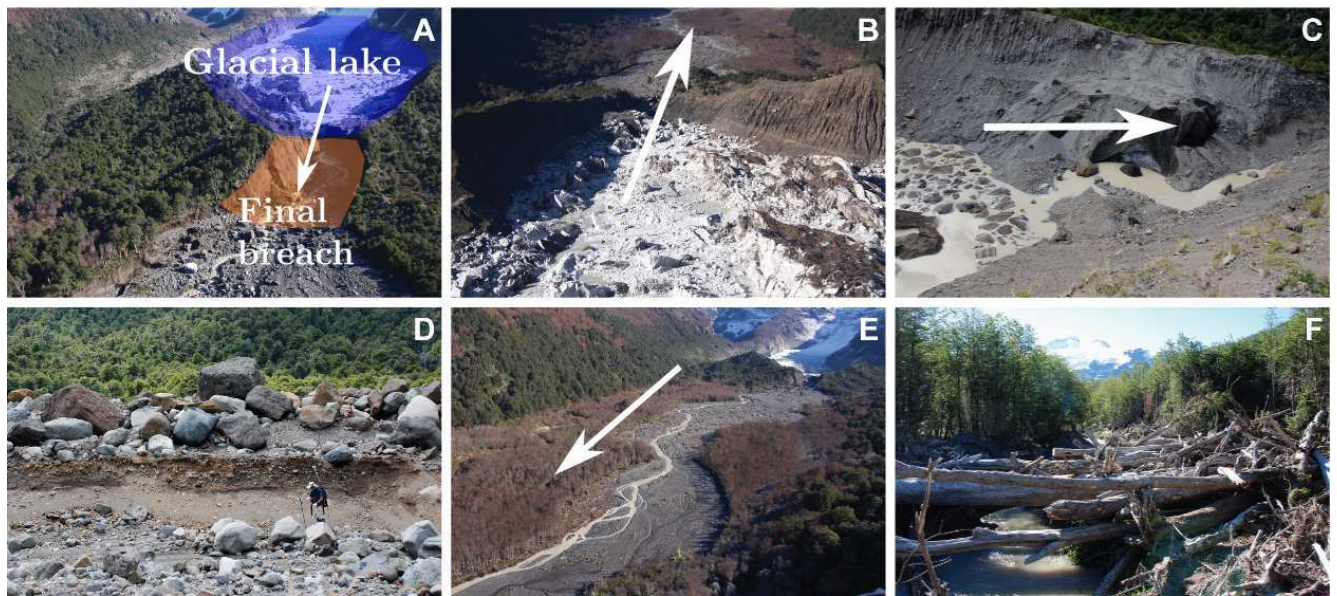


Figure 7.17: Illustrations of glacial lake and final breach shape extensions and outburst flood impacts after Worni et al. (2012).

model by raising the lake water-level to two meters above the lake outlet bottom.

7.5.2 Numerical model set-up

The site geometry was discretized with an unstructured mesh of $\sim 30,000$ triangular cells. The mesh is shown in Figure 7.18 and was adapted to the lake geometry and the natural embankment structure. It was locally densified at the moraine embankment, whereas the lake and the downstream floodplain were discretized coarsely. The model topography was based on a 30 year old digital elevation model which is supposed to be a valid representation for the situation before the breach. The extent of the glacial lake was estimated based on recent aerial photos to account for the glacier retreat during the last decades. As outflow boundary at the downstream floodplain a zero-gradient outflow condition was set, assuming no velocity gradients at the outlet.

The moraine embankment is composed of unconsolidated alluvial material. It consists of coarse blocks and boulders embedded in a matrix of sand and gravel and was represented in the model with six grain classes

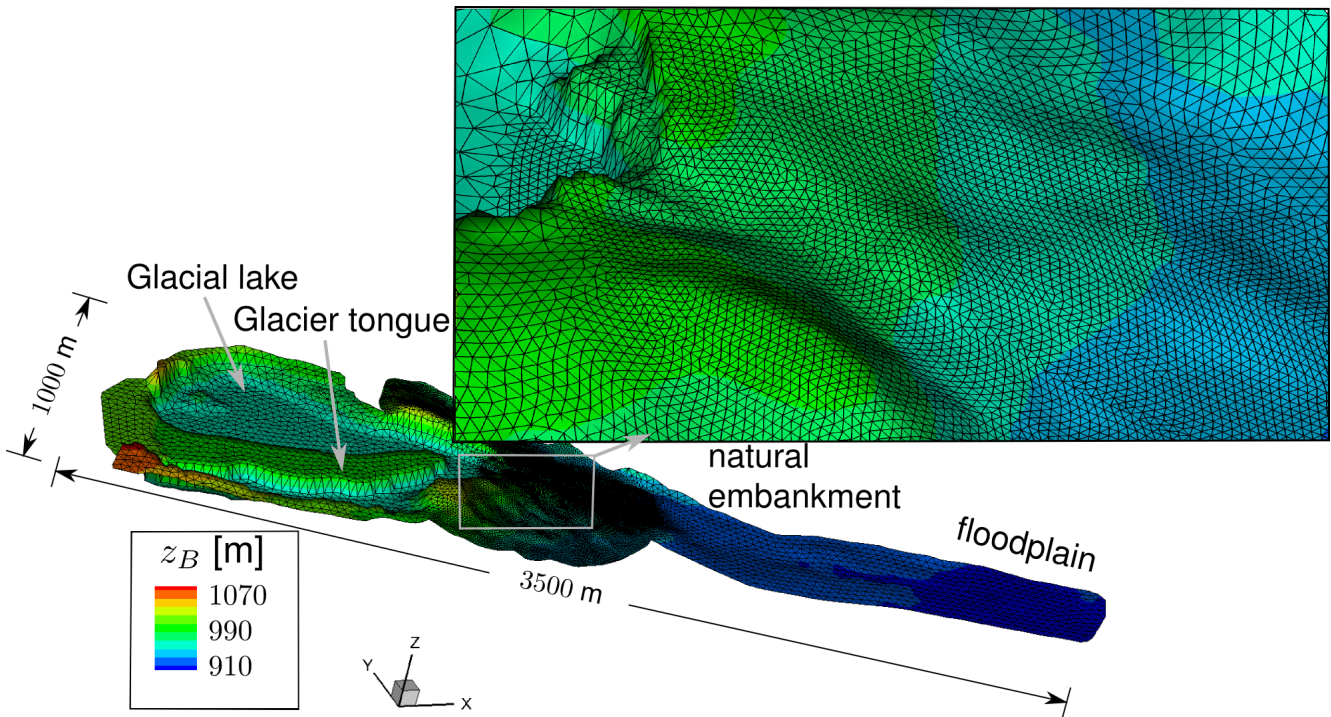


Figure 7.18: *Unstructured mesh of the local site with close-up of the moraine embankment.*

listed in Table 7.8. The modified-MPM bed-load transport formula was applied in combination with suspended-load for fractional transport. The friction coefficient was determined dynamically from the grain compositions using the same approach as outlined above for the field-scale dam breach in section 7.4.2. The CFL -number was set to 1.0 resulting in time step sizes of $\Delta t \approx 0.1$ s.

Table 7.8: *Properties of moraine embankment material and grain classes applied in the model.*

grain 1	grain 2	grain 3	grain 4	grain 5	grain 6	porosity	grain dens.[kg/m ³]
1.0 mm	8.0 mm	22.0 mm	64.0 mm	128.0 mm	180.0 mm	[-]	
11.0 %	17.0 %	24.0 %	24.0 %	14.0 %	10.0 %	0.15	2650

The critical failure angles for the slope failure modelling were assessed based on the field observations. Figure 7.19 depicts two characteristic breach side wall sections. The wetted failure angle was estimated

to $\gamma_{wet} = 40^\circ$ corresponding to the observed angles in the lower parts of the side walls. The steep slopes in the upper parts were accounted for by setting $\gamma_{coh} = 40^\circ$, leading to maximum angles of $\gamma_{dry} = 80^\circ$. The deposition failure angle was set to $\gamma_{dep} = 15^\circ$ as in the model tests presented above.



Figure 7.19: Measured side wall angles in lower and upper breach sections.

The variably saturated sub-surface flow was modelled within the moraine embankment using a 3D lattice consisting of a total of $\sim 1,500,000$ cells with the size of $\Delta x = 1.6$ m. Steady-state conditions were computed with a constant lake water-level equal to the lake outlet height. The lake thereby infiltrated into the upstream parts of the embankment and the water ex-filtrated at its downstream toe. Further, additional external sources were placed over the entire mesh to represent the rainfall event with $q_{inf} \approx 1$ mm/h (Worni *et al.* (2012)). The VGM model was applied and the overall model parameters are listed in Table 7.9.

Table 7.9: Parameters applied for sub-surface flow modelling at natural moraine embankment.

θ_R [-]	θ_S [-]	k_f [m/s]	α [1/m]	n_V [-]	h_s [m]	Δx [m]	Δt [s]
0.01	0.15	$1E-6$	6	1.9	-0.01	1.6	50

7.5.3 Simulation results

A similar breach formation was observed as outlined in the tests before. The outflowing water accelerated at the steepest moraine embankment section, situated about 150 m below the lake outlet. The accelerating flow eroded a breach channel and thereby steepened the slope. This erosion front moved backwards to the lake outlet as indicated in Figure 7.20 (a).

As soon as the breach channel reached the lake outlet after about one hour, the discharge increased rapidly, leading to an increase in surface erosion and a lowering lake water-level. This situation is illustrated in Figure 7.20 (b).

After about three hours, the outflow ceased due to the rapid lowering of the lake water-level in a way that the sediment transport and the breach advance came to an end. The transported masses directly deposited in the downstream floodplain. The final breach geometry can be seen in Figure 7.20 (c) and has similar extents compared to the field measurements. The measurements suggest, however, a slightly curved breach channel, whereas the simulated final breach channel had a straight course. This breach channel curvature was only observed during the first breach stages, instead (Figure 7.20 b).

The final erosion depths along the breach channel are compared with field measurements in the left part of Figure 7.21. The erosion depths thereby show a satisfying accordance with some larger deviations directly at the lake outlet. These deviations may be attributed to the possible presence of inner ice blocks in the moraine embankment according to Worni *et al.* (2012). The material deposition led to a gradation of the material as expected. The simulated deposition heights showed deviations from the measurements and were generally shifted in downstream direction. A possible cause for these differences may be the underestimation of the presence of large boulders in the embankment material composition, which are not transported further downstream by the flow powers.

The obtained hydrograph is illustrated in the right part of Figure 7.21 with a peak discharge of $\sim 7700 \text{ m}^3/\text{s}$. The breach discharge led to wide

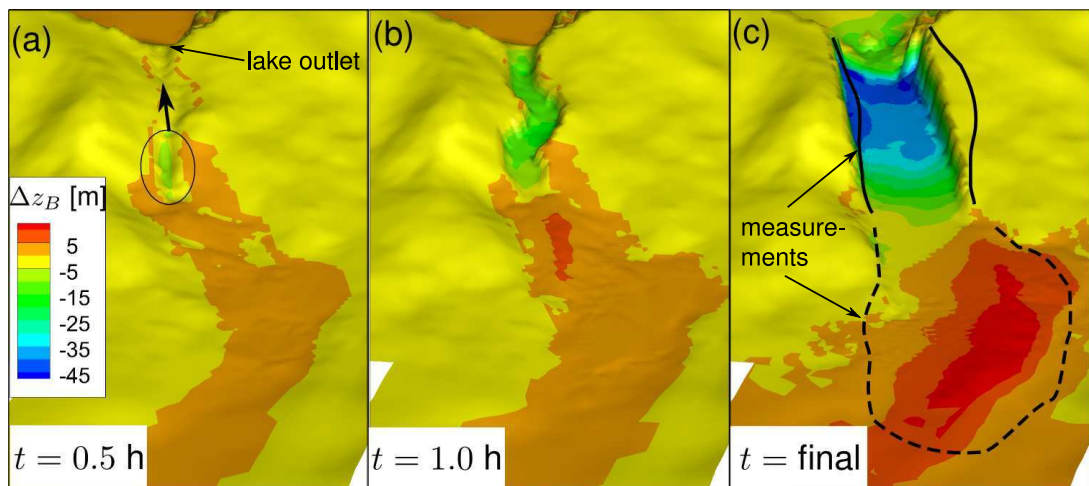


Figure 7.20: *Temporal advance of moraine embankment breach. (a) Breach initiation and backward travelling erosion front. (b) Curved breach channel lowering the lake outlet. (c) Final breach geometry with spatial extents of measured bed erosion (solid) and aggradation (dashed).*

inundations in the downstream areas as reported by eye-witnesses.

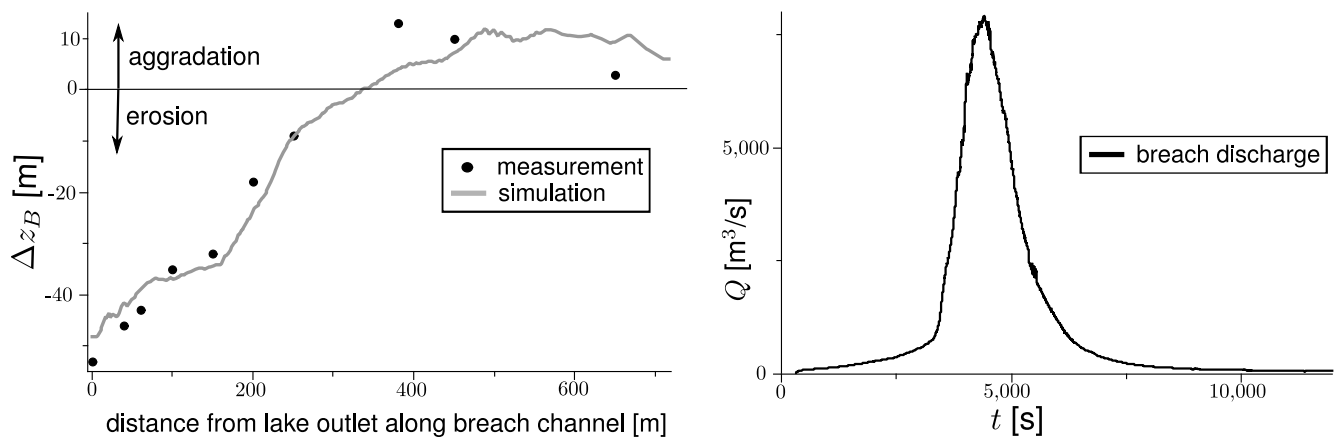


Figure 7.21: *Left: comparison of simulated (line) and measured (points) erosion depths and aggradation heights. Right: simulated breach outflow hydrograph.*

Conclusively, the combined model was stable during the simulation and provided useful results for the analyses of a complex natural hazard event of large extents. Despite the large amounts of moved sediment masses, mass continuity was satisfied using the dual-mesh approach.

7.6 Summary

The model was applied to breach scenarios with increasing complexity to investigate and validate the model components and to demonstrate its practical applicability.

At first, the model was applied to an idealized plane dyke breach at laboratory-scale. The test allows for investigations of the purely vertical erosion without side wall failures. The results are in good accordance with the laboratory measurements. Empirical transport formulas can basically reproduce the progressive erosion, despite the violation of several underlying assumptions. The best fit to the measured data was obtained with the modified-MPM transport formula.

The model was then applied to another laboratory study regarding a spatial dyke breach. In previous numerical investigations mainly integral breach parameters were compared, which are limited meaningful and do not allow for reliable validations of the side-wall failure modelling. Therefore comparisons with the measured 3D breach formation were made and basically confirmed the applicability of the geometrical approach if three adequate failure angles are applied.

The third test concerned a field-scale dam in Norway, consisting of a wide-ranging grain composition, which was overtopped in a controlled experiment. The model was able to basically reproduce the outflow hydrograph and the final breach width. The influence of the sub-surface flow on the breach advance was qualitatively investigated and indicates that higher water saturations accelerate the breach initiation but may lead to peak discharges of similar extent. Furthermore, the conclusion is drawn that both transport mechanisms, i.e. bed- and suspended-load, should be considered in cases of wide-ranging grain compositions at field-scale. Reported cohesive effects during breaching could not be captured and demonstrate the model limitations.

Finally, the failure of a natural moraine embankment of large extents and complex geometry was simulated. The breach event took place in a mountainous region and field investigations provide the opportunity for model comparisons. The test demonstrates the advantages of

unstructured meshes which can be adapted to irregular geometries and locally refined. The model reproduced the basic erosion characteristics and breach formation, but deviations were observed for the material depositions.

All simulations and sub-models proved to be stable and robust without numerical instabilities. The shock-capturing hydrodynamic modelling successfully handles the transitions from sub- to super-critical flow conditions as well as the wetting and drying of cells. Similar, the side wall failure modelling did not cause instabilities, despite the discontinuous mass movements. The sub-surface flow model also demonstrated its suitability for practical scenarios. As a consequence, the combined model can serve as useful and practical tool for analyses of embankment breaches, under regard of the mentioned limitations and the general need for calibration.

sensitivity →

computational expense ↓	dry angle γ_{dry}^{**} (chapter 8.3.5)	Shields-parameter Θ_{crit}^* (chapter 8.2.4)	material porosity p (chapter 8.2.4)
	control volume thickness h_{cv}^1 (chapter 8.4.4)	friction coefficient k_{str} (chapter 8.2.4)	pre-factor transport formula (linear variation)
	settling velocity w_S^2	deposition angle γ_{dep}^* (chapter 8.3.5)	
		wet angle γ_{wet}	
		reference concentration height z_R^2	
	turbulence modelling (chapter 3.3.3)	nr grain classes n_g^{*1} (chapter 8.4.4)	bed-load (chapters 8.2.4 & 8.4.4)
		seepage/apparent cohesion (chapter 8.4.4)	suspended-load (chapter 8.4.4)
	semi-coupling (Appendix E)		

* sensitivity for breach initiation
** sensitivity for later breach phases

¹ fractional transport
² suspended-load transport

Figure 7.22: Matrix representation of parameter sensitivity in dependence of the computational expense.

The model sensitivity to different parameters and settings was additionally examined by varying them within reasonable ranges in the tests. Results and conclusions for various model parameters and settings are qualitatively summarized in Figure 7.22 in dependence of their associated computational expense. It is emphasized, however, that these assessments are of qualitative nature and may differ depending on the investigated scenario and result in mutual side-effects which were not investigated.

Generally, a distinction can be drawn between the breach initiation and the later breach phases. The initiation determines whether and how fast the breach forms and is difficult to assess and sensitive to small variations in the model parameters. The later breach phases, in contrast, are less sensitive to parameter variations and largely determine the shape of the outflow hydrograph and the peak discharge.

8

Summary and Outlook

8.1 Summary

A numerical breach model was developed for progressive embankment breaches due to overtopping flow. It aims at homogeneous earth embankment structures consisting mainly of non-cohesive material. Multiple physical processes were identified as relevant for the breach formation and are numerically modelled with a coupled approach: the overtopping flow, the embankment surface erosion, side wall failures and the sub-surface flow through the embankment.

The developed breach model is based on the software *BASEMENT*. The software was further development and improvements were incorporated for breach modelling which consider additional aspects compared to previous investigations. Further objectives of this work were the investigation and validation of the model components with test applications and to provide a simulation tool suitable for engineering practice. Major aspects and conclusions regarding breach modelling and the practical model applicability are summarized below.

Model aspects

The 2D Shallow-Water equations are solved to describe embankment overtopping using a shock-capturing Godunov-type approach. The induced surface erosion is modelled with 2D sediment continuity and advection-diffusion equations in combination with empirical formulas for sediment transport. The latter were adapted to embankment breach conditions by modifying the Shields-parameter for steep slopes and apparent cohesion effects.

Differing from most previous models, unstructured meshes with triangular and quadrilateral cells are applied to discretize the site geometry. These allow for flexible adaptations to geometrical structures like embankments, reservoirs and downstream flooding sites. They also ease local mesh refinements around the initial breach location, which was identified as a pre-requisite for accurate side wall failure modelling. Further, a second-order accurate spatial discretization is used for the hydrodynamical modelling, allowing for accurate representations of strongly uneven terrains. The arising problems, as the violation of sediment mass continuity, were overcome by the introduction of a dual-mesh discretization with an additional computational mesh for sediment transport.

Side-wall failures and subsequent mass movements are modelled with a geometrical approach based on critical failure angles. A novel failure algorithm was developed and validated which is specially adapted to unstructured meshes and the dual-mesh approach. It applies three different failure angles and was enhanced compared to previous approaches by considering the apparent cohesion in a heuristic manner. A correlation was assumed hereby between the forming side wall angles and the theoretical soil shear strength as a function of the water saturations and pore-water pressures.

In previous models mainly integral parameters, like the breach outflow, were used for comparison with measurements. These are, however, insufficient for a meaningful validation of the side wall failure modelling. To improve this situation, successful comparisons were made against a measured 3D breach formation.

A sub-surface flow model for variably-saturated flow in earth embankments was developed and integrated into the breach model. It bases on a recent numerical solution of the 3D Richards equation using the Lattice-Boltzmann method on a structured 3D lattice. The model was validated against tests involving water infiltration and seepage flow through homogeneous and heterogeneous embankments. It computes the saturations and pore-water pressures within the embankment, which are needed to assess effects of apparent cohesion for the embankment erosion. A coupling algorithm was developed for the dynamical setting of

boundary conditions and lattice adaptations during breaching. As side-effect, the successful model tests also demonstrated the suitability of this recent numerical solution approach for realistic engineering scenarios, whereas previous investigations only concerned idealized tests with simple geometries.

Most previous breach models considered only homogeneous embankments with a single grain diameter and focused either on bed- or suspended-load transport. The presented model, instead, considers both transport mechanisms and fractional transport of multiple grain classes. This allows for investigations of heterogeneous, composite embankments. Further, it is seen advantageous regarding the different transport mechanisms occurring at breach initiation and later breach phases and at scenarios with wide-ranging grain compositions, where some particles are transported as bed- and others as suspended-load.

Application aspects

Academic software is often difficult to use and not flexible enough for requirements in practice. To at least partially overcome this limitation, all sub-models and algorithms were integrated into the software *BASEMENT*, providing a graphical user interface, consistent data input structure and a high level of parametrization. It further eases model coupling and allows for efficient data exchange between the sub-models. Further, the involved sub-models do not differ crucially in their performance and allow for efficient combined simulations. Parallel computation on shared-memory architectures was thereby provided to exploit the powers of present computational hardware.

The breach model was successfully tested against measurements of two laboratory embankment breach studies. It was additionally applied to two field-scale scenarios including a naturally formed moraine embankment in a mountainous area of large extents. Although these field-scale tests only allow for qualitative comparisons, they demonstrate the robustness and suitability of the numerical schemes and techniques for natural hazard events.

Multiple physical processes are involved at embankment breaches, which are modelled with different approaches relying on empirical or semi-empirical parameters. It is generally difficult to judge a-priori how sensitive the model will react to their variations and therefore some sensitivity analyses were made. Although the results must be taken with caution due to the largely differing types and characteristics of embankments, they shall provide some insights and guidance for the model set-up.

8.2 Outlook

Subsequent research and model improvements may include more physically-based representations of the breach processes with fewer simplifications, enhancements of the numerical schemes and additional tests cases.

A main problem for current breach models is the large uncertainty involved in the empirical closures for surface erosion modelling. To improve this situation, new transport or entrainment formulas may be derived, which are particularly suited for the conditions at embankment breaches, including effects of material compaction. Beside the surface erosion, the modelling of side-wall failures with the geometrical approach relies on severe simplifications and is seen as a major short-coming of the present model. Improvements should be made which do not rely on the assumption of instantaneous adaptations of the side wall slopes to critical values and allowing for more spatially extended considerations. Equilibrium-limit methods are alternative approaches, whereas their adaptation to unstructured meshes and the 3D breach formation is unclear and requires future investigations. More general approaches are 3D geotechnical continuum models, which have the drawbacks of high complexity and large computational expense.

Especially during the breach initiation phase, the numerical model has to cope with water flow and sediment transport on typically rather steep embankment slopes. The applied hydraulic and sediment transport modelling, however, mostly assume small bed slopes in their simplifying as-

sumptions or empirical derivations. Model improvements should be made to enhance the validity and performance of the model for steep slope conditions.

Other fields for model enhancements are the underlying governing equations for water flow and sediment transport. More generalized formulations could be applied to account for effects of the water-sediment interactions. The use of non-equilibrium transport approaches is also supposed to improve the surface erosion modelling. This aspect is of special relevance for the encountered problems with suspended-load transport at laboratory-scale, where the assumption of immediate formation of equilibrium concentration profiles seems inappropriate. Future research is also needed for the modelling of the complex effects of apparent cohesion on the surface erosion.

Various numerical schemes are used in this work which all have potential for future improvements. Mainly first-order accurate schemes are used which could be extended to higher-orders. However, this is of questionable benefit regarding the large uncertainties in the empirical closures and the associated increased computational efforts. An alternative to the classical continuum approaches could also be the simulation of 3D surface and sub-surface flows, and perhaps the mass sliding after slope failures, using the Lattice-Boltzmann method within a unified framework on a single mesh. The method seems promising for such tasks due to its simplicity and extendibility to different physical flow processes.

Additional breaching tests should be made to further investigate the breach model and its components. Especially the effects of material compaction and apparent cohesion should be investigated in more detail with quantitative comparisons. The initiation of additional experimental studies would be helpful in this respect to provide more data for reliable model validation, including embankments with different degrees of saturations.

The model in its present form enables the representation of heterogeneous embankments with zones of different material compositions. No tests were made, however, regarding these aspects and there is a general lack of such investigations. Similarly, the effects of surface protections for embankment slopes were not investigated despite their practical rele-

vance. Further problems hereby are the scarcity of available data measurements for comparison and the more complex geotechnical considerations involved. From the user perspective, additional pre-processing tools need to be developed to ease the model set-up for heterogeneous embankments.

Finally, it has to be noted that embankments built of cohesive material are of utter importance, especially regarding river and coastal dykes. Failures of cohesive embankments are even more complex than those involving non-cohesive material. Future efforts and research will have to be directed to investigate these processes and to develop suitable numerical models. The investigations of non-cohesive embankment breaches thereby can be a preliminary step in this direction to provide a better process understanding and insights in the involved numerical challenges.

A

Numerical Solution of Overtopping Flow

The solution of the Shallow-Water equations using the FV method is performed in two main steps:

1. The volume integrals are transferred into surface integrals for the flux calculation using the Gauss-theorem. Then, the fluxes at the cell edges need to be determined, and
2. These in- and outgoing edge fluxes are balanced over each cell and used in combination with the source terms to update the solution of the conserved variables.

The fluxes F, G over the edges between adjacent cells need to be evaluated for the first step. Much research was directed to shock-capturing solution schemes for the hyperbolic SWE in the past and a variety of solution techniques were developed and are a pre-requisite for stable and robust breach models. Godunov-type approaches (Godunov (1959)) were adapted and transferred from the Euler equations to the SWE to cope with these difficulties. The fluxes are determined by formulating a local 'Riemann problem', which corresponds to a 1D dam-break problem at the edge interface between two cells $(i, i+1)$ with the variables U_i as sketched in the right part of Figure A.1. This 1D local Riemann problem is solved at each cell edge for each time step. An exact Riemann solver is applied for its solution following Toro (2001), which has good accuracy and stability properties in comparison with other shock-capturing schemes according to Zoppou and Roberts (2003).

At the second step, the computed edge fluxes are summed up for each cell to update the conserved variables \mathbf{U} . Applying the explicit Euler time integration and an operator-splitting scheme, the conserved variables of cell i at the new time level $n + 1$ are obtained from values at the present time level n as

$$\frac{\mathbf{U}_i^{n+1} - \mathbf{U}_i^n}{\Delta t} + \frac{1}{A_{hyd,i}} \sum_{j=1}^{n_E} (\mathbf{F}, \mathbf{G})_{i,j}^n \cdot \vec{n}_j l_j = \mathbf{S}_i, \quad (\text{A.1})$$

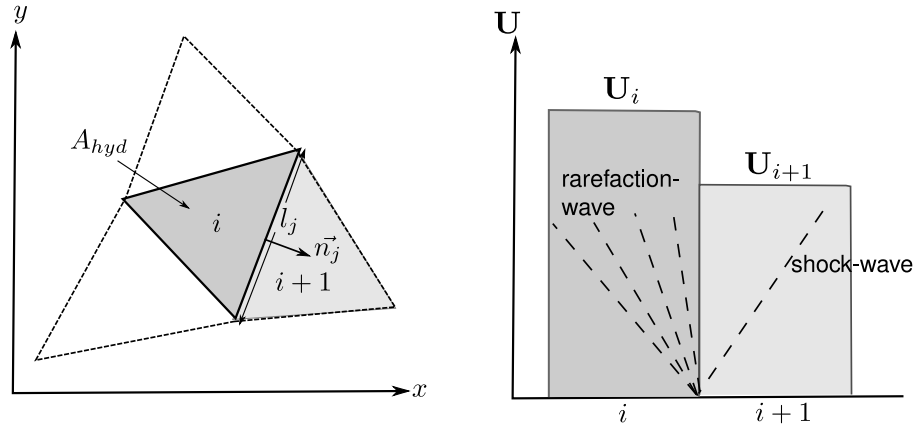


Figure A.1: *Left: configuration sketch for flux computation at edge j between cells i and $i + 1$. Right: formulation of local Riemann problem at edge j with initial state (solid) and emerging wave patterns (dashed).*

with edge index j , cell area $A_{hyd,i}$, edge normal vector \vec{n}_j , number of edges n_E and l_j as the edge length as sketched in the left part of Figure A.1. This Godunov-type approach is first-order accurate, whereas extensions to higher-order schemes are possible and are often made in combination with Total Variation Dimishing (TVD)-schemes to prevent numerical oscillations as presented in Toro (2001) or Valiani *et al.* (2002). More details and implementation aspects are outlined in Faeh *et al.* (2012).

To guarantee mass continuity and positive depths in all cells, a correction of the depths and volumetric fluxes is applied in situations where the outgoing fluxes exceed the available water volume of a cell, following Begnudelli and Sanders (2006).

Regarding the modelling of embankment breaches and flood wave propagations, there is need for special treatments of the interfaces between dry cells and wet cells, i.e. cells under water. These moving dry-wet interfaces are often source of instabilities and numerical artefacts, as e.g. reported by Broich (1997) for his breach model. The status whether a cell is wetted or not is determined using a minimum water depth h_{min} as threshold. If the water depth is below this threshold, the cell is considered as dry and wetted otherwise. In addition, situations may occur where cells are only partially wetted, due to the varying bed-levels over the cell. The treatment of such partially wetted cells is often simplified such that only the continuity equation is solved and the momentum equations are neglected. Here, however, the momentum equations are also solved for partially wetted cells following the method of Komaei (2004) and improvements presented in Faeh *et al.* (2012). This procedure has larger computational efforts but can lead to more accurate velocities at dry-wet interfaces. Such accurate velocities are seen advantageous for the surface erosion modelling especially at the narrow breach channel, which may be only few cells wide at breach initiation.

B

Numerical Solution of Surface Erosion

Solution of advection-diffusion equations

The n_g advection diffusion equations 3.5 are integrated over the hydraulic cells following the FV method. They are solved for the concentrations C_g at the new time level $n + 1$ using an explicit Euler time integration. After applying the Gauss-theorem and re-arranging the terms, the discrete form of the equations is obtained as

$$\frac{(C_i h_i)^{n+1} - (C_i h_i)}{\Delta t} + \frac{1}{A_{hyd,i}} \sum_j^{n_g} (\phi_{adv,j} - \phi_{dif,j}) = s_g. \quad (B.1)$$

The advective fluxes $\phi_{adv,j}$ over the cell edges j are computed as products of the specific discharges uh, vh and the cell concentrations C_g using an upwind weighting.

The diffusive fluxes $\phi_{dif,j}$ are computed using the water depths and concentration gradients at each edge. These gradients at the edges are determined as mean value of the gradients at the left and right elements. More information about the implementation, which was not part of this work, is given in Faeh *et al.* (2012).

Solution of sediment continuity equations

The FV method in combination with an explicit Euler time integration is applied for the solution of sediment continuity equations 3.3 and 3.4. The solution is performed in two main steps:

1. Integration of the balance equations over the sediment cells and applying the Gauss-theorem to transform the integrals over the cells into integrals over the edges. A main task is the determination of the bed-load fluxes q_{Bg} at the sediment edges, and
2. Balance of the bed-load fluxes over each sediment cell and evaluation of the source terms s_g , s_{fg} and s_{lg} . These are then used to update the primary variables of sediment transport.

In the first step, the transport capacities $q_{Bg,hyd}$ are determined for each cell of the hydraulic mesh. Empirical bed-load transport formulas are used as described in section 3.3.2. Computing the transport for the hydraulic cells has the main advantage that the required flow variables, like the bottom shear stress, are directly known and must not be interpolated¹. Furthermore, the computations depend on the local bed slope, which is clearly defined within each hydraulic cell by its vertex elevations. The computed transport capacities are hereby assumed to act in direction of the depth-averaged flow velocities.

To determine the sediment flux $q_{Bg,j}$ on a sediment edge j two methods were implemented:

- Projection of the calculated transport rate of the hydraulic cell $\vec{q}_{Bg,hyd}$ onto the normal vector \vec{n}_j of the sediment edge. This is easily possible because each sediment edge lies completely within a hydraulic cell (Figure B.1, left), or
- Determination of an area-weighted, averaged transport capacity $\overline{q}_{Bg,i}$ for each sediment cell i . Then, the flux over the sediment edge is evaluated as linear combination of the transport capacities of the adjacent sediment cells (Figure B.1, right).

Both approaches led to similar results. The latter approach is used herein, because it allows for a simple upstream weighting.

¹In case of fractional transport multiple transport capacities have to be calculated for each hydraulic cell, because different parts of the cell can have different grain compositions.

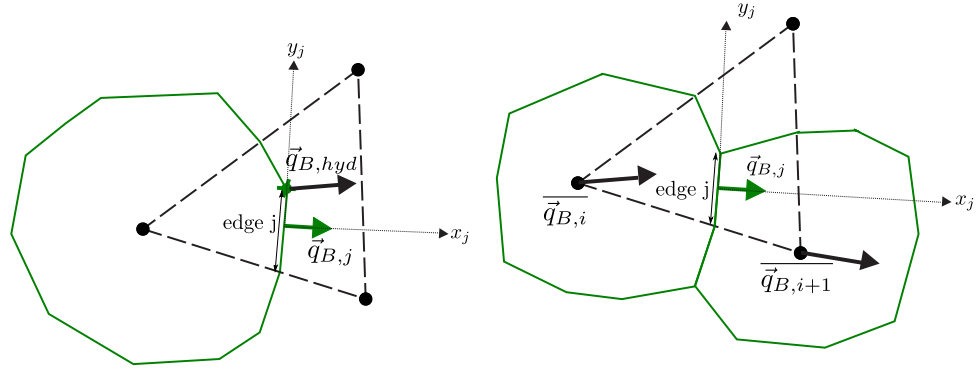


Figure B.1: *Left: projection of transport capacity onto the sediment edge j . Right: determination of transport capacity on sediment edge j from averaged values of the adjacent sediment cells.*

In addition, a flux correction algorithm is applied to consider cases of limited sediment supply due to non-erodible beds, like surface protections or underlying rock (Faeh *et al.* (2012))².

In the second step, the fluxes are balanced over each sediment cell to determine the net sediment in- or outflow and the resulting change in bed-level. The discrete form of the Exner-equation is used to determine the new bed-level z_B^{n+1} and reads

$$(1-p) \frac{z_B^{n+1} - z_B^n}{\Delta t} + \frac{1}{A_{sed}} \sum_{g=1}^{ng} \sum_j [(q_{Bg,x,j}, q_{Bg,y,j}) \cdot \vec{n}_j] l_j = \sum_{g=1}^{ng} (s_{lg} - s_g). \quad (\text{B.2})$$

In a similar way, the sorting equations are formulated in discrete form for each grain class and determine the new grain compositions β_g at the new time level $n+1$ as

$$(1-p) \frac{(h_{cv} \beta_g)^{n+1} - (h_{cv} \beta_g)^n}{\Delta t} + \frac{1}{A_{sed}} \sum_j [(q_{Bg,x}, q_{Bg,y}) \cdot \vec{n}_j] l_j = s_{lg} - s_g + s_{fg}. \quad (\text{B.3})$$

²After this correction step, the bed-load fluxes no longer represent the theoretical transport 'capacity', but the actual bed-load flux.

C

Equilibrium Functions for LBM

The equilibrium functions f^{eq} determine the equilibrium state of the distribution function f and are functions of the macroscopic quantities θ and h_w .

For the θ formulation of the 2D Richard's equation, f^{eq} reads

$$f_q^{eq} = \begin{cases} (1.0 - 5/3c_s^2) \cdot \theta & q = 0 \\ t_q \cdot (\theta c_s^2) & q = 1, 3 \\ t_q \cdot (\theta c_s^2 + I_z \cdot c) & q = 1, 5, 6 \\ t_q \cdot (\theta c_s^2 - I_z \cdot c) & q = 4, 7, 8, \end{cases} \quad (\text{C.1})$$

and in 3D f^{eq} can be formulated as

$$f_q^{eq} = \begin{cases} (1.0 - 7/3c_s^2) \cdot \theta & q = 0 \\ t_q \cdot (\theta c_s^2) & q = 1, 2, 3, 4 \\ t_q \cdot (\theta c_s^2 + I_z \cdot c) & q = 5, 7, 8, 9, 10 \\ t_q \cdot (\theta c_s^2 - I_z \cdot c) & q = 6, 11, 12, 13, 14. \end{cases} \quad (\text{C.2})$$

Accordingly, the equilibrium function for the mixed θ - h_w formulation is given in 2D as

$$f_q^{eq} = \begin{cases} \theta - 5/3c_s^2 \cdot h_w & q = 0 \\ t_q \cdot (h_w c_s^2) & q = 1, 3 \\ t_q \cdot (h_w c_s^2 + I_z \cdot c) & q = 1, 5, 6 \\ t_q \cdot (h_w c_s^2 - I_z \cdot c) & q = 4, 7, 8, \end{cases} \quad (\text{C.3})$$

and in 3D as

$$f_q^{eq} = \begin{cases} \theta - 7/3c_s^2 \cdot h_w & q = 0 \\ t_q \cdot (h_w c_s^2) & q = 1, 2, 3, 4 \\ t_q \cdot (h_w c_s^2 + I_z \cdot c) & q = 5, 7, 8, 9, 10 \\ t_q \cdot (h_w c_s^2 + I_z \cdot c) & q = 6, 11, 12, 13, 14. \end{cases} \quad (\text{C.4})$$

The weighting factors t_q for the n_q lattice directions in the equilibrium distributions can be derived from the chosen lattice configuration. The applied values for the D2Q9 and D3Q15 configurations are given in Table C.1 after Mohamad (2011).

q	t_q (D2Q9)	q	t_q (D3Q15)
1-4	1/3	1-6	1/3
5-8	1/12	7-14	1/24

Table C.1: Lattice weighting coefficients t_q for directions q in 2D and 3D lattice.

To close the solution of the equilibrium functions, a formulation of the advective, gravitational term \vec{I} is required, which acts in vertical downward direction. Its vertical component calculates as

$$I_z = -k_r(\theta)k_f. \quad (\text{C.5})$$

D

Side Wall Failure Modelling Algorithm

Computational algorithm

The main computational steps of the side wall failure algorithm are summarized below. The set-up and the used variables are sketched in Figure 5.5.

1. The steepness of the cell slope is used as indicator if a slope failure occurs. If the material was previously deposited, then γ_{dep} is set as failure angle, otherwise γ_{wet} or γ_{dry} are used depending on the present water depth.
2. For each sediment edge m within a hydraulic cell, a failure volume V_m is determined which has to be transported over the edge to flatten the slope so that it no longer exceeds the critical value (Figure 5.5). The size of V_m depends on the deviation between the present cell slope \vec{S}_{cell} and its critical cell slope \vec{S}_{crit} which shall be set. These slopes are projected on the normal vector \vec{n}_m of the sediment edge and the pyramidal volume V_m is determined to

$$V_m = \frac{1}{3} A_m \underbrace{l_{char,m} (\vec{S}_{cell} \vec{n}_m - \vec{S}_{crit} \vec{n}_m)}_{\text{height of pyramid}}, \quad (D.1)$$

where m = index of sediment edge, A_m = area above the sediment edge and $l_{char,m}$ = characteristic length. If the material was previously deposited and γ_{dep} is set, then V_m must be limited to the deposited material in the cell.

3. The gravitationally-induced flux $\vec{q}_{Bgrav,m}$ at the sediment edge m is obtained by dividing the volume V_m by the present time step size Δt as

$$\vec{q}_{Bgrav,m} = \frac{V_m}{\Delta t} \vec{n}_m. \quad (D.2)$$

This flux is then added to the bed-load transport resulting in a total sediment flux at the edge as

$$\vec{q}_{Btot,m} = \vec{q}_{B,m} + \vec{q}_{Bgrav,m}. \quad (D.3)$$

4. The new vertex elevations z_B are computed by applying the equations and methods outlined for the surface erosion modelling in chapter 3. Situations with limited sediment supply due to fixed bed (e.g. underlying rock) or embankment surface protections are hereby taken into account and strict mass continuity is guaranteed by the dual-mesh approach.
5. The flattening of a cell slope involves changes of its vertex elevations (Figure 5.5). These affect in turn all adjacent cells and may steepen their corresponding slopes. Therefore the algorithm is applied in an iterative manner until finally no more slopes exceed the critical value¹. In principle, the introduction of a maximum number of iterations additionally provides an opportunity to control the propagation speed of the mass sliding.

A detailed case diagram for the failure algorithm is illustrated in Figure D.1 for single grain compositions. Cases of dry and wetted cells are distinguished as well as cases where the material has been deposited after side wall failures. For wetted cells a constant failure angle is applied, whereas otherwise the failure angle is computed as function of the water saturation and pore-water pressures.

¹To reduce the computational expense, the iteration considers only the affected adjacent cells.

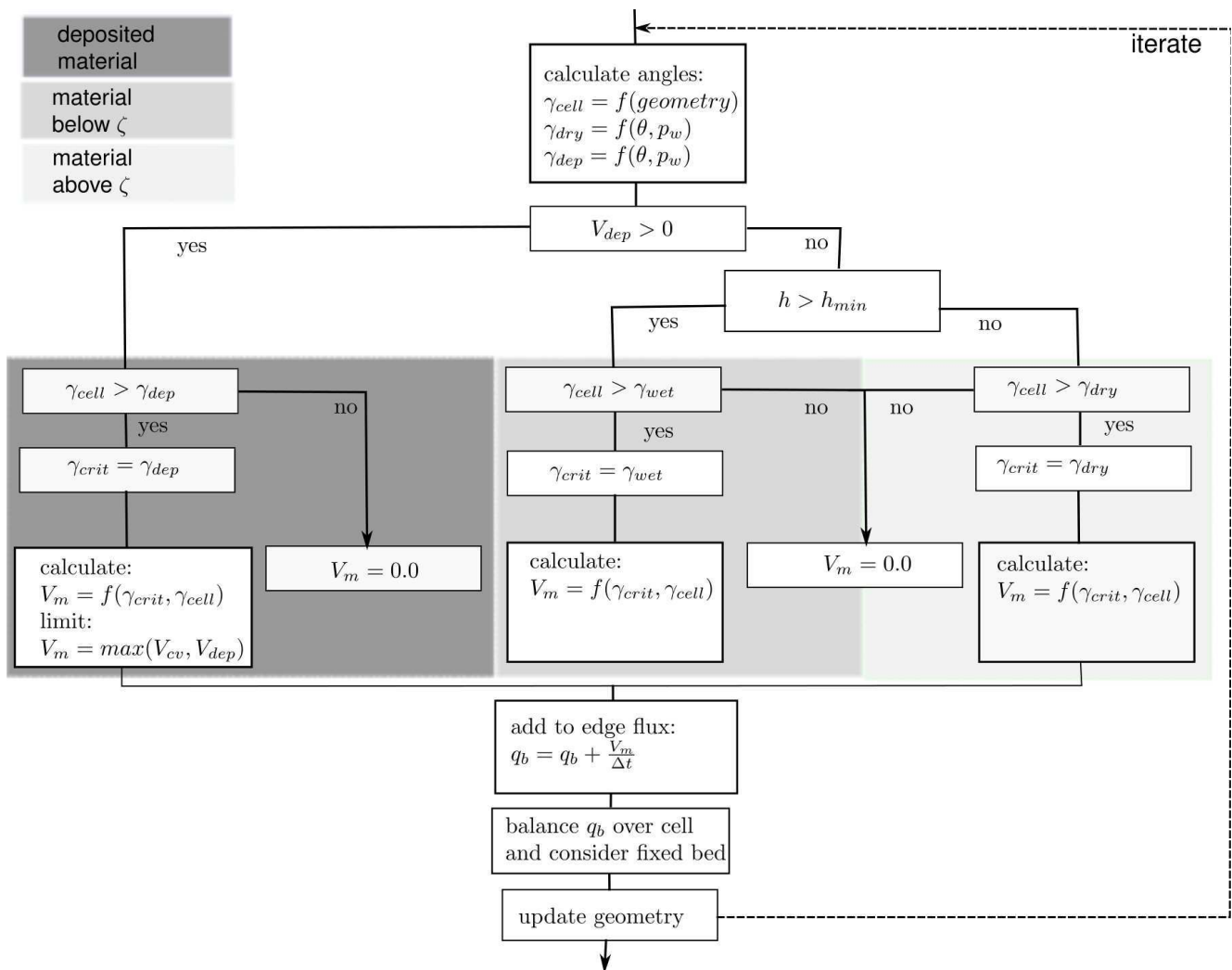


Figure D.1: Computational algorithm of geometrical approach for the hydraulic cell with slope angle γ_{cell} . (V_m = failed sediment volume, V_{dep} = deposited volume portion, V_{cv} = bed-load control volume portion).

Modification for fractional transport

The above algorithm is applicable to single grain computations only. In case of fractional transport, the failure volume V_m may be composed of parts from multiple soil layers which are mixed with each other. A detailed modelling of these mixing processes would require to track the individual particle motions and interactions, what is not feasible here. Instead, the sediment sorting equations 3.4 are applied to consider the grain mixing and the continuity of the failed masses. For this purpose, the above algorithm has to be modified such that the failure volume V_m is limited to material within the bed-load control volume of the sediment cell portion.

Since the bed-load control volume may be significantly smaller than the failure volume, the transported material in one time step may be insufficient to establish the critical slope at once and slow down the failure process. Therefore the algorithm is applied repeatedly to flatten the slope successively until the critical failure angle is established.

Influence of grid resolution

Due to the distinction between angles for material above and below the water surface, the side wall failures depend on the water depth in the breach channel. If the side wall is coarsely discretized with a single cell, the water depth must exceed at least half the breach channel height until γ_{wet} is set². This situation is illustrated in Figure D.2 (a). In contrast, in case of finer discretized side walls, the failure angles are assigned to the cells more accurately. Then, the failure will take place already at smaller water depths as illustrated in Figure D.2 (b).

Out of these reasons the accuracy of the geometrical approach depends on the mesh resolution. A high mesh resolution hereby is favourable and is usually on the safe side ($\Delta x \ll h$). This condition is difficult to satisfy, however, especially during breach initiation under small

²In this algorithm, a cell is classified as wetted if its centre of gravity lies below the water surface.

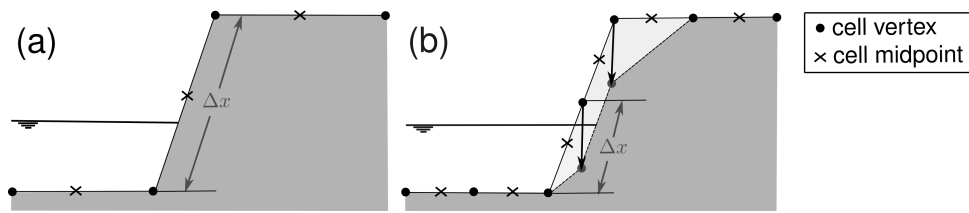


Figure D.2: *Dependence on grid resolution. (a) Coarse discretization of side wall without failure at indicated water depth. (b) Fine discretization with failure at indicated water depth.*

water depths. Using an unstructured mesh is advantageous in this respect, because one can refine the mesh at the initial breach location. In situations where this location is unknown a-priori, it is recommended to locate it during pre-investigations and then refine the mesh within this region.

E

Uncoupled vs. Coupled Modelling

In the following sections, advantages and disadvantages are discussed of uncoupled, semi-coupled and full-coupled modelling for the interconnection of the overtopping flow and the embankment erosion. In addition, the necessity of coupled modelling is briefly investigated using two test cases for progressive embankment erosion of non-cohesive embankments.

Uncoupled modelling

The uncoupled modelling ('asynchronous modelling') adopts a quasi-steady solution procedure for the hydrodynamics and sediment transport. It assumes that changes in the bed-level z_B and the grain size composition β_g during a computational time step are small and negligible compared to changes in the flow variables. Using this assumption, the flow properties are first determined based on the current bed topography. Afterwards, the transport is computed based on these flow properties which are assumed to be constant until the end of the time step. After the time step, the cell slopes are updated due to the changed bed-levels and new friction coefficients are determined from the new grain compositions. The basic procedure is sketched in the left part of Figure E.1.

This approach is computationally efficient and is flexible regarding the implementation of arbitrary and complex transport formulas. It also allows for non-erodible beds and embankment surface protections to be easily incorporated into the model (Kassem and Chaudhry (1998)). If explicit methods with small time step sizes are applied as it is done here, the

differences to fully-coupled approaches are often said to be insignificant, since the bed-level changes are small compared to changes in the flow variables (Savary (2007)). On the other hand, Cao *et al.* (2002) stated that uncoupled models can lead to inaccuracies in simulations with very large transport rates and rapid bed-level changes. Another drawback is the possible occurrence of instabilities at the model boundaries if strong bed-level changes occur. Such problems, however, rather concern strong suspended-load transport with implicit methods and cannot be simply transferred to breach models with small explicit time steps. Furthermore, Cao *et al.* (2002) also stated that the differences between uncoupled and coupled schemes are more significant for bed aggradation than for erosion, whereas the latter is dominant at embankment breaches.

Fully-coupled modelling

In fully-coupled schemes ('synchronous modelling'), the hydrodynamic and sediment transport equations are solved simultaneously. Such approaches are more difficult to implement and computationally more expensive, but consider the mutual process interactions during each computational step. In the last years several models with fully-coupled

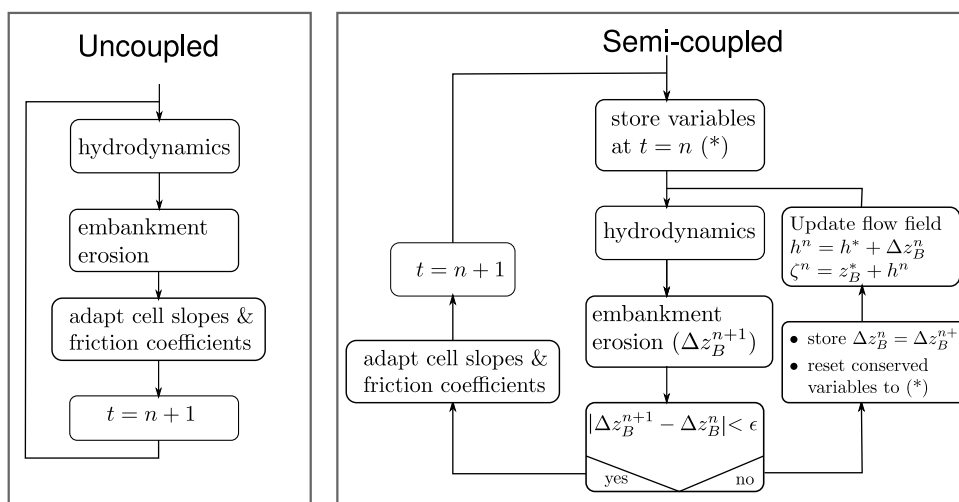


Figure E.1: Numerical schemes for interconnection of hydrodynamics and embankment erosion modelling. Left: uncoupled modelling. Right: (iterative) semi-coupled modelling.

schemes were presented, as for example by Wu and Wang (2008), Xia *et al.* (2010) or Cao *et al.* (2011). These lead to accurate and stable simulation schemes for model scenarios with large and rapid bed-level changes. Wu even stated that coupled approaches should be regarded as state-of-the-art for breach modelling (ASCE/EWRI-Task-Committee (2011)).

A common limitation of these models is, however, that they consider the sediment transport as suspended-load (or total-load) only. This is questionable regarding the erosion mechanisms at non-cohesive embankment breaches. Applying a fully-coupled scheme to bed-load transport instead, raises numerical difficulties as mentioned in Rousselot (2005). This is especially true regarding the commonly used bed-load transport formulas involving a critical shear-stress threshold. Although recent work addresses some of these difficulties using complex numerical techniques (Diaz *et al.* (2007)), the robustness, efficiency and applicability to engineering scenarios needs further research. Another disadvantage concerns the incorporation of non-erodible beds or embankment surface protections, which is not or only limited possible for fully-coupled approaches as outlined by Kassem and Chaudhry (1998).

Semi-coupled modelling

The semi-coupled modelling is similar to the uncoupled modelling, whereas the computations are iteratively repeated. The effects of bed-level changes of the last iteration step are hereby taken into account for the flow variables during the new iteration step. Such a semi-coupled algorithm was presented by Kassem and Chaudhry (1998) and is sketched in the right part of Figure E.1.

The main disadvantage of this approach is its computational expense, which is usually larger than for fully-coupled modelling (Cao *et al.* (2002)) and may even multiply the overall simulation run-time. Furthermore, it suffers in principle from the same theoretical stability problems as the uncoupled modelling and it guarantees no strict mass conservation regarding the water phase. Beside these aspects, the semi-coupling also

shares the advantages of the uncoupled modelling regarding the flexible incorporation of arbitrary transport formulas and embankment surface protections. Furthermore, it allows to easily integrate the side wall failures into the iterative algorithm without the need for special treatment, what is not yet feasible with fully-coupled modelling.

Necessity of coupled modelling

In general, there is a lack of appropriate measures to quantify the necessity for coupled modelling with regard to embankment breaches. Therefore comparisons of uncoupled and semi-coupled schemes were made for two scenarios of a laboratory plane dyke breach and a field-scale spatial dam breach, described in sections 7.2 and 7.4.

The overtopping flow is strong in the plane breach test and erodes the embankment rapidly. Despite the large bed-level changes, the breach progress was virtually indistinguishable for uncoupled and semi-coupled modelling and therefore is not shown here.

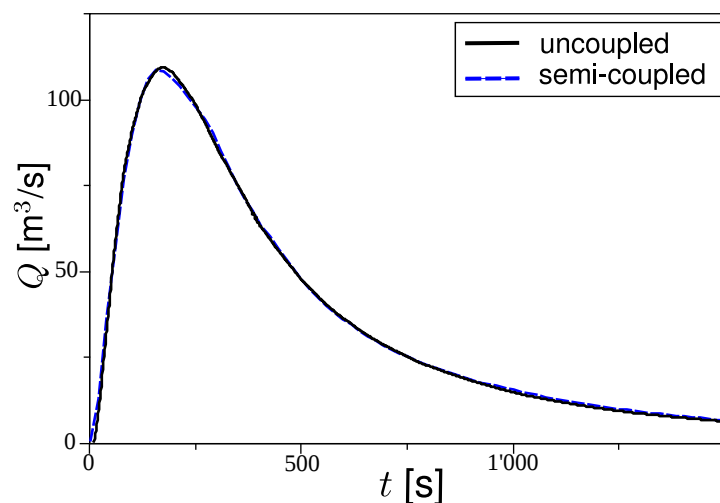


Figure E.2: *Simulated breach outflow hydrographs of a spatial embankment breach obtained with uncoupled (solid) and semi-coupled (dashed) modelling.*

The spatial breach additionally involves considerable suspended-load transport and side wall failures. Nevertheless, the deviations in the breach hydrographs obtained with uncoupled and semi-coupled mod-

elling were very small as illustrated in Figure E.2. These deviations are regarded as insignificant here, especially when compared to the overall uncertainties involved in breach modelling. These results indicate that in case of explicit breach simulations the uncoupled modelling is usually adequate.

F

Notation

variable	description	unit
c	characteristic wave speed at overtopping flow	[m/s]
c_{coh}	soil cohesion effect	[N/m ²]
c_m	lattice mesh speed in LBM model ($= \Delta x / \Delta t$)	[m/s]
c_q	discrete linkage in lattice of LBM model	[m/s]
c_s^2	constant in LBM model	[m/s]
d	sediment grain diameter	[m]
d_{90}	sediment grain diameter of 90% sieve curve	[m]
D_*	dimensionless sediment grain diameter	[-]
f	particle distribution function in LBM model	[-]
f^{eq}	equilibrium particle distribution function in LBM model	[-]
g	gravitational acceleration	[m/s ²]
h	flow water depth of overtopping flow	[m]
h_{cv}	thickness of bed-load control volume ($= z_B - z_F$)	[m]
h_E	embankment height	[m]
h_s	air-entry pressure head for a soil	[m]
h_w	pore-water pressure head ($= p_w / (\rho g)$)	[m]
i	hydraulic gradient $\partial h_w / \partial x$ driving the sub-surface flow	[m/s]
k_δ	local slope correction factor for critical Shields-parameter	[-]
k_f	(saturated) hydraulic soil conductivity	[m/s]
k_r	dimensionless relative hydraulic conductivity	[-]
k_{str}	bed friction coefficient after Strickler	[m ^{1/3} /s]
l	edge length of hydraulic or sediment cell	[m]
l_{char}	characteristic length applied in failure modelling	[m]
l_E	embankment base length	[m]
n	discrete time level in numerical approach	[s]
n_E	number of edges of a cell	[-]
n_g	number of grain classes	[-]

variable	description	unit
n_q	discrete number of linkages in LBM method	[-]
n_V	soil parameter for VGM constitutive model (= n in literature)	[-]
p	material porosity	[-]
p_a	pore-air pressure in soil	[N/m ²]
p_w	pore-water pressure in soil	[N/m ²]
q	discrete lattice direction in LBM model	[-]
q_B	bed-load transport rate/capacity at sediment edge	[m ² /s]
$q_{B,hyd}$	bed-load transport capacity at hydraulic cell	[m ² /s]
$q_{B,grav}$	gravitationally-induced flux due to side wall failure	[m ² /s]
q_{inf}	external water source for LBM model (e.g. rainfall)	[mm/h]
s	specific density (= ρ_s/ρ)	[-]
s_{fg}	sediment source for exchange with sub-layer	[m/s]
s_g	sediment source for exchange with suspended-phase	[m/s]
s_{lg}	external sediment source or sink	[m/s]
Δt	time step size in numerical model	[s]
t_q	weighting factors for the lattice directions in LBM model	[-]
u	depth-integrated flow velocity in x -direction	[m/s]
u_*	bottom shear stress velocity (friction velocity)	[m/s]
v	depth-integrated flow velocity in y -direction	[m/s]
w	depth-integrated flow velocity in z -direction	[m/s]
w_S	settling velocity of grain particle	[m/s]
Δx	cell size	[m]
z_B	elevation of terrain surface	[m]
z_F	bottom elevation of bed-load control volume	[m]
z_R	reference height for reference concentration C_R	[m]
A	base area of hydraulic or sediment cell	[m ²]
B_1, B_2	constants for calibration of apparent cohesion for surface erosion	[-]
C	depth-averaged sediment concentration in suspended-phase	[-]
CFL	dimensionless Courant-number	[-]
C_{nb}	near-bed sediment concentration for deposition	[-]
C_R	reference sediment concentration for entrainment	[-]
D	diffusivity in Richard's equation	[m/s]
D_g	dimensionless deposition rate for suspended-load transport of grain g	[-]
E_g	dimensionless entrainment rate for suspended-load transport of grain g	[-]
E_{tot}	total sediment mass error over entire domain	[m ³]
E_{spec}	area specific total sediment mass error over entire domain	[m]
K	variably-saturated soil conductivity (= $k_f k_r$)	[m/s]
L_s	adaptation length for non-equilibrium transport	[m]

variable	description	unit
Mn	dimensionless Movability-number for inception of suspended-load	[-]
P	gradient of the water retention curve at transition to saturated zone	[m]
S_B	bed slope term vector	[-]
S_f	bed friction slope term vector	[-]
V_{dep}	deposited sediment volume	[m ³]
V_m	failure sediment volume in geometrical approach	[m ³]
V_w	water volume within hydraulic cell	[m ³]
α	soil parameter for modified VGM constitutive model	[1/m]
β_g	grain fraction of grain g in grain composition	[-]
γ^b	internal friction angle for apparent cohesion after Fredlund	[°]
γ_{dep}	deposition failure angle for collapsed masses	[°]
γ_{dep}'	deviation from deposition failure angle due to saturation	[°]
γ_{dry}	failure angle above water surface	[°]
γ_{cell}	slope angle of hydraulic cell	[°]
γ_{rep}	angle of repose of the material	[°]
γ_{wet}	failure angle below water surface	[°]
δ	local slope angle in flow or transversal direction	[°]
κ	von Kármán constant = 0.4	[-]
λ	soil parameter for BCM constitutive model	[-]
ν_t	turbulent eddy viscosity for Boussinesq approach	[m ² /s]
ω	relaxation parameter for collision operator in LBM model	[-]
ρ	water density	[kg/m ³]
ρ_s	sediment density	[kg/m ³]
σ_n	total stress in soil	[N/m ²]
σ_w	water surface tension	[N/m]
τ_B	bottom shear stress of overtopping flow	[N/m ²]
τ_{coh}	additional soil shear strength due to apparent cohesion	[N/m ²]
τ_{crit}	critical shear stress for incipient motion	[N/m ²]
$\tau_{crit,ini}$	initial critical shear stress for embankment surface protection	[N/m ²]
τ_S	soil shear strength	[N/m ²]
τ_{xx}	turbulent shear stress	[N/m ²]
θ	effective water saturation in sub-surface model	[-]
θ_w	water content of soil	[-]
θ_S	saturated water content of soil (= porosity p)	[-]
θ_R	residual dry water content of soil	[-]
ϑ	free adjustable constant in LBM model	[-]
ν	kinematic viscosity of water	[m ² /s]
Γ	turbulent eddy diffusivity	[m ² /s]
Ω	collision operator in LBM model	[-]
Π	transport allocation factor for portioning of bed- and suspended load	[-]
Θ	Shields-parameter for particle stability in grain composition	[-]
Θ_{crit}	critical Shields-parameter for inception of particle motion	[-]

Table F.1: Applied variables with associated descriptions and units.

List of Tables

1.1	Comparison of different physically-based 1D models	20
1.2	Comparison of different physically-based 2D models	21
3.1	Comparison of different Movability numbers	67
3.2	Initial grain composition of mobile bed in Günters Test	77
4.1	Water contents and soil parameters at laboratory dyke	102
4.2	Dam geometry of homogeneous field-scale dam	104
4.3	Dam geometry of heterogeneous field-scale dam	105
4.4	Soil properties for heterogeneous field-scale dam	105
7.1	Dyke geometry and material properties for plane breach	141
7.2	Geometry and material properties for spatial breach test	148
7.3	Sub-surface flow parameters at spatial dyke	150
7.4	Geometry of field-scale test dam	158
7.5	Material properties of field-scale test dam	159
7.6	Sub-surface flow parameters at field-scale dam	160
7.7	Grain classes of the field-scale embankment	165
7.8	Embankment material properties and grain class distribution . . .	169
7.9	Sub-surface flow parameters at natural embankment	170
C.1	Lattice weighting coefficients t_q for directions q	190
F.1	Applied variables with associated descriptions and units	203

List of Figures

1.1	Historical breach events of earth embankments	10
1.2	Common failure mechanisms for earth embankments	12
1.3	Sketch of progressive and head-cut erosion	13
1.4	Failure modes due to overtopping	14
1.5	Major relevant physical processes	16
1.6	Classification of modelling approaches	17
2.1	Cross-sectional view through breach channel	28
2.2	1D sketch for hydrodynamic and erosion modelling	29
2.3	Cell-centered discretization for hydrodynamic modelling	39
2.4	Sudden dam break on dry and wet terrains	42
2.5	Sudden dam break on sloped terrain	43
2.6	Comparison of water levels at Malpasset dam break	44
3.1	Transport modes of sediment transport	47
3.2	Definition sketch of balance volume	54
3.3	Problems of cell-centered discretization	69
3.4	Dual-mesh approach - definition sketch	70
3.5	Volume identity in dual-mesh approach	71
3.6	Vertical discretization with bed-load control volume	73
3.7	Comparison of bed-levels of aggradation front	77
3.8	Final grain compositions of bed armouring layer	78
4.1	Embankment with zones of different of saturations	82
4.2	Levels of description of different num. techniques	92

4.3	Definition of the distribution function f of the Boltzmann eq.	92
4.4	Lattice cells in 2D in 3D	94
4.5	Pressure-head and velocity field within confined domain	100
4.6	Vertical infiltration front propagation	101
4.7	Simulation of seepage front propagation at laboratory dyke	103
4.8	Sub-surface flow through a homogeneous, field-scale dam	104
4.9	Sub-surface flow through a heterogeneous, field-scale dam	106
5.1	Failure types at non-cohesive embankments	110
5.2	Limit-equilibrium method and continuum modelling	114
5.3	Critical failure angles above and below the water surface	119
5.4	Critical failure angles as functions of the water saturation	122
5.5	Configuration sketch and parameters for failure modelling	123
5.6	Failure of bed step with standing water pool	124
5.7	Failure of a vertical peak with quadratic base area	125
5.8	Failure of inclined bed step in partially-saturated domain	125
6.1	Model coupling and data exchange for combined modelling	127
6.2	Dynamical assignment of pressure and seepage boundaries	133
6.3	Update of 3D lattice due to breach advance	134
7.1	Experimental set-up of plane dyke breach	141
7.2	Dyke and water-level profiles at plane breach	143
7.3	Simulated τ_B and Fr at plane dyke breach	144
7.4	Plane dyke sensitivity analyses	146
7.5	Sketch of experimental set-up of spatial dyke breach	148
7.6	Seepage lines for spatial dyke breach	150
7.7	Simulated qualitative spatial dyke breach development	152
7.8	Integral parameter and longitudinal dyke erosion	153

7.9	Development of transversal spatial breach profiles	154
7.10	Transversal profiles for variations of failure angles	156
7.11	Site-conditions of IMPACT dam breach	158
7.12	Unstructured mesh for IMPACT dam breach	160
7.13	Saturation and seepage line within dam body	161
7.14	Comparison with IMPACT dam breach	162
7.15	Sensitivity analyses of transport mechanisms and seepage	163
7.16	Sensitivity analyses regarding n_g and h_{cv}	165
7.17	Illustrations of glacial lake and breach extensions	168
7.18	Unstructured mesh representing the moraine embankment	169
7.19	Measured side wall angles in lower and upper sections	170
7.20	Temporal breach advance of natural embankment breach	172
7.21	Breach outflow hydrograph of natural embankment breach	172
7.22	Matrix representation of parameter sensitiveness	174
A.1	Configuration sketch for flux computation at edge	184
B.1	Sediment flux determination for dual-mesh approach	188
D.1	Computational algorithm of geometrical approach	193
D.2	Dependence on grid resolution.	195
E.1	Interconnection of hydrodynamics and erosion	197
E.2	Hydrographs for semi-coupled and uncoupled modelling	199

Bibliography

- Abbott, M., 1979. Computational hydraulics: Elements of the free-surface flow. Pitman, London.
- Achterberg, E., Braungardt, C., Morley, N., Elbaz-Poulichet, F., Leblanc, M., 1999. Impact of los frailes mine spill on riverine, estuarine and coastal waters in southern Spain. *Water Research* 33 (16), 3387–3394.
- Aguilar, J., Dorronsoro, C., Fernández, E., Fernández, J., García, I., Martín, F., Ortiz, I., Simón, M., 2000. El desastre ecológico de Aznalcóllar. Web report - <http://edafologia.ugr.es/donana/aznal.htm>, (in Spanish).
- Al-Riffai, M., Nistor, I., 2010. Impact and analysis of geotechnical processes on earthfill dam breaching. *Natural Hazards* 55, 15–27.
- Alcrudo, F., Mulet, J., 2007. Description of the Tous dam break case study (Spain). *Journal of Hydraulic Research* 45, 45–57.
- Ali, K., Achterberg, J., Li, M., Zhu, Y., 2003. Effect of seepage on sediment transport in channels. In: *International Conference on Estuaries and Coasts*, Hangzhou, China, pp. 1003–1012.
- Amoudry, L., Liu, P.-F., 2009. Two-dimensional, two-phase granular sediment transport model with applications to scouring downstream of an apron. *Coastal Engineering* 56, 693–702.
- ASCE/EWRI-Task-Committee, A., 2011. Earthen embankment breaching. *Journal of Hydraulic Engineering* 137 (12), 1549–1564.
- Ashida, K., Michiue, M., 1971. An investigation over river bed degradation downstream of a dam. In: *Proceedings of 14th IAHR Congress* 3, Paris, France, pp. 247–256.
- Bagnold, R., 1966. An approach to the sediment transport problem from general physics. Professional paper 422-1, US Geological Survey.

- Balmforth, N., von Hardenberg, J., Provenzale, A., Zammett, R., 2008. Dam breaking by wave-induced erosional incision. *Journal of Geophysical Research* 113, 1–12.
- Basco, D., 1989. Limitations of De Saint Venant Equations. *Journal of Hydraulic Engineering* 115, 950–965.
- Bear, J., Cheng, A.H.-D., 2010. *Modeling Groundwater Flow and Contaminant Transport*. Springer, Dordrecht Heidelberg London New York.
- Beffa, C., 1994. Praktische Lösung der tiefengemittelten Flachwassergleichungen. In: Vischer, D. (Ed.), VAW-Mitteilung Nr. 133, Versuchsanstalt für Wasserbau, Hydrologie und Glaziologie (VAW), ETH Zürich.
- Begnudelli, L., Sanders, B., 2006. Unstructured Grid Finite-Volume Algorithm for Shallow-Water Flow and Scalar Transport with Wetting and Drying. *Journal of Hydraulic Engineering* 132 (4), 371–384.
- Begnudelli, L., Sanders, B., Bradford, S., 2008. Adaptive Godunov-based Model for Flood Simulation. *Journal of Hydraulic Engineering* 134 (6), 714–725.
- Bell, R., 1989. Non-equilibrium bedload transport by steady and non-steady flows. Research report no. 80-23, University of Canterbury.
- Bell, R., Sutherland, A., 1989. Nonequilibrium bedload transport by steady flows. *Journal of Hydraulic Engineering* 1983 (3), 351–367.
- Bermudez, A., Dervieux, A., Desideri, J., Vazquez, M., 1998. Upwind schemes for the two-dimensional Shallow-Water equations with variable depth using unstructured meshes. *Computational Methods in Applied Mechanical Engineering* 155 (1-2), 49–72.
- Bhatnagar, P., Gross, E., Krook, M., 1954. A model for collision processes in gases. I. Small amplitude processes in charged and neutral one-component systems. *Physical Review* 94 (3), 511–525.
- Borah, D., Alonso, C., Prasad, S., 1982. Routing graded sediments in streams: Formulations. *Journal of Hydraulics Division* 108 (12), 1486–1503.
- Bowles, J., 1984. *Physical and geotechnical properties of soils*, 2nd Edition. McGraw-Hill, New York.

- Broich, K., 1997. Computergestützte Analyse des Dammerosionsbruchs. Ph.D. Thesis, Mitteilungen Heft 61, Institut für Wasserwesen, Universität der Bundeswehr München, (in German).
- Brooks, R., Corey, A., 1964. Hydraulic properties of porous media. Hydraulic paper 3, Colorado State University.
- Bundesamt für Wasserwirtschaft, L., 1982. Hochwasserschutz an Fließgewässern, Wegleitung 1982. Eidgenössisches Verkehrs- und Energiewirtschaftsdepartement.
- Camenen, B., Larson, M., 2008. A general formula for noncohesive suspended sediment transport. *Journal of Coastal Research* 24, 615–627.
- Cao, Z., Day, R., Egashira, S., 2002. Coupled and decoupled numerical modeling of flow and morphological evolution in alluvial rivers. *Journal of Hydraulic Engineering* 128 (3), 306–321.
- Cao, Z., Yue, Z., Pender, G., 2011. Landslide dam failure and flood hydraulics. Part II: coupled mathematical modeling. *Natural Hazards* 59 (2), 1021–1045.
- Capart, H., 2000. Dam-break induced geomorphic flows and the transition from solid- to fluid-like behaviour across evolving interfaces. Ph.D. Thesis, L'Université catholique de Louvain.
- Capart, H., Young, D., 2002. Two-layer shallow water computations of torrential geomorphic flows. In: Bousmar, D., Zech, Y. (Eds.), *Proceedings of River Flow 2002*, Balkema, Louvain-la-Neuve, Belgium, pp. 1003–1012.
- Chanson, H., 2004a. Discussion: Modeling a washout of dams. *Journal of Hydraulic Research* 42 (5), 563–566.
- Chanson, H., 2004b. *The Hydraulics of Open Channel Flow : An Introduction*, 2nd Edition. Butterworth-Heinemann, Oxford.
- Chapuis, R., Aubertin, M., 2001. A simplified method to estimate saturated and unsaturated seepage through dikes under steady-state conditions. *Canadian Geotechnical Journal* 38, 1321–1328.
- Chapuis, R., Chenaf, D., Brussière, B., Aubertin, M., Crespo, R., 2001. A user's approach to assess numerical codes for saturated and unsaturated seepage conditions. *Canadian Geotechnical Journal* 38, 1113–1126.

- Chen, H., Lee, C., 2004. Runout Analysis of Slurry Flows with Bingham Model. *Journal of Geotechnical and Geoenvironmental Engineering* 128 (12), 1032–1042.
- Chen, X., Ma, J., Dey, S., 2010. Sediment transport on arbitrary slopes: Simplified model. *Journal of Hydraulic Engineering* 136 (5), 311–317.
- Cheng, N., Chiew, Y., 1999. Incipient sediment motion with upward seepage. *Journal of Hydraulic Research* 37 (5), 665–681.
- Clague, J., Evans, S., 2000. A review of catastrophic drainage of moraine-dammed lakes in British Columbia. *Quaternary Science Reviews* 19, 1763–1783.
- Coleman, S., Andrews, D., Webby, M., 2002. Overtopping breaching of noncohesive homogeneous embankments. *Journal of Hydraulic Engineering* 128 (9), 829–838.
- Courant, R., Friedrichs, K., Lewy, H., 1928. Über die partiellen Differenzgleichungen der mathematischen Physik. *Mathematische Annalen* 100 (1), 32–74, (in German).
- Crespo, R., 1993. Modélisation des écoulements à travers les ouvrages de retenue et de confinement des résidus miniers par un logiciel d'éléments finis. Master's thesis, École Polytechnique de Montréal, Montréal, (in French).
- Cundall, P., 2001. A discontinuous future for numerical modelling in geomechanics? In: Anagnostopoulos, A., Pachakis, M., Tsatsanifos, C. (Eds.), *Proceedings of the Institution of Civil Engineers Geotechnical Engineering*, vol. 149, IOS Press, pp. 41–47.
- Cunge, J., Holly, F., Verwey, A., 1980. *Practical aspects of computational river hydraulics*. Pitman Advanced Publishing, London.
- D'Ambrosio, D., Gregorio, S.D., Iovine, G., Lupiano, V., Rongo, R., Spataro, W., 2003. First simulations of the sarno debris flows through cellular automata modelling. *Geomorphology* 54, 91–117.
- D'Eliso, C., Kortenhaus, A., Oumeraci, H., 2006. Breaching of coastal dikes: Detailed breaching model. Report Nr. 937, Leichtweiß-Institut für Wasserbau und Wasserwirtschaft, TU Braunschweig.

- Denlinger, R., Iverson, R., 2004. Granular avalanches across irregular three-dimensional terrain: 1. Theory and computation. *Journal of Geophysical Research* 109, 1–14.
- Denlinger, R., O'Connell, R., 2008. Computing Nonhydrostatic Shallow-Water Flow over Steep Terrain. *Journal of Hydraulic Engineering* 134 (11), 1590–1602.
- Diaz, M., Fernandez-Nieto, E., Ferreiro, A., 2007. Sediment transport models in shallow water equations and numerical approach by high order finite volume methods. *Computer & Fluids* 37, 299–316.
- Dressler, R., 1958. Unsteady non-linear waves in sloping channels. *Proceedings of the Royal Society of London. Series A, Mathematical and Physical Sciences* 247, 186–198.
- Evans, S., Hermanns, R., Strom, A., Scarascia-Mugnozza, G., 2011. *Natural and Artificial Rockslide Dams*. Springer, Heidelberg, Dordrecht, London, New York.
- Faeh, R., 2007. Numerical Modeling of Breach Erosion of River Embankments. *Journal of Hydraulic Engineering* 133 (9), 1000–1009.
- Faeh, R., Mueller, R., Rousselot, P., Vetsch, D., Volz, C., Vonwiler, L., Veprek, R., Farshi, D., 2012. *System Manuals of BASEMENT (Basic Simulation Environment for Computation of Environmental Flow and Natural Hazard Simulation)*. Online Program Manual, www.basement.ethz.ch, Versuchsanstalt für Wasserbau, Hydrologie und Glaziologie (VAW), ETH Zürich, Switzerland.
- Fentie, B., Yu, B., Rose, C., 2004. Comparison of seven particle settling velocity formulae for erosion modelling. In: *Conserving Soil and Water for Society: Sharing Solutions*, ISCO 2004 - 13th International Soil Conservation Organisation Conference, Brisbane.
- Flekkoy, E., 1993. Lattice Bhatnagar-Gross-Krook models for miscible fluids. *Physical Review E* 47 (6), 4247–4257.
- Foster, M., Fell, R., Spannagle, M., 1998. *Analysis of embankment dam incidents*. Report UNICIV, R-3743, Sydney, Australia: The University of New South Wales, ISBN 85841-349-3.

- Franca, M., Almeida, A., 2002. Experimental tests on rockfill dam breaching process. In: Hydraulic and Hydrological Aspects of Reliability and Safety Assessment of Hydraulic Structures, International IAHR Symposium, St. Petersburg.
- Fread, D., 1985. BREACH: An erosion model for earthen dam failures. NWS Report, National Oceanic and Atmospheric Administration, USA.
- Fredlund, D., Morgenstern, N., Widger, R., 1978. The shear strength of unsaturated soils. *Canadian Geotechnic Journal* 15 (3), 313–321.
- Fredlund, D., Rahardjo, H., 1993. *Soil Mechanics for Unsaturated Soils*. John Wiley & Sons, Inc.
- Gauche, J., Marche, C., Mahdi, T., 2010. Experimental investigation of the hydraulic erosion of noncohesive compacted soils. *Journal of Hydraulic Engineering* 136 (11), 901–913.
- Ginzburg, I., 2005. Equilibrium type and link-type lattice Boltzmann models for generic advection and anisotropic-dispersion equation. *Advances in Water Resources* 28 (11), 1171–1195.
- Ginzburg, I., 2006. Variably saturated flow described with the anisotropic Lattice Boltzmann methods. *Computers & Fluids* 35, 831–848.
- Ginzburg, I., Carlier, J., Kao, C., 2004. Lattice Boltzmann approach to Richard's equation. In: Miller, C. (Ed.), *Proceedings of the CMWR XV*, Elsevier, pp. 583–597, June 13-18, Chapel Hill, NC, USA.
- Ginzburg, I., d'Humières, D., 1996. Local Second-Order Boundary Methods for Lattice Boltzmann Model. *Journal of Statistical Physics* 84 (5/6), 927–971.
- Godunov, S., 1959. Finite Difference Methods for the Computation of Discontinuous Solutions of the Equations of Fluid Dynamics. *Mathematicheskii Sbornik* 47 (3), 271–306.
- Gray, J., Wieland, M., Hutter, K., 1999. Gravity-driven free surface flow of granular avalanches over complex basal topography. *Proceedings: Mathematical, Physical and Engineering Sciences* 455 (1985), 1841–1874.
- Günter, A., 1971. Die kritische mittlere Sohlenschubspannung bei Geschiebemischtungen unter Berücksichtigung der Deckschichtbildung und der turbulenzbedingten Sohlenschubspannungsschwankungen. In: Vischer, D. (Ed.), *VAW*

- Mitteilung-Nr. 3, Versuchsanstalt für Wasserbau, Hydrologie und Glaziologie (VAW), ETH Zürich, (in German).
- Gyr, A., Hoyer, K., 2006. Sediment Transport A Geophysical Phenomenon. Springer, The Netherlands.
- Hahn, W., Hanson, G., Cook, K., 2000. Breach morphology observations of embankment overtopping tests. In: Joint Conference on Water Resources Engineering and Water Resources Planning and Management, 104, ASCE, p. 411.
- Hirano, M., 1971. River bed degradation with armouring. Transactions of JSCE 3 (2), 194–195.
- Hunziker, R., Jaeggi, M., 2002. Grain Sorting Processes. Journal of Hydraulic Engineering 128 (12), 1060–1068.
- Ikedo, S., 1982. Lateral bed-load transport on side slopes. Journal of the Hydraulics Division 108 (11), 1369–1373.
- IPCC, 2007. Climate change 2007. Assessment Report 4. Tech. rep., Intergovernmental panel on climate change, IPCC, Geneva, Switzerland, <http://www.ipcc.ch>, November 2011.
- IRR, 1992. Der Alpenrhein und seine Regulierung. IRR - Internationale Rheinregulierung, Rorschach.
- Iverson, R., 1997. The physics of debris flows. Reviews of geophysics 35 (3), 245–296.
- Julien, R., 1995. Erosion and sedimentation. Cambridge University Press, Cambridge, UK.
- Kassem, A., Chaudhry, M., 1998. Comparison of coupled and semicoupled numerical models for alluvial channels. Journal of Hydraulic Engineering 124 (8), 794–802.
- Khan, A., Steffler, P., 1996. Vertically averaged and moment equations model for flow over curved beds. Journal of Hydraulic Engineering 122 (1), 3–9.
- Kliche, C., 1999. Rock slope stability. Tech. rep., Society for Mining, Metallurgy, and Exploration Inc.

- Komaei, S., 2004. A robust implicit shallow water equations solver on unstructured grid. Ph.D. Thesis, Mitteilungen Heft 91, Institut für Wasserwesen der Universität der Bundeswehr München.
- Kroekenstoel, D., van Velzen, E., 2010. Morphologische Berechnungen mit Sedimentmischungen. Zukunftsmusik oder eine realistische Alternative? Bericht Nr. II-19 der KHR, Internationale Kommission für die Hydrologie des Rheingebietes, (in German).
- Krüger, S., Rutschmann, P., 2006. Modeling 3d supercritical flow with extended shallow-water approach. *Journal of Hydraulic Engineering* 132 (9), 916–926.
- Kuai, K., Tsai, C., 2009. Stochastic non-equilibrium bedload transport model. In: *World Environmental and Water Resources Congress 2009: Great Rivers*, American Society of Civil Engineers, pp. 6239–6247.
- Lam, L., Fredlund, D., Barbour, S., 1987. Transient seepage model for saturated-unsaturated soil systems: a geotechnical engineering approach. *Canadian Geotechnical Journal* 24, 565–580.
- Landestalsperrenverwaltung-Sachsen, 2005. Analyse der Deichbrüche an Elbe und Mulde während des Hochwassers 2002 im Bereich Sachsen. Wissenschaftliche Studie (unveröffentlicht), Institut für Wasserbau und Technische Hydromechanik (IWD) der Technischen Universität Dresden, (in German).
- Leopardi, A., Oliveri, E., Greco, M., 2002. Numerical simulation of gradual earth dam failure. In: *2nd International Conference New Trends in Water and Environmental Engineering for Safety and Life: Eco-compatible Solutions for Aquatic Environments*, Italy.
- Lin, B., 1984. Current study of unsteady transport of sediment in China. In: *Proceedings of Japan-China Biateral Seminar on River Hydraulics and Engineering Experiences*, Japan, Tokyo-Kyoto.
- Liu, H., 1957. Mechanics of sediment-ripple formation. *Journal of the Hydraulics Division* 83 (2), 1–23.
- Liu, N., 2012. The numerical solution of Richards Equation using the Lattice Boltzmann Method. *Applied Mechanics and Materials* 188, 90–95.
- Londe, P., 1987. Malpasset dam failure. *Engineering Geology EGGOAO* 24 (1-4), 295–329.

- Lövoll, A., 2004. Breach formation in embankment dams. Results from Norwegian field tests. In: EBL Kompetanse: Stability and Breaching of Embankment Dams, Norway, Oslo.
- Lu, N., 2008. Is matric suction a stress variable? *Journal of Hydraulic Research* 134 (7), 899–905.
- Lu, Y., Chiew, Y.-M., Cheng, N.-S., 2008. Review of seepage effects on turbulent open-channel flow and sediment entrainment. *Journal of Geotechnical and Geoenvironmental Engineering* 46 (4), 476–488.
- Macchione, F., 2008. Model for predicting floods due to earthen dam breaching. I: Formulation and evaluation. *Journal of Hydraulic Engineering* 134 (12), 1688–1696.
- Malcherek, A., 2009. Sedimenttransport und Morphodynamik. Online Script, <http://www.unibw.de/rz/dokumente/fakultaeten>, Institut für Wasserwesen der Universität der Bundeswehr München, (in German).
- Mei, R., Luo, L., Shyy, W., 1999. An Accurate Curved Boundary Treatment in the Lattice Boltzmann Method. *Journal of Computational Physics* 155, 307–330.
- Meyer-Peter, E., Müller, R., 1948. Formulas for bed-load transport. In: 2nd Meeting IAHR Appendix II, Stockholm, pp. 39–64.
- Mohamad, A., 2011. *Lattice Boltzmann Method - Fundamentals and Engineering Applications with Computer Codes*, 1st Edition. Springer-Verlag, London.
- Mohammadian, A., Roux, D.Y.L., 2006. Simulation of shallow flows over variable topographies using unstructured grids. *International Journal for Numerical Methods in Fluids* 52, 473–498.
- Mohapatra, P., Eswaran, V., Bhallamudi, S., 1999. Two-dimensional analysis of dam-break flow in vertical plane. *Journal of Hydraulic Engineering* 125 (2), 183–192.
- Morales, W., 2010. Response to dyke overtopping and erosion: Soil mechanics analysis. In: APUNCH - Advanced Process UNDERstanding and prediction of hydrological extremes and Complex Hazards, internal project meeting.

- Morales, W., Mayor, P., Springman, S., Vogel, A., 2011. In-situ and laboratory water retention characteristics in a silty sand dyke. In: Anagnostopoulos, A., Pachakis, M., Tsatsanifos, C. (Eds.), Proceedings of the 15th European Conference on Soil Mechanics and Geotechnical Engineering, IOS Press, pp. 641–646.
- Morris, M., 2004. IMPACT: Investigation of Extreme Flood Processes and Uncertainty. Breach Formation (wp2). Tech. rep., HR Wallingford, http://www.impact-project.net/wp2_technical.htm.
- Morris, M., Hanson, G., Hassan, M., 2008. Improving the accuracy of breach modelling: why are we not progressing faster? *Journal of Flood Risk Management* 1, 150–161.
- Mualem, Y., 1976. A new model for predicting the hydraulic conductivity of unsaturated porous media. *Water Resources Research* 12 (3), 513–522.
- Niemayer, M., 2007. Einfluss der Breschenbildung auf die Flutwellenausbreitung bei Damm- und Deichbrüchen. Ph.D. Thesis, Institut für Wasserbau und Wasserwirtschaft (IWW), RWTH Aachen, (in German).
- Nistor, I., Rennie, C., 2005. Modelling and risk evaluation of dam structural safety. In: Proceedings of the annual conference of the Canadian Society for Civil Engineering, CSCE, Toronto, Canada, CD-ROM, 8.
- Niswonger, R., Prudic, D., Regan, R., 2006. Documentation of the unsaturated-zone flow (UZF1) package for modeling unsaturated flow between the land surface and the water table with MODFLOW-2005. U.S. Geological techniques and methods book 6, chapter a19, U.S. Geological Survey Water-Resources Investigations Report 02-4231, <http://pubs.usgs.gov/tm/2006/tm6a19/>, version of 04.02.2012.
- Oberg, A.-L., Sallfors, G., 1997. Determination of shear strength parameters of unsaturated silts and sands based on the water retention curve. *Geotechnical Testing Journal* 20 (1), 40–48.
- O'Donnell, C., 2000. The effect of pore pressure on sediment transport. Ph.D. Thesis, University of Liverpool.
- Paquier, A., 2002. Test cases of dam breach simulation. Comments about Cemagref's results. In: CADAM Proceedings, Munich.

- Parker, G., 1990. Surface-based bedload transport relation for gravel rivers. *Journal of Hydraulic Research* 28 (4), 417–436.
- Pham-Van, S., 2009. Application of different model concepts for simulation of two-phase flow processes in porous media with fault zones. Ph.D. Thesis, TU Berlin, Book Series Volume 3.
- Pham-Van, S., Hinkelmann, R., Nehrig, M., Martinez, I., 2011. A comparison of model concepts and experiments for seepage processes through a dike with a fault zone. *Engineering Applications of Computational Fluid Mechanics* 5 (1), 149–158.
- Pickert, G., Jirka, G., Bieberstein, A., Brauns, J., 2004. Soil/water interaction during the breaching process of overtopped embankments. In: Greco, M., Carravetta, A., Morte, R.D. (Eds.), *Proceedings of the Conference River-Flow 2004*, Balkema.
- Pickert, G., Weitbrecht, V., Bieberstein, A., 2011. Breaching of overtopped river embankments controlled by apparent cohesion. *Journal of Hydraulic Research* 49 (2), 143–156.
- Pontillo, M., Schmocker, L., Greco, M., Hager, W., 2010. 1D numerical evaluation of dike erosion due to overtopping. *Journal of Hydraulic Research* 48 (5), 573–582.
- Quan, T., Oumeraci, H., 1989. Numerical modelling of wave overtopping-induced erosion of grassed inner sea-dike slopes. *Natural Hazards DOI* 10.1007/s11069-012-0155-z, 1–31.
- Raudkivi, A., 1989. *Loose Boundary Hydraulics*. Balkema, Rotterdam, Netherlands.
- Richards, L., 1931. Capillary conduction of liquids through porous mediums. *Physics* 1 (5), 318–333.
- Rickenmann, D., 1991. Hyperconcentrated flow and sediment transport at steep slopes. *Journal of Hydraulic Engineering* 117 (11), 1419–1439.
- Rico, M., Benito, G., Salgueiro, A., D'iez-Herrero, A., Pereira, H., 2007. Reported tailings dam failures. A review of the European incidents in the worldwide context. *Journal of Hazardous Materials* 152, 846–852.

- Ritter, A., 1892. Die Fortpflanzung der Wasserwellen. Zeitschrift Verein Deutscher Ingenieure 36, 947–954, (in German).
- Rousselot, P., 2005. Numerische Simulation eines hochinstationären Problems, Dammerosion. Master's thesis, Versuchsanstalt für Wasserbau, Hydrologie und Glaziologie (VAW), ETH Zürich, Switzerland, (in German).
- Rozov, A., 2003. Modeling of washout of dams. Journal of Hydraulic Research 41 (6), 565–577.
- Sabbagh-Yazdi, S., B, N.M., Zounemat-Kermani, M., 2007. Velocity profile over spillway by finite volume solution of slopping depth averaged flow. In: 2nd IASME/WSEAS Int. Conf. on Continuum Mechanics, World Scientific and Engineering Academy and Society (WSEAS), Portoroz, Slovenia, pp. 99–106.
- Sabbagh-Yazdi, S., Jamshidi, M., 2012. A depth-averaged hydrodynamic model for gradual breaching of embankment dams due to overtopping considering suspended sediment transport. Journal of Hydraulic Engineering(accepted, pre-published).
- Saiedi, S., 1981a. Experience in design of a laboratory flume for sediment studies. International Journal of Sediment Research 8 (3), 89–101.
- Saiedi, S., 1981b. A non-dimensional coupled numerical model of alluvial flow. International Journal of Sediment Research 9 (2), 59–79.
- Saiedi, S., 1997. A coupled modeling of alluvial flows. Journal of Hydraulic Engineering 123 (5), 440–446.
- Samani, J.M.V., Kouwen, N., 2002. Stability and erosion in grassed channels. Journal of Hydraulic Engineering 128 (1), 40–45.
- Sametz, L., 1981. Beitrag zur Frage der Flutwellenbildung bei progressiven Dambrüchen infolge Überströmung. Ph.D. Thesis, Institut für Wasserbau und Wasserwirtschaft, TU Graz, (in German).
- Savary, C., 2007. Transcritical transient flow over mobile beds boundary conditions treatment in a two-layer shallow-water model. Ph.D. Thesis, L'Université catholique de Louvain.
- Schmocker, L., Hager, W., 2008. Hydraulik von Deichbrüchen. In: Minor, H.-E. (Ed.), Internationales Symposium 2008 Zürich, Neue Anforderungen an den Wasserbau, Zürich, Switzerland, (in German).

- Schmocker, L., Hager, W., 2009. Modelling of dike breaching due to overtopping. *Journal of Hydraulic Research* 47 (5), 585–597.
- Schmocker, L., Rühli, E., Mayor, P., Weitbrecht, V., Springman, S., Boes, R., 2011. Design and hydraulic modelling of a fuse plug spillway. In: Schleiss, A., Boes, R. (Eds.), *Dams and Reservoirs under Changing Challenges*, CRC Press, Lucerne, Switzerland.
- Schubert, J., Sanders, B., Smith, M., Wright, N., 2008. Unstructured mesh generation and landcover-based resistance for hydrodynamic modeling of urban flooding. *Advances in Water Resources* 31 (12), 1603–1621.
- Schuster, R., Costa, J., 1986. Landslide dams: Processes, risk, and mitigation. *American Society of Civil Engineers Geotechnical Special Publication* 3, 1–20.
- Shields, A., 1936. Anwendung der Ähnlichkeitsmechanik und der Turbulenzforschung auf die Geschiebebewegung. *Mitteilungen der Preussischen Versuchsanstalt für Wasserbau und Schiffbau* Nr.6, Berlin, Germany, (in German).
- Singh, V., 1996. *Dam Breach Modeling Technology*. Kluwer Academic Publishers.
- Singh, V., Scarlatos, P., Collins, J., Jourdan, M., 1988. Breach erosion of earthfill dams (beed) model. *Natural Hazards* 1 (2), 161–180.
- Soares-Frazao, S., Canelas, R., Cao, Z., Cea, L., Chaudhry, H., Moran, A.D., Kadi, K.E., Ferreira, R., Cadorniga, I.F., Gonzalez-Ramirez, N., Greco, M., Huang, W., Imran, J., Coz, J.L., Marsooli, R., Paquier, A., Pender, G., Pontillo, M., Puertas, J., Spinewine, B., Swartenbroekx, C., Tsubaki, R., Villaret, C., Wu, W., Yue, Z., Zech, Y., 2012. Dam-break flows over mobile beds: experiments and benchmark tests for numerical models. *Journal of Hydraulic Research* 50 (4), 364–375.
- Soares-Frazao, S., Grelle, N., Spinewine, B., Zech, Y., 2007. Dam-break induced morphological changes in a channel with uniform sediments: measurements by a laser-sheet imaging technique. *Journal of Hydraulic Research* 45 (Supplement 1), 87–95.
- Spinewine, B., 2005. Two-layer flow behaviour and the effects of granular dilatancy in dam-break induced sheet-flow. Ph.D. Thesis, L'Université catholique de Louvain.

- Spinewine, B., Capart, H., le Grelle, N., Soares-Fraza, S., Zech, Y., 2007. Experiments and computations of bankline retreat due to geomorphic dam-break floods. In: Bousmar, D., Zech, Y. (Eds.), *Proceedings of River Flow 2002*, Balkema, Louvain-la-Neuve, Belgium, pp. 651–661.
- Stanczak, G., 2008. Breaching of sea dikes initiated from the seaside by breaking wave impact. Ph.D. Thesis, Leichtweiß-Institut der Universität Braunschweig and Faculty of Engineering of University of Florence.
- Steffler, P., Jin, Y.-C., 1993. Depth-averaged and moment equations for moderately shallow free surface flow. *Journal of Hydraulic Research* 21 (1), 5–17.
- Stoffel, M., Huggel, C., 2012. Effects of climate change on mass movements in mountain environments. *Progress in Physical Geography* 36 (3), 421–439.
- Stoker, J., 1957. *Water Waves. The Mathematical Theory with Applications*. Interscience, London.
- Succi, S., 2001. *The Lattice Boltzmann Equation for Fluid Dynamics and Beyond*. Clarendon Press Oxford, Oxford.
- Swartenbroekx, C., Soares-Fraza, S., Staquet, R., Zech, Y., 2010. Two-dimensional operator for bank failures induced by water-level rise in dam-break flows. *Journal of Hydraulic Research* 48 (3), 302–314.
- Takahashi, T., 1981. Debris flow. *Annual Reviews of Fluid Mechanics* 13, 57–77.
- Terzaghi, K., 1936. The shearing resistance of saturated soil and the angle between the planes of shear. In: *Proceedings of 1th International Conference on Soil Mechanics and Foundation Engineering*, pp. 54–56.
- Tingsanchali, T., Chinnarasri, C., 2001. Numerical modelling of dam failure due to flow overtopping. *Hydrological Sciences Journal* 46 (1), 113–130.
- Toro, E., 2001. *Shock-Capturing Methods for Free-Surface Shallow Flows*. John Wiley & Sons, Inc.
- Valiani, A., Caleffi, V., Zanni, A., 2002. Case study: Malpasset dam-break simulation using a two-dimensional finite volume method. *Journal of Hydraulic Engineering* 128 (5), 460–472.

- van der Smán, R., Ernst, M., 1999. Convection-diffusion lattice Boltzmann scheme on a orthorhombic lattice. *Journal of Computational Physics* 160, 766–782.
- van Genuchten, M., 1980. A closed-form equation for predicting the hydraulic conductivity of unsaturated soils. *Soil Science Society of America Journal* 44 (5), 892–898.
- van Rijn, L., 1984. Sediment transport 2: Suspended load transport. *Journal of Hydraulic Engineering* 110 (11), 1613–1641.
- van Rijn, L., 1989. Handbook: sediment transport by current and waves. Report H 461, Delft Hydraulics, Netherlands.
- Vanapalli, S., Fredlund, D., Pufahl, D., Clifton, A., 1996. Model for the prediction of shear strength with respect to soil suction. *Canadian Geotechnical Journal* 33, 379–392.
- Verruijt, A., 2006. Soil Mechanics. Online Script, <http://www.scribd.com/doc/28778842/Soil-Mechanics-Book-civil-engineering>, Delft University of Technology.
- Vogel, T., van Genuchten, M., Cislerova, M., 2001. Effect of the shape of the soil hydraulic functions near saturation on variably saturated flow predictions. *Advances in Water Resources* 24 (2), 133–144.
- Vonwiller, L., Boes, R., Volz, C., 2011. Numerical simulation of small earthfill dam breaching. In: Zenz, G., Hornich, R. (Eds.), *International Symposium UFRIM, Urban Flood Risk Management*, Graz, Austria.
- Voss, C., Provost, A., 2010. SUTRA, a model for saturated-unsaturated variable-density ground-water flow with solute or energy transport. *Water-resources investigations report 02-4231*, U.S. Geological Survey, <http://water.usgs.gov/nrp/gwsoftware/sutra/sutra.html>.
- Wahl, T., 1998. Prediction of embankment dam breach parameters: A literature review and needs assessment. *Dam safety research report DSO-98-004*, U.S. Department of the Interior, Bureau of Reclamation.
- Wang, Z., Bowles, D., 2006. Three-dimensional non-cohesive earthen dam breach model. Part 1: Theory and methodology. *Advances in Water Resources* 29 (10), 1528–1545.

- Wong, M., Parker, G., 2006. Reanalysis and Correction of Bed-Load Relation of Meyer-Peter and Müller Using Their Own Database. *Journal of Hydraulic Engineering* 132 (11), 1159–1168.
- Worni, R., Stoffel, M., Huggel, C., Casteller, A., Volz, C., Luckman, B., 2012. Analysis and dynamic modeling of a moraine failure and glacier lake outburst flood at Ventisquero Negro, Patagonian Andes (Argentina). *Journal of Hydrology* 444-445, 134–145.
- Wu, W., 2004. Depth-averaged two-dimensional numerical modeling of unsteady flow and nonuniform sediment transport in open channels. *Journal of Hydraulic Engineering* 130 (10), 1013–1024.
- Wu, W., 2007. *Computational River Dynamics*. Taylor & Francis / Balkema, Leiden, Netherlands.
- Wu, W., Marsooli, R., He, Z., 2012. Depth-averaged two-dimensional model of unsteady flow and sediment transport due to noncohesive embankment break/breaching. *Journal of Hydraulic Engineering* 138 (6), 503–516.
- Wu, W., Wang, S., 2008. One-dimensional explicit finite-volume model for sediment transport. *Journal of Hydraulic Research* 46 (1), 87–98.
- Xia, J., Lin, B., Falconer, R., Wang, G., 2010. Modelling dam-break flows over mobile beds using a 2d coupled approach. *Advances in Water Resources* 33 (2), 171–183.
- Yoon, T., Kang, S., 2004. Finite volume model for two-dimensional shallow water flows on unstructured grids. *Journal of Hydraulic Engineering* 130 (7), 678–688.
- Zoppou, C., Roberts, S., 2003. Explicit schemes for dam-break simulations. *Journal of Hydraulic Research* 129 (1), 11–34.